DTU Library

Cable Aerodynamic Control
Wind tunnel studies

Kleissl, Kenneth

Publication date:
2013

Document Version
Publisher's PDF, also known as Version of record

[Link back to DTU Orbit](#)

Citation (APA):
Kleissl, K. (2013). *Cable Aerodynamic Control: Wind tunnel studies*. Technical University of Denmark. B Y G D T U. Rapport

Cable Aerodynamic Control

- Wind tunnel studies

Kenneth Kleissl

Ph.D. Thesis

Supervisors:

Associate Professor Christos T. Georgakis
Associate Professor Holger Koss, DTU Byg

Assesment Committee:

Dr. Guy L. Larose, National Research Council Canada, Canada
Ph.D Allan Larsen, COWI A/S, Denmark
Associate Professor Gregor Fischer, DTU Byg

Cable Aerodynamic Control
-Wind tunnel studies

Preface

This thesis is submitted in partial fulfilment of the requirements for the Danish Ph.D. degree. The work has been carried out at the Department of Civil Engineering at the Technical University of Denmark and took place in the period between September 2010 to December 2012, with Associate Professor Christos T. Georgakis as main supervisor and Associate Professor Holger Koss as co-supervisor.

This thesis is based upon published and under-review articles in ISI journals. The first part introduces the main problems and the motivation of this work, while each of the subsequent five chapters are made up by separate and unedited reproduction of above mentioned journal papers. Lastly, the combined work is discussed and conclusions are made in respect to the initially introduced problems, together with other outcomes of the work.

Kongens Lyngby, the 31st December 2012

Kenneth Kleissl

Preface to published version

The thesis was defended at a public defence on Tuesday 14 May 2013. The official assessment committee consisted of Associate Professor Gregor Fischer (chairman), Technical University of Denmark, Ph.D Guy L. Larose, National Research Council Canada, and Ph.D Allan Larsen, COWI A/S.

Lyngby, the 14th May 2013

Kenneth Kleissl

Acknowledgements

Firstly, I would like to express my deepest thanks to my main supervisor Associate Prof. Christos T. Georgakis for his support and encouragement throughout the entire course of this project and for intrusting me with the freedom to work in my own way, for which I am grateful. Also a special thank to my co-supervisor Associate Prof. Holger Koss for sharing his experience within experimental wind tunnel testing and his valuable discussions and brainstorming.

Lastly, I am grateful for the loving support of my friends and family, in particular my wife Sussi Kleissl for being there every step of the way.

Abstract

This dissertation investigates the possibility of preventing wind-induced cable vibrations on cable-stayed bridges using passive aerodynamic means in the form of cable surface modifications. Especially the phenomenon of rain-wind induced vibrations, which is known as the most common type of these vibrations and capable of inducing severe vibrations. The recent increase in the number of cable stayed bridges continuously becoming longer and lighter have resulted in a high number of observations of cable vibrations.

A detailed literature review of the various types of passive means led to a categorization of the different control technics together with an identification of two key mechanisms for reduction of the design drag force. During this project extensive experimental work examining the aerodynamics of the currently used cable surface modifications together with new innovative proposals have been conducted.

The two current prevailing systems consisting of helically filleted cables and cables with a pattern-indented surface were directly compared under the same conditions and both applications were found with attractive properties. The pattern-indented surface maintained a low supercritical drag force due to the high intensity of streamwise vorticity, whereas the helical fillets resulted in a more gradual flow transition because of the spanwise variation. During yawed flow conditions, the asymmetrical appearance of the helical solution was found to induce a significant lift force with a sudden change in the lift during the flow transition, which could be the reason for a dry limited amplitude vibration observed only for cables with helical applications. Dry inclined galloping was only seen with the plain reference cable model, even though only the helically filleted cable was capable of reducing the intensity of the axial flow and disrupting the near wake flow structures. Similar studies during wet conditions with artificial simulation of light rain in the wind tunnel showed that the plain cable suffered from severe rain-wind induced vibrations. But despite the presence of both upper and lower rivulets on the surface modified systems, no significant rain-wind induced vibrations were successfully simulated.

Finally, by combining the understanding from the state of the art in the field and the experience from the currently applied solutions, several new innovative surface modified systems were tested. While a proper discrete helical arrangement of Cylindrical Vortex Generators resulted in a superior drag performance, only systems applying "mini-strakes" were capable of complete rivulet suppression. When the strakes was positioned in a staggered helical arrangement, the innovative system avoided all previous mentioned types of vibrations, had a supercritical drag similar to that of the pattern-indented surface, and a superior suppression of rivulets compared to any of the currently applied systems.

Resumé

Denne afhandling undersøger muligheden for at forhindre vind-inducerede kabelsvingninger på skråstagsbroer ved hjælp af passive aerodynamiske midler i form af kabeloverflademodifikationer. Fænomenet Rain-Wind Induced Vibrations er kendt som den mest almindelige type af disse svingninger og er i stand til at inducere kraftige vibrationer. Den seneste udvikling i antallet af skråstagsbroer, der i stigende grad bliver længere og lettere, har resulteret i et stort antal observationer af kabelsvingninger.

En detaljeret gennemgang af litteraturen om de forskellige typer af passive midler har ført til en kategorisering af de forskellige kontrolteknikker samt en identifikation af to centrale mekanismer til brug for reduktion af vind-belastningen ved design. Undervejs i projektet er der udført et omfattende eksperimentelt arbejde i en klimatisk vindtunnel med henblik på at undersøge aerodynamikken af de aktuelt anvendte kabeloverflademodifikationer samt en sammenligning med nye innovative forslag.

De to pt. fremherskende systemer, der består af kabler med spiralformede fremspring og kabler med mønstrede fordybninger i overfladen, er sammen-lignet under identiske forhold, hvor de begge viste at have positive egenska-ber. Overfladen med de mønstrede fordybninger opretholdte en lav super-kritisk vindbelastning, forårsaget af en unik langsroterende hvirveldannelse, mens de spiralformede fremspring resulterede i en mere gradvis overgang i strømningstilstand på grund af den geometriske variation langs kablet. Ved skrå vindforhold forvoldte den asymmetriske fremtræden af det spiralformede kabel en betydelig løftekraft og en pludselig ændring i denne ved overgangen til superkritisk strømningstilstand. Dette kan være årsagen til de amplitude-begrænsede svingninger, der alene er observeret for kablerne med spiralfor-mede fremspring og under tørre forhold. Fænomenet Dry Inclined Galloping blev alene observeret for kablet med en plan overflade, på trods af at kun kab-let med de spiralformede fremspring var i stand til at reducere intensiteten af den aksiale strømning og forstyrre hvirvelstrukturerne på læsiden af kablet. Lignende undersøgelser under simulering af let regn viste, at kablet med en plan overflade led af voldsomme regn- og vind-forårsagede svingninger. På

trods af tilstedeværelsen af løbende regnvand på både over og undersiden af de to overflademodificerede kabler, forekom der ingen væsentlige regn- og vind-inducerede svingninger for disse kabler.

På baggrund af den opnåede forståelse fra litteraturgennemgangen og erfaringer fra forsøgene med de allerede anvendte løsninger, er flere nye innovative kabeloverflader blevet testet. Mens et specifikt adskilt spiralformet arrangement af cylindriske hvirvelgeneratorer resulterede i en overlegen vindbelastningsperformance, var det kun systemerne, som anvendte "strakes", der var i stand til fuldstændig at undertrykke formationerne af løbende regnvand. Når disse "strakes" blev anbragt i et forskudt spiralformet arrangement, undgik kablet alle de tidligere nævnte typer af vibrationer, samtidigt med at det havde en superkritisk vindbelastning svarene til overfladen med de mønstrede fordybninger. Dette samtidig med at kablet stadig havde en overlegen undertrykkelse af de løbende regnvandsformationer i forhold til de nuværende anvendte systemer.

Contents

Chapter 1

Introduction

Wind loads on structures are of increasing interest with the continuous development of longer, lighter, and more slender structures. The reduced stiffness and lowered inherent structural damping results in the structures becoming more susceptible to wind action effects and thus more prone to flow-induced vibrations. It is therefore of increasing importance that adequate thought are given to the wind actions at the design phase and that sufficient understanding and control strategies are available for the designers.

One such example is the recent years development of cable stay bridges. Starting around the 1970s, cable stay bridges have become increasingly popular, as improvements in materials and technology have resulted in cable stays bridges becoming a fast and economical way to cross medium to long spans. But with the rapidly increasing span lengths new aerodynamic phenomenons are arising, forcing an increased understanding of these wind-structure interactions.

While the long and light bridge decks already in the forties had their first setback in relation to the appearance of flutter instability, such as at the Tacoma Narrows Bridge, it was not before 1986 that cable stays experienced the first severe type of vibration: the occurrence of Rain-Wind Induced Vibration (RWIV). This strong vibration of inclined cable stays of up to 2 metres amplitude occurring under moderate windy and rainy days was firstly reported by Hikami (1986). Examples of bridges with a history of cable vibrations include the Second Severn Crossing (UK), Øresund Bridge (DK-SE), Dongting Bridge (CN), and the Fred Hartman Bridge (USA), to name a few. With RWIV still making up about 95% of the cable stay vibration incidences, there is a major interest in being able to fully control this type of vibrations. Photos showing the spectacular nature of these vibrations are presented in Figure 1.1.

Figure 1.1*: Photos of excessive cable vibrations. (left) is from Second Severn Crossing and (right) is from the Meikou bridge (photo by Prof. Tomomi Yagi).*

The remaining vibration incidences are made up by several other known aerodynamic vibration mechanisms, broadly categorised as traditional von Kármán and high reduced-velocity vortex-shedding, drag crisis, dry inclined galloping and ice or sleet-induced.

Even though the excessive vibrations rarely lead to ultimate cable failure, both premature fatigue damage and bridge closures are common issues. Moreover bridge operators are concerned about the users' confidence and their apparent feeling of safety when crossing the bridge.

Even in the ultimate limit state, the stay cable aerodynamics are of increasing importance due to high static wind loading. For the longer spanning stay cable bridges the ratio of horizontal wind loading induced through the cables are increasing compared to the bridge deck and pylons and often exceeds the combined effect of these. This is mostly because the cables are the main contributor to bridge span stiffness and retaining the stiffness for increasing spans and thus cable lengths, requires an increased cross-sectional cable area or number of cables. The longest spanning stay cable bridges experience up to 70% of the total horizontal wind loading through the stay cables. The drag force performance of stay cables are therefore becoming essential for further development of the bridge span lengths.

The cable suppliers or the owners of cable-supported bridges facing these challenges often revert to counter-measures such as mechanical dampers placed near the bridge deck or crossties to reduce vibrations. These applications, often considered as aesthetically disturbing, are becoming less effective for the increasing spans. The cables would greatly benefit from supplementing passive aerodynamic vibration control methods using shape or surface modifications. Moreover, such aerodynamic means may also provide the cables with a reduced drag force – regardless of bridge span.

Aerodynamic means of vibration control are usually developed in an ad-hoc fashion and are mostly known in relation to the countering of classical von Kármán vortex shedding, which may result in Vortex Induced Vibration (VIV). Such aerodynamic control, significantly reducing the need of damping devices, can also be applied successfully on cable stays if designed accordingly.

Today two prevailing systems exist: the helical fillets and the pattern-indented surface, both shown in Figure 1.2.
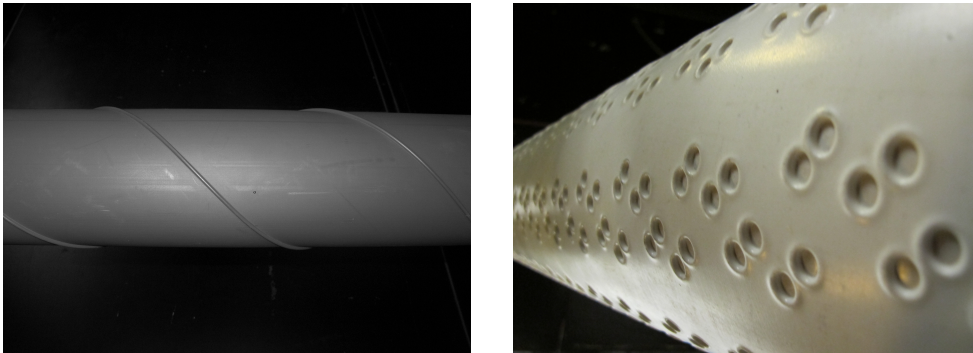
Figure 1.2: *Photos of the two prevailing aerodynamic control surfaces: the helical fillets (left) and the pattern-indented surface (right).*

Helical fillets are comprised of two near round protrusions positioned on the cable surface in a spiral pattern whilst the pattern-indented surface consists of a discrete distribution of dimples with a protruding periphery. Both of the prevailing systems have a beneficial effect towards the avoidance of RWIV and the need for additional mechanical damping devices is reduced. Though despite the positive performance reported from wind tunnel studies, observations on bridges by cable manufactures and bridge operators have led to reports of incidences where these systems are incapable of hindering cable vibrations. Today the only solution to this is to increase the level of mechanical damping.

1.1 Objectives

The fact that two significantly different prevailing systems are still both in use with the intent of countering the same problem, indicates that an ideal application has not yet been developed. The overall objective is therefore to prevent or at least significantly reduce the occurrence of cable vibrations, such as RWIV, on cable stay bridges through means of passive aerodynamic control, doing so with a minimum negative impact on, or preferably a reduction of, the design drag coefficient.

1.2　　Methodology

To achieve the aforementioned objectives the present work is divided into three parts:

- The first part involves an examination of the state of the art and an understanding of how passive aerodynamic means affect water rivulet formation and RWIV. Furthermore their drag coefficient and possible mechanisms of drag reduction are examined.

- Secondly the present understanding of the currently used passive aerodynamics means on bridges stay cables should be enhanced and a direct comparison of them is undertaken, as different researchers, in different facilities, with varying wind-tunnel flow characteristics and performance, have developed each separately.

- The third and final part is to use this newly gained understanding and experience to propose a more suitable application in relation to the aforementioned objectives.

The complex interaction between the stay cable and the two moving fluids present during RWIV, together with the incomplete understanding of the phenomenon and the three-dimensional turbulence structures introduced by the surface modifications makes it most difficult to use any of the available numerical methods. The present work is therefore entirely based on wind tunnel testing.

As the disturbing effect of the surface modifications on the water rivulets is essential to this work, a climatic wind tunnel facility allowing for proper simulation of rain is a necessity. Furthermore as the presence of water rivulets prevent the use of proper scaled cable models due to the importance of surface tension and surface wettability, full-scale sectional cable models are also needed. This was in 2010 made possible by the construction of a collaborative DTU-FORCE Technology testing facility funded by Femern A/S, at which all experimental work during this project was carried out.

1.3　　Thesis outline

The present thesis is divided into 7 chapters. This introduction (Chapter 1) is followed by 5 chapters each made up by separate and unedited reproductions of journal papers either already published and in the process of being so.

- Chapter 2 contains a preliminary study covering rather significant shape modifications.

- Chapter 3 presents a detailed literature review of passive aerodynamic means.

- Chapter 4 is the first part of the detailed comparison of the existing solutions covering experiments with statically fixed cable models.

- Chapter 5 is the second part of the detailed comparison of the existing solutions covering experiments with dynamically supported cable models.

- Chapter 6 covers the innovative surface modifications proposed.

Finally, a summary of the main conclusions as well as recommendations for future research are presented in Chapter 7.

Chapter 2

Preliminary work

This chapter is a study based on experimental work carried out in Kleissl (2009) and considers the effects of rather significant shape modifications. At this point the above stated objective was not finalized and it is therefore only considered as a preliminary study.

Paper I

"Aerodynamic control of bridge cables through shape modification: A preliminary study"

K. Kleissl & C.T. Georgakis

Aerodynamic control of bridge cables through shape modification: A preliminary study

K. Kleissl *, C.T. Georgakis

Department of Civil Engineering, Technical University of Denmark, Building 118, Brovej, 2800 Kgs. Lyngby, Denmark

A R T I C L E   I N F O

A B S T R A C T

This paper examines the viability of modifying bridge cable shape and surface for the purpose of controlling wind-induced vibrations. To this end, an extensive wind-tunnel test campaign was carried out on various cable shapes about the critical Reynolds number region. Cable shapes were chosen to passively modify the flow in a particular manner. Tested shapes included those which have some form of waviness, faceting and shrouding. Section models were tested using a static inclined rig, allowing them to be installed at yawed cable–wind angles for both smooth and turbulent flow conditions. The aerodynamic damping of the tested cylinders is evaluated by applying both 1- and 2-dof quasi-steady aerodynamic instability models. This allows for the prediction of regions of aerodynamic instability, as a function of flow angle and Reynolds number. Whilst the plain, wavy and faceted cylinders are predicted to suffer from either dry inclined galloping, "drag crisis" or Den Hartog galloping, the shrouded cylinder is found to be stable for all angles of attack, albeit with an increase in drag at typical design wind velocities. Finally, turbulent flow is found to introduce an increased amount of aerodynamic damping mainly by providing a more constant lift force over tested Reynolds numbers.

1. Introduction

The existence of wind-induced vibrations of cables on cable-supported bridges has become increasingly apparent over the last 20 years (Kumarasena et al., 2007). These vibrations can be predominately attributed to several known aerodynamic vibration mechanisms, broadly categorised as wind–rain–cable interaction, traditional von Kármán and high reduced-velocity vortex-shedding, drag crisis, dry inclined cable galloping and ice or sleet-induced. Examples of bridges with a history of cable vibrations include the First and Second Severn Crossings, Øresund Bridge, Great Belt East Bridge, Faroe Bridge, Humber Bridge and the Fred Hartman Bridge. Reports of vibrations on Japanese bridges are also plentiful (Hikami, 1986; Hikami and Shiraishi, 1988; Matsumoto et al., 2003; Saito et al., 1994). A general overview of excitation mechanisms can be found in Païdoussis et al. (2011).

Aerodynamic vibration control refers to the means of eliminating undesirable vibrations of a structure through careful modification of the structural shape and surface, either passively or actively. To date, aerodynamic vibration control of cables has focused mainly on the alleviation of rain–wind-induced vibrations, as they tend to cause the most severe

---

* Corresponding author. Tel.: +45 4525 5048; fax: +45 4588 3282.
 E-mail address: kenk@byg.dtu.dk (K. Kleissl).
 URL: http://www.cesdyn.byg.dtu.dk (C.T. Georgakis).

motions. As the drag forces on the cables can be a decisive parameter in the overall design of a cable-supported bridge, efforts have been made to generate counter-measures effective in mitigating rain–wind-induced vibrations that also keep the drag coefficient at a minimum. Applied aerodynamic vibration control measures have included helixes (Flamand, 1995), longitudinal grooves and protuberances (Saito et al., 1994) and the introduction of discrete surface roughness using dimples (Miyata et al., 1994). These counter-measures have been found to be particularly effective against rain–wind-induced vibrations, as rivulet formation is retarded or blocked.

Nevertheless, the aforementioned vibration control measures have not been designed or tested to counter all of the known aerodynamic vibration mechanisms. This paper presents the results of preliminary investigations into the performance of several new cable shapes and surfaces, designed for the elimination of not only rain–wind-induced vibrations, but also vibrations due to vortex-shedding and other forms of cable galloping.

2. Choice of shapes

Based on the current level of understanding of wind-induced cable vibration mechanisms, several main flow features attributable to each mechanism can be identified. For rain–wind-induced vibrations, the formation of one or two longitudinal water rivulets seems to be a necessary prerequisite for the generation of cable motion. For galloping, an unfavourable variation or value of lift over the critical Reynolds number range is important for the development of negative aerodynamic damping. In the case of vortex-shedding, a uniform cable profile allows for the development of correlated vortex streets over long lengths of the cable. Tactically, an appropriate selection of shape modification would account for and/or counter the varying flow features of each mechanism, whilst keeping the existing benefits of the circular cable section.

Bearing this in mind and after having reviewed many existing proposals for cable shape modification (Kleissl, 2009), three shape modifications to the plain circular cylinder were chosen for wind-tunnel testing. As a reference, a plain circular cylinder was also tested concurrently. The shape modifications included shrouding, waviness and hexagonal facetting (see Fig. 1).

2.1. Shrouded cylinder

Perforated shrouding of a cylinder was initially proposed by Price (1956). In the two decades that followed, extensive research was undertaken on its application to chimneys (Knell, 1969; Walshe, 1968; Walshe and Wootton, 1970; Wootton and Yates, 1970; Zdravkovich and Volk, 1972), as it was found effective at suppressing vortex-induced vibrations. More recently, it has been used for vortex-shedding suppression on very long submerged cables in the offshore industry (Allen and Henning, 2004) and for bridge pylons for the Stretto di Messina Bridge (Larose et al., 1993, 1995).

Fig. 1. Tested models. (a) Circular cylinder. (b) Shrouded cylinder. (c) Wavy cylinder. (d) Facetted cylinder.

The perforated shrouding is chosen as it should be able to suppress vortex-shedding, cable axial flow and rivulet generation, whilst retaining an inner diameter Reynolds number-independent drag coefficient of 0.8. The shroud is believed to be effective due to three important processes:

- Significant base bleed as the flow is injected into the dead air region immediately behind the cylinder increasing the leeward pressure.
- Flow is ejected into the free shear layer making it turbulent and thicker.
- A vortex formation region that is about twice as long as on a plain cylinder.

The geometric parameters of the perforation were chosen so as to achieve the lowest possible drag according to the data available in ESDU 80025 (1986). This resulted in a circular hole pattern with a triangular distribution and a hole area of $0.269D$, where D is the diameter of the inner cylinder. The shroud of the present study had an open area ratio of 38.7% and a cylinder/shroud-diameter ratio of 0.838 corresponding to a shroud gap size of $w_{gap}=0.097D$.

2.2. Wavy cylinder

The wavy cylinder was constructed to have an along-length sinusoidal variation in profile according to Lam et al. (2004), Ahmed and Bays-Muchmore (1992) and Ahmed et al. (1993). According to the aforementioned authors, this variation in profile produces a reduction in drag in the subcritical Reynolds number region, as the waviness is believed to disorganise and reduce the correlation length for vortex-shedding. Furthermore, the waviness was expected to hinder the formation of any secondary axial flow when tested for yawed angles.

To avoid an unnecessarily large increase in drag, cylinder diameter enlargement was kept to a minimum. The choice of a sinusoidal surface variation of $a=0.0486D_{min}$ leads to an average increase in diameter of approximately 10%. The corresponding sinusoidal wavelength or period of $\lambda=1.649D_{min}$ was chosen, which results in a degree of cylinder obliqueness of $a^2/(\lambda D_{min})=0.00143$, expressed in the normalised form proposed by Lam et al. (2004).

2.3. Faceted hexagonal cylinder

Bearman and Owen (1998) showed that drag reduction can be achieved through the introduction of a wavy pattern of clearly defined flow separation lines on the surface of a cylinder. This can be achieved through surface faceting. The fixed separation lines stabilise the drag over Reynolds number and the wavy pattern helps the avoidance of Den Hartog galloping. To achieve the desired variation on flow separation, flat irregular trapezoidal facets (see Fig. 2(a)) were periodically positioned in opposing directions consecutively along the length of the cylinder. The longitudinal length of this varying geometry was chosen so that the model had the same number of periods as for the wavy test model. The resulting pattern can be seen in Figs. 2(a) and (b).

The maximum increase in base diameter was set to 20%, again to limit the increase in drag. This resulted in a protrusion of $e=0.1 \cdot D$, as illustrated in Fig. 2(a), and thus a maximum to minimum width ratio of $B/b=1.75$ for each single facet.

The inspiration for this shape comes from Constantin Brancusi's unique architectonic sculpture Endless Column, which has been referred to as "aeroelastically indifferent" owing to its remarkable aeroelastic stability (Dragomirescu et al., 2009).
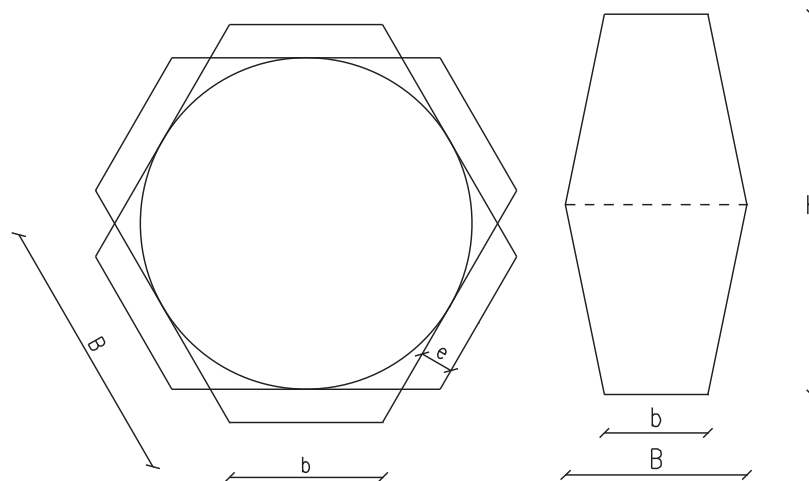

Fig. 2. (a) Cross-section of the hexagonal faceted cylinder and (b) single facet.

3. Aerodynamic instability

Although the aforementioned cable shapes were chosen to control a wide variety aerodynamically induced vibrations, only those from tests in dry conditions and resulting from negative aerodynamic damping are presented herewith. Low drag coefficients and dry galloping stability were considered "gateway" criteria when selecting modifications for further examination.

Negative net damping arises when the magnitude of the negative aerodynamic damping exceeds that of the cables mechanical damping. As the mechanical damping of a cable can often be considered negligible, the theoretical evaluation of aerodynamic instability is based only on the evaluation of aerodynamic damping in its nondimensional form. The nondimensional aerodynamic damping parameter Z_a is defined as

$$Z_a = \frac{\zeta_a m f_n}{\mu},\tag{1}$$

where ζ_a is the aerodynamic damping ratio, m is mass per unit length, μ is the dynamic fluid viscosity and f_n is the undamped natural frequency.

The aerodynamic damping of the tested cylinders is evaluated by applying both 1- and 2-dof quasi-steady aerodynamic instability models proposed by Macdonald and Larose (2006, 2008a). For these models to be valid, it is assumed that the reduced velocity for the cylinder ($V/f_n D$) is greater than 20. The aerodynamic damping is given by Eqs. (2) and (3) for the 1- and 2-dof model, respectively, where Eq. (3) is a simplified expression only covering cylinders with rotational symmetry:

$$Z_a = \frac{Re}{8\pi}\cos(\alpha)\left\{\cos(\alpha)\left[C_D\left(2\sin(\phi)+\frac{\tan^2(\alpha)}{\sin(\phi)}\right)+\frac{\partial C_D}{\partial Re}Re\sin(\phi)+\frac{\partial C_D}{\partial\phi}\cos(\phi)-\frac{\partial C_D}{\partial\alpha}\frac{\tan(\alpha)}{\sin(\phi)}\right]\right.$$
$$\left.-\sin(\alpha)\left[C_L\left(2\sin(\phi)-\frac{1}{\sin(\phi)}\right)+\frac{\partial C_L}{\partial Re}Re\sin(\phi)+\frac{\partial C_L}{\partial\phi}\cos(\phi)-\frac{\partial C_L}{\partial\alpha}\frac{\tan(\alpha)}{\sin(\phi)}\right]\right\},\tag{2}$$

$$Z_a = \Re\left[\frac{Re}{16\pi}\left\{h(C_D)-\sqrt{g^2(C_D)+g^2(C_L)-h^2(C_L)}\right\}\right],\tag{3}$$

in which $\Re[\ ]$ indicates the real part and where $g(C_F)$ and $h(C_F)$ are given by

$$g(C_F) = C_F\left(2\sin\phi-\frac{1}{\sin\phi}\right)+\frac{\partial C_F}{\partial Re}Re\sin\phi+\frac{\partial C_F}{\partial\phi}\cos\phi,$$

$$h(C_F) = g(C_F)+\frac{2C_F}{\sin\phi}.$$

It should be noted that in the above expressions, the nondimensional aerodynamic damping parameter is a function of only the force coefficients, Reynolds number, the cable–wind angle ϕ and the angle of attack α.

Both 1- and 2-dof models were employed, as the 2-dof solution asymptotically moves towards the 1-dof solution when the in- and out-of-plane frequencies of the cable start to detune (Macdonald and Larose, 2008b). By considering both models, vertical bridge hangers (perfectly tuned) and long inclined stay cables (detuned) are covered. For the evaluation of aerodynamic instability, the 1-dof model is applied for the detuned cases using a worst case vibration direction, i.e. angle of attack, while for perfectly tuned cases the 2-dof model is applied using a closed form solution for a perfectly tuned system. Gjelstrup and Georgakis (submitted for publication) have developed a 3-dof aerodynamic instability model, but this has not been employed, as the tests revealed an absence of measurable moment coefficients.

As a word of caution, it should be clarified that the mechanism(s) behind inclined cable vibrations is still partially unresolved and it is unknown if the quasi-steady theory is applicable at full scale on real bridge stays. As the stability observations in this preliminary study are exclusively based on quasi-steady model predictions, this might lead to potential limitations regarding the findings herewith. Further investigations and experimental full scale validation are therefore necessary to support these findings.

4. Wind-tunnel tests

Both the reference and shape-modified sections were tested for varying flow conditions, angles of attack and cable inclinations at the closed circuit wind-tunnel facility at FORCE Technology, Lyngby, Denmark. The wind-tunnel test section has a height of 0.70 m and a width of 1.00 m. Wind velocities of up to 60 m/s can be generated in smooth flow ($I_x=0.5\%$ turbulence intensity) and 35 m/s in turbulent flow, with an along-wind turbulence intensity of approximately $I_x=6.5\%$. The turbulent flow is generated through a turbulence grid installed in the wind tunnel 0.84 m upstream of the test models. The turbulence grid consists of a square wooden mesh with centre-to-centre distance of 0.08 m and a grid beam width of 0.018 m. In turbulent conditions, the resulting integral length scale of the flow is estimated to be $L_{ux}/D=0.6$ (Fig. 3). Even when considering model scaling, this is well below what would be found in nature, but this is a well-known problem when testing in wind-tunnels.
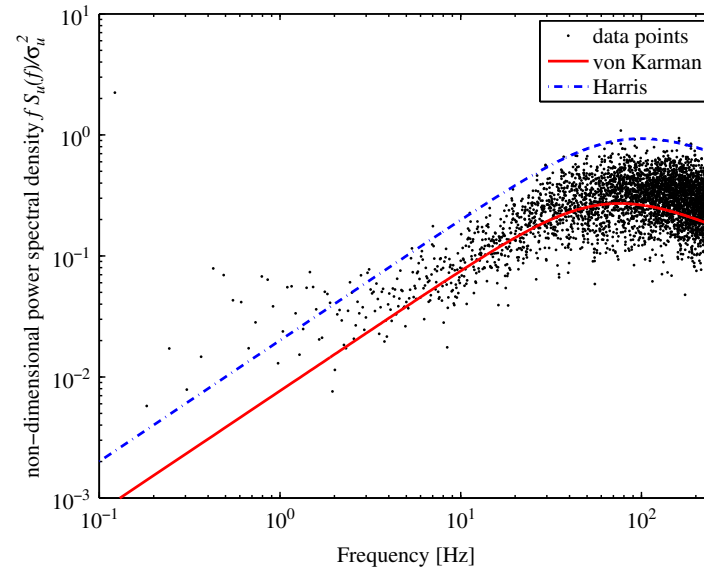
Fig. 3. Nondimensional power spectral density for turbulent flow at 20 m/s. The fit of the Harris spectrum required a length downscaling by a factor of 5000 in relation to atmospheric turbulence.

Fig. 4. Illustration of the test set-up. (a) Outside view on the testing section. (b) Section model installed in the inclined test rig.

4.1. Test set-up

The reference section model and cores of the shape-modified models were comprised of 95 cm long PMMA (Plexiglass) tubes, with a 70 mm diameter. These were fitted outside a stiffening bar with spacers and with small fastening holes at the ends (see Fig. 1(a)). The surface of both the wavy and the faceted models were produced as three-dimensional prints through RPT (rapid prototyping). For this, FullCurer840 VeroBlue RPT material was used, allowing for the production of almost any geometry, including overhangs and undercuts (Objet Geometries Ltd., 2009). Compared to the reference model this RPT material comes with the cost of increased surface roughness, measured to have an arithmetic average of approximately $R_a = 14\ \mu m$.

The section model was suspended between two 3-component force gauges mounted on the outside of the tunnel walls with a combined load range of ± 30 kg and an A/D resolution of 42.45 mN which corresponds to an accuracy of $\pm 2\%$ for the drag coefficients. The model joints extended through holes cut in the Plexiglas window. The whole rig was mounted on aluminium bars that fit across the door opening, screwed into the door frame (see Fig. 4(a)). Play-less disk joints at both ends of the section model ensured that only the desired force components were measured. A worm-drive was used to rotate the section model, which thereafter was fixed in both ends by tightening screws. An electronic inclinometer was used to measure the angle of wind incidence. All six gauges were plugged into DC strain-gauge amplifiers and the resulting signals were passed through an analogue low pass filter at 80 Hz. The inclined test rig, as shown in Fig. 4(b), was designed so that cable models could be tested at varying cable–wind angles ϕ in the range of $60°$–$90°$. The flow angle ϕ is defined so that $\phi = 90°$ corresponds to flow perpendicular to the cable axis, as shown in Fig. 5.

4.1.1. Aspect ratio and end conditions

The reference cylinder had an aspect ratio of 14:1. This is generally considered to be low and ideally would be increased to ensure the generation of secondary flow structures (e.g. axial flow) that might develop (Hayashi and Kawamura, 1995).
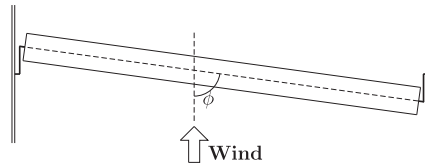
Fig. 5. Plan view of the cable–wind angle ϕ.

Unfortunately, as the focus here was on covering the critical Reynolds number range, the aspect ratio could not be increased further, even with roughening of the cable surface. Nevertheless, Zuo and Jones (2009) observed the formation of a three-dimensional vortex structure in the wake of a yawed cylinder with an aspect ratio of just 16:1.

For yawed cylinders, varying end conditions will generally result in varying load coefficients and vibration onset velocities and amplitudes (Yagi et al., 2009). The use of half spheres at the model ends may be favourable for a faster development of leeward axial flow compared to the use of end-plates, but they also induce vortices at the ends, which combined with the low aspect ratio could be significant. Generally it is still unclear which end conditions are the most appropriate for studying flow around an infinitely long yawed cylinder when employing a wind-tunnel model of finite length. Ramberg (1983) suggested the use of inclined end-plates though the amount of inclination depends on the yaw angle. Due to this general uncertainty, "free ends" were chosen here.

4.1.2. Set-up interference and blockage correction

To reduce the error on the force coefficients due to the use of support arms at the cylinder ends, the results are corrected based on reference measurements made with only the arms of the inclined set-up installed at various angles. Note that this was done without the presence of the model. Thus, any possible flow interactions due to the presence of the model are not included in the correction. To verify the correction, comparative tests were undertaken, but were only possible with the flow normal to the section. For the comparative tests, both the inclined rig and a rig directly fixed to the walls were used. The comparison was found to be favourable, even though a slight increase in drag was observed when using the inclined test rig. This small increase is believed to be the result of a proportional absence of the wall boundary layer effect.

The drag coefficient results are corrected for a test section blockage of 10% by the method of Allen and Vincenti (1944) including the correction by Dalton (1971) given by the following equation:

$$C_D = C'_D \left(1 - \frac{1}{4}\left(\frac{D}{H}\right)^2 - \frac{C'_D}{2}\frac{D}{H}\right), \tag{4}$$

where C'_D is the measured drag coefficient, D is the cylinder diameter and H is the wind-tunnel height for a horizontal cylinder.

The force coefficients are found according to Eq. (5) without employing the "cosine rule":

$$C_i = \frac{2F_i}{\rho U^2 DL}, \tag{5}$$

where F_d and F_l are the drag and lift forces on the cylinder per unit length and normal to its axis, respectively. ρ is the fluid density, D is a representative dimension of the cross-section (here taken to be the transverse diameter), L is the actual cylinder length and U is the upstream undisturbed wind velocity.

As a basis for the performance evaluation of the shape-modified cables, all force coefficients are determined using the internal circular diameter, which is equivalent to that of the plain circular cylinder.

4.2. Plain cylinder

The drag and lift coefficients from the smooth flow tests for a slightly roughened cylinder are presented in Fig. 6. A slight roughening of the surface of the cylinder measured to be around $R_a = 0.8\ \mu m$ (arithmetic average of absolute values) was introduced to simulate surface pollutants that might be found on an actual bridge cable. The roughness had the added effect of ensuring that the cylinder's critical Reynolds number region fell within the testable wind velocity range. The plot legend "direct" refers to the case where the test model is directly installed on the fixed static rig, while the legends $\phi = 60°, \ldots, 90°$ refer to the tests performed at various cable–wind angles using the inclined test rig.

The drag coefficient curves have the same overall shape and tendency, but generally exhibit a reduction in value with the increased skewness of the flow. The exception to this is the drag coefficient corresponding to cable–wind angle $\phi = 80°$, in which a slight increase in drag is observed for Reynolds numbers between 2 and 2.5×10^5, followed by a steep drop. A similar observation has been reported by Larose et al. (2005). The curve of the drag coefficients for $\phi = 90°$ agrees well with the one obtained without the inclined test rig, though both appear slightly lower than typically expected 1.2 (Zdravkovich, 1997). The lift coefficients are much less structured, but nearly all show an increase in magnitude in the critical Reynolds number range. Near the critical Reynolds number (TrBl1), events in the local microstructure such as nonuniform surface roughness can lead to changes in the macrostructure and thus the lift coefficient (Schewe, 1983).
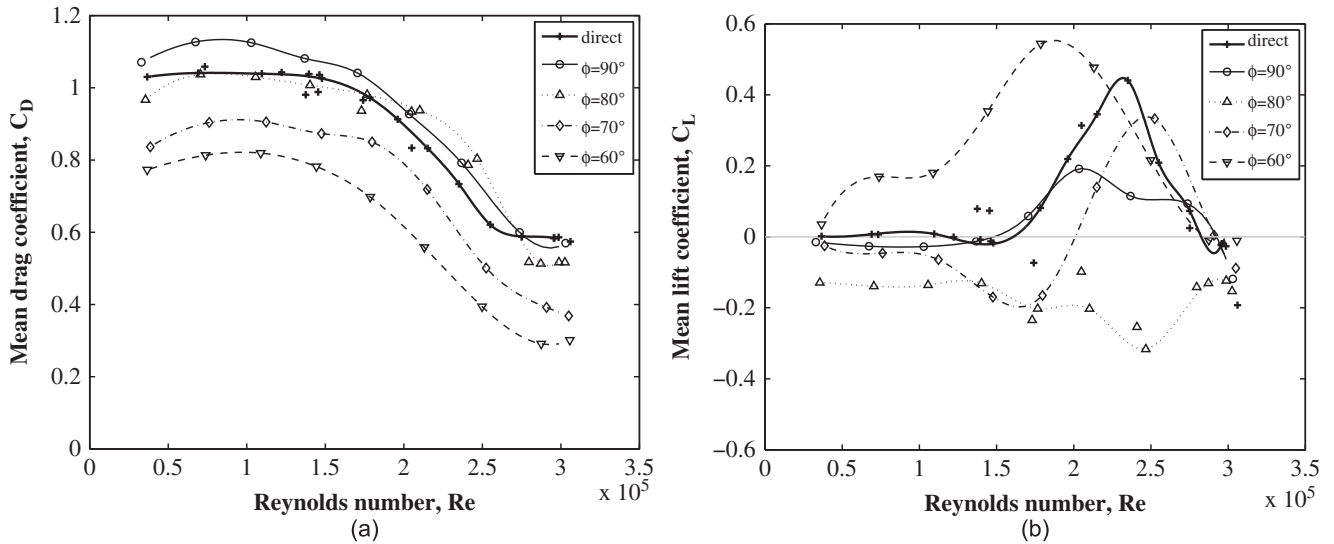
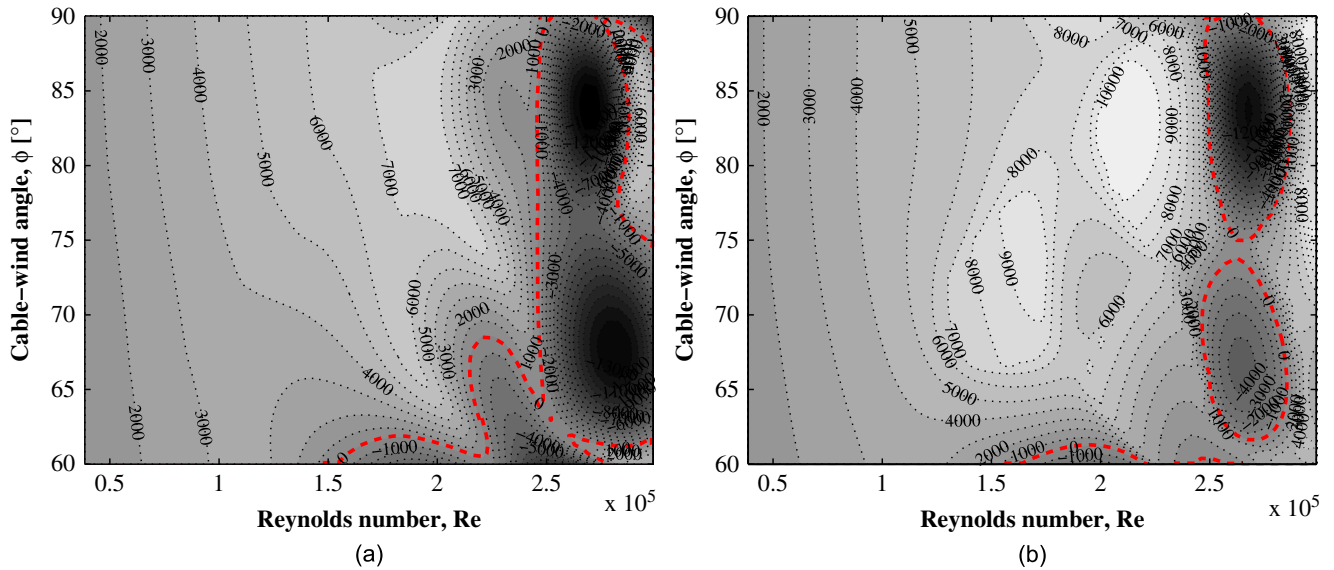**Fig. 6.** (a) Drag and (b) lift coefficients for plain cylinder in smooth flow.

Fig. 7. Nondimensional aerodynamic damping for plain cylinder in smooth flow. (a) Z_a for detuned system. (b) Z_a for perfectly tuned system.

The model orientation that was tested varied as the inclined rig was rotated. Thus, the re-positioning of the model about its axis may have affected these results.

Based on splined force coefficient curves, the nondimensional aerodynamic damping is computed for both the detuned and perfectly tuned systems (1-dof and 2-dof). The dashed contour line represents the transition to negative aerodynamic damping and thus the point at which the risk of aerodynamic instability develops.

From the contour plots in Fig. 7, regions of instability emerge in the critical Reynolds number region at cable–wind angles around 67° and 83° and are mainly the result of the sudden dip in the drag coefficient, i.e. "drag crisis" instability.

Both models also predict some instability at the edge of the tested yawing range which appears outside the critical region. The fact that the models predict large regions of instability for the plain cylinder at skew winds is to be expected, as several preceding investigations have already shown. Matsumoto et al. (1995) observed galloping instability as a result of an artificial axial flow leading to corresponding yawed angles in the range of $45° - 60°$. This corresponds well with the observed instability region occurring at the edge of the tested yawed angles of 60°.

4.3. Shrouded cylinder

In Fig. 8, the resulting drag and lift coefficients of the shrouded cylinder in smooth flow are presented. The drag coefficient is found to be nearly constant for all tested wind velocities, showing the elimination of the Reynolds number dependency. The drag coefficient of approximately 0.95 is higher than expected, which could be attributable to scaling
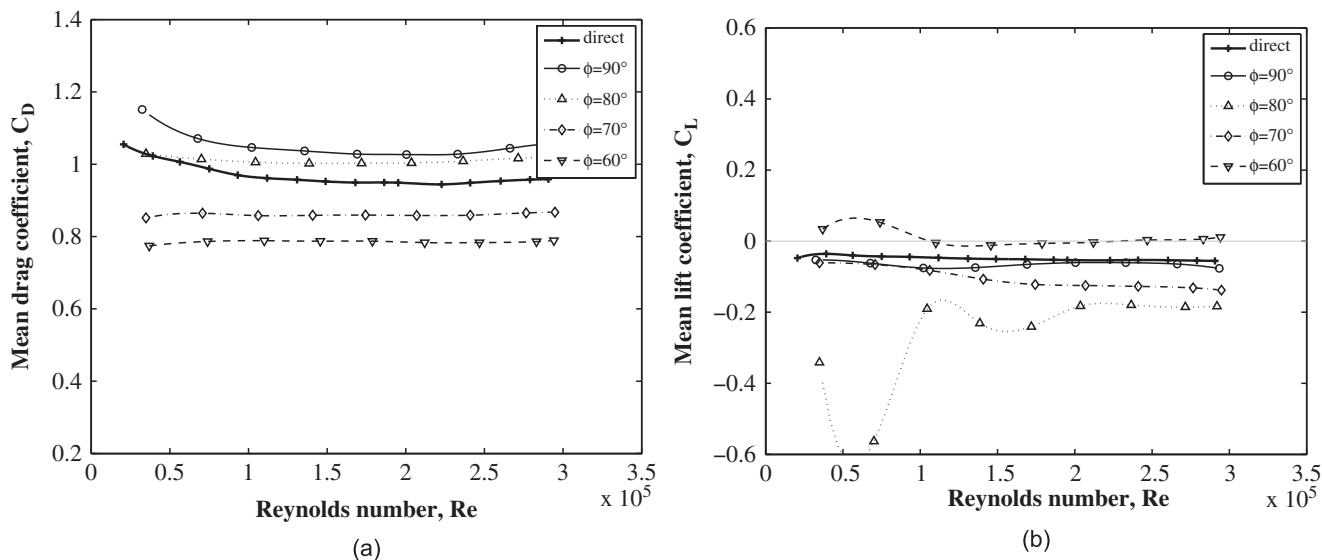
Fig. 8. (a) Drag and (b) lift coefficients for shrouded cylinder in yawed smooth flow.

Fig. 9. Nondimensional aerodynamic damping for shrouded cylinder in yawed smooth flow. (a) Z_a for detuned system. (b) Z_a for perfectly tuned system.

effects, as the perforation was scaled according to the cylinder diameter. The lift coefficients on the whole also remain steady and near zero, baring a single measurement point, in contrast to the plain cylinder. This indicates that the shrouding might successfully disrupt the coherence of the vortex formation. This is later verified through examination of the total rms lift fluctuations, which are significantly lower for the shrouded cylinder (Fig. 16(a)).

The distribution of the nondimensional aerodynamic damping is shown in Fig. 9. The shrouded cylinder is predicted to be stable in the whole parameter range considered.

4.4. Wavy cylinder

The results for the wavy cylinder in Fig. 10 look overall very much like a typical circular cylinder. The transition to turbulent flow happens earlier, although this could be the result of the surface of the RPT material being slightly rougher. The dip in drag is steeper than for the plain cylinder and the drag curves do not smoothen or "straighten" with increased flow skewness. Nevertheless, the shape of the curves does not depend on the flow angle, which indicates the waviness might reduce secondary flow structures, leaving the normal component of the flow to dominate.

The lift coefficients resemble those for the plain cylinder, though the waviness has significantly reduced the magnitude of the lift forces. The weakening of this asymmetry is believed to be due to a reduced correlation length along the model.

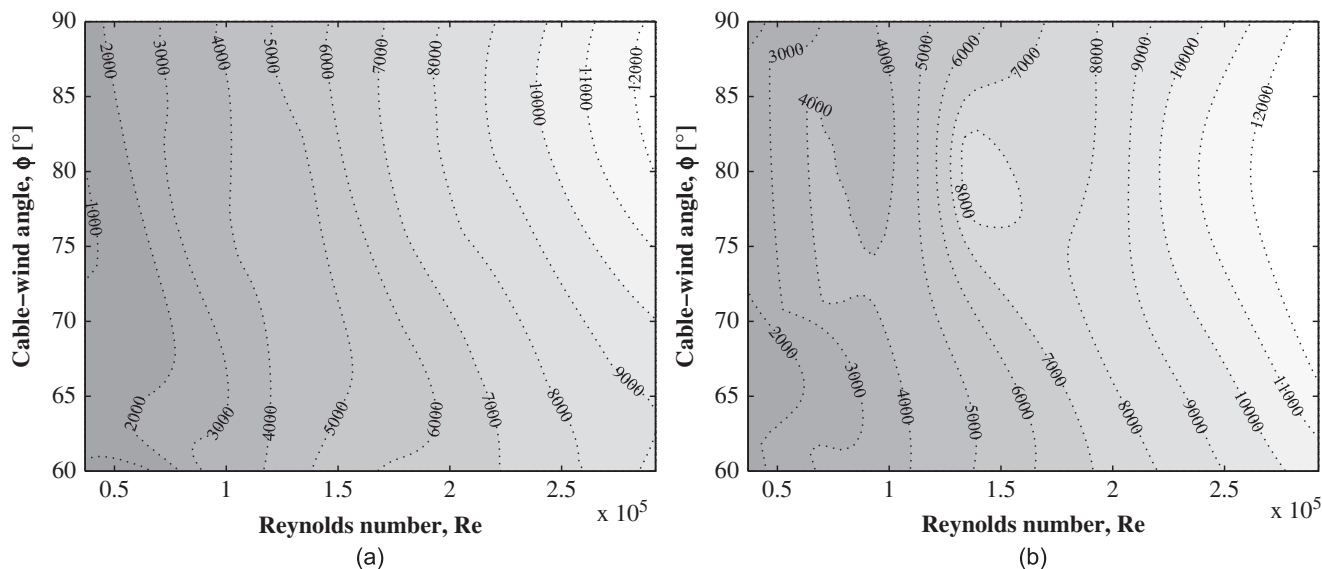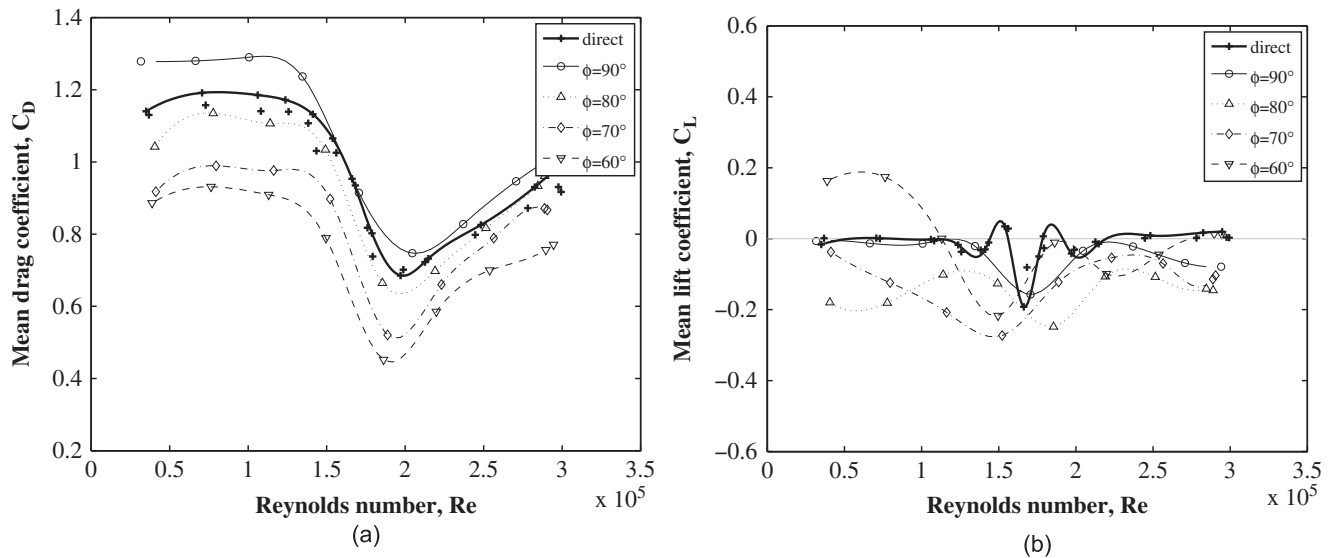**Fig. 10.** (a) Drag and (b) lift coefficients for wavy cylinder in yawed smooth flow.
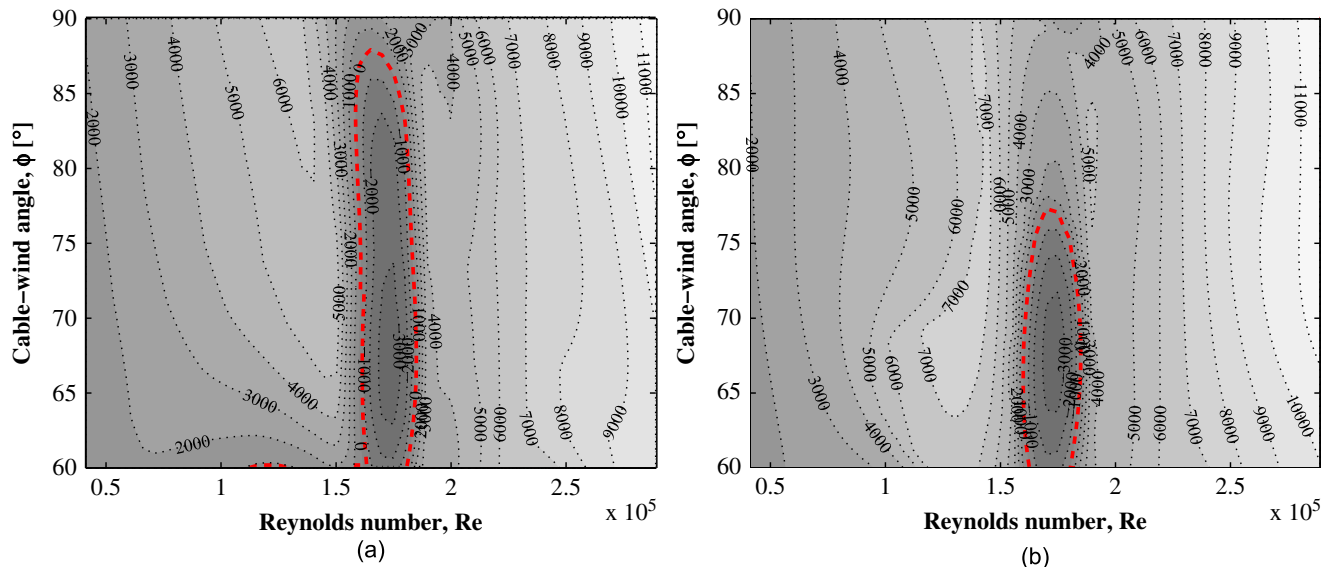
Fig. 11. Nondimensional aerodynamic damping for wavy cylinder in yawed smooth flow. (a) Z_a for detuned system. (b) Z_a for perfectly tuned system.

The results for the aerodynamic damping are shown in Fig. 11, where it can be seen that negative aerodynamic damping is localised around the critical Reynolds number region, though the two models are not in full agreement over the whole cable–wind angle range. It should be noted that from the instability analysis undertaken based only on test data obtained without use of the inclined test rig, instability is also predicted at $\phi = 90°$. In any case, "drag crisis" instability is predicted for the wavy cylinder around the critical Reynolds number region.

4.5. Faceted hexagonal cylinder

The results obtained from the faceted hexagonal cylinder in smooth flow are shown in Fig. 12. The angle α provided in the legends refers to the wind angle of attack, as the particular model was only tested for $\phi = 90°$, without the inclined test rig. Tests at other cable–wind angles are not presented, as pealing of the surface facets, rendered the results unreliable.

For the tested angles, the drag coefficient is observed to be relatively unaffected by Reynolds number. As mentioned earlier, this can be attributed to the well-defined flow separation points, as a result of the facetting. The largest drag coefficient of approximately 2.0 appears at $\alpha = 30°$, where a row of facets is directly upstream.

A smaller drag coefficient was expected from this cylinder, particularly for $\alpha = 0°$, as this corresponds to the case where a wavy edge is upstream, whilst the edges at the shoulders are forcing a waviness in the separation lines. Bearman and Owen (1998) reported that this combination resulted in a drag reduction. If the drag coefficient is determined based
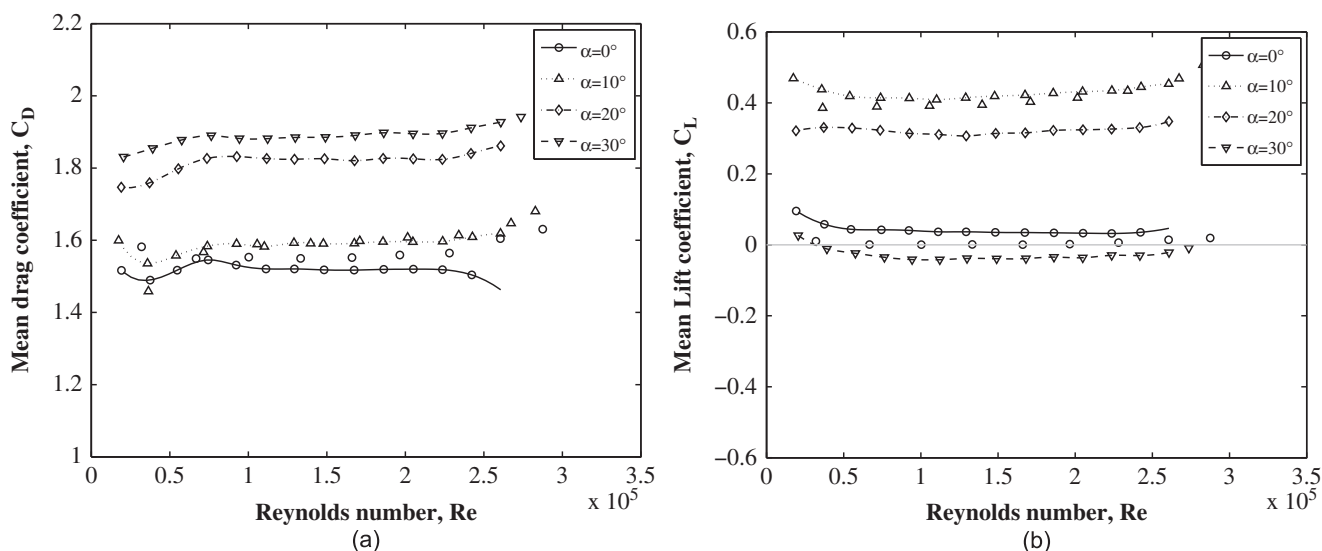
Fig. 12. Force coefficients for faceted hexagonal cylinder in smooth flow. (a) Drag coefficient. (b) Lift coefficient.
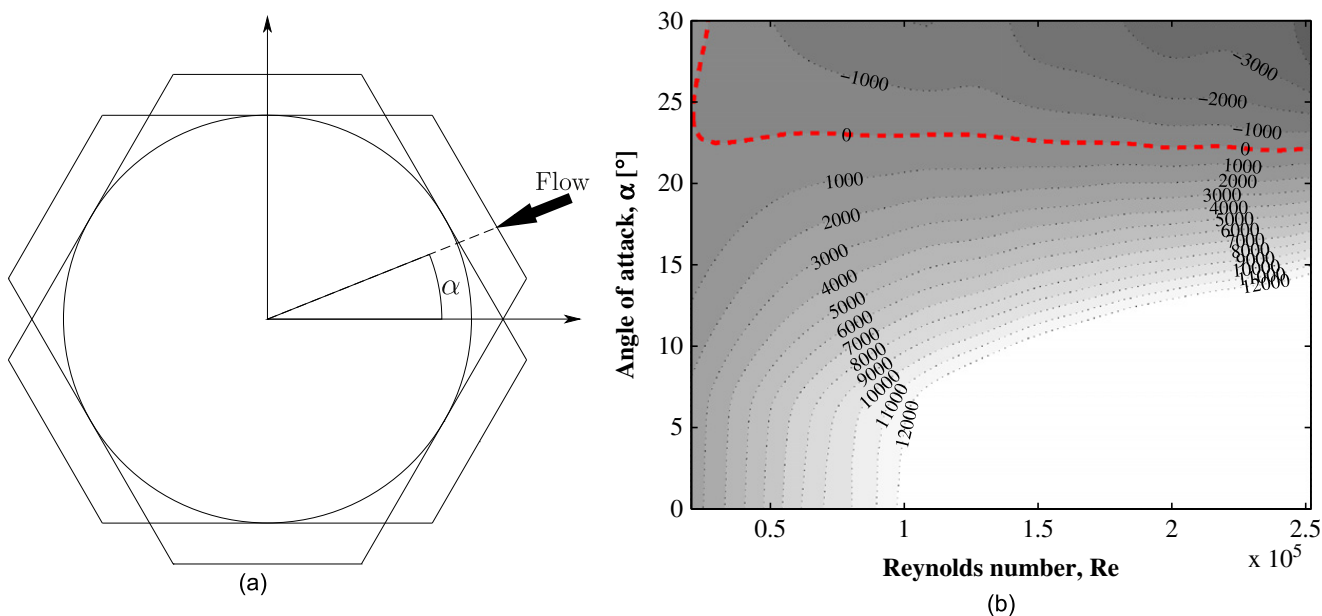
Fig. 13. Faceted hexagonal cylinder. (a) Hexagon angle. (b) Nondimensional aerodynamic damping for faceted hexagonal cylinder in smooth flow.

on the maximum cylinder diameter (approx. 20% larger), the drag would be comparable to that of an octagonal cylinder having a drag coefficient in the range of $1.0-1.5$ (Hansen, 2006).

The resulting aerodynamic stability, as a function of wind angle of attack, can be seen in Fig. 13(b). Aerodynamic instability is determined for a wind angle of attack of $\alpha = 23^{\circ} - 30^{\circ}$. Here, negative aerodynamic damping is a result of a negative lift gradient.

With the force coefficients nearly independent of Reynolds number, aerodynamic instability can also be determined by applying the traditional Den Hartog criterion (1947).

4.6. Lift force fluctuations

Another important element in aerodynamic design and control is the unsteady cross-stream force (fluctuating lift). With the test set-up employed, only the total rms lift fluctuations can be estimated using the total force method discussed by Norberg (2003). Some flow distortion is expected due to limited aspect ratios and lack of properly controlled end conditions. Even so, this analysis is still considered valid as a performance evaluation relative to the plain reference cylinder. The resulting rms lift fluctuations in smooth flow are shown in Figs. 14–16(a), where only tests performed without the inclined test rig are included. The plain cylinder is observed to generally have the largest fluctuations for the considered conditions, whilst the fluctuations for the wavy cylinder are found to be less pronounced and without any

peaks. The last model considered is the shrouded cylinder which is found to have significantly lower lift fluctuations compared to the other two models. An analysis of the lift fluctuations in the frequency domain is made. The frequency distributions of the lift force are determined using Fast Fourier Transformation (FFT) to compute the power spectral density (PSD) of the lift coefficient. The spectral density is computed for each of the flow velocities tested and based on a discrete number of spectra, leading to two-dimensional contour plots. For the plain cylinder, the results are shown in Fig. 14(b) where the left ordinate denotes the Reynolds number, the right ordinate the reduced velocity and the abscissa the frequency. Along with the PSD plot, the lift force rms is shown as a subfigure for the specific model, with flow states and transitions highlighted. For the plain cylinder this is shown in Fig. 14(a). From the PSD, three straight lines stand out. The line completely independent of Reynolds number is identified as the first natural frequency of the model at $f_n = 29.4$ Hz. The other two lines are periodically shed vortices that are linearly proportional with the flow velocity, with corresponding Strouhal number St=0.196 and $St_{1/3} = 0.066$, i.e. Kármán vortex-shedding and an apparent subharmonic of the natural shedding frequency. The lower vortex-shedding frequency has previously been observed by Shirakashi et al. (1985) and later also by Matsumoto et al. (2001). From this, the rms peak observed around Re=1.5×10^5 in Fig. 14(a) can be explained by a higher correlation due to motion caused by an incidence of resonance between the Kármán vortex-shedding and the test rig's first vibration mode. The starting point of the critical Reynolds number regime is observed at Re=1.8×10^5. At this point the mean drag coefficient has just started its dip (see Fig. 6(a)) and the vortex-shedding structure suddenly disappears, which also leads to a step down in the rms lift force. In the critical Reynolds number region, increased activity is observed at very low frequencies, which are believed to be the occurrence of single separation bubbles reappearing or shifting sides at a low rate. At a Reynolds number of Re=2.5×10^5, the transition from the critical to the supercritical region occurs. At this point the mean drag coefficient has reached its minimum value (see Fig. 6(a)) and the appearance of low frequency single separation bubbles has stopped, leading to a step reduction in the rms lift forces. The remaining fluctuations are believed to be the result of buffeting.

The same frequency analysis was undertaken for the wavy cylinder, with the resulting PSD contour shown in Fig. 15(b). A similar pattern is observed for this model. The add-on of the wavy RPT parts has not changed the first natural frequency which is still appearing at $f_n = 29.4$ Hz. The waviness has shifted the Strouhal number to St=0.170, whilst the apparent subharmonic has moved to $St_{1/3} = 0.055$. This is again at one-third the main shedding frequency. The shift in Strouhal number is due to the shape change and as a result of the inner diameter being used as reference. The starting point of the critical Reynolds number regime is now at Re=1.4×10^5, which again coincides with the start of the dip for the mean drag coefficient (see Fig. 10(a)) and the apparent sudden disappearance of vortex-shedding structure. Thus, it is believed that the reason no rms peak is appearing for the wavy cylinder is simply due to the critical region suppressing the vortex-shedding before it reaches the natural frequency. In the critical Reynolds number region, the single separation bubble is again appearing as low frequency lift fluctuations. This is occurring up to Re=1.9×10^5, where the flow state shifts to the supercritical Reynolds number region, indicated by a step down in the lift force fluctuations. After the final transition to the supercritical state, the levels of rms lift for the plain and wavy cylinder agree.

The last model considered is the shrouded cylinder for which the PSD is shown in Fig. 16(b). The first natural frequency of the test rig has changed to $f_n = 30.6$ Hz. This is a result of the shrouding adding stiffness, without the analogous addition of mass. From the frequencies it is not possible to identify any form of vortex-shedding, indicating that the flow is most likely already beyond the critical region due to the high level of turbulence generated by the shrouding. The level of rms lift force at the lower velocities seems to match what the former two models experienced in the supercritical Reynolds number region.
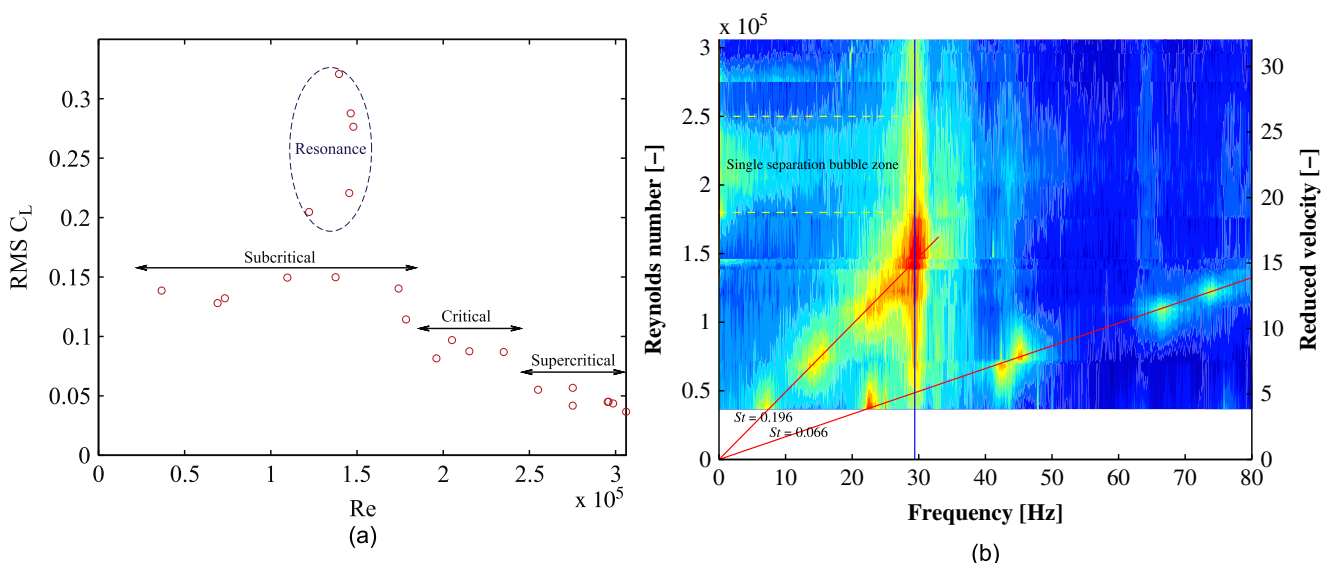

Fig. 14. Power spectral density for plain circular cylinder in smooth perpendicular flow without inclined rig. (a) Lift force rms. (b) PSD contour plot.
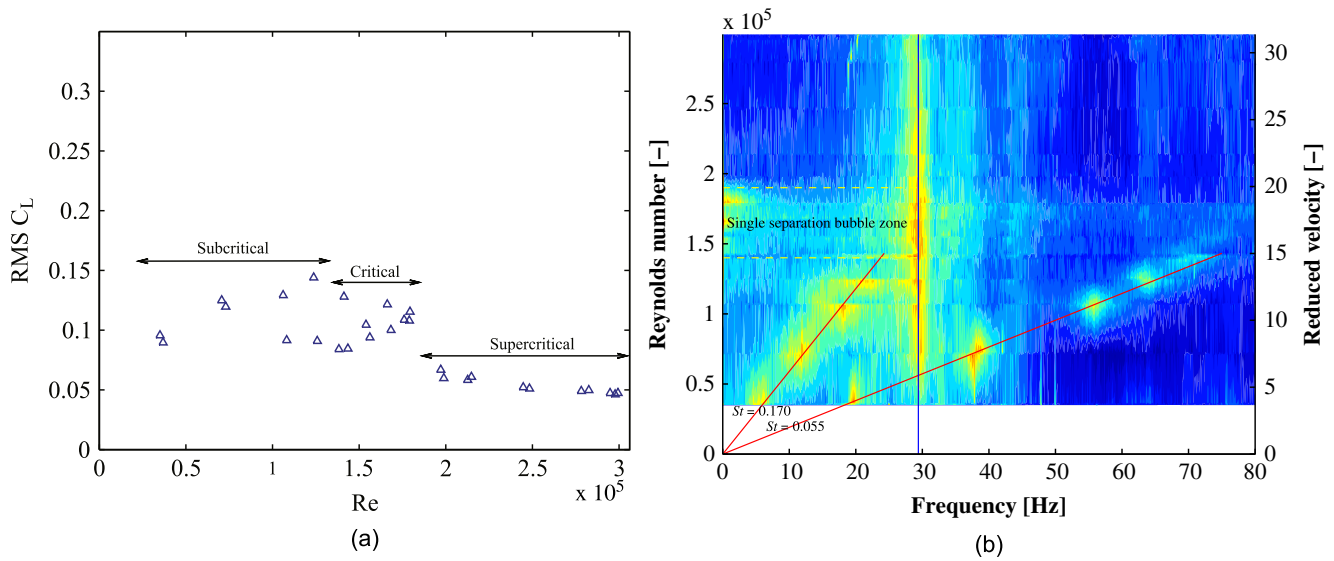
Fig. 15. Power spectral density for wavy circular cylinder in smooth perpendicular flow without inclined rig. (a) Lift force rms. (b) PSD contour plot.
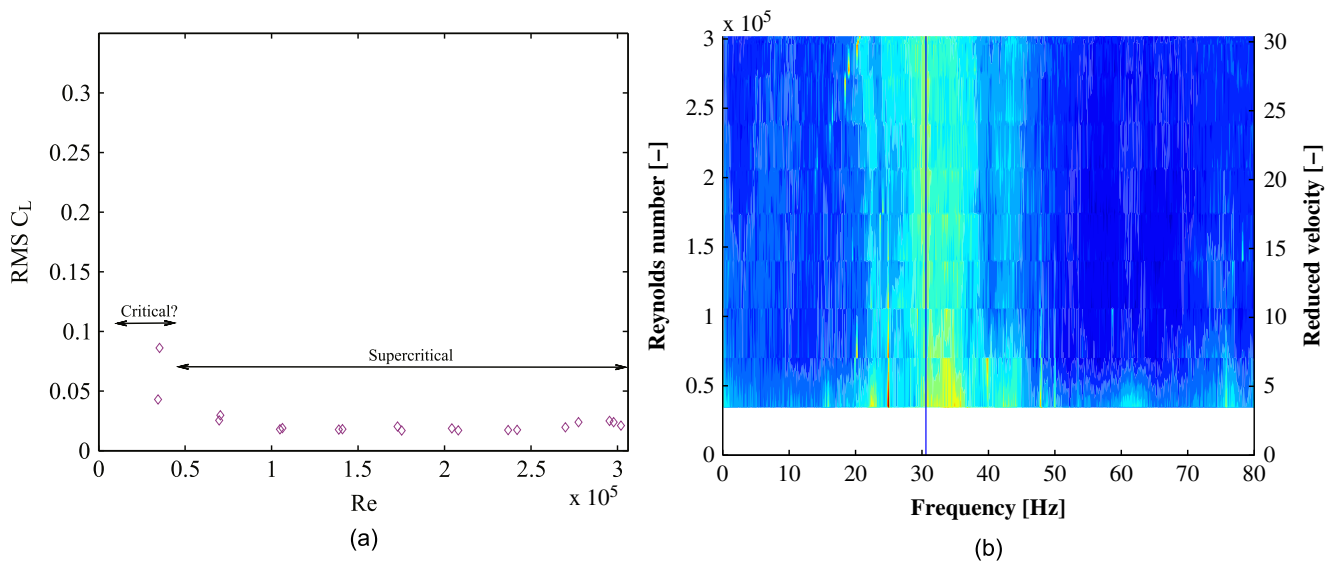
Fig. 16. Power spectral density for shrouded circular cylinder in smooth perpendicular flow without inclined rig. (a) Lift force rms. (b) PSD contour plot.

Corresponding results for the different yawed positions are not presented, though some general observations are shortly discussed. The inclined test rig had its first fundamental mode around 15 Hz depending on the set-up inclination. For yawed angles, no apparent subharmonics of the natural shedding frequency were observed. Shirakashi et al. (1985) mention that it could be caused by end effects at the side wall where the cylinder passes through, though further testing with a more controlled flow at the cylinder ends would be needed to verify this. For the plain cylinder the vortex-shedding exhibited a Strouhal number of St=0.196 (as for flow normal to the cylinder) when taking the velocity component perpendicular to the cylinder. Shirakashi et al. (1986) also observed how the cosine rule (independence principle) apparently applies well for the reduction of the vortex-shedding frequency, although it is actually the secondary flow in the wake just behind the cylinder causing it. Hogan and Hall (2010) also showed how the independence principle predicted the shedding frequency reasonably well for yaw angles within a range of 30° from flow normal to the cylinder.

4.7. Turbulent flow

All the aforementioned tests were also carried out in turbulent flow conditions. The results of these tests can be found in Fig. 17.

In turbulent flow, the plain cylinder experiences an earlier transition to turbulent shear flow, as might be expected. Furthermore, the drag coefficients continuously drop with increasing Reynolds number when using the inclined test rig, which is in slight disagreement with the results obtained from the directly fixed rig and what is generally reported in the
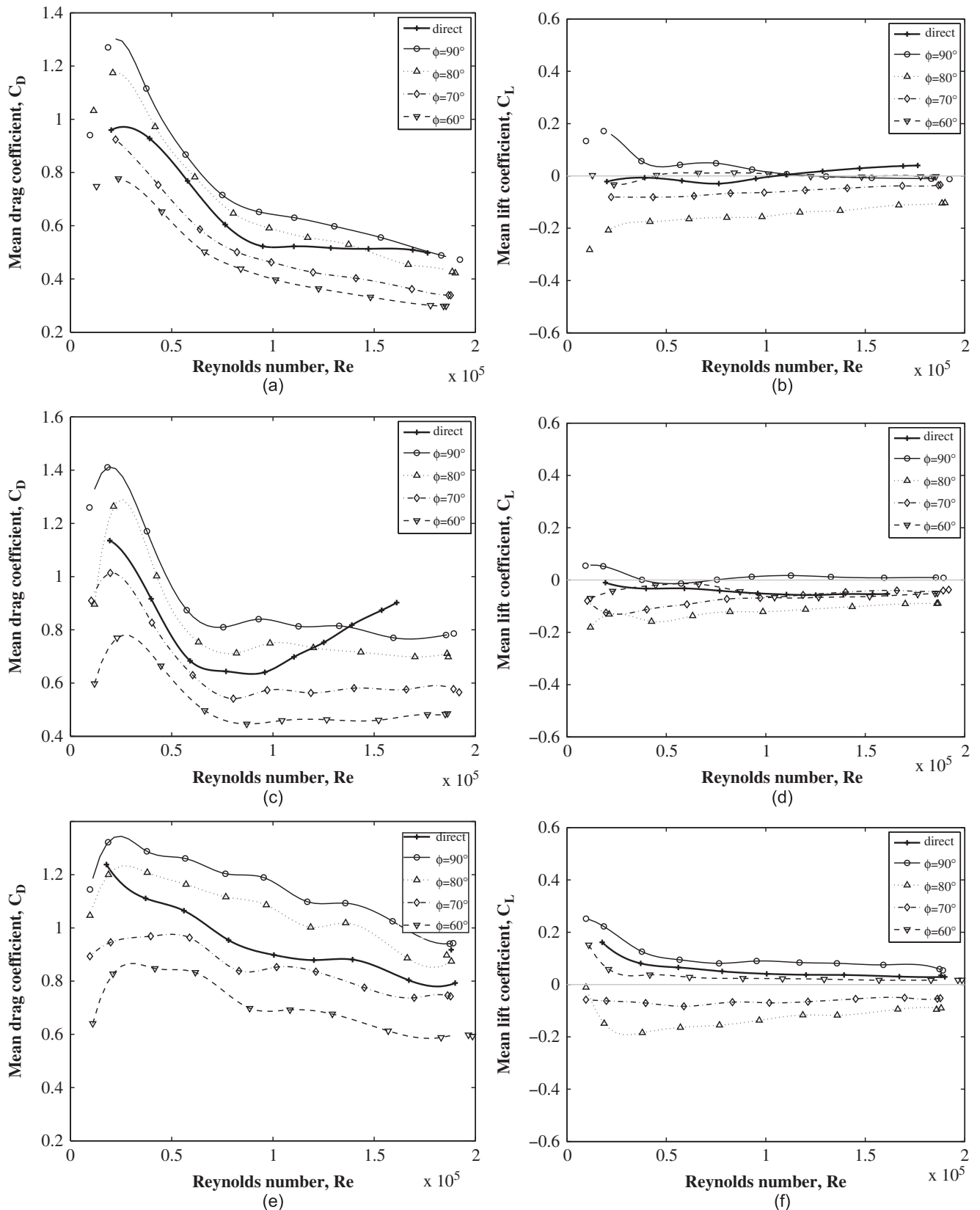
Fig. 17. Drag and lift coefficients for cylinders in yawed turbulent flow. (a) Drag coefficients for plain cylinder. (b) Lift coefficients for plain cylinder. (c) Drag coefficients for wavy cylinder. (d) Lift coefficients for wavy cylinder. (e) Drag coefficients for shrouded cylinder. (f) Lift coefficients for shrouded cylinder.

literature (ESDU 80025, 1986). The lift coefficients appear invariant over the tested Reynolds number range, indicating that the single-sided separation bubbles, which are the most likely cause for asymmetric lift under smooth flow, have now been suppressed by turbulence. A similar behaviour was reported by Larose et al. (2005).

For the wavy cylinder, the turbulent flow produces several of the same effects as observed for the plain cylinder. The drag coefficients experience an earlier transition and the lift forces also appear more stable. After the transition, the drag stays constant, although a small rise in drag is observed without the inclined test rig.

For the inclined shrouded cylinder, this characteristic gradual reduction of the drag coefficient for increasing Reynolds number is observed again, but this time both test set-ups agree on this continuous drop. Generally the drag development in the supercritical Reynolds number region appears to be very sensitive to the addition of this free-stream turbulence, while the lift forces always stabilise.

In all cases, an aerodynamic stability analysis reveals that the tested cylinders are stable, for all tested wind velocities and cable–wind angles of attack, under this specific turbulent flow. This may not, though, be the case for atmospheric turbulence.

5. Concluding remarks

As previously reported, the evaluation of the aerodynamic instability shows that the plain cylinder could be prone to "drag crisis" and dry inclined galloping at specific skew winds.

The experimental investigation of the shrouded cylinder shows that it has a very low dependency on the Reynolds number and that the maximum drag coefficient is only slightly above 1.0 based on the inner diameter. The shroud appears to have a stabilizing affect on the circular cylinder and appears to significantly reduce the vortex-induced oscillating lift forces.

The wavy cylinder shows a significant Reynolds number dependency in the critical region and generally exhibits the properties of a rough circular cylinder. No significant increase in drag is found, indicating some effectiveness of the waviness. Even though the wavy cylinder has been shown in the literature to be effective in the subcritical region, the steep dip in drag results in the prediction of a "drag crisis" instability. Outside the critical Reynolds number region it is more stable than the circular cylinder which could be due to a possible reduced axial flow or a lower correlation length along the cylinder.

The aerodynamic forces of the hexagonally faceted cylinder are found to be independent of Reynolds number, but with a high drag coefficient in the range of $1.5-2.0$. The cylinder also experiences significant variation in drag over angle of attack. The faceted cylinder is predicted to be unstable, as it needs to have less angular dependency in the geometry—both to avoid Den Hartog galloping and to reduce the relatively large drag coefficients observed. Note that all of the aforementioned predictions of instability need to be verified experimentally. Flow visualisation or PIV measurements would be needed to confirm the presence of any significant secondary flow effect on the cylinders.

On-going research by the authors aims to examine the effectiveness of these and other shape modifications under larger cable–wind angles, better flow conditions, varying climatic conditions and dynamically. Tests are currently being undertaken in a new climatic wind-tunnel facility described by Georgakis et al. (2009).

Acknowledgements

References

Ahmed, A., Bays-Muchmore, B., 1992. Transverse flow over a wavy cylinder. Physics of Fluids A 4 (9), 1959–1967.

Ahmed, A., Khan, M.J., Bays-Muchmore, B., 1993. Experimental investigation of a three-dimensional bluff-body wake. AIAA Journal 31 (3), 559–563.

Allen, D.W., Henning, D.L., 2004. Partial shroud with perforating for VIV suppression, and method of using. United States Patent 6,685,394 B1, February.

Allen, H.J., Vincenti, W.G., 1944. Wall interference in a two-dimensional-flow wind tunnel with consideration of the effect of compressibility. Technical Report 782, National Advisory Committee for Aeronautics, pp. 155–183.

Bearman, P.W., Owen, J.C., 1998. Reduction of bluff-body drag and suppression of vortex shedding by the introduction of wavy separation lines. Journal of Fluids and Structures 12 (1), 123–130.

Dalton, C., 1971. Allen and Vincenti blockage corrections in a wind tunnel. AIAA Journal 9 (9), 1864–1865.

Den Hartog, J., 1947. Mechanical Vibrations. McGraw-Hill, New York.

Dragomirescu, E., Yamada, H., Katsuchi, H., 2009. Experimental investigation of the aerodynamic stability of the Endless Column, Romania. Journal of Wind Engineering and Industrial Aerodynamics 97 (9–10), 475–484.

ESDU 80025, 1986. Mean forces, pressures and flow field velocities for circular cylindrical structures: single cylinder with two-dimensional flow. Technical Report 80025, IHS ESDU International plc, UK.

Flamand, O., 1995. Rain–wind induced vibration of cables. Journal of Wind Engineering and Industrial Aerodynamics 57 (2–3), 353–362.

Georgakis, C.T., Koss, H.H., Ricciardelli, F., 2009. Design specifications for a novel climatic wind tunnel for the testing of structural cables. In: 8th International Symposium on Cable Dynamics, Paris, France, pp. 333–340, September.

Gjelstrup, H., Georgakis, C.T. A quasi-steady 3 degree-of-freedom model for the determination of the onset of bluff body galloping instability. Journal of Fluids and Structures, in press, doi:10.1016/j.jfluidstructs.2011.04.006.

Hansen, J.H., 2006. Galloping induced vibrations. Master's Thesis, DTU Byg, DTU Byg, Building 118, Brovej, 2800 Kgs. Lyngby, Denmark.

Hayashi, T., Kawamura, T., 1995. Non-uniformity in a flow around a yawed circular cylinder. Flow Measurement and Instrumentation 6 (1), 33–39.

Hikami, Y., 1986. Rain vibrations of cables of cable-stayed bridges. Journal of Japan Association of Wind Engineering 27, 17–28 (in Japanese).

Hikami, Y., Shiraishi, N., 1988. Rain–wind induced vibrations of cables stayed bridges. Journal of Wind Engineering and Industrial Aerodynamics 29 (1–3), 409–418.

Hogan, J.D., Hall, J.W., 2010. The spanwise dependence of vortex-shedding from yawed circular cylinders. Journal of Pressure Vessel Technology 132 (3), 031301.

Kleissl, K., 2009. Vibration control of bridge cables. Master's Thesis, DTU Byg, DTU, Building 118, Brovej, 2800 Kgs. Lyngby, Denmark, August.

Knell, B.J., 1969. The drag of a circular cylinder fitted with shrouds. NPL Aero Report 1297, May.

Kumarasena, S., Jones, N.P., Irwin, P., Taylor, P., Aug 2007. Wind-induced vibration of stay cables. Report FHWA-HRT-05-083, US Federal Highway Administration URL: ⟨http://www.fhwa.dot.gov/bridge/pubs/05083/index.cfm⟩.

Lam, K., Wang, F.H., Li, J.Y., So, R.M.C., 2004. Experimental investigation of the mean and fluctuating forces of wavy (varicose) cylinders in a cross-flow. Journal of Fluids and Structures 19 (3), 321–334.

Larose, G.L., Damsgaard, A., Diana, G., Falco, M., 1993. Wind tunnel investigations of the power for the stretto di messina bridge. Journal of Wind Engineering and Industrial Aerodynamics 48 (2–3), 379–393.

Larose, G.L., Falco, M., Cigada, A., 1995. Aeroelastic response of the towers for the proposed bridge over stretto di messina. Journal of Wind Engineering and Industrial Aerodynamics 57 (2–3), 363–373 (Proceedings of the First IAWE European and African Regional Conference).

Larose, G.L., Zasso, A., Giappino, S., 2005. Experiments on a yawed stay cable in turbulent flow in the critical Reynolds number range. In: 6th International Symposium on Cable Dynamics, Charleston, USA, pp. 279–286.

Macdonald, J.H.G., Larose, G.L., 2006. A unified approach to aerodynamic damping and drag/lift instabilities, and its application to dry inclined cable galloping. Journal of Fluids and Structures 22 (2), 229–252.

Macdonald, J.H.G., Larose, G.L., 2008a. Two-degree-of-freedom inclined cable galloping–part 1: general formulation and solution for perfectly tuned system. Journal of Wind Engineering and Industrial Aerodynamics 96 (3), 291–307.

Macdonald, J.H.G., Larose, G.L., 2008b. Two-degree-of-freedom inclined cable galloping–part 2: analysis and prevention for arbitrary frequency ratio. Journal of Wind Engineering and Industrial Aerodynamics 96 (3), 308–326.

Matsumoto, M., Yagi, T., Sakai, S., Ohya, J., Okada, T., 2003. Aerostatic force/aerodynamic response characteristics of inclined/yawed cable. In: Proceedings of the 11th International Conference on Wind Engineering, pp. 1713–1720.

Matsumoto, M., Yagi, T., Shigemura, Y., Tsushima, D., 2001. Vortex-induced cable vibration of cable-stayed bridges at high reduced wind velocity. Journal of Wind Engineering and Industrial Aerodynamics 89 (7–8), 633–647.

Matsumoto, M., Yamagishi, M., Aoki, J., Shiraishi, N., 1995. Various mechanism of inclined cable aerodynamics. In: 9th International Conference on Wind Engineering, New Dehli, India, pp. 759–769, January.

Miyata, Y., Yamada, H., Hojo, T., 1994. Experimental study on aerodynamic characteristics of cables with patterned surface. Journal of Structural Engineering 40A (March), 1065–1076.

Norberg, C., 2003. Fluctuating lift on a circular cylinder: review and new measurements. Journal of Fluids and Structures 17 (1), 57–96.

Objet Geometries Ltd., 2009. Fullcure materials brochure URL: ⟨www.objet.com/Materials/FullCure_Materials/⟩.

Païdoussis, M.P., Price, S.J., de Langre, E., 2011. Fluid–Structure Interactions: Cross-Flow-Induced Instabilities, first ed. Cambridge University Press, 32 Avenue of the Americas, New York, NY 10013-2473, USA.

Price, P., 1956. Suppression of the fluid-induced vibration of circular cylinders. Journal of the Engineering Mechanics Division of the American Society of Civil Engineers 82 (EM3), 1030-1–1030-22 July.

Ramberg, S.E., 1983. The effects of yaw and finite length upon the vortex wakes of stationary and vibrating circular cylinders. Journal of Fluid Mechanics 128, 81–107.

Saito, T., Matsumoto, M., Kitazawa, M., 1994. Rain–wind excitation of cables on cable-stayed Higashi–Kobe bridge and cable vibration control. In: Proceedings of the International Conference on Cable-Stayed and Suspension Bridges, Deauville, France, vol. 2, pp. 507–514, October.

Schewe, G., 1983. On the force fluctuations acting on a circular in crossflow from subcritical up to transcritical Reynolds numbers. Journal of Fluid Mechanics 133, 265–285.

Shirakashi, M., Ishida, Y., Wakiya, S., 1985. Higher velocity resonance of circular cylinder in crossflow. Journal of Fluids Engineering 107 (3), 392–396.

Shirakashi, M., Wakiya, S., Hasegawa, A., 1986. Effect of the secondary flow on Karman vortex shedding from a yawed cylinder. Bulletin of The Japan Society of Mechanical Engineers (JSME) 29 (250), 1124–1128. April URL: ⟨http://ci.nii.ac.jp/naid/110002358597/en/⟩.

Walshe, D.E., 1968. Wind-tunnel investigations of the dynamic behaviour of some tall stacks and gas-turbine exhaust towers. In: Symposium on Wind Effects on Buildings and Structures, Loughborough University of Technology, pp. 17.1–17.14.

Walshe, D.E., Wootton, L.R., 1970. Preventing wind-induced oscillations of structures of circular section. Institution of Civil Engineers 47 (1), 1–24.

Wootton, R., Yates, D., 1970. Further experiments on the drag of perforated shrouds. Natl. Phys. Lab. (UK), Aero Rep 1321, July.

Yagi, T., Naito, H., Liang, Z., Shirato, H., 2009. Evaluation of aerodynamic forces on inclined cable in consideration of end conditions of model for wind tunnel tests. In: 8th International Symposium on Cable Dynamics, Paris, France, pp. 151–158, September.

Zdravkovich, M.M., 1997. Flow Around Circular Cylinders: A Comprehensive Guide Through Flow Phenomena, Experiments, Applications, Mathematical Models, and Computer Simulations. 1. Fundamentals, vol. 1. Oxford University Press.

Zdravkovich, M.M., Volk, J.R., 1972. Effect of shroud geometry on the pressure distributed around a circular cylinder. Journal of Sound and Vibration 20 (4), 451–455.

Zuo, D., Jones, N.P., 2009. Wind tunnel testing of yawed and inclined circular cylinders in the context of field observations of stay-cable vibrations. Journal of Wind Engineering and Industrial Aerodynamics 97 (5–6), 219–227.

Chapter 3

Background review

This chapter presents a detailed literature review of relevant passive aerodynamic means, intended to collect the present understanding of how these means affect water rivulet formation and RWIV together with their level of drag coefficient and possible mechanisms of drag reduction.

Paper II

"Aerodynamic control of bridge cables through shape modification: a review"

K. Kleissl & C.T. Georgakis

Aerodynamic control of bridge cables through shape modification: a review

K. Kleissl*, C.T. Georgakis

Department of Civil Engineering, Technical University of Denmark, Building 118, Brovej, 2800 Kgs. Lyngby, Denmark

Abstract

In this review, passive aerodynamic control methods for bridge cables such as direct transition to turbulence, early separation and reattachment, and wake dephasing and 3-D disturbance are presented. A detailed discussion is included of the currently used helical fillets, pattern-indented applications, O-rings, and axial protuberances together with introducing a variety of alternative possible control approaches. Finally, the supercritical drag performance, the suppression of wind-induced vibrations, and the ability to prevent rivulet formation are discussed in relation to use on bridge cables.

Keywords: Passive aerodynamic control, Shape modification, Bridge cable vibration, Passive damping device, Aerodynamic instability, drag reduction

1. Introduction

Through improved bridge monitoring and a greater openness between bridge owners and engineers, it has become increasingly apparent that a large number of the world's long span cable-supported bridges suffer some form of wind-induced vibrations of the stay cables (Kumarasena et al., 2007). These vibrations have the potential to lead to long-term fatigue damage and economic loss, through a reduction of consumer confidence. Examples of bridges with a history of cable vibrations include the First and Second Severn Crossings, Øresund Bridge, Great Belt East Bridge, Humber Bridge and the Fred Hartman Bridge.

Attempts to eliminate or dampen these vibrations have been met with varying degree of success. In general there basically exist three means for control of wind-induced cable vibrations: mechanical means, structural means and aerodynamic means. Today the most common approach against vibrations of bridge cables are to install mechanical dampers at the low ends of the cables, possible also with cross-ties to shorten the effective free length of the cable-stays (Virlogeux, 1998). With the continuously increasing spans the damping

---

*Corresponding author. Tel.: +45 4525 5048; fax: +45 4588 3282.

Email address: kenk@byg.dtu.dk (K. Kleissl)

URL: http://www.cesdyn.byg.dtu.dk (C.T. Georgakis)

devices need to be install even higher and the number of cross-ties increases to stop wind-induced vibrations. For the Tatara Bridge the dampers were required to be installed at a height of more than 5 meters from the bridge deck (Mori et al., 2008), which yields stiffness, esthetics, and maintenance problems. While decreasing the aesthetic appeal of a cable-stayed bridge, mechanical dampers can also be costly to implement, require routine maintenance and typically only optimized for a few modes of vibration.

The aerodynamic means are a desirable solution to the cable-stay vibration problem as they demands little maintenance effort thus more reliable performance and are generally cost-effective (Yamaguchi and Fujino, 1998; Phelan et al., 2005). Furthermore can they be effective over a wide range of wind velocities and vibration modes and can be design to be aesthetically pleasing. They work by weakening the exciting mechanisms by disturbing or reducing wind-induced dynamic force acting on the cable (Ito, 1999). This is mostly achieved by introducing or changing the turbulent structures in the otherwise highly organized near-wake, as one of the most significant features of turbulent flows is their ability to transfer momentum and other properties at much greater rates than non-turbulent flows. However, it should be noted that because the exciting mechanisms of different vibration types differ, the aerodynamic measures needs to counter all phenomenon concerned.

Circular sections are used in a wide range of engineering applications, from flow induced forces on lightning columns, chimneys, electrical and structural cables to tidal and wave loads on offshore risers for example. This literature review is the result of an extensive literature study on passive aerodynamic control measures covering both existing applications and earlier investigations. Because of the many types of tested control measures, several reviews have already been written on the topic of "fluid-dynamic attenuators", though they are now either out-dated (Every et al., 1982b,a; Zdravkovich, 1981, 1984; Blevins, 1990) or incomplete (Kumar et al., 2008; Naudascher and Rockwell, 2005; Modi et al., 1995; Williamson and Govardhan, 2008; Taggart and Tognarelli, 2008; Virlogeux, 1998, 1999; Ito, 1999; Nebres and Batill, 1993; Persoon and Noorlander, 1999). Therefore this in depth review, considering all the types of passive aerodynamic measures for omnidirectional applications.

Beside reviewing, the objective is to discuss the potential of these applications as passive aerodynamic devices on modern cable supported bridges. The evaluation is based on a performance criteria, where they should decrease the wind-induced vibrations whilst minimizing drag and lift forces. With a primary focus on drag reduction in a 'dry' state with flow normal to the cable and preferable in the ULS design range of $Re = 5 - 8 \times 10^5$.

Near-wake stabilizer devices such as streamlined fairings, ribbons, stubs, fringes, fibers, saw-tooth fins, guiding plates, guiding vane, splitter plates, flags and slits/holes all discussed in above mention reviews, exhibit a low flexibility with respect to the direction of the wind. Such unidirectional devices are not of any use in regards to bridge cables and in the following, only omnidirectional or near omnidirectional solutions are therefore considered.

Methods known to induce significant increase of drag are left out or only briefly mentioned if the principle relates to similar solutions.

2

1.1. Classification of Control Methods

Several forms of classification of passive modifications have been proposed in literature, e.g. according to their geometric form, the way they affect the flow, 2D versus 3D forcing or boundary-layer control versus direct-wake control etc.

In the light of the classifications proposed by Choi et al. (2008) and Zdravkovich (1981) the authors developed the categorization graphically presented in Fig. 1, on which control methods can be mapped. The classification focuses on through which technics the method

Modifications:

1. Uniform roughness
2. Circumferential Riblets
3. Vortex generators

4. Axial protrusions
5. Axial grooves
6. Dimples
7. Pattern-indented

8. Helical strakes
9. Helical wires & fillets
10. Helical grooves & channels
11. Circumferiential perturbations
12. Wavy cylinders
13. Hemispherical bumps
14. Polygonal & faceted cylinders
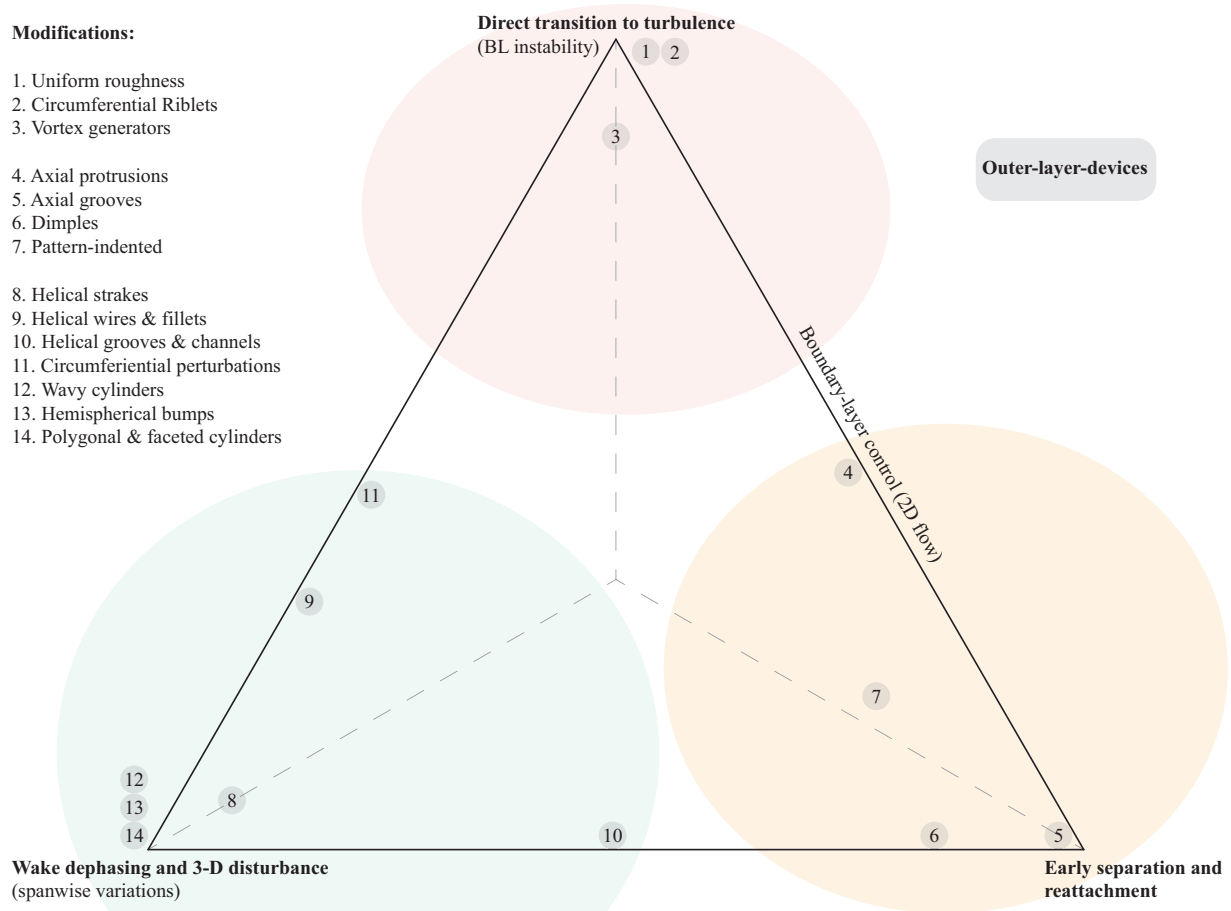
Figure 1: Graphical illustration of the classification of control methods.

controls the flow. These have been proposed as:

- Direct transition to turbulence (boundary-layer instability).

- Early separation and reattachment (shear-layer instability).

- Wake dephasing and 3-D disturbance (three-dimensional wake structures).

- Outer-layer-devices affecting the entrainment layers.

3

2. Direct transition to turbulence

On a bluff body such as a circular cylinder, delaying the moveable flow separation is a classical way of producing a significant drag reduction. To delay the main separation, one should enhance the near-wall streamwise momentum near and before the separation point, so it can overcome the adverse pressure gradient formed in the rear part of the cylinder. One way of realizing an enhancement of the near-wall momentum is through a direct transition of the boundary-layer flow to turbulence. The trigging of such boundary-layer instability is naturally limited to the subcritical Reynolds numbers where such instability have not yet occurred.

2.1. Surface roughness

A most well known approach to trigger the transition to turbulence at lower flow velocities is through increased surface roughness. The vorticity generated by the roughness increases the near wall momentum through turbulent mixing. The vast amount of literature on flow around circular cylinders with uniformly distributed roughness includes Fage and Warsap (1929); Achenbach (1971, 1974, 1981); Szechenyi (1975); Güven et al. (1980); Buresti (1981); Basu (1985); Ribeiro (1991); Shih et al. (1993).

When producing turbulence and suppressing laminar separation it is important that the boundary layer do not become unnecessary think, as thick turbulent wall-bound flows suffers more drag. This drag penalty associated with the supercritical flow velocities is illustrated at Fig. 2, where the drag coefficient development for various degree of uniform surface roughness are shown.
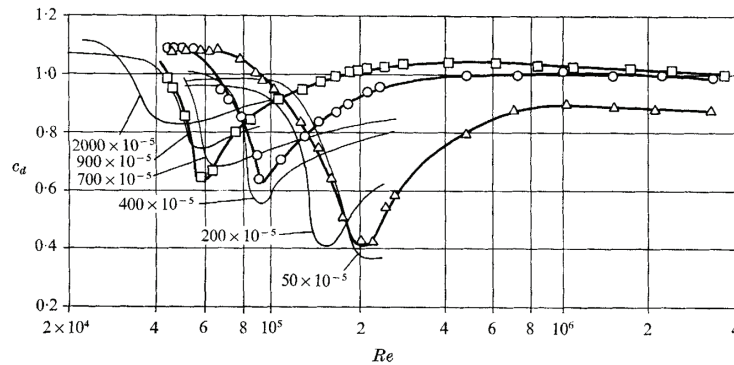
Figure 2: Surface roughness effect on drag coefficient for circular cylinder. Reproduced from Achenbach (1971).

2.2. Circumferential Riblets

Throughout the eighties, much research were done on reducing the skin friction drag through applying regular roughness surfaces (Walsh, 1983; Bandyopadhyay, 1986; Wilkinson et al., 1988; Choi, 1989; Parker and Sayers, 1999). The inspiration were often found from marine mammals e.g. the naturally present riblets within the skin of fast sharks

4

(Bechert and Bartenwerfer, 1989). Riblets are small grooves or surface protrusions aligned with the direction of flow, and leads to an anisotropic roughness to a surface. The existence of these riblets affect the position at which vortices can be created on the surface and alter the shear layer development. They are used to trip boundary-layers into controlled turbulence and e.g. been used both on ship hulls and on aircraft in flight where they are applied to reduce skin friction in turbulent boundary layers.

When experiencing the severe adverse pressure gradients of a circular cylinder, it were initially expected that an increased boundary layer thickness and reduced turbulence intensity would lead to an earlier separation (Fiedler and Fernholz, 1990). However, the function of the micro-grooves may not simply be the increase of viscous-sublayer thickness and reduced turbulence intensity (Choi, 1989), as most of the fish bodies where the inspiration came from (dolphins, sharks, dogfish, fin whale etc.) are of bluff body shape where the form drag may dominate the skin friction drag. Leung (1988) believe that the presence of the regular grooves and thus a larger boundary layer thickness, momentum thickness, etc. enhance the transition to turbulence so that it occurs at a lower Reynolds number than that of smooth cylinder. Though, the minimally attached flow in the grooves may also be a mechanism by which fluid of higher momentum is redirected to the base flow region to effect an increase in pressure (Gad-El-Hak and Bushnell, 1991).

Leung (1988) investigated cylinders with different sizes of circumferential grooves and found, that cylinders with grooves undergoes earlier flow transitions like for increased surface roughness with similar degree of roughness, see Fig. 3. Through comparison with literature such as Fig. 2, Ko et al. (1987) observed that the drag coefficient of the V-grooved cylinders seems to be lower than that of the equivalent rough cylinders in the supercritical regime. Further studies of flow around a circular cylinder with circumferentially cut V-
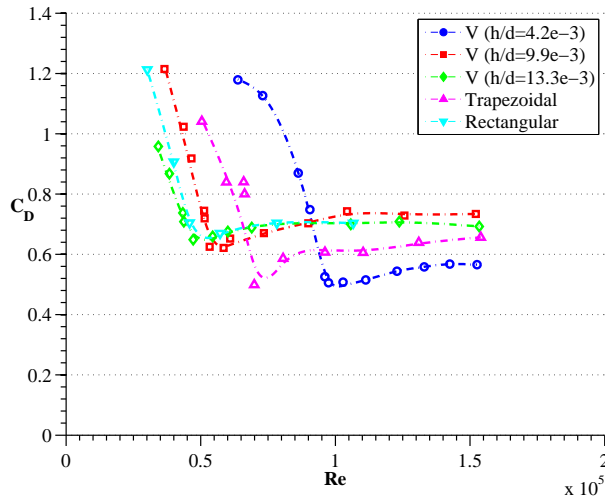

Figure 3: Variation of drag coefficient over Reynolds numbers for a cylinder with circumferential grooves. Data reproduced from Leung (1988).

grooves were done in Leung and Ko (1991). While confirming the shift of the flow regime,

the radial velocity profiles developing over the cylinders were found to differ dramatically from those of smooth and circumferentially grooved cylinders.

In an experimental investigation by Lim and Lee (2002, 2003) of U- and V-shape circumferential grooved cylinders in the subcritical Reynolds number range $(8 \times 10^3 - 1.4 \times 10^5)$, it were found that the U-grooved cylinder experience the earliest transition to the critical Reynolds number region together with an elongated vortex formation region of more than 50%. The delayed vortex formation could be explained by a reduction of longitudinal vortices which Lee et al. (2005) found through PIV measurements of a cylinder with micro-riblet film within the subcritical Reynolds number regime. These vortices have properly been broken into smaller eddies by the sharp peaks of the circumferential V-grooves.

While circumferential grooves may have some preferable supercritical features, it should be noted that know to the authors such cylinders have never been studied in yawed flow conditions. A plane riblet surface typically become ineffective at about 15° flow misalignment.

2.3. Vortex generators

Conventional passive vortex generators (VGs) were first proposed by Taylor (1947) and have been used for many applications to control flow separation for turbulent boundary layers. Vortex generators are small plates, in the form of wedges, fences, fairing, etc., mounted to the surface and protrude into the flow. They basically work by generating an strong overturning macro-vortical motion of the near-wall flow (Gad-El-Hak and Bushnell, 1991) causing high energy air outside the boundary layer to be fed into the lower energy region within the boundary layer and thus through mixing enhancement result in an enhanced momentum in the vicinity of the wall. Initially with device heights on the order of the boundary-layer thickness, though later replaced with low profile VGs (also known as submerged VGs, micro-VGs, sub-boundary layer VGs and micro-vanes) due to the less device drag penalty. Some of the various types of VGs are shown at Fig. 4 and most of them are considered in the comprehensive review on low-profile passive VGs by Lin (2002). Devices which generate embedded streamwise vortices in a boundary layer tend to

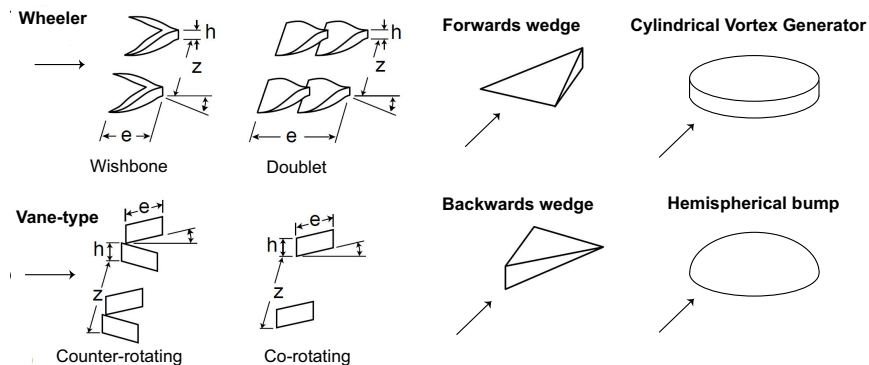
Figure 4: Various types of low-profile vortex generators. Partly reproduced from Lin (2002).

be more effective in mitigating flow separation than devices generating transverse vortices.

The later typically also require more complete spanwise coverage which tend to increase the form drag. Generating excessively strong counter-rotating vortices force pockets of recirculating flow to rise above the surface via the strong upsweep motion of vortices and hence are not as efficient as corotating devices. However, corotating vortices with too close a spacing undergo mutual vorticity cancelation (Gad-El-Hak and Bushnell, 1991).

Due to the vast amount of literature on VGs, only studies with these mounted on circular cylinders are considered in the following. As one of the early studies of VGs on circular cylinders, Joubert and Hoffman (1962) investigated the effect of relative large co-rotating VGs (1.2 times the boundary layer height). While, the optimum VG position of 50° degrees from the forward stagnation line resulted in a 71% reduction in drag, it also lead to an significant increase in the supercritical regime due to the high device drag penalty. In a subsequent study, Johnson and Joubert (1969) investigated the effect of equally spaced triangular vanes ($h/D = 0.033$) mounted on a circular cylinder. They found that, at the positions $40 - 80°$ (defined from the forward stagnation point) the drag coefficient appear rather constant within the supercritical regime, see Fig. 5. And despite, that the VGs fitted at 70° and 80° degrees are both located in the region where separation would already have occurred without the VGs, they still perform well and properly mainly through affecting the free shear layers behind the cylinder. Later, Igarashi (1985) studied
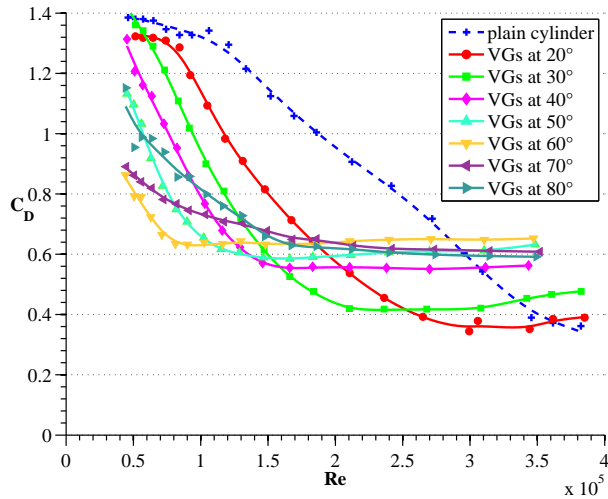
Figure 5: Drag coefficient over Reynolds numbers for various position angles of the VGs. Data reproduced from Johnson and Joubert (1969).

the use of band-saw blades with various heights ($0.006 - 0.044\,D$, BL: $0.5 - 4.0$) used as a VG on a circular cylinder in the subcritical range of Reynolds numbers. Also here the 50° degree position were found to lead to the lowest possible drag coefficient. In a study by Yoon (2005) various types of tabs fixed at the shoulders of a circular cylinder were tested and reported to both reduce drag and attenuates Kármán vortex shedding in the wake. Ünal and Atlar (2010) applied rectangular vane-type vortex generators ($h/D = 0.023$) on a circular cylinder in subcritical flow regime. The VGs delayed the flow separation and enforced the shear layers to get closer to each other i.e. bend inwards and decrease the

width of the near-wake. This resulted in a reduced drag and the higher concentration of the shear layer, due to the smaller width, lead to longer formation distances.

Recent studies by Duriez et al. (2006, 2008); Mai et al. (2008); Pujals et al. (2010) have found that flat Cylindrical Vortex Generators (CVG) like the one shown in Figure 6(a) are effective at sustaining adverse pressure gradients and their symmetric design make them independent of the flow direction. For better to understand the effect of these circular low-profile vortex generators, Heine et al. (2010) tested them at varying azimuth angle on a circular cylinder at Re= 2.2×10^5. The cylindrical devices had a $0.1\,D$ diameter, $0.01\,D$ height and $0.33\,D$ spanwise spacing, where D is the cylinder diameter. Depending of the position, they caused three different categories of characteristic flows. For positions between $15°$ and $78°$ from the stagnation line, the separation is delayed and the shear-layers moves closer to the wake center line, resulting in a 25% pressure drag reduction. Surface visualization with the VGs at $60°$ is shown at Fig. 6(b). The small-scale turbulent flow behind the CVGs is able to persist the adverse pressure gradient longer, allowing it to break through the separation line of the undisturbed flow between the generators. The large velocity difference generate a region of high shear, resulting in the formation of a steady pair of counter-rotating vortices. These pairs of vortices leaks larger-scale streamwise vorticity into the wake which stabilizes the narrow wake provided by the delayed separation.
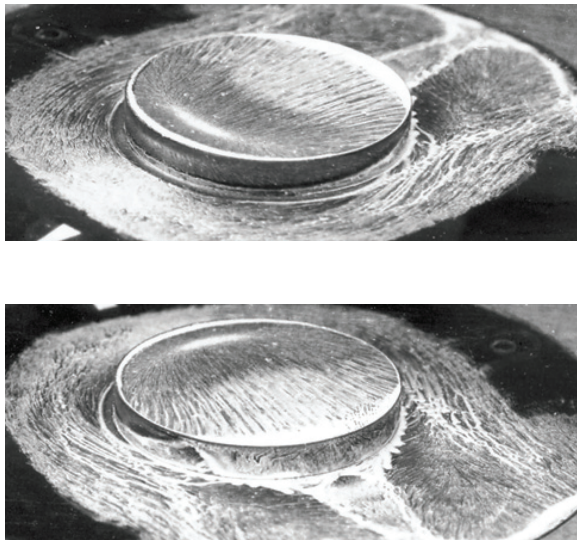
(a) Cylindrical structure submerged in turbulent boundary layer ($H/D = 0.175$). Reproduced from Tsutsui (2011).

(b) Circular cylinder with CVGs at $60°$. Reproduced from Heine et al. (2010).

Figure 6: Surface oil-flow patterns on cylindrical VGs.

While VGs are relatively practical and a cost effective solution, they only result in a delayed main separation if positioned correctly. And for this also to be an omnidirectional application there would have to be VGs well-distributed all over the cylinder surface with various rotations or with a symmetric design. One such application where already proposed

by Sallet and Berezow (1972); Sallett (1980) where a uniform matrix of small rubber studs formed as circular cylinders were mounted on the larger test cylinder. The intension where to generate a high intensity of vorticity at a right angle to the cylinder axis and thus the primary axis of classical vortex shedding to prevent the formation of these vortices behind the cylinder.

A similar study of an omnidirectional application of VGs was done by Yagi et al. (2011a). They tested a circular cylinder with rectangular solid protuberances in a random-like distribution shown in Figure 7. The shape and size of VGs resulted in a significant drag penalty and while the flow transition occurred earlier the subcritical drag coefficient was 1.4 while decreasing to 0.83 in the supercritical flow regime.
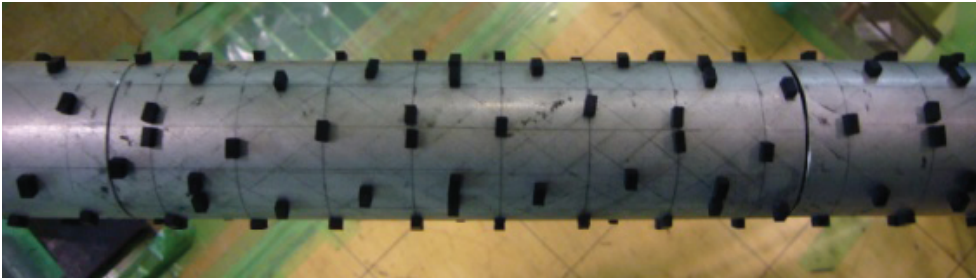

Figure 7: Circular cylinder with distributed rectangular VGs. Reproduced from Yagi et al. (2011a).

Finally, recent work by the authors (Kleissl and Georgakis, 2013b) showed how low-profile CVGs in a proper arrangement, using spanwise variations discussed in section 4, yields promising supercritical drag results. The work involved testing a variety of omni-directional performing patterns using $D/80$ high CVGs with diameter of either $D/20$ or $D/11$. A selection of the obtained drag coefficient curves are shown in figure 8(b). The large amount for streamwise vorticity generated strengthens the separated shear layers and results in a near constant drag coefficient within the supercritical flow regime. Furthermore the applied pattern can force an earlier and prolonged flow transition thus avoiding any sudden changes in drag nor lift coefficient near the critical Reynolds number. A photo of the best performing pattern (A5) with only 0.58 supercritical drag coefficient are shown in figure 8(a).

3. Early separation and reattachment

Another way of realizing an enhancement of the near-wall momentum is through an early separation and flow reattachment with strong near-wall momentum. This also changes the boundary-layer flow characteristics from laminar to turbulent and thus delays the main separation, resulting in a drag reduction. However, now by shear-layer instability. The free-shear layer is more susceptible to flow transition as disturbances existing in the boundary layer rapidly grow along the separated shear layer. The turbulence generated by the shear layer instability entrains part of the high-momentum fluids in the free stream toward the cylinder surface, allowing the flow to reattach with increased near-wall momentum, thus forming a separation bubble and delay the main separation. A mechanism

9

(a) Photo of Model A5 with helically distributed of CVGs.
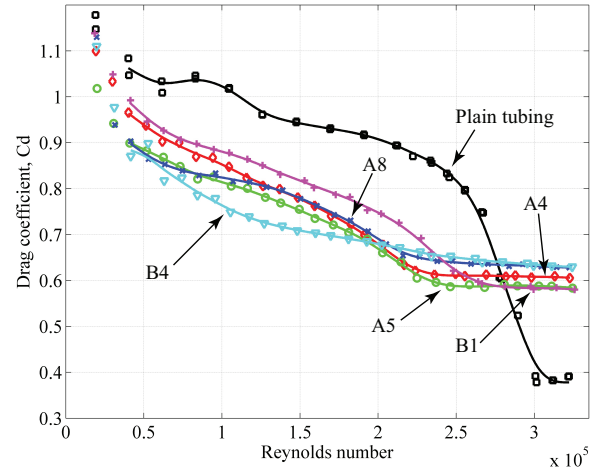
(b) A selection of the obtained drag coefficient curves for models with helically distributed CVGs.

Figure 8: Illustration of the applied pattern of CVGs and the corresponding drag coefficients (Kleissl and Georgakis, 2012a).

very similar to that observed in the drag crisis. The trigging of such shear-layer instability is limited to the subcritical Reynolds numbers where such instability have not yet occurred. Also, for sufficiently low Reynolds number, the laminar flow separation will not reattach to the surface, leading to higher form drag. However, in the intermediate Reynolds number range of typically $10^4 - 10^6$, transition to turbulence takes place in the free-shear layer due to its increased susceptibility (Gad-El-Hak and Bushnell, 1991).

3.1. Axial protrusions

One of the first and most intensively investigated control approaches is to applying a tripping wire, or a pair of wires, on the upstream side of a cylinder. In unidirectional situations this is most successful in controlling the transition and can induce significant drag reductions (see e.g. Hover et al. (2001)). A recent study on boundary-layer tripping by Behara and Mittal (2011), also developed a flow transition hypothesis describing very well how small trips may introduce a two-staged staggered flow transition due to a stepwise transition, one for each of the cylinder's shoulders. This is often recognized in experimental work, as surface imperfections on the model can imitate these small trips. Often with inspiration from the tripping wire approach, proposals for omnidirectional applications exist trying to reproduce these features using several protrusions all around the cylinder. An illustration of some of the various axial protrusion control inputs to generate this early separation are shown in Figure 9.

One general disadvantage from applying these fixed parallel perturbations is that the systematic disturbance along the length of the cylinder generate a high correlation length. This stabilises the two-dimensional flow structures and can enhance the regularity of vortex shedding, even throughout the supercritical regime (Walshe and Wootton, 1970; Naumann
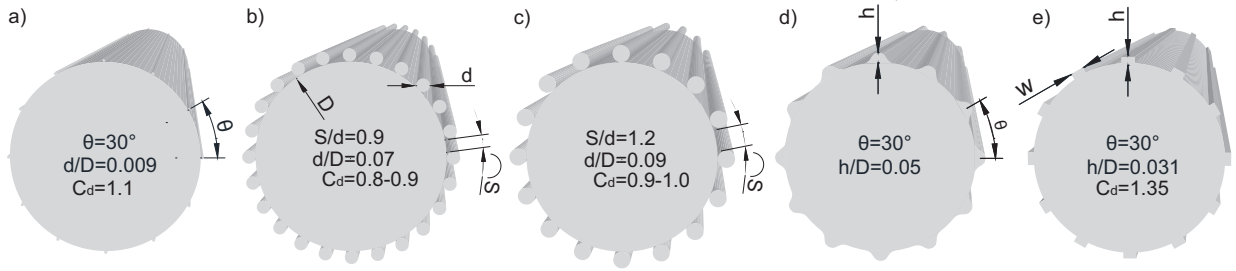
10

Figure 9: Overview of the various types of axial protrusions.

and Quadflieg, 1974; Naudascher and Rockwell, 2005). Hover et al. (2001) also observed that it lead to an earlier frequency lock-in.

Flamand (1993, 1994, 1995) considered having rods of $0.009\,D$ diameter parallel to the stay axis every $30°$ (see Fig. 9(a)). While the rods effectively directed the upper rivulet and limited its circumferentially movement, the drag coefficient was found beyond 1.05 (see Fig. 10).

Later Flamand and Boujard (2009) tested even smaller protrusions, only $0.13\,\mathrm{mm}$ and $0.26\,\mathrm{mm}$ thick and $2\,\mathrm{mm}$ wide. In both cases the stripes were glued following the cylinder axis and positioned every $12°$. The corresponding drag coefficients based on pressure rings are shown in Figure 10 and at Reynolds number 3.33×10^5 the mean drag was measured to only 0.43. These very thin protrusions appear most effective in reducing drag and keeping it low in the supercritical regime. While it is unknown how rivulets are affected by these very low protrusions, further verification of the effectiveness is of great interest.
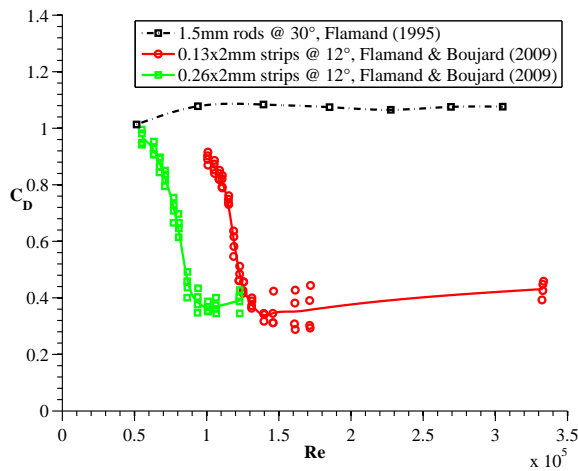
Figure 10: Drag coefficients obtained for different longitudinal protrusions. Data reproduced from Flamand (1995); Flamand and Boujard (2009).
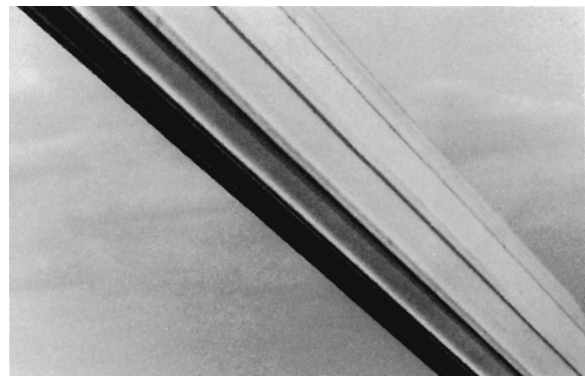

Figure 11: Photo of the cable with longitudinal channels used on the Higashi-Kobe Bridge. Photo by Prof. N.J. Gimsing.

Other studies considered more significant protrusions in sizes up to 10% of the cylinder diameter. One of these is Nigim and Batill (1997), where the flow characteristics for equally

11

spaced protrusions with circular cross-section was investigated. Among many combinations of protrusion sizes and spacing only the two case shown in Figure 9(b-c) performed as omnidirectional. At Reynolds number of 3×10^4 based upon the base cylinder diameter, Nigim and Batill (1997) found the lowest drag coefficient, just below 0.9, to occur for the smallest ($d/D = 0.07$) and most dense ($S/d = 0.9$) protrusion array tested.

Recent CFD analysis of 40° yawed cylinders fitted with strakes was made by Yeo and Jones (2010, 2011). Among three models a cylinder fitted with 12 axial strakes with $0.05D$ thickness (see Fig. 9(d)). Compared to a plain cylinder the drag coefficient approximately doubled while the flow structure, vorticity and peak frequency all showed angle-of-attack dependency. The cable was therefore only found as an near omnidirectional application. While not documented for the other surfaces, cylinders with protrusions spaced with 30° or more are most likely not performing fully omnidirectional and its affect on stability would have to be investigated.

The last type of longitudinal protrusions is equally spaced rectangular protrusions (see Fig. 9(e)), also known as gear-shaped cross-sections. The use of longitudinal channels was developed in Japan for the Higashi-Kobe Bridge (Yamada et al., 1991). The main idea was to have these deep longitudinal channels along the cable, which would drive the water down without allowing any transverse movements. The design later utilized on the Higashi-Kobe Bridge is shown at Figure 11. The axial protrusions is positioned every 30° with a height of $h/D = 0.031$ and a width of $w/D = 0.069$. During the preliminary studies for the bridge Saito et al. (1994) tested a range of different types of surface modifications and among these found the parallel protrusions as the most effective application for restraining rain-wind induced and inclined cable vibrations. Matsumoto et al. (1992) also reported that these axial protrusions significantly reduces the intensity of axial flow behind the cable and interrupt the formation of upper rivulets. Only some high speed vortex induced vibrations has been observed with this cable (Matsumoto et al., 1995). According to the on-site observations, only dry cable vibrations identified as vortex-induced vibrations have occurred. Though these were later suppressed by increasing the structural damping.

But a major drawback with this cable is that it introduces a drag coefficient of 1.2 at the design wind velocity (Miyata et al., 1998) and according to Virlogeux (1999) drag coefficient of up to 1.35 was observed at the supercritical region.

In an attempt to reduce the drag coefficient, Yagi et al. (2011b) completed a parameter study where: the number of parallel rectangular protrusions and the protrusion width were varied. The results are shown in Figure 12, where it is seen that increasing the number of protrusions lowered the drag coefficient down to a level of approximately 0.8. Since the protrusion height was kept unchanged compared to the Higashi-Kobe Bridge, it would be fair to expect that the rivulet suppression abilities still remains. For the case with the most protrusions applied to cable surface, the drag development starts to resembles that of a rough circular cylinder.

3.2. Axial Grooves

The surface modifications discussed so far are all protruding the surface, though they could just as well consist of indentations. A familiar example is the dimpled surface of

(a) Sketch of surface modifications

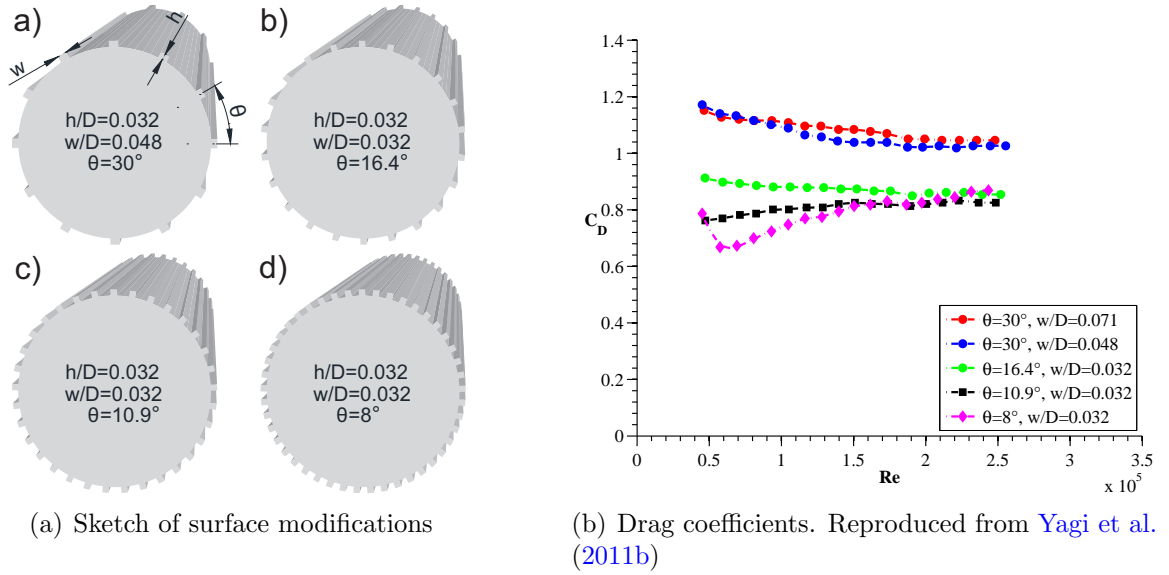(b) Drag coefficients. Reproduced from Yagi et al. (2011b)

Figure 12: Axial rectangular protrusions tested by Yagi et al. (2011b).

golf balls (Bearman and Harvey, 1976) designed to maximize the velocity range during which the ball experiences the low-drag supercritical Reynolds number regime. While indentations typically cannot "catch" the flow in the same way as protrusions does, they cause much less of the drag penalty normally associated with surface protrusions. Inspired from the flow phenomena about golf balls, the aerodynamic properties of indented circular cylinders have been investigated, in hope of reproducing properties such as large drag reduction and maintaining a nearly constant drag coefficient in the supercritical Reynolds number regime.

The mechanism introducing this drag reduction was explained by Choi et al. (2006), who found that indentations causes a local flow separation and trigger the shear layer instability along the separated shear layer, resulting in the generation of a large turbulence intensity. At Figure 13 this is illustrated together with how the flow reattaches to the surface with a higher momentum near the wall, which helps overcoming the adverse pressure gradient and delaying the main separation.

On the downside, if the flow should fail to reattach at the downstream end of the groove, then separation of flow from the cylinder could be advanced instead. And like for any other axial modifications, the systematic disturbance and possible also separation along the length of the cylinder generate a highly 2-dimensional flow with high correlation length.

One of the first to investigate the effect of axial circular grooves on the flow around a circular cylinder is Kimura and Tsutahara (1991). This was done by only having a single groove in each cylinder, so that the effect of the groove position on the separation point could be observed. By flow visualization and numerical simulations at subcritical Reynolds number, all three depths of grooves tested were found effective in moving the separation point backward at a position range of $75 - 83°$. The grooves had no effect when positioned
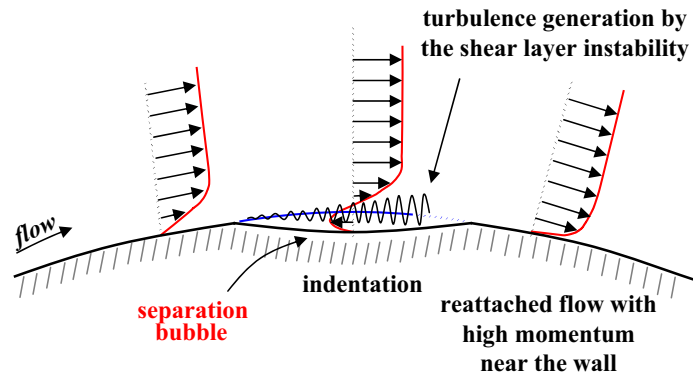
13

Figure 13: Illustration of drag-reduction mechanism of indentations. Reproduced from Choi et al. (2006) (colored version from Choi et al. (2008)).

at a position less than 75°, though at higher Reynolds numbers a slight negative effect would be expected.

According to Miyazaki (1999), parallel U-shaped groovings were cut into the surface of the polyethylene cover on the Yuge Bridge. A photo of the cable is shown at Figure 14(a). The grooves have a $0.02\,D$ depth, $0.04\,D$ width and are positioned every 10°. The surface
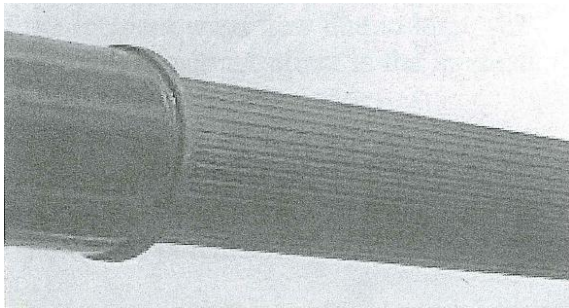
(a) Photo of the cable with U-stripe shaving. Reproduced from Yamaguchi and Fujino (1998)
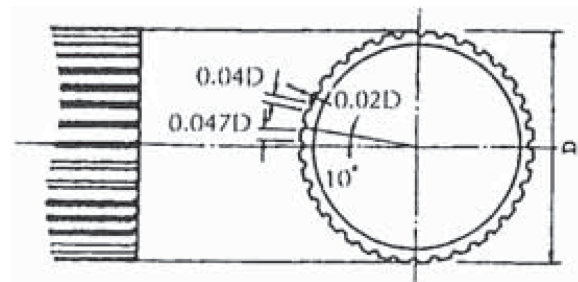
(b) Cross-sectional sketch of longitudinal grooved cable surface. Reproduced from Miyazaki (1999)

Figure 14: The U-shaped grooved cable surface of the Yuge Bridge.

prevented the formation of rivulets by raising the apparent Reynolds number up to the supercritical region, consequently changing the pressure distribution due to reattachment and shifting of separation point. The grooves also appear to forcefully guide the water flowing down the cable surface thus preventing rivulets from forming in particular places.

Confirmed by the use of both experimental tests and numerical simulations, Yamagishi and Oki (2004) found that a circular cylinder with triangular grooves has a 15% reduction of the mean drag coefficient compared to a cylinder with circular grooves (see Fig. 15). This also match the observation that triangular grooves delays the final separation approximately 10° further than with circular grooves.

Later the effect of the number of grooves were investigated in Yamagishi and Oki (2005)

14

by considering three cylinders with 20, 26 and 32 triangular grooves, respectively. These drag results are also shown in figure 15 and they found that the more grooves the earlier the transition. The supercritical drag coefficient of about 0.8 appear unaffected by the number of grooves.
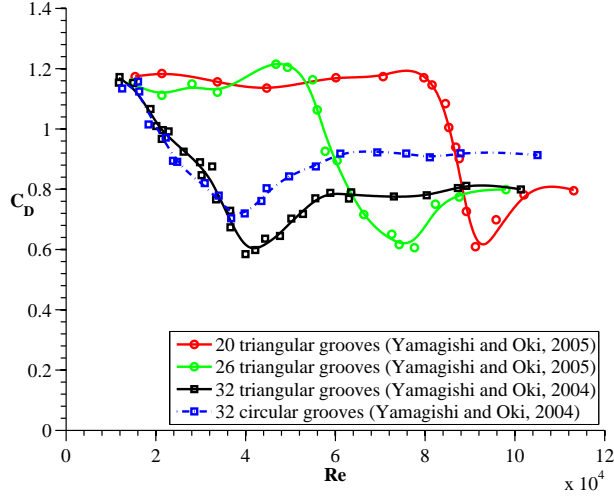

Figure 15: Mean drag coefficient of circular cylinders with a varying number of triangular and circular grooves. Reproduced from (Yamagishi and Oki, 2004, 2005).

3.3. Dimples

A dimpled cylinder also apply the drag reduction mechanism illustrated in figure 13. But in contrast to the cylinders with axial grooves, the dimples furthermore introduces two types of 3-dimensional flow structures. One local effect from each of the dimples and a spanwise variation highly dependent on the surface distribution of the dimples. The local 3-dimensional effect is generated by the flow not passing directly over the centre of the dimple. These non-centered streamlines, passing the dimple closer to its periphery, obtain some streamwise vorticity. This results in a pair of counter-rotating vortices being produced in the wake of each of the dimples, similar to the CVGs mentioned in section 2.3.

Bearman and Harvey (1993) measured the drag coefficient for a dimpled cylinder having a ratio of the depth of the dimples to the diameter of the cylinder as $k/D = 9 \cdot 10^{-3}$, corresponding to the ratio from a typical golf ball and a dimple diameter of approximately $0.1D$. The drag measurements are shown at Figure 16 together with the drag coefficients of a smooth and two equivalent sand-roughened cylinders. The dimpled cylinder experience an early flow transition similar to the equivalently sand-roughened cylinders. But the drop in drag coefficient at the critical Reynolds number is not as significant and do not rise as much either in the supercritical region. Though the drag coefficient is not found as remaining constant after the drop, this is still quite attractive with regard to the structural design. Especially since no optimisation of dimensions or distribution was attempted in this study.
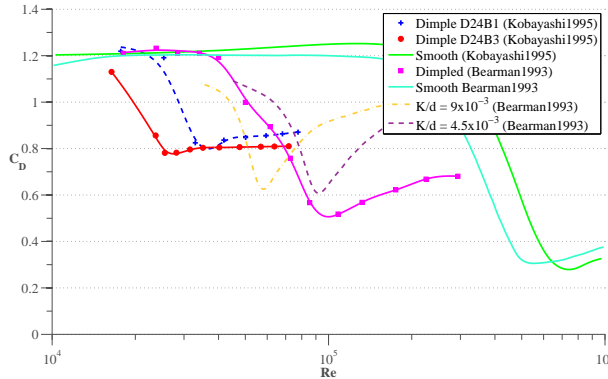
15

Figure 16: Drag coefficient for uniform distributed circular dimples. Reproduced from Kobayashi et al. (1995); Bearman and Harvey (1993).

Kobayashi et al. (1995) measured drag and dynamic response on two test models with uniformly distributed dimples. The dimples were drilled into the surface of the models with a hole diameter of $0.1\,D$ and depth of $0.01\,D$ and $0.03\,D$, respectively. The dimples were positioned at every $15°$ circumference and at a distance of $0.131\,D$ along the cylinder axis. The drag results are shown in figure 16. The dimpled cylinders experience an early flow transition and especially the model with the deeper dimples has a near constant supercritical drag of 0.8. The two models were both found to have significant lower dynamic response with water on the surface than a corresponding circular cylinder. This were believed to the cause of the dimples preventing the formation of a rivulet. At the upper part of the cylinders water drops were formed though these drops went down through the line of dimples, only covering two or three lines.

Though never tested on circular cylinders, other shapes of dimples have been found more effective in reducing the drag, such as hexagonal spherical dimples tested by Bearman and Harvey (1976). Ever since, a vast number of various shapes of dimples such as e.g. spherical polygonal dimples (Morgan and Sullivan, 2010) have been patented.

3.4. Pattern-Indented

The Pattern-Indented surface is the name for the type of the cable surface processing applied firstly on the Tatara Bridge and later also the Stonecutter Bridge and Sutong Bridge. The surface consist of lumps of discrete roughness in a unique pattern. The roughness is made up of surface indentations where the thermal procedure have left the indents with a protruding periphery. The fundamental idea is to reproduce the low drag flow state from the critical Reynolds number, at the design velocities in the supercritical Reynolds number regime by controlling the flow separation (Miyata et al., 1995).

3.4.1. Grid-like roughness

Firstly, this fundamental idea of near constant drag was illustrated by the use of grid-like grating surface roughness. The test models with this surfacing are shown in figure 17(a) while the drag results for both grid-like and equivalent uniform roughness are shown in

16

figure 17(b). The models with the grid-like surface roughness keeps the critical flow state
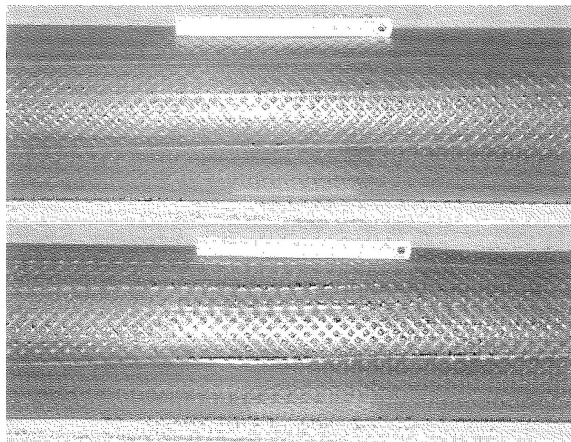
(a) Photo of grid-like surface models. $R_z = 600\mu m$ (top) and $R_z = 1200\mu m$ (bottom).

(b) Comparison of drag coefficients for uniform and grid-like roughness.

Figure 17: Models with a grid-like surface roughness. Reproduced from Miyata et al. (1993, 1994a,b).

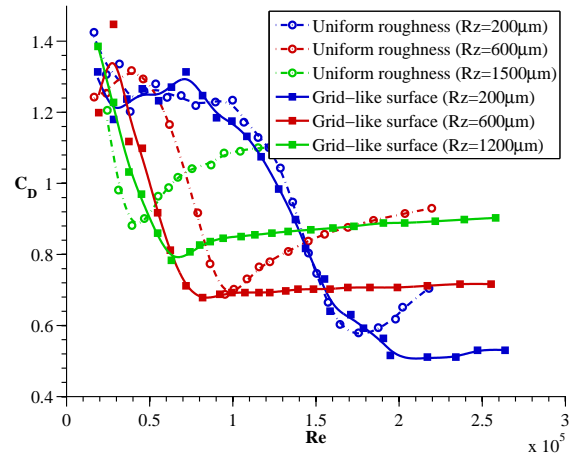throughout the supercritical Reynolds number regime, resulting in a low and near constant drag coefficient. Whereas the drag for the uniform roughness rises during the supercritical regime. Shih et al. (1993) also tested models with grid-like roughness by attaching square-mesh wire screens. But possible due to the different type of grid design the supercritical drag showed no tendency to stay constant.

3.4.2. Preliminary test models

During the preliminary studies for the Tatara Bridge, two types of patterns where under consideration. Full scale models of these two are shown in figure 18, both with a relative surface roughness of 1.1% of the cable diameter. The roughness was described in terms of the depth of the concavities or the height of the convex sections (Miyata et al., 1994a).
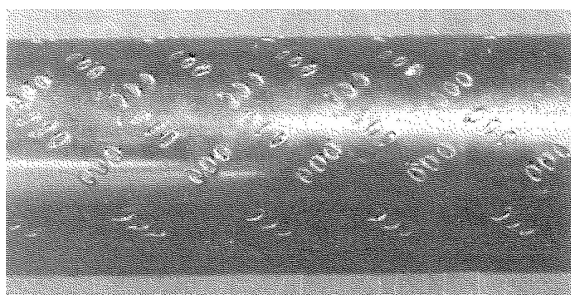
(a) Photo of the Discrete concave pattern model.
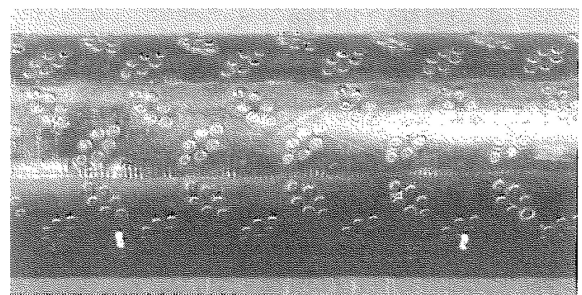
(b) Photo of the Discrete convex pattern model.

Figure 18: Preliminary patterned test models. Reproduced from Miyata et al. (1993).

Drag coefficient results for these models (named C_2 and C_3 are shown in figure 19 together with a smooth cylinder as reference. For both the pattern-indented models, the

Figure 19: Drag coefficients from different tests with pattern-indented cable surfaces. Data reproduced from Miyata et al. (1994a); Hojo et al. (2000); Yagi et al. (2010); Kleissl and Georgakis (2012a).

relative high surface roughness results in a very early flow transition at only $Re = 6.4 \times 10^4$. After the transitions, both of the applied patterns successfully keeps the drag near constant. The surfaces are therefore both found very effective in remaining a critical flow state throughout the supercritical flow regime.

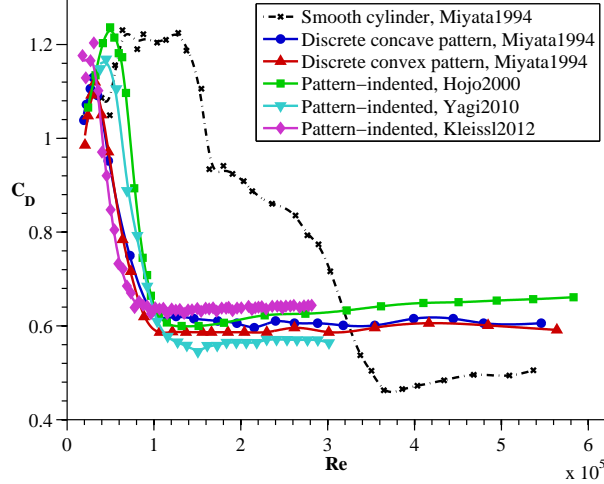Even though the two models applied different patterns of concavities and convexities, they still perform extremely similar. This indicates that it is primarily the discrete roughness which gives these flow characteristics.

When tested in a dynamic test rig with rain simulation, both models outperform the smooth model and succeeded in disturbing consistent formation of water rivulets (Miyata et al., 1994b,a). This was explained with the supercritical flow state already appearing at the low wind velocities where rain vibrations typically occur. The supercritical flow state results in a negative pressure peak at about 80°, which appear to suppress the formation of rivulets on the upper surface (Miyata et al., 1998)

The pressure distribution on the C_2 model was also measured within its range of near constant drag and was found similar to that of a plain cylinder in its supercritical Reynolds number regime. The separation point was found stable at 110° which is approximately 10° further backward than on the plain surface model, leading to a narrower wake width (Miyata et al., 1994b).

Hojo et al. (1995) pointed out that the combination with rough areas which easily trigger turbulence meanwhile ensuring a smooth portion on the surface is the key to obtaining a near constant supercritical drag. Therefore a parametric study was carried out where the angular distance between the different lumps of roughness and the denseness of each roughness lump were varied. The less dense lumps positioned every 30° resulted in the lowest drag slightly above 0.5 (Miyata et al., 1995).

3.4.3. Final Pattern-Indented design

From consideration of ease of manufacturing and installation, it was decided that the surface roughness should be in the form of oval depressions distributed in a pattern as shown at Figure 20 (Hojo et al., 2000).

(a) Cable from the Tatara Bridge. Reproduced from Katsuchi and Yamada (2009b).
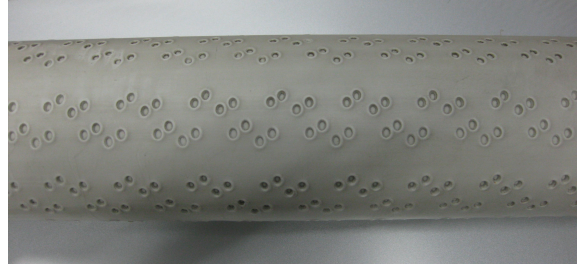
(b) Cable from the Sutong Bridge.

Figure 20: Final design of the Pattern-Indented cable surface.

The corresponding development of the drag coefficient are also shown in figure 19. The lowest drag of 0.61 was found right after the flow transition. But in the supercritical regime the drag slightly rises, reaching a drag of 0.66 at $Re = 5.83 \times 10^5$. This pattern was not as effective as the previous tested which kept a lower drag in the supercritical regime. Though the design drag coefficient of 0.7 was still found acceptable, since keeping the same low level of wind loads as on a normal smooth cable was a major reason for adopting the pattern-indented cable surface for the Tatara Bridge (Miyata, 2003).

Hojo et al. (2000) found that the supercritical pressure distribution and rivulet suppression abilities remained as the previous version. Though some rain-induced vibrations was observed at a low wind velocity range of approximately $6\,\mathrm{m/s}$, despite that the surface treatment effectively suppressed the upper rivulet (Miyata et al., 1998). This lower rivulet driven small amplitude RWIV was later confirmed during tests by the authors in Kleissl and Georgakis (2013a).

In an earlier study Matsumoto et al. (1989) pointed out that maintenance against dust might be necessary during its service life to avoid leaving the upper indents ineffective. To evaluate the need for this, Hojo et al. (2000) confirm the cable's vibration suppressions effects even when the upper indents had been made flat as to simulate dust filling the indents. This indicate though, that the protruding periphery around the indents may be the more important part of the treatment.

In the following years after the completion of the Tatara Bridge, bridge monitoring showed no reports of rain-induced vibrations (Yamaguchi et al., 1999; Fujiwara et al., 1999). The only vibration incidents observed were at low velocities and identified as vortex-induced vibrations. Later Miyata (2003) pointed out that a few stay cables have experienced reports of about $0.25\,D$ of damped vibration under wind speeds of $10 - 20$ m/s during rainfall, which matching the predictions from the wind tunnel tests by Hojo et al. (2000).

3.4.4. After studies

Recently, several wind tunnel studies have further investigated the Pattern-indented surface. Firstly, Katsuchi and Yamada (2009a,b) investigation both the onset of dry galloping and the axial flow intensity at yawed positions. The surface pattern of the scaled test model was reproduced according to the Tatara Bridge, but the shape of the indents were not reproduced exactly, as they lacked the protruding periphery around the indentations. This model did not reproduce the early flow transition within the tested Reynolds number range of $\sim 0.6 - 1.8 \times 10^5$ for flow normal to the indented model. This strongly indicates that the protrusions are the source for triggering the early flow transition.

Later, Katsuchi et al. (2010); Katsuchi and Yamada (2011) repeated the wind experiments with a real cable sample model, which with the increased roughness from the protrusions lead to the early flow transition. In the supercritical regime the model exhibited a similar vibration response as the dry instabilities observed for both the previous model and a plain cylinder. Furthermore also a strong axial flow comparable with that of a plain cable was found along the leeward side of cable.

Kleissl and Georgakis (2012b) also observed, applying a smoke and laser visualization approach, that the axial flow appears to be unaffected by the pattern-indented surface. The drag coefficients obtained in this study are presented in figure 19 and shows an even earlier flow transition while the supercritical drag is of similar size. Using surface oil visualizations (see Fig. 21), it was observed that the protruding peripheries seem to guide the flow around the indents together with a periodic waviness of the separation line having a wave period identical to that of the surface pattern. The separation line breakthroughs
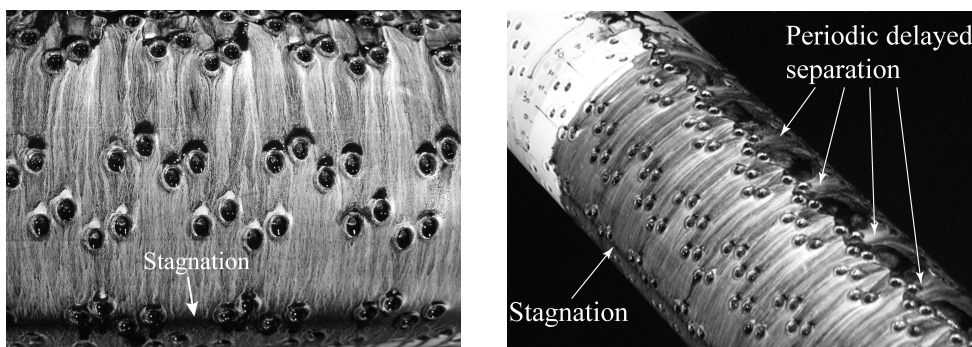
Figure 21: Surface oil visualization on pattern-indented surface.

are comparable with those observed with the CVGs in figure 6(b). It was furthermore noticed that the von Karman vortex shedding continued throughout the tested supercritical Reynolds numbers. This could be a result of a near straight-line separation forced by the line-like pattern. As pointed out in section 3.1, a forced straight-line separation enhances the regularity of alternating vortex shedding and may even stabilize it into the supercritical Reynolds numbers. Finally, it was shown in Kleissl and Georgakis (2011b) that due to the angular periodicity of the pattern on the pattern-indented cable, the lift coefficient suffered an dependency on the wind-angle of attack. When evaluating the Den Hartog galloping

criterion (Den Hartog, 1947) and neglecting structural damping, galloping instability was predicted within the supercritical flow regime.

The last study which has reported drag force measurements for a reproduced Pattern-indented cable is Yagi et al. (2010, 2011b). The results are presented in figure 19 and show a seminar level of drag as previously reported. This model was also tested in a static inclined rig with artificial rain simulation. Here the appearance of an upper rivulet was confirmed despite of a wind velocity within the supercritical regime. There are therefore some uncertainty about whether the Pattern-indented surface are capable of inhibiting the formation of an upper rivulet.

4. Wake dephasing and 3-D disturbance

So far, only means of controlling the boundary-layer or triggering its transition to turbulence have been discussed. These may also indirectly affects the cylinder wake due to the delayed separation, but this section covers effects which controls directly the wake field and its characteristics through spanwise variations. The near-wake of a circular cylinder has a high degree of organization and its turbulent structures are characterised by various scales, ranging from large-scale vortical structures (e.g. vortex shedding dominated by spanwise vorticity), and intermediate-scale structures (longitudinal or rib-like structures primarily aligned in the spanwise-streamwise plane) to Kolmogrov scale structures. Periodic geometric changes in the spanwise direction near the separation point can disrupt the two-dimensional shear layers by triggering a three-dimensional flow instability which initiates periodic vortex dislocations in the wake (Naumann and Quadflieg, 1974). The three-dimensionally redistributed shear layers become less susceptible to rolling up into a organized Kármán vortex street. Maull and Young (1974) found that longitudinal streamwise vortices acts as a boundary between two regions of vortex shedding, allowing for both dephasing and detuning of the vortex shedding. Thus, in between the spanwise periodic disturbances, cells of phase mismatched vortex shedding may still remain. Such cellular shedding naturally significantly reduces the correlation length. Since the base pressure depends on the development of the free shear layers and especially the vortex formation length (Bearman, 1965), a side benefit of breaking the nominally two-dimensional nature of the wake structures by vortex dislocations, is an increased base pressure and therefore also a mechanism of base drag reduction. If the drag penalty of the geometric modifications is small, a total drag reduction may be obtained. Studies have also pointed out the importance of the presences of streamwise vortices in the wake (Tanner, 1972; Darekar and Sherwin, 2001; Rodriguez, 1991) as streamwise vorticity is an excellent mean of turbulent transfer of the ambient pressure into the low-pressure region behind the cylinder as well as reducing the interaction between the separated shear layers and thus delaying the vortex formation. Further discussion of this control approach on non-circular bodies and details of a possible optimal wave length in included in the review by Choi et al. (2008).

This control measure may, depending of its extent, either significantly attenuates the Kármán vortex shedding followed by a drag increase or it may lead to a modest reduction

of both drag force and vortex shedding. The applications which significantly increases drag are of no interest in relation to bridge cables and are only shortly discussed.

Over time a large number of different application types have been proposed, many of which obtaining their spanwise variations by introducing a helical/twisting shape. Most of these will be discussed in the following and are illustrated at Fig. 22. The principe of how
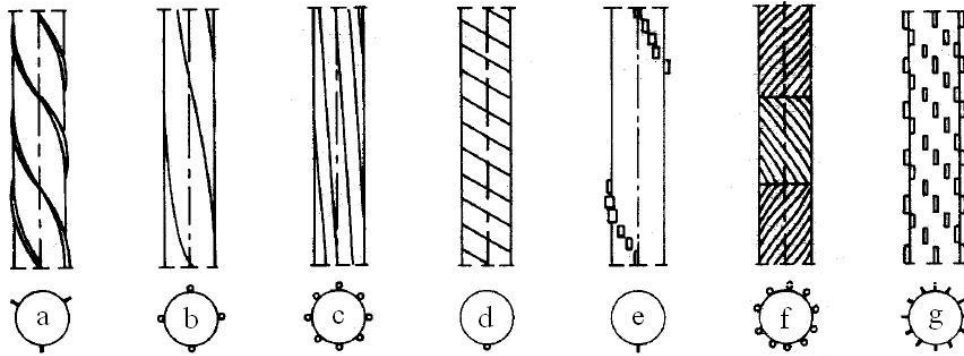

Figure 22: Illustration of different types of omnidirectional surface protrusions. Reproduced from Zdravkovich (1981).

these helixes may affect the free shear-flows and the wake width is illustrated in figure 23. Here it is shown how, at different sections along the cable, the helix is either resulting in an earlier, delayed, or unaffected separation point. The mirrored effect on the other cable side often lead to periodic asymmetries in the wake structures. The spanwise spacing between the modifications also determines whether regions of unaffected separation and wake width may appear.

Various definitions have been applied in the literature for defining the pitch length of the twist. Though in this work, all given pitch lengths are in accordance with the definition: "the axial length in which a filament or strand firstly returns to its original relative position".

4.1. Helical strakes

The first of the helical applications is know as "Helical strakes" and consist of typically three sharp-edged protrusions and an example is illustrated at Figure 22(a). With a rather significant height of $10 - 12\%$ of the cylinder diameter, the strakes introduce a three-dimensional disturbance in the flow by disorganizes the vortex structures in the wake. This is disrupting the coherence of vortex formation and help suppressing vortex induced vibrations (VIV) (Wong, 1977). The relatively large size ($> 0.1\,D$) of helical strakes generally increase the inherent drag of static cylinders. But for structures, such as deep water marine risers, where VIV motion may increase the drag loading even more, the VIV suppression abilities of the helical strakes can become an advantage. Though in relation to cable-stays on bridges where VIV only occurs at low wind velocities this is not an issue, as any possible VIV induced increased drag force is insignificant compared to design drag
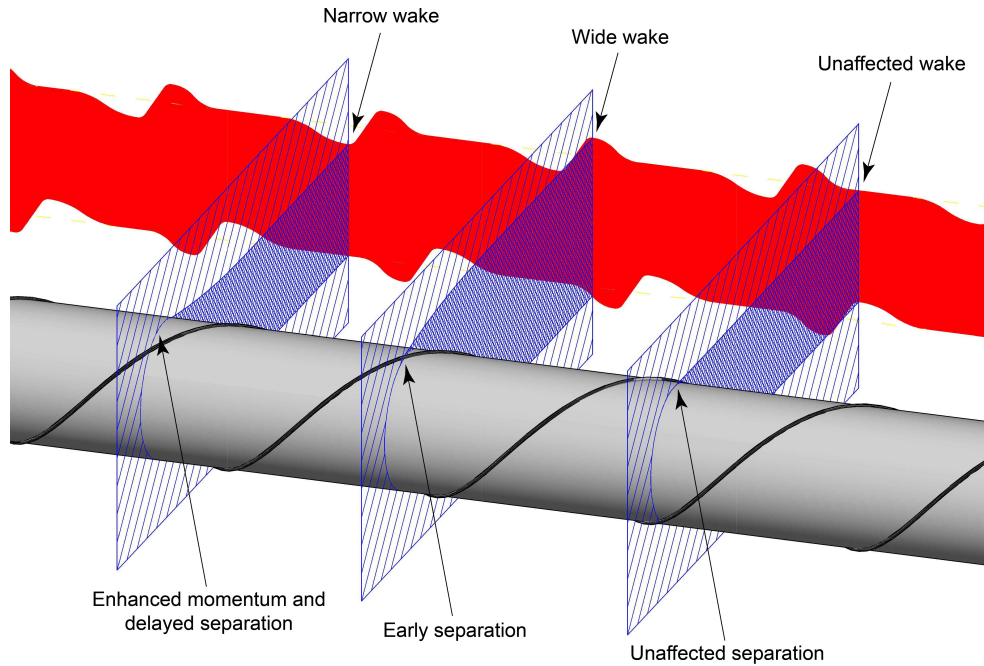
Figure 23: Illustration of the wavy wake width.

forces at much higher wind velocities. As the higher drag makes the helical strakes less attractive for cable-stays, their performance is only shortly summarized.

The use of three helical strakes was initially proposed by (Scruton and Walshe, 1957) and later patented (Scruton and Walshe, 1963). They performed experiments on a range of different strake heights ($h = 0.03\,D$ to $h = 0.12\,D$) for a fixed pitch length of $15\,D$. Even though the lowest strakes gave a noticeable reduction of the aerodynamic excitation, the largest reduction were found for the highest strakes. In the following years many experiments were carried out to optimize these parameters, often in relation to VIV of chimneys. The optimum strakes were found with a height of $0.10 - 0.12\,D$ and a $4 - 5\,D$ pitch length (Woodgate and Maybrey, 1959; Walshe and Wootton, 1970; Ruscheweyh, 1972; Blevins, 1990). Though introducing increased free-stream turbulence reduce their effectiveness (Vickery and Watkins, 1962; Gartshore et al., 1980). The corresponding drag coefficients was measured to be between $1.2 - 1.45$ and with a very low dependency on the Reynolds number (Cowdrey and Lawes, 1959; Simiu and Scanlan, 1978; Wong and Cox, 1980; Assi et al., 2010). A more detailed review of helical strakes can be found in Zdravkovich (1981).

During the recent decade a tendency for even larger strakes of up to $0.25\,D$ have appeared Frank et al. (2004); Trim et al. (2004, 2005); Brankovic and Bearman (2006); Pinto et al. (2006); Korkischko et al. (2007); Pontaza et al. (2009). Especially within the field of deep water marine risers where VIV suppression is essential. While the drag of these are higher, the corresponding wake structures show some most attractive properties. Bearman and Brankovic (2004); Constantinides and Oakley (2006); Korkischko and Meneghini

23

(2010); Zhou et al. (2011) all made flow visualizations around cylinders with helical strakes. From these studies it is observed that the enhanced three-dimensional character of the flow primarily is controlled by the following three effects.

Streamwise vortices The strakes introduce the presence of small-scale secondary shear layer vortices with strong streamwise vorticity, together with higher velocities at these positions.

Spanwise variation These secondary vortices seem to separate the wake into cells, matching the length between the strakes. This disruption of the vortical structures in the spanwise direction lowers the spanwise correlation and prevent the Kármán-like roll up from occurring.

Shear layer interaction The streamwise vortices also seem to reduce the interaction between the two shear layers, as suppressing the larger spanwise vortices restricts the momentum transfer through the center region of the wake. Resulting in a near constant wake width and increased vortex formation length.

An alternative orientation of the helical strakes was proposed by Novak (1967), where individual axial strakes are positioned in a staggered helical pattern as illustrated at Fig. 22(e). Furthermore a similar four-starting helix was later proposed by Alexandre (1970) shown at Fig. 22(g). Both applications applied relative large straks which resulted in significantly increased drag forces despite a decent suppression of VIV.

Finally it should be pointed out how helical applications performs differently if exposed to yawed flows. Yeo and Jones (2010, 2011) showed how helical strakes generated different flow structure on each side of the cylinder, thus only disturbing the rolled-up shear layer flow on the side with the strakes not aligned along the flow path. Which for helical stranded cables is known to result in a steady lift force (Nebres and Batill, 1993).

4.2. Helical wires & fillets

This section considers helical windings with a circular or near-circular cross-section. Helically wrapped wires were initially proposed in the fifties by Price (1956). The original purpose was, like with helical strakes, to combat vortex-induced vibrations (VIV) through preventing the formation of continuous vortices of full cylinder length by forcing flow separation to occur at different azimuth angles in adjacent cross sections. While the helical strakes generally seem superior against VIV due to their sharp egdes and thus stronger secondary streamwise vorticity, the helical wires are easy applicable due to the practical round shape which are well suited for retrofitting on existing structures.

The optimum configuration for VIV suppression are usually found for three or four larger helixes ($d \geq 0.1\,D$) with around a $12\,D$ pitch length (Weaver, 1961; Rispin et al., 1977; Wilson and Tinsley, 1989; Nebres and Batill, 1992). Though such larger sizes of helixes all suffer from an increased drag penalty (Wilson and Tinsley, 1989; Phelan et al., 2005).

Studies of the near-wake structures and vorticity of cylinders with helical wires within $0.06 D - 0.10 D$ confirmed the existence of periodic structures in the spanwise direction with localized increased streamwise vorticity and elongations of the vortex formation regions (Lee and Kim, 1997; Chyu and Rockwell, 2002; Sirisup et al., 2004). While these smaller sizes of helical wires still somewhat reduced the lift force fluctuations, the tests with helical wires lower than $0.08 D$ also found reduced wake width and drag coefficient. Thus if the wires are sufficiently small the beneficial effects from the disturbed and narrower wake may surpass the drag penalty from the helical wires them self.

An schematic illustration of four different flow categorizations a cylinder with a helical wire experience depending on the angular position of the wire are shown in Figure 24. These where developed in a more fundamental investigation by Nebres and Batill (1993) with only a single straight wire at different angular positions on a circular cylinder and shows how a wire may both significantly delay the final separation or provoke an earlier separation depending on its position. When arranged helically this results an a periodic waviness in the separation line and wake width as illustrated in Figure 23.
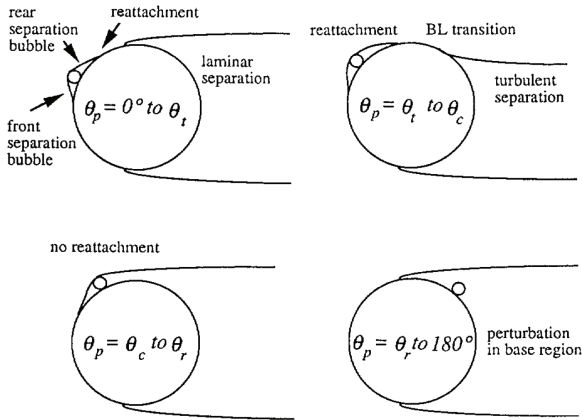

Figure 24: Schematic of the different flow regimes as a function of the protrusion angular position. Reproduced from Nebres and Batill (1993).
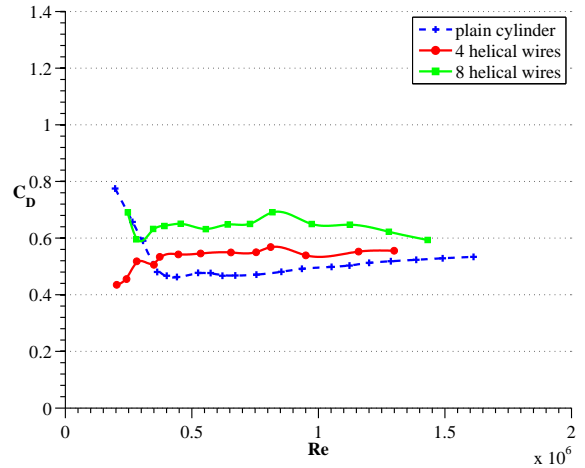
Figure 25: Drag coefficient curves for small helical wires. Reproduced from Nakagawa et al. (1959, 1963).

The effect of further reducing the size of the helical wires were studied by Nakagawa et al. (1959, 1963). For this; one, four, and eight windings (see Fig. 22(b-d)) with wire diameters of only $d = 0.004 D$ were investigated at supercritical Reynolds numbers of $\sim 4 - 10 \times 10^5$. At a wind velocity which could very well correspond to a design case for a typical stay cable, the drag coefficient was measured to 0.57 with four helical wires (see Figure 25), which is less than with equivalent uniform roughness. The four helical wires also significantly reduced the wind-induced oscillations throughout the tested range of velocities, though some excitation still occur at Strouhal number $St = 0.2$.

It was not until 1992, though, that tests on the use of helical applications (usually referred to as helical fillets or ribs) on a bridge stay cable were undertaken at CSTB

(Nantes) in connection with the design of the Normandy Bridge (Flamand, 1995) and later at the Danish Maritime Institute by Larose and Smitt (1999), in relation with the design of the Øresund Bridge. Their tests showed a strong reduction of RWIVs through the disruption of the formation of a coherent upper rivulet in the presence of light rain. As a consequence, a variety of helical fillet designs have emerged in the last decade, often with varying pitch lengths and fillet sizes.

During pre-studies for the Normandy Bridge (Flamand, 1993, 1994, 1995) tested spir-alled wires of different sizes and steps and found the best RWIV amplitude reduction for a single wire of $d = 0.008\,D$ diameter with a $1.88\,D$ pitch length. Though to ease the tube manufacturing process a symmetric application was applied, using double-starting helical fillets with same height and a $3.75\,D$ pitch length. These only near-round protrusions are known as helical fillets (or ribs) as they no longer resembles wires. The different manufac-turing technics e.g. welding or extrusion usually result in the fillets being slightly wider than their height. The helically filleted cable model was found successful in preventing the coherence of the vibrations of the water rivulets and with a relative low drag coefficient shown in Figure 26.
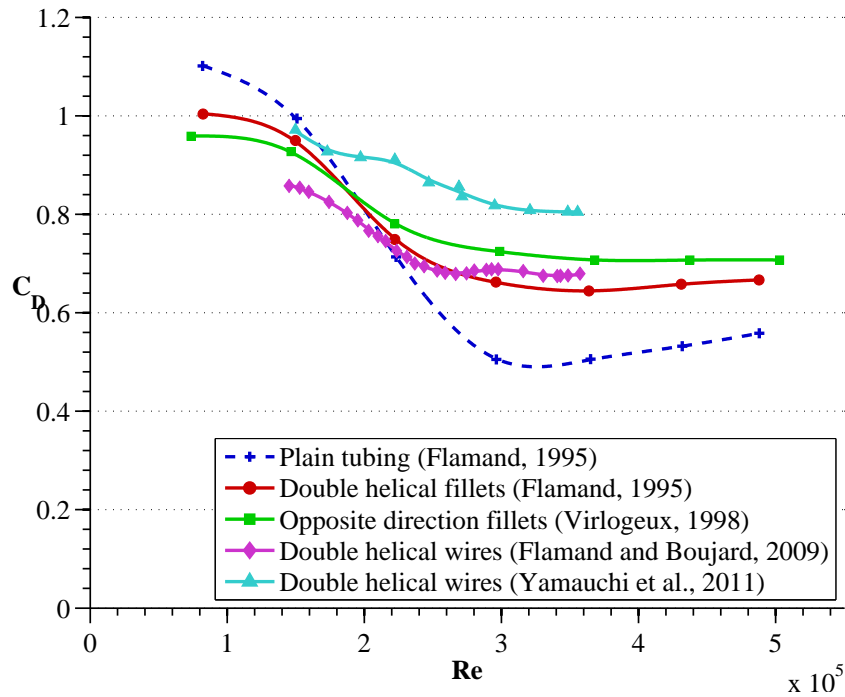
Figure 26: Data for different helical protrusions, reproduced from (Flamand, 1995; Flamand and Boujard, 2009; Virlogeux, 1998; Yamauchi et al., 2011).

Later similar findings for the Øresund Bridge (see Figure 27) was published by Larose and Smitt (1999) for a larger cable diameter also with double helical fillets with $d = 0.008\,D$ height and the same pitch. The tests showed a strong reduction of the RWIV by disrupting the formation of a coherent upper rivulet.

26
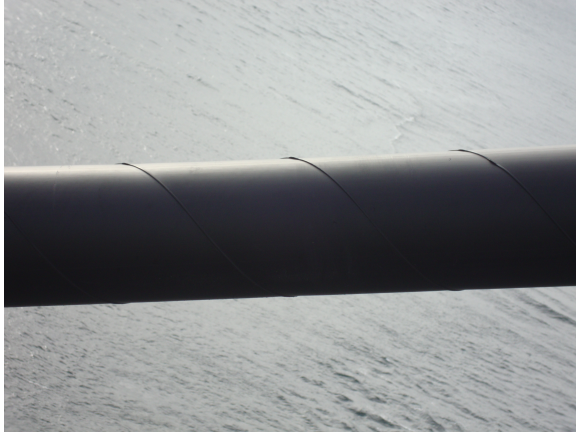
Figure 27: Photo of the double-starting helical fillets applied on the cables of the Øresund Bridge between Denmark and Sweden.

Figure 28: Drag coefficient over Reynolds number for varying cable diameter with same fillet sizes together and two arrangements of mini-strakes.

Based on the above mentioned test campaigns with helical fillets Stubler et al. (1999) claims a 95% RWIV amplitude reduction when comparing to a similar cable without fillets. And according to Virlogeux (1998) the application of these helical fillets was supposedly afterwards patented by Freyssinet, while the solution was originally suggested by an engineer of the Danish Maritime Institute (Virlogeux, 1999).

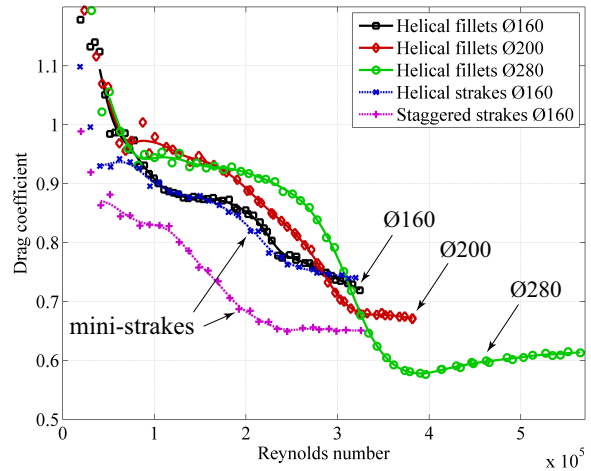Beside a mistake with swaped legends, the drag coefficient curves presented in Virlogeux (1998) also include the findings for a cable model with two helical fillets in each direction. The extra fillets make the cable suffer a drag penalty in the supercritical regime (see Figure 26) resulting in a increased drag coefficient of 0.7.

Further RWIV wind tunnel validation tests for the Rion-Antirion Bridge are presented in Flamand (2001). Here both 180 mm and 225 mm plain cables without the helical fillets experience strong RWIV. While no vibrations were observed after the cables were fitted with double-starting helical wires with $0.017\,D$ height at $1.39\,D$ pitch length and $0.013\,D$ height at $1.56\,D$ pitch angle for the smaller and larger cable diameter, respectively.

During an investigation including the critical Reynolds number regime, Flamand and Boujard (2009) measured the drag on a cable model with two helical wires with $0.011\,D$ diameter at $3\,D$ pitch length. The average drag coefficient measured over four rings of pressure taps are shown in Figure 26. While the increased fillet height resulted in a slightly increased drag coefficient of 0.68 at supercritical Reynolds number, the pressure distributions showed a rather smooth flow transition thus avoiding any sudden significant lift forces.

Even though helical fillets are generally found to significant reduce the RWIV amplitude, recent full-scale monitoring of the Øresund Bridge by Acampora and Georgakis (2011) continue to observe possible cases of RWIV, thus the helical fillets may only have a limited suppression effect on the formation on rivulets.

The use of several different fillet sizes combined with the fact that the pitch angle and

fillet size is often kept on various sizes of cable diameters significantly increases the variety of designs currently in use (Kleissl and Georgakis, 2013a). An example of such cable diameter dependency is shown in Figure 28, where drag measurements by the authors are presented for three different original full-scale HDPE tubing samples provided from different cable manufactures. All three samples have double helical fillets with an approximate height of $3.5 - 4$ mm and a pitch angle of $45°$. The results shows how continuously reducing the relative fillet hight by improper scaling makes the drag approaches that of a plain smooth cylinder.

But while a reduced relative helical fillet height appears beneficial for the drag performance, it has also been found that too small helixes can actually enhance the RWIV phenomena and results in larger amplitudes than observed without any helix. This observation was made by Gu and Du (2005) during a detailed parametric study intended to further clarify the RWIV phenomena. The test campaign involved evaluation of the RWIV suppressing ability of double helical wires of diameters $0.004\,D$, $0.008\,D$, $0.025\,D$ and $0.058\,D$ with pitch lengths varying from $1.25\,D$ to $5\,D$. The smallest wire diameter surprisingly enough enhanced the RWIV amplitudes while the second smallest only partially suppressed the RWIVs depending on the pitch length. For the two largest helical wire diameters tested the RWIVs were suppressed at all the tested pitch lengths and directions.

Similar wind tunnel evaluation of the necessary size of the helical wires to suppress RWIV were done by Zhan et al. (2008) and Yamauchi et al. (2011). While Zhan et al. (2008) found both the tested wire sizes of $0.004\,D$ and $0.007\,D$ capable, Yamauchi et al. (2011) found that a minimum wire size of $0.007\,D$ is necessary to suppress the RWIV.

Furthermore, helical wires have been found capable of suppressing wake-induced flutter of parallel stay cables (Mori et al., 2008). Though while several aerodynamics applications have a beneficial effect on phenomenons such as wake-induced vibrations, this topic is outside the scope of this review paper.

It should be noted that reproduction of the RWIV phenomena in wind tunnels and most likely also on the bridges are most sensitive to the surface energy state of the cable model (Kleissl and Georgakis, 2013a). Usually the surface energy of the cable models have to be artificially raised using various surface treatments to even get the phenomena to occur on plain cable models. It is therefore essential that future studies on the suppression of RWIV also document the energy state of the surface e.g. trough a droplet contact angle or similar parameter and possible also the expected values on actual bridges.

As also previously pointed out for the helical strakes, helical applications appear asymmetric when exposed to yawed wind. This was confirmed in Kleissl and Georgakis (2012b), where static force measurements on a helically filleted cable at several cable-wind angles showed significant lift coefficients and oil visualization showed strongly asymmetric flow behavior. The authors also later found in Kleissl and Georgakis (2013a) that during such yawed dry flow conditions the occurrence of significant dry limited-amplitude vibrations for several different helical applications including two sizes of helical fillets.

A possible way of avoiding such asymmetries could be to introduce periodic shifts in the pitch direction of the wires as for the herring bone pattern (Sallet and Berezow, 1972; Sallett, 1980) shown at Figure 22(f).

Recently, the authors proposed in Kleissl and Georgakis (2013b) an optimization of the near round cross-sectional shape of the helical fillets, to enhance the ability to drive water rivulets of the cable surface together with further increasing the amount of streamwise turbulence generated. The suggested shape are shown in figure 29(b) and consist of a sharp edged tip increasing the vorticity and a concave side which produces a ramping effect for the rivulets. For this, the naming "strakes" is reintroduced due to the resemblance in shape with the larger helical strakes discussed in section 4.1. These mini-strakes were tested in two different arrangements both shown in figure 29(a). One copying the standard double-starting 45° pitch angle of the current helical filleted cables and the second using a more innovative staggered helical pattern. The drag coefficients with these mini-strakes
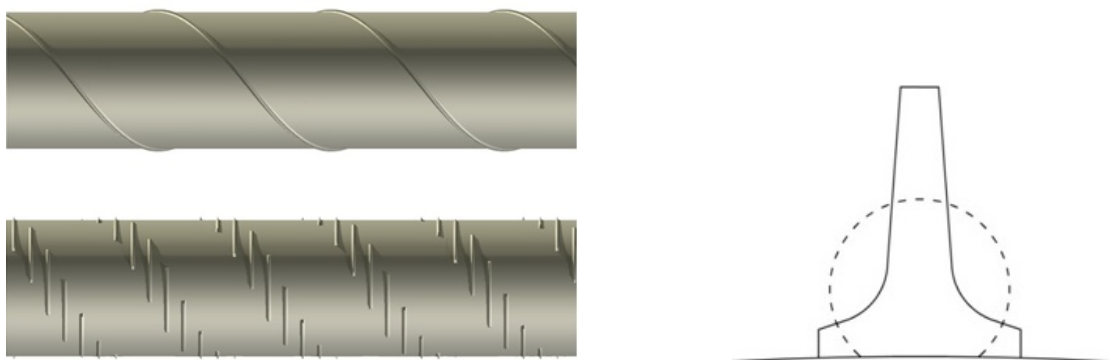
(a) Illustration of the helical and staggered arrangement the mini-strakes were tested in.

(b) Comparison of the cross-sectional shapes of the mini-strakes and the near round fillets.

Figure 29: Illustration of the innovative shape and pattern proposed by Kleissl and Georgakis (2013b).

are given in figure 28. The helically arranged mini-strakes and fillets experience similar drag force despite the 50% increased height of the strakes, indicating that the enhanced vorticity counteracts the increased drag penalty. The staggered helical arrangement had a drag coefficient of only 0.65, as the circumferential orientation of the strakes reduces the drag penalty. Furthermore, both the cable models with strakes was found superior for preventing rivulet formation compared with cables with normal near round helical fillets.

4.3. Helical Grooves & Channels

Another method for introducing spanwise disturbances without the drag penalty from large protrusions has been explored within the field of deep risers. The idea is to invert the helical strakes into helical grooves following similar helixes around the circular cylinder. A comprehensive study on such a triple-starting rectangular helical grooves were done in Huang (2006); Huang et al. (2007); Huang (2010, 2011). For groove depths in the order of 0.15 D the application was found to significantly suppress VIV with down ro only 0.6 drag coefficient. Though as the internal cross-sectional area is already highly utilized to minimize the cable stay diameters, this application would require larger outer diameters e.i. loosing its drag performance edge. But as the large helical protrusions ended up as small

helical fillets on the cable stays, these large grooves could have potential in the form of much smaller helical grooves. Such grooves may also be an excellent approach for catching and guiding away water rivulets.

Another similar method with more and less deep helical channels was studied in Yagi et al. (2010, 2011b,a). The channels are formed by attaching several rectangular protrusions (like for the Higashi-Kobe Bridge shown in Figure 11) at a certain helical pitch angle. In an attempt to minimize the drag coefficient several configurations with various pitch angles or number of channels were tested. The resulting drag coefficients are shown in Figure 30 where the lowest drag coefficient of 0.63 was obtained for a configuration with 12 protrusions of 5×7.5 mm at 27° pitch angle (see Figure 31(a)). This optimal configuration
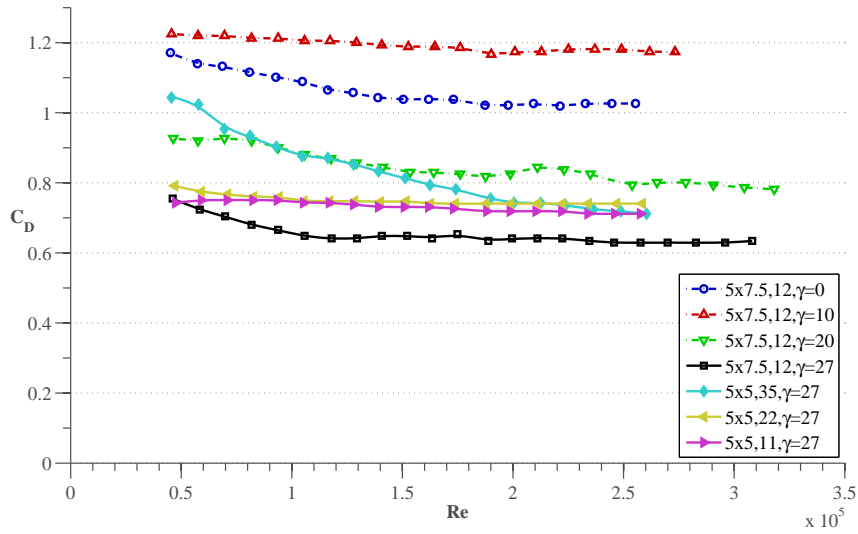
Figure 30: Drag coefficient over Reynolds number for various helical channels, Reproduced from Yagi et al. (2010, 2011b,a).

was furthermore found to mitigate the Kármán vortex shedding and inhibits the formation of water rivulets (Yagi et al., 2011b).

Though, the authors later reproduced the supposedly optimal configuration (see Figure 31) and retested it under enhanced flow conditions as part of a comparison study (Kleissl and Georgakis, 2013b). The new tests results showed that the minimum drag coefficient was around 0.95 which is in strong disagreement with the original findings. This cast some doubt about the drag performance of these helical channels and further testing is needed for final verification.

4.4. Circumferential perturbations

Another approach for introducing spanwise variations and 3-dimensional wake disturbances is to have a type of circumferential perturbation at regular intervals along the cable stays.

(a) Photo of test model with 12 protrusions of 5 × 7.5 mm at $\gamma = 27°$ pitch angle. Reproduced from Yagi et al. (2010).
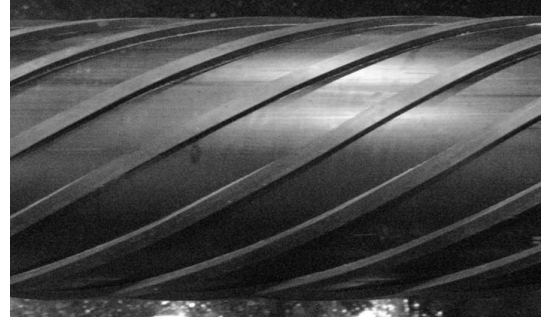
(b) Photo of a reproduction of the optimal configuration tested in Kleissl and Georgakis (2013b)

Figure 31: Photos of the optimal helical channel configuration according to Yagi et al. (2011b).

4.4.1. Circular Rings

The first to propose the use of circular rings was Sallet and Berezow (1972), where the intension were to avoid vortex shedding from suddenly occurring along the total length of the cylinder. It was not until 1998 that they were considered for cable stays. During several series of wind tunnel testing circular rings with a diameter of $0.125\,D$ to $0.05\,D$ at a spacing of $1.5\,D$ to $3\,D$ along the cable were found to be effective while $5\,D$ spacing was too much (Phelan et al., 2005). The rings increased the aerodynamic damping in dry conditions during high wind velocities and disturbs the formation of a continuous upper rivulet when exposed to rain simulation. While the extra aerodynamic damping may be the result of increased drag force, it did help suppress the otherwise present divergent dry galloping type of vibration and the velocity-restricted RWIV is assumed eliminated based on the disturb rivulet.

Further tests were done in Sarkar and Gardner (2000) where circular rings of an intermediate diameter of $0.071\,D$ at a spacing of $2\,D$ and $4\,D$ were investigated. The divergent high wind velocity vibration response was significantly reduced, especially for the smaller spacing.

After showing promising dynamic performance in wind tunnel test setups, prototypes with ring diameter of $0.139\,D$ and $3\,D$ spacing were manufactured and placed along the full length of two monitored Veterans' Memorial Bridge cable-stays (Phelan et al., 2006). A photo of the mounted prototypes are shown in Figure 32. During the following six months monitoring, no RWIV events occurred while several events were recorded prior to the installation. Under the conditions which previously led to RWIV, the fitted cables experienced a significantly lower maximum RMS acceleration. The vibration events left were identified as VIV, where the rings only resulted in a minor maximum RMS reduction. Finally it is noted that the application has been patented in Sarkar et al. (2002).

A cable model with somewhat smaller rings with only $0.02\,D$ diameter and a $3.57\,D$ spacing was studied by Yamauchi et al. (2011). During rain simulation the rivulet was quickly reestablished after crossing the rings, though some of the water was blown of at

Figure 32: Circular rings mounted on two of the Veterans' Memorial Bridge cable-stays. Reproduced from Phelan et al. (2006).
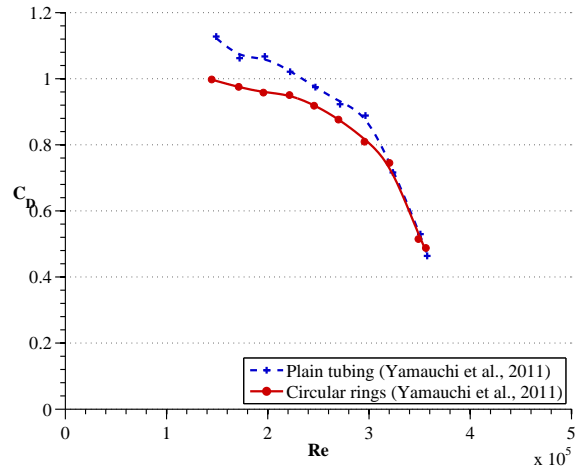
Figure 33: Drag coefficient over Reynolds number for HDPE tubing with and without circular rings. Reproduced from Yamauchi et al. (2011).

the rings. This, depending on the amount of damping, either resulted in a reduction or a complete mitigation of the RWIV. The study also included measurements of the drag coefficient which are shown in figure 33. The results show that the small circular rings provided a drag reduction within the subcritical regime, possible due to reduced correlation length and 3-dimensional wake disturbances from the rings. Furthermore, the velocity at which the transition to turbulent flow occurs are observed unaffected by the rings. How the rings influence the supercritical drag and possible design drag coefficients are not known.

A detailed investigation of the flow around static cylinders with circular rings was done in Lim and Lee (2004). Two of the tested models in this study are shown in Figure 34. Circular rings with $d = 0.017\,D$ diameter and $0.165\,D$ spacing was found to provide a drag reduction of 9%, though only within the subcritical Reynolds number regime up to $Re = 1.2 \times 10^5$. Furthermore flow visualizations confirmed the presence of narrower wake and how the rings elongates vortex formation region.
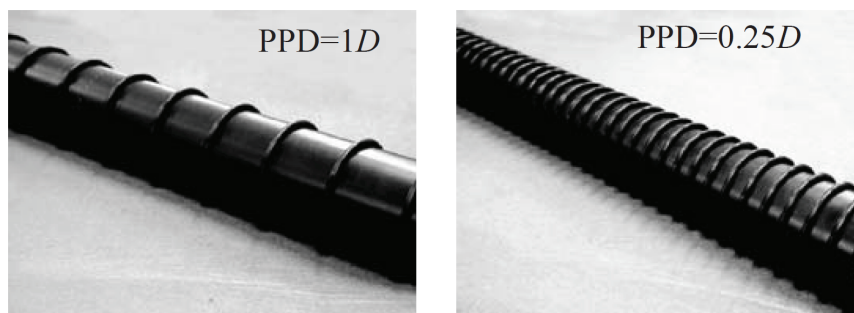

Figure 34: Cylinders with O-rings attachments. Reproduced from Lim and Lee (2004).

4.4.2. Other shapes & elliptical fittings

In the previous mentioned work by Phelan et al. (2005) on circular rings, another variation with elliptical rings was also tested. The application was only found effective at certain angles as the skew angle between the cable axis and the ring made the performance dependent on the wind angle of attack. Furthermore the drag force measurements with wind normal to the cable axis showed a 5% increase of the drag coefficient in the subcritical flow regime at $Re = 1.67 \cdot 10^5$.

In a similar study by Wenbo and Zhixing (2005) also considering elliptical rings they were found effective against RWIV. Though if the ring interval become too large water rivulets would form.

While it may be a bit impractical, an elliptical protrusion could utilize that the wind is always near horizontal. E.i. if the angle of the elliptical ring matches the cable inclination the wind would stay parallel to the rings and the drag coefficient may not suffer the same penalty. Such an idea using thick horizontal elliptical plates as illustrated in figure 35 was proposed and tested in Matsumoto et al. (1998); Matsumoto (1998). Since the modification should be sufficient for preventing water rivulets from forming, only the formation of axial flow and the high reduced velocity dynamic response were studied and in both cases a reduction was found.
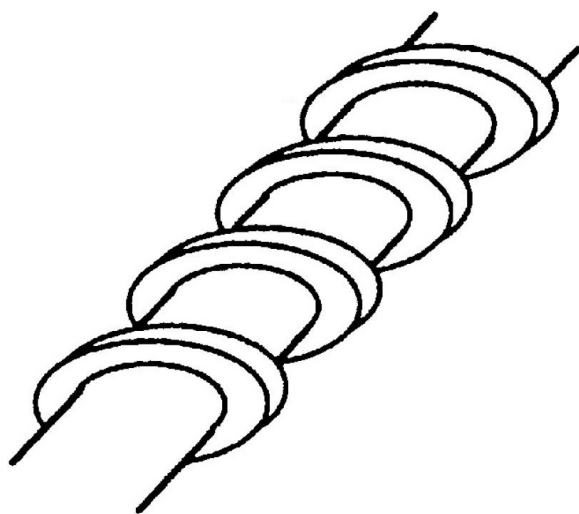
Figure 35: Sketch of the thick horizontal elliptical plates. Reproduced from Matsumoto (1998).
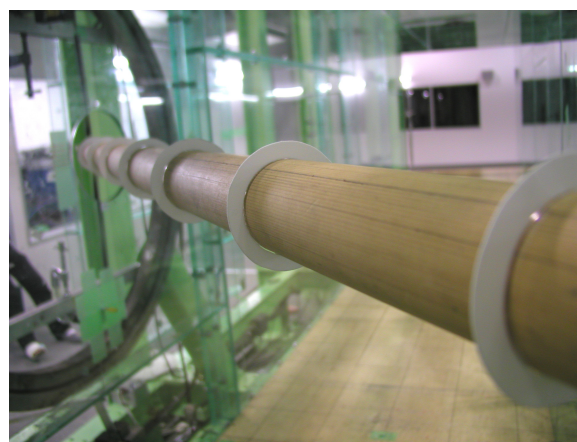
Figure 36: Photo of the thin circular plates. Reproduced from Matsumoto et al. (2007)

One way to definitely suppress the axial flow and significantly reduce the spanwise vortex correlation is to apply thin circular plates as shown in figure 36. These were considered by Matsumoto et al. (2007) and despite the expected suppressed axial flow the cable model still experienced a type of dry galloping onset. Though the vibration did not seem governed by the damping level as both higher and lower Scruton numbers experienced less vibration. The application would furthermore be most impractical and significantly increased aerodynamic forces should be expected.

An alternative would be cylinders with stepwise changes in the outer diameter (usually named stepped cylinders). They were originally proposed as spaced concentric bushings to prevent the formation of continuous vortices of full cylinder length by Price (1956). Beside dephasing the vortex shedding, the adjacent sections with different diameters also causing vortices to be discharged at different frequencies. Due to the vortex excitation suppressing nature they have mainly been investigated as applications for marine cables, where they are known as collars. Though compared with the other available VIV suppressing devices they were generally proven to be ineffective (Naudascher and Rockwell, 2005).

In the latest study by Nakamura and Igarashi (2007, 2008) the design was optimized with respect to minimizing the drag coefficient. After realizing that it is the streamwise vorticity generated at the steps which introduces the wake disturbance, the length ratio covered with collars was significantly reduced. With a optimum collar configuration of $1.3\,D$ diameter, $1\,D$ length and $6\,D$ spacing as shown in figure 37 the subcritical drag force was reduced by 15%. The flow visualizations observed a narrowing of the wake together with a weakening of the fluctuating lift due to suppression of vortex shedding.

Figure 37: Near-wake flow visualization of cylinder with collars with optimal configuration. Reproduced from Nakamura and Igarashi (2008).

4.5. Wavy cylinders

This section considers wavy cylinders also known as sinusoidal or varicose cylinders where the diameter is varying in a sinusoidal manner along its spanwise direction. This type of cylinder have been extensively studied for its control of drag force and vortex formation.

With a proper design of the waviness large drag reduction of up to 22% have been reported at subcritical Reynolds numbers $\sim 1 - 4 \times 10^4$ (Lam et al., 2004a; Nguyen and Lee, 2004; Lee and Nguyen, 2007). Though it is important to note that these reductions

are found on drag coefficients based on the mean cylinder diameter. If such wavy cylinders were to be applied for cable stays the effectively useable area would correspond to the minimum diameter of the wavy cylinder. Thus for such application it is only fair that its drag force is compared against a normal circular cylinder with a diameter matching the minimum diameter of a wavy cylinder. With this correction, the 22% drag reduction reported by Nguyen and Lee (2004); Lee and Nguyen (2007) now correspond to a 30% increase due to a relative large geometric amplitude, while the 20% reduction reported by (Lam et al., 2004a) remain as a reduction though only of 2%. Furthermore several studies found that the drag coefficient for wavy cylinders tends to increase for increasing Reynolds number (Lam et al., 2004a,b; Lee and Nguyen, 2007). Thus at its best, the wavy cylinder will most likely only keep an unchanged drag performance and should only be considered because of its other beneficial affects.

The reason why the wavy cylinder is capable of maintaining the level of drag force despite an increased frontal area is because the spanwise variation increases the base pressure at any spanwise location (Lam et al., 2004a) which then counteracts the adverse effect of the larger frontal area. Figure 38(a) illustrate how the wavy geometry introduce small spanwise velocity components (Ahmed and Bays-Muchmore, 1992; Wang et al., 2004; Lam et al., 2004b) which make the surface streamlines collect near the nodes, where the terminology 'nodes' and 'saddles' is used for the axial locations of the maximum and minimum diameter, respectively. The intensified flow near the nodes raises its momentum which delays the flow separation thus resulting in a wavy separation line along the cylinder span. Furthermore Zhang et al. (2005) found that a pair of counter-rotating secondary streamwise vortices, concentrated at each side of the nodes, develops from the rolling-up of the shear layer separated from the cylinder surface. The delayed separation at the nodes combined with high momentum and streamwise vorticity results in a constant and more narrow wake width than at the saddle points (Ahmed et al., 1993; Lam et al., 2004b; Nguyen and Lee, 2004; Wang et al., 2005). A sectional view illustrating the difference in separation point and wake width for nodes and saddles planes are shown in figure 38(b).

These strong spanwise variations significantly reduce the correlation length along the cylinder and disturbs the development of large-scale spanwise vortices and the regularity of vortex shedding. The formation region of the wavy cylinder have also been found much longer than for a circular cylinder (Lam et al., 2004b; Lee and Nguyen, 2007). Such a lengthening of the vortex formation region also transports eddies farther away from the base of the cylinder, which causes a smaller fluctuating lift to be observed from the already weakened vortex shedding. Furthermore is the shedding frequency also disturbed by the continuously varying cylinder diameter.

Recently further optimization of the wavy cylinder have been carried out in Lam and Lin (2007, 2008b,a, 2009) using three-dimensional numerical methods. Though since the configuration where optimized with respect to drag coefficient based on the average diameter and not the minimum, the findings are only an approximation. The optimal design and the flow characteristic did in outline match the observations of the previously experimental studies, but still only considering low Reynolds numbers.

finally Lam et al. (2010) investigated a yawed wavy cylinder at subcritical Reynolds
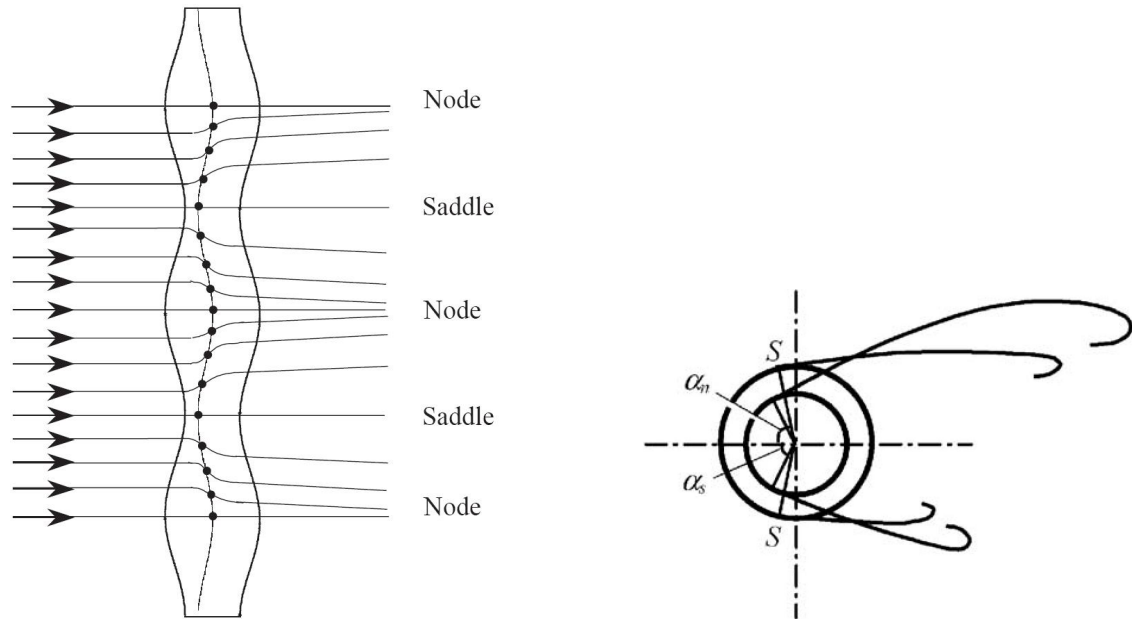
(a) Side view illustrating the surface streamlines and separation line.

(b) Sectional view showing the later separation point and the narrower wake width of the node points compared with the saddles points.

Figure 38: Illustration of surface flow patterns and near-wake structures of a wavy cylinder. Reproduced from Lam et al. (2004b).

number. As the yaw angle increases the advantageous effects on drag and vortex shedding was found to disappear. The effect of the cylinder waviness against axial flow, rivulet formation and other wind-induced vibrations together with its drag performance at critical and supercritical Reynolds numbers is not known.

4.6. Hemispherical bumps

In order to reproduce some of the effects of the wavy cylinder and the previously discussed helical applications, Owen et al. (2001) investigated a circular cylinder with hemispherical bumps (also known as caps) attached to the side as shown at Fig. 39. The bumps were positioned with a fixed 1.75 D longitudinal spacing and a step of 45° in the angular position arranging them in a spiral pattern with 7 D half pitch length. By attaching the bumps in a spiral pattern, the dependency on the angle of attack was reduced significantly. Though the relative large angular step only makes this a near-omnidirectional application. Drag force measurements by Owen et al. (2001) shows a near constant drag coefficient of 0.91 for Reynolds numbers within $2 \times 10^4 - 10^5$ corresponding to a subcritical flow regime. While this subcritical drag coefficient corresponds to a 24% reduction, the supercritical drag force performance have not been investigated.

Beside reducing the drag force, the helically arranged bumps also significantly weakens the VIV excitation. But even though shedding cannot be detected when the model is fixed, the fluid-structure interaction for a flexible model can help the synchronization and build
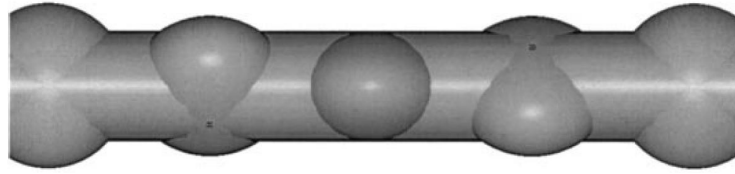
Figure 39: Circular cylinder fitted with a helical arrangement of bumps. Reproduced from Owen et al. (2001).

up of VIV (Bearman and Brankovic, 2004). This promising concept, both reducing drag and VIV compared to a plain cylinder, was afterwards patented in Bearman et al. (2005).

4.7. Polygonal & faceted cylinders

In this section different angular cylinders are considered, where the sharp edges are used to fix the stagnation and separation lines forcing a spanwise variation disturbing the wake and the discharged vortices.

According to the Glauert-Den Hartog criterion, it is clear that straight polygonal cylinders e.g. considered by Szalay (1989); ESDU 79026 (1980) and many more, do not have sufficient aeroelastic stability. Even if sufficiently high-order polygons is considered to bring down the dependency on angle of attack the parallel sharp edges would only straighten the separation lines and enhance the spanwise correlation.

But by e.g. adding a longitudinal twist to the polygonal cylinder, the sharp edges will reduce the correlation by introducing a spanwise variation. Known to the authors, Hojo (1992) was the first to consider such a twisted polygonal shape for bridge cable stays as to prevent RWIV. For a cable model with a hexagonal cross-section and a $10°$ pitch angle ($43\,D$ pitch length) the dynamic tests showed a complete suppression of RWIV while the plain cable suffered strong RWIV under same conditions.

Later a similar study was made by Kobayashi et al. (1995) also considering twisted polygonal for cables stays. Three different polygon sections with 6, 12 and 24 sides respectively all with a twist of $90°$ per $10D$ corresponding to a pitch length of $40\,D$. The drag coefficient measured for each of these cable models are shown in figure 40. Here the polygons with 6 and 12 sides have a relative high drag coefficient both ending up above 1.0 at Reynolds number 8×10^4 while the model with 24 sides may end up at a lower supercritical drag level. The twisted hexagonal model was not considered further due to its high drag coefficient. During evaluation of RWIV both the polygonal models formed two or three rivulets formed at the sides of the rearward edges while the circular cylinder only formed a single larger rivulet. Despite the different rivulet behavior, both polygonal models suffered from RWIV though with a reduced amplitude compared to the circular cylinder.

Another type of shape also having several sharp edges with a spanwise varying position is a faceted cylinder. One such example which received much attention due to its remarkable aeroelastic stability is the unique architectonic sculpture 'Brancusi's Endless Column' inaugurated in Romania at 1938 by Constantin Brancusi. The column has been referred

37
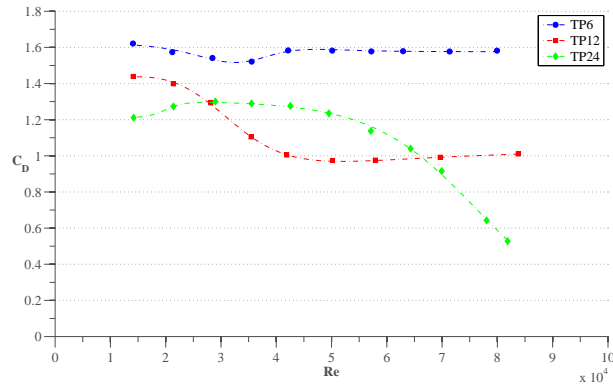
Figure 40: Drag coefficient for three twisted polygonal sections. Reproduced from Kobayashi et al. (1995).

to as aeroelastic indifferent because of its unconventional shape shown in figure 41 and have been the object of several aeroelastic studies (Lungu et al., 2002; Solari et al., 2002; Gabbai, 2008; Dragomirescu et al., 2009).

Figure 41: Picture of Brancusi's Endless Column after completed restoration 2000. Photo: Scott Laws.

Figure 42: Faceted hexagonal cylinder.

While the faceted cylinder in general seem to have several good attributes this specific shape are inapplicable to cable stays due to its large drag and wind angle of attack dependency. But inspired by this sculpture the authors recently tested a similar faceted cylinder adjusted to be suited for an application on cable stays (Kleissl and Georgakis, 2011a). To better fit around a circular cylinder the facet arrangement was updated with an increased number of facets as shown in figure 42. The wind tunnel tests found that both the drag force and the angle of attack dependency were reduced. But with a drag coefficient around 1.5 the design is far from applicable.

Even though the these faceted cylinders were found to increase the drag force, they are still included here as the principal of having skew sharp edges still may proof more effective if further optimized.

5. Outer-layer-devices (OLD)

Outer-layer-devices (OLD's) covering the different variation of shrouds which affect the entrainment layers

A shroud is a surrounding shell offsetted from the original surface and which allows a part of the flow to penetrate. Over time three types of shrouds have been proposed: the perforated cylindrical shroud, axial slats shroud and axial rods shroud as shown in figure 43.
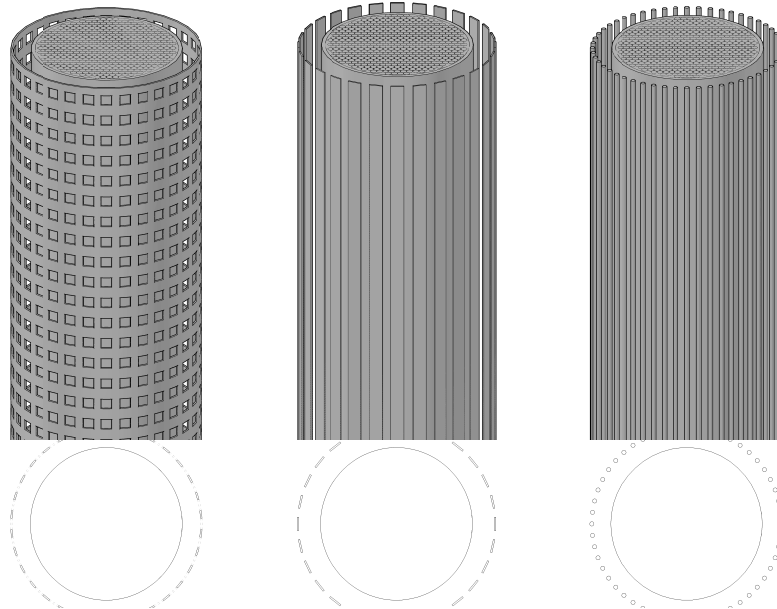
Figure 43: Illustration of a) Perforated cylindrical shroud b) Axial slats shroud c) Axial rods shroud.

Due to the limited recent work within the fields of omnidirectional shrouds, the existing detailed review by Zdravkovich (1981) are still too a large extend covering the main development and have only been followed by the individual studies by Wong and Cox (1980); Wong and Kokkalis (1982); Galbraith (1980, 1981); Airey et al. (1988); Molin (1993)

Shrouds are generally found to successfully suppress any VIV but can be susceptible to mechanical damage and may be impractical and expensive. By introducing a significant base bleed and fluid ejection into the free shear layers the shrouds increases base pressure, significantly delays the vortex formation and have little dependence on Reynolds number. Despite the increased outer shroud diameter the level of the drag coefficient lies within $0.8 - 1.1$ when based on the inner cylinder diameter. While a shrouded cable is expected to eliminate the wind induced vibrations (Kleissl and Georgakis, 2011a), the drag coefficient is still larger than current applications within supercritical Reynolds numbers.

6. Concluding remarks

In this review, the control methods was organized onto groups of control technics and classified accordingly. Four categorizations were introduced; (a) direct transition to turbulence by using a boundary-layer instability, (b) early separation and reattachment by the use of a shear-layer instability, (c) wake dephasing and 3-D disturbance by the generation of three-dimensional wake structures, and (d) outer-layer-devices affecting the entrainment layers.

As the drag force at the design wind velocity is crucial on bridge cables, drag reduction technics within the supercritical flow regime becomes essential. Based on the observations for the approaches considered in this review, two technics prevails both suppressing supercritical vortex shedding. Minimizing spanwise and increasing streamwise voticity within the shear layers minimizes the shear layer interaction and delays the vortex formation region. Alternatively the vortex shedding can be disturbed by introducing three-dimensional wake structures by using spanwise variations. Obtaining one or preferable a combination of these by surface modifications generating a minimum of form drag penalty is expected to yield the optimal supercritical drag reduction.

So even though VIV is of less importance for bridge cables it do, beside the lift force fluctuations, also widens the wake and reduces base pressure and thus its suppression could be the key to maintaining a low supercritical drag force.

Furthermore, the presence of streamwise vorticity may be able to further delay the already turbulent flow separation due to its better transfer of momentum.

Finally the surface modifications should be capable of disturbing or even prevention the formation of water rivulets so as to avoid any excessive RWIVs.

7. References

Acampora, A., Georgakis, C. T., 2011. Recent monitoring of the oresund bridge: Rain-wind induced cable vibrations. In: Proceedings of the 13th International Wind Engineering Conference, Amsterdam.

Achenbach, 1971. Influence of surface roughness on the cross-flow around a circular cylinder. Journal of Fluid Mechanics 46, 321–335.

Achenbach, 1974. The effects of surface roughness and tunnel blockage on the flow past spheres. Journal of Fluid Mechanics 65, 113–125.

Achenbach, E., 1981. On vortex shedding from smooth and rough cylinders in the range of reynolds numbers 6×10^3 to 5×10^6. Journal of fluid mechanics 109, 239–251.

Ahmed, A., Bays-Muchmore, B., Sep 1992. Transverse flow over a wavy cylinder. Physics of Fluids A 4 (9), 1959–1967.

Ahmed, A., Khan, M. J., Bays-Muchmore, B., Mar 1993. Experimental investigation of a three-dimensional bluff-body wake. AIAA Journal 31 (3), 559–563.

Airey, R., Hartnup, G., Stewart, D., 1988. A study of two vortex suppression devices for fitting to marine risers. In: Proceedings of the 7th International Conference on Offshore Mechanics and Arctic Engineering, New York. Vol. 2. pp. 245–251.

Alexandre, M., 1970. Experimental study of the action of vortex shedding on cylinders with longitudinally welded fins. In: Paper presented at Euromech Colloq. 17, Cambridge (U.K.).

Assi, G., Bearman, P., Kitney, N., Tognarelli, M., 2010. Suppression of wake-induced vibration of tandem cylinders with free-to-rotate control plates. Journal of Fluids and Structures 26 (7-8), 1045–1057.

Bandyopadhyay, P. R., 1986. Review—mean flow in turbulent boundary layers disturbed to alter skin friction. Journal of Fluids Engineering 108 (2), 127–140.

Basu, R., 1985. Aerodynamic forces on structures of circular cross-section. part 1. model-scale data obtained under two-dimensional conditions in low-turbulence streams. Journal of Wind Engineering and Industrial Aerodynamics 21 (3), 273 – 294.

Bearman, P., Feb 1965. Investigation of flow behind two-dimensional model with blunt trailing edge and fitted with splitter plates. Journal of Fluid Mechanics 21 (2), 241–256.

Bearman, P., Brankovic, M., 2004. Experimental studies of passive control of vortex-induced vibration. European Journal of Mechanics - B/Fluids 23 (1), 9 – 15, bluff Body Wakes and Vortex-Induced Vibrations.

Bearman, P., Owen, J., Szewczyk, A., Jun 2005. Vortex shedding and drag force reduction. United States Patent 6,908,063 B2.

Bearman, P. W., Harvey, J. K., 1976. Golf ball aerodynamics. Aeronautical Quarterly 27 (May), 112–122.

Bearman, P. W., Harvey, J. K., Oct 1993. Control of circular cylinder flow by the use of dimples. AIAA Journal 31 (10), 1753–1756.

Bechert, D. W., Bartenwerfer, M., 1989. The viscous flow on surfaces with longitudinal ribs. Journal of Fluid Mechanics 206, 105–129.

Behara, S., Mittal, S., 2011. Transition of the boundary layer on a circular cylinder in the presence of a trip. Journal of Fluids and Structures 27 (5-6), 702–715.

Blevins, R. D., 1990. Flow-Induced Vibration, second edition, reprint edition 2001 Edition. Krieger Publishing Company, Malabar, FL, Krieger Drive, Malabar, FL 32950.

Brankovic, M., Bearman, P., 2006. Measurements of transverse forces on circular cylinders undergoing vortex-induced vibration. Journal of Fluids and Structures 22 (6-7), 829 – 836, bluff Body Wakes and Vortex-Induced Vibrations (BBVIV-4).

Buresti, G., 1981. The effect of surface roughness on the flow regime around circular cylinders. Journal of Wind Engineering and Industrial Aerodynamics 8 (1-2), 105 – 114.

Choi, H., Jeon, W.-P., Kim, J., 2008. Control of flow over a bluff body. Annual Review of Fluid Mechanics 40 (1), 113–139.

Choi, J., Jeon, W.-P., Choi, H., 2006. Mechanism of drag reduction by dimples on a sphere. Physics of Fluids 18 (4), 41702–1–4.

Choi, K.-S., 1989. Near-wall structure of a turbulent boundary layer with riblets. Journal of Fluid Mechanics 208, 417–458.

Chyu, C.-K., Rockwell, D., 2002. Near-wake flow structure of a cylinder with a helical surface perturbation. Journal of Fluids and Structures 16 (2), 263 – 269.

Constantinides, Y., Oakley, Jr., O. H., 2006. Numerical prediction of bare and straked cylinder viv. ASME Conference Proceedings 2006 (47497), 745–753.

Cowdrey, C. F., Lawes, J. A., Jul 1959. Drag measurements at high reynolds numbers of a circular cylinder fitted with three helical strakes. Natl. Phys. Lab.(UK), Areo Report 384.

Darekar, R. M., Sherwin, S. J., 2001. Flow past a square-section cylinder with a wavy stagnation face. Journal of Fluid Mechanics 426, 263–295.

Den Hartog, J., 1947. Mechanical Vibrations. McGraw-Hill, New York.

Dragomirescu, E., Yamada, H., Katsuchi, H., 2009. Experimental investigation of the aerodynamic stability of the Endless Column, Romania. Journal of Wind Engineering and Industrial Aerodynamics 97 (9-10), 475 – 484.

Duriez, T., Aider, J.-L., Wesfreid, J. E., jul 2006. Base flow modification by streamwise vortices: application to the control of separated flows. In: Proceedings of ASME Joint U.S. - European Fluids Engineering Summer Meeting, Miami, FL.

Duriez, T., Aider, J.-L., Wesfreid, J. E., 2008. Control of a separated flow over a smoothly contoured ramp using vortex generators. IUTAM Symposium on Flow Control and MEMS 7, 437–441.

ESDU 79026, 1980. Mean fluid forces and moments on cylindrical structures: polygonal sections with rounded corners including elliptical shapes. Technical Report 79026, IHS ESDU International plc, UK.

Every, M. J., King, R., Griffin, O. M., 1982a. Hydrodynamic loads on flexible marine structures due to vortex shedding. Journal of Energy Resources Technology 104 (4), 330–336.

Every, M. J., King, R., Weaver, D. S., 1982b. Vortex-excited vibrations of cylinders and cables and their suppression. Ocean Engineering 9 (2), 135 – 157.

Fage, A., Warsap, J., Oct 1929. The effects of turbulence and surface roughness on the drag of a circular cylinder. In: Aeronautical Research Council R. & M. No. 1283. pp. 248–255.

Fiedler, H., Fernholz, H.-H., 1990. On management and control of turbulent shear flows. Progress in Aerospace Sciences 27 (4), 305 – 387.

Flamand, O., Jun 1993. Rain-wind induced vibration of cables. In: et al., T. M. (Ed.), proceedings of the 2nd European Conference on Structural Dynamics, Trondhein, Norway. A.A. Balkema, Rotterdam, The Netherlands.

Flamand, O., Oct 1994. Rain-wind-induced vibration of cables. In: Proceedings of the International Conference on Cable-Stayed and Suspension Bridges, Deauville, France. Vol. 2. pp. 523–531.

Flamand, O., 1995. Rain-wind induced vibration of cables. Journal of Wind Engineering and Industrial Aerodynamics 57 (2-3), 353 – 362.

Flamand, O., 2001. An explanation of the rain-wind induced vibration of inclined stays. In: 4th International Symposium on Cable Dynamics, Montrãl.

Flamand, O., Boujard, O., Jul 2009. A comparison between dry cylinder galloping and rain-wind induced excitation. In: Proceeding of the 5th European & African Conference on Wind Engineering, Florence.

Frank, W., Tognarelli, M., Slocum, S., Campbell, R., Balasubramanian, S., May 2004. Flow-induced vibration of a long, flexible, straked cylinder in uniform and linearly sheared currents. In: Offshore Technology Conference, Houston, Texas. No. 16340-MS.

Fujiwara, T., Yamaguchi, K., Manabe, Y., 1999. Vibration control of cables of the tatara bridge. Bridges & Foundations Engineering 5, 16–19, in Japanese.

Gabbai, R. D., 2008. Influence of structural design on the aeroelastic stability of Brancusi's Endless Column. Journal of Engineering Mechanics 134, 462.

Gad-El-Hak, M., Bushnell, D., mar 1991. Separation control - review. ASME Transactions Journal of Fluids Engineering 113, 5–30.

Galbraith, R., 1981. Aspects of the flow in the immediate vicinity of a porous shroud. Journal of Wind Engineering and Industrial Aerodynamics 8 (3), 251 – 258.

Galbraith, R. A. M., 1980. Flow pattern around a shrouded cylinder at re = 5 x 103. Journal of Wind Engineering and Industrial Aerodynamics 6 (3-4), 227 – 242.

Gartshore, I. S., Khanna, J., Laccinole, S., 1980. The effectiveness of vortex spoilers on a circular cylinder in smooth and turbulent flow. In: Proceeding of the Fifth International Conference on Wind Engineering. pp. 1371–1379.

Gu, M., Du, X., 2005. Experimental investigation of rain-wind-induced vibration of cables in cable-stayed bridges and its mitigation. Journal of Wind Engineering and Industrial Aerodynamics 93 (1), 79 – 95.

Güven, O., Farell, C., Patel, V. C., 1980. Surface-roughness effects on the mean flow past circular cylinders. Journal of Fluid Mechanics 98 (04), 673–701.

Heine, B., Schwermer, T., Raffel, M., jul 2010. The effect of vortex generators on the flow around a circular cylinder. In: 15th Int Symp on Applications of Laser Techniques to Fluid Mechanics, Lisbon, Portugal.

Hojo, T., Feb 1992. Experimental study on rain vibration and suppression method of cables in cable-stayed bridges. J. of Wind Engineering Structures 50 (50), 19–26, in Japanese.

Hojo, T., Yamazaki, S., Miyata, T., Yamada, H., 1995. Development of aerodynamically stable cables for cable-stayed bridges having low resistance. Bridges & Foundations Engineering 6, 27–32, in Japanese.

Hojo, T., Yamazaki, S., Okada, H., Jul 2000. Development of lowdrag aerodynamically stable cable with indented processing. Special Issue on Steel Structure 82, Nippon Steel Corporation.
URL http://www.nsc.co.jp/en/tech/report/pdf/8203.pdf

Hover, F. S., Tvedt, H., Triantafyllou, M. S., 2001. Vortex-induced vibrations of a cylinder with tripping wires. Journal of Fluid Mechanics 448, 175–195.

Huang, S., Jun 2006. Preliminary tank testing of VIV suppression of helical grooves. In: Proceedings of the 25th International Conference on Offshore Mechanics and Arctic Engineering, Hamburg, Germany. Vol. 4. pp. 469–473.

Huang, S., Feb 2010. Cylinder drag reduction by the use of helical grooves. In: Proceedings of the HYDRALAB III Joint User Meeting, Hannover, Germany.

Huang, S., 2011. Viv suppression of a two-degree-of-freedom circular cylinder and drag reduction of a fixed circular cylinder by the use of helical grooves. Journal of Fluids and Structures 27 (7), 1124–1133.

Huang, S., Clelland, D., Day, S., James, R., Jun 2007. Drag reduction of deepwater risers by the use of helical grooves. In: Proceedings of the 26th International Conference on Offshore Mechanics and Arctic Engineering, San Diego, California, USA. Vol. 1. pp. 561–565.

Igarashi, T., 1985. Effect of vortex generators on the flow around a circular cylinder normal to an airstream. Bulletin of the JSME 28 (236), 274–282.

Ito, M., Jun 1999. Stay cable technology: Overview. In: Proceedings of the IABSE Conference, Cable-Stayed Bridges - Past, Present and Future, Malmo, Sweden.

Johnson, Joubert, 1969. The influence of vortex generators on the drag and heat transfer from a circular cylinder normal to an airstream. Transactions of the ASME. Series C, Journal of Heat Transfer 91 (1), 91–99.

Joubert, P., Hoffman, E., 1962. Drag of a circular cylinder with vortex generators. J Roy Aeronaut Soc 66, 456–457.

Katsuchi, H., Yamada, H., 2009a. Surface pressure and axial flow measurements for indented-surface stay cable. In: 8th International Symposium on Cable Dynamics, Paris, France.

Katsuchi, H., Yamada, H., Jun 2009b. Wind-tunnel study on dry-galloping of indented-surface stay cable. In: 11th Americas Conference on Eind Engineering, San Juan, Puerto Rico.

Katsuchi, H., Yamada, H., Oct 2011. Dry galloping characteristics of indented stay cables in turbulent flow. In: 9th International Symposium on Cable Dynamics, Shanghai, China. pp. 359–364.

Katsuchi, H., Yamada, H., Sasaki, E., Inamori, K., Kaga, S., 2010. Study on dry-galloping of inclined cable with real indented surface. In: Proceedings of the 21st National Symposium on Wind Engineering, Japan. pp. 387–392, in Japanese.

Kimura, T., Tsutahara, M., 1991. Fluid dynamic effects of grooves on circular cylinder surface. AIAA Journal 29 (12), 2062–2068.

Kleissl, K., Georgakis, C., 2011a. Aerodynamic control of bridge cables through shape modification: A preliminary study. Journal of Fluids and Structures 27 (7), 1006–1020.

Kleissl, K., Georgakis, C., 2011b. Comparison of the aerodynamics of bridge cables with helical fillets and a pattern-indented surface in normal flow. In: Proceedings of The 13th International Conference on Wind Engineering, Amsterdam, Netherlands.

Kleissl, K., Georgakis, C., 2012a. Comparison of several innovative bridge cable surface modifications. In: Proceedings of The 7th International Colloquium on Bluff Body Aerodynamics & Applications, Shanghai, China.

Kleissl, K., Georgakis, C., 2012b. Comparison of the aerodynamics of bridge cables with helical fillets and a pattern-indented surface. Journal of Wind Engineering and Industrial Aerodynamics 104 - 106 (0), 166 – 175.
URL http://www.sciencedirect.com/science/article/pii/S0167610512000554

Kleissl, K., Georgakis, C., 2013a. Comparison of the aerodynamic stability of bridge cables with a smooth surface, helical fillets and a pattern-indentation. Submitted for Journal of Wind Engineering and Industrial Aerodynamics.

Kleissl, K., Georgakis, C., 2013b. Innovative bridge cable surface modifications for the avoidance of rwiv. Submitted for Journal of Fluids and Structures.

Ko, N. W. M., Leung, Y. C., Chen, J. J. J., 1987. Flow past V-groove circular cylinders. AIAA Journal 25 (6), 806–811.

Kobayashi, H., Minami, Y., Miki, M., 1995. Prevention of rain-wind induced vibration of an inclined cable by surface processing. In: Proceedings of the 9th International Conference on Wind Engineering, New Delhi, India. pp. 753–758.

Korkischko, I., Meneghini, J., 2010. Experimental investigation of flow-induced vibration on isolated and tandem circular cylinders fitted with strakes. Journal of Fluids and Structures 26 (4), 611 – 625.

Korkischko, I., Meneghini, J., Gioria, R., Jabardo, P., Casaprima, E., Franciss, R., 2007. An experimental investigation of the flow around straked cylinders. In: Proceedings of the 26th International Conference on Offshore Mechanics and Arctic Engineering, San Diego, California, USA.

Kumar, R. A., Sohn, C. H., Gowda, B. H. L., 2008. Passive control of vortex-induced vibrations: an overview. Recent patents on Mechanical Engineering 1, 1–11.

Kumarasena, S., Jones, N. P., Irwin, P., Taylor, P., Aug 2007. Wind-induced vibration of stay cables. Report FHWA-HRT-05-083, US Federal Highway Administration. URL http://www.fhwa.dot.gov/bridge/pubs/05083/index.cfm

Lam, K., Lin, Y., 2008a. Numerical simulation on the control of drag force and vortex formation by different wavy (varicose) cylinders. IUTAM Symposium on Flow Control and MEMS 7, 415–419.

Lam, K., Lin, Y., Zou, L., Liu, Y., 2010. Investigation of turbulent flow past a yawed wavy cylinder. Journal of Fluids and Structures 26 (7-8), 1078–1097.

Lam, K., Lin, Y. F., 2007. Drag force control of flow over wavy cylinders at low reynolds number. Journal of Mechanical Science and Technology 21 (9), 1331–1337.

Lam, K., Lin, Y. F., 2008b. Large eddy simulation of flow around wavy cylinders at a subcritical reynolds number. International Journal of Heat and Fluid Flow 29 (4), 1071 – 1088.

Lam, K., Lin, Y. F., 2009. Effects of wavelength and amplitude of a wavy cylinder in cross-flow at low reynolds numbers. Journal of Fluid Mechanics 620, 195–220.

Lam, K., Wang, F. H., Li, J. Y., So, R. M. C., 2004a. Experimental investigation of the mean and fluctuating forces of wavy (varicose) cylinders in a cross-flow. Journal of Fluids and Structures 19 (3), 321 – 334.

Lam, K., Wang, F. H., So, R. M. C., 2004b. Three-dimensional nature of vortices in the near wake of a wavy cylinder. Journal of Fluids and Structures 19 (6), 815 – 833.

Larose, G., Smitt, L. W., Jun 1999. Rain/wind induced vibrations of parallel stay cables. In: Proceedings of the IABSE Conference, Cable-Stayed Bridges - Past, Present and Future, Malmo, Sweden.

Lee, S.-J., Kim, H.-B., 1997. The effect of surface protrusions on the near wake of a circular cylinder. Journal of Wind Engineering and Industrial Aerodynamics 69-71, 351 – 361, proceedings of the 3rd International Colloqium on Bluff Body Aerodynamics and Applications.

Lee, S.-J., Lim, H.-C., Han, M., Lee, S. S., 2005. Flow control of circular cylinder with a v-grooved micro-riblet film. Fluid Dynamics Research 37 (4), 246 – 266.

Lee, S.-J., Nguyen, A.-T., 2007. Experimental investigation on wake behind a wavy cylinder having sinusoidal cross-sectional area variation. Fluid Dynamics Research 39 (4), 292 – 304.

Leung, Y.-C., 1988. Investigation of flows over grooved surfaces. Ph.D. thesis, University of Hong Kong.

Leung, Y. C., Ko, N. W. M., 1991. Near wall characteristics of flow over grooved circular cylinder. Experiments in Fluids 10, 322–332, 10.1007/BF00190248.

Lim, H.-C., Lee, S.-J., Oct 2002. Flow control of circular cylinders with longitudinal grooved surfaces. AIAA Journal 40 (10), 2027–2036.

Lim, H.-C., Lee, S.-J., 2003. Piv measurements of near wake behind a u-grooved cylinder. Journal of Fluids and Structures 18 (1), 119 – 130.

Lim, H.-C., Lee, S.-J., 2004. Flow control of a circular cylinder with o-rings. Fluid Dynamics Research 35 (2), 107 – 122.

Lin, J. C., 2002. Review of research on low-profile vortex generators to control boundary-layer separation. Progress in Aerospace Sciences 38 (4-5), 389 – 420.

Lungu, D., Bartoli, G., Righi, M., Vacareanu, R., Villa, A., 2002. Reliability under wind loads of the brancusi endless column, romania. In: International Journal of Fluid Mechanics Research. Vol. 29. pp. 323–328.

Mai, H., Dietz, G., Geißler, W., Richter, K., Bosbach, J., Richard, H., de Groot, K., 2008. Dynamic stall control by leading edge vortex generators. Journal of the American Helicopter Society 53 (1), 26–36.

Matsumoto, M., 1998. Observed behavior of proto type cable vibration and its generation mechanism. In: Bridge Aerodynamics, Proceedings of the International Symposium on Advances in Bridge Aerodynamics. pp. 189–211.

Matsumoto, M., Daito, Y., Kanamura, T., Shigemura, Y., Sakuma, S., Ishizaki, H., 1998. Wind-induced vibration of cables of cable-stayed bridges. Journal of Wind Engineering and Industrial Aerodynamics 74-76, 1015 – 1027.

Matsumoto, M., Shiraishi, N., Shirato, H., 1992. Rain-wind induced vibration of cables of cable-stayed bridges. Journal of Wind Engineering and Industrial Aerodynamics 43 (1-3), 2011–2022.

Matsumoto, M., Yagi, T., Hatsuda, H., Shima, T., Tanaka, M., dec 2007. Sensitivity of dry-state galloping of cable stayed bridges to scruton number. In: Seventh International Symposium on Cable Dynamics, Vienna, Austria. pp. 331–338.

Matsumoto, M., Yamagishi, M., Aoki, J., Shiraishi, N., Jan 1995. Various mechanism of inclined cable aerodynamics. In: 9th International Conference on Wind Engineering, New Dehli, India. pp. 759–769.

Matsumoto, M., Yokoyama, K., Miyata, T., Fujino, Y., Yamaguchi, H., 1989. Wind-induced cable vibration of cable-stayed bridges in japan. In: Proc. of Japan-Canada Joint Workshop on Bridge Aerodynamics. pp. 101–110.

Maull, D., Young, R., 1974. Vortex shedding from a bluff body in a shear flow. In: Proceedings of the IUTAM-IAHR Symposium on flow-induced structural vibrations, Karlsruhe, Germany, August 14-16, 1972.

Miyata, T., 2003. Historical view of long-span bridge aerodynamics. Journal of Wind Engineering and Industrial Aerodynamics 91 (12-15), 1393–1410.

Miyata, T., Yamada, H., Fujiwara, T., Hojo, T., Sep 1998. Wind-resistant design of cables for the tatara bridge. In: IABSE Symposium on Long-span and High-rise Structures, Kobe, Japan. Vol. 79. pp. 51–56.

Miyata, T., Yamada, H., Hojo, T., Oct 1994a. Aerodynamic response of PE stay cables with pattern-indented surface. In: Proceedings of the International Conference on Cable-Stayed and Suspension Bridges, Deauville, France. Vol. 2. pp. 515–522.

Miyata, T., Yamada, H., Hojo, T., Yamazaki, S., Oct 1995. On aerodynamically stable PE-stay-cables with decreased drag force by introduction of newly developed lumped surface roughness. In: Proc., Int. Symp. on Cable Dynamics, Liege, Belgium. pp. 481–488.

Miyata, Y., Yamada, H., Hojo, T., 1993. Experimental study on aerodynamic characteristics of cables with patterned surface. Bridge and Foundation Engineering 27 (9), 30–36, in Japanese.

Miyata, Y., Yamada, H., Hojo, T., Mar 1994b. Experimental study on aerodynamic characteristics of cables with patterned surface. Journal of Structural Engineering 40A, 1065–1076.

Miyazaki, M., Jun 1999. Aerodynamic and structual dynamic control system of cable-stayed bridge for wind induced vibration. In: Proceedings of the IABSE Conference, Cable-Stayed Bridges - Past, Present and Future, Malmo, Sweden.

Modi, V. J., Welt, F., Seto, M. L., 1995. Control of wind-induced instabilities through application of nutation dampers: a brief overview. Engineering Structures 17 (9), 626 – 638, auxiliary damping systems for mitigation of wind-induced vibration.

Molin, B., 1993. A potential flow model for the drag of shrouded cylinders. Journal of Fluids and Structures 7 (1), 29 – 38.

Morgan, W. E., Sullivan, M. J., May 2010. Golf ball with spherical polygonal dimples.

Mori, K., Yamada, I., Kusuhara, S., 2008. Vibration control for cable systems of long-span bridges. In: Proc. of the 6th International Cable Supported Bridge Operators' Conference, Takamatsu, Japan.

Nakagawa, K., Fujino, T., Arita, Y., Ogata, Y., Masaki, K., 1959. An experimental investigation of aerodynamic instability of circular cylinders at supercritical reynolds numbers. In: Proceedings of The Ninth Japanese Congress of Applied Mechanics, Tokyo. pp. 235–240.

Nakagawa, K., T. Fujino, Y. A., Shima, T., Jun 1963. An experimental study on aerodynamic devices for reducing wind-induced oscillatory tendencies of stacks. In: International Conference on Wind Effects on Buildings and Structures, Teddington, U.K. pp. 774–795.

Nakamura, H., Igarashi, T., 2007. Reductions in drag and fluctuating forces for a circular cylinder by attaching cylindrical rings. Journal of Fluid Science and Technology 2 (1), 12–22.

Nakamura, H., Igarashi, T., 2008. Omnidirectional reductions in drag and fluctuating forces for a circular cylinder by attaching rings. Journal of Wind Engineering and Industrial Aerodynamics 96 (6-7), 887 – 899, 5th International Colloquium on Bluff Body Aerodynamics and Applications.

Naudascher, E., Rockwell, D., 2005. Flow-Induced Vibrations: An Engineering Guide. Dover Publications, Inc., 31 East 2ns Street, Mineola, N.Y. 11501.

Naumann, A., Quadflieg, H., 1974. Vortex generation and its simulation in wind tunnels. In: Proceedings of the IUTAM-IAHR Symposium on flow-induced structural vibrations, Karlsruhe, Germany, August 14-16, 1972.

Nebres, J., Batill, S., 1993. Flow about a circular cylinder with a single large-scale surface perturbation. Experiments in Fluids 15 (6), 369–379.

Nebres, J. V., Batill, S. M., jan 1992. Flow about cylinders with helical surface protrusions. 30th AIAA Aerospace Sciences Meeting and Exhibit, Reno, Nevada 92 (0540), 1992.

Nguyen, A.-T., Lee, S.-J., May 2004. Experimental investigation on wake behind a sinusoidal cylinder. In: Proceeding of Tenth Asian Congress of Fluid Mechanics, Sri Lanka.

Nigim, H. H., Batill, S. M., 1997. Flow ablout cylinders with surface perturbations. Journal of Fluids and Structures 11 (8), 893 – 907.

Novak, M., 1967. On problems of wind-induced lateral vibrations of cylindrical structures. In: Int. Semin. on Wind Effects in Buildings and Structures, Ottawa. Vol. 2. pp. 429–457.

Owen, J. C., Bearman, P. W., Szewczyk, A. A., 2001. Passive control of VIV with drag reduction. Journal of Fluids and Structures 15 (3-4), 597 – 605.

Parker, K., Sayers, A. T., 1999. The effect of longitudinal microstriations and their profiles on the drag of flat plates. Proceedings of the Institution of Mechanical Engineers, Part C: Journal of Mechanical Engineering Science 213 (8), 775–785.

Persoon, A., Noorlander, K., Mar 1999. Full-scale measurements on the erasmus bridge after rain/wind induced cable vibrations. Tech. Rep. NLR-TP-99063, National Aerospace Laboratory NLR, this report is based on a presentation held at the 10th International Conference on Wind Engineering, Copenhagen, Denmark, June 21-24, 1999.

Phelan, R. S., Mehta, K. C., Sarkar, P. P., Chen, L., Aug 2005. Investigation of wind-rain-induced cable-stay vibrations on cable-stayed bridges: Final report. Tech. Rep. TX-0-1400-1, Texas Tech University, Department of Civil Engineering, Lubbock, Texas 79409-1023.

Phelan, R. S., Sarkar, P. P., Mehta, K. C., 2006. Full-scale measurements to investigate rain–wind induced cable-stay vibration and its mitigation. Journal of Bridge Engineering 11 (3), 293–304.

Pinto, A., Broglia, R., Mascio, A. D., 2006. Numerical investigation of the unsteady flow at high reynolds number over a marine riser with helical strakes. In: Proceedings of the 25th International Conference on Offshore Mechanics and Arctic Engineering, Hamburg, Germany. pp. 587–595.

Pontaza, J. P., Menon, R. G., Chen, H.-C., 2009. Three-dimensional numerical simulations of flows past smooth and rough/bare and helically straked circular cylinders allowed to undergo two degree-of-freedom motions. Journal of Offshore Mechanics and Arctic Engineering 131 (2), 021301.

Price, P., Jul 1956. Suppression of the fluid-induced vibration of circular cylinders. Journal of the Engineering Mechanics Division of the American Society of Civil Engineers 82 (EM3), 1030–1–1030–22.

Pujals, G., Depardon, S., Cossu, C., 2010. Drag reduction of a 3d bluff body using coherent streamwise streaks. Experiments in Fluids 49, 1085–1094.

Ribeiro, J. D., 1991. Effects of surface roughness on the two-dimensional flow past circular cylinders i: mean forces and pressures. Journal of Wind Engineering and Industrial Aerodynamics 37 (3), 299 – 309.

Rispin, P., Webster, B., Stasiewicz, J., Nov 1977. An evaluation of several techniques for reducing cable strum. Tech. Rep. SPD 732-01, David W. Taylor Naval Ship Research and Development Center, Bethesda, Maryland 20084.

Rodriguez, O., 1991. Base drag reduction by control of the three-dimensional unsteady vortical structures. Experiments in Fluids 11, 218–226.

Ruscheweyh, H., 1972. Tip effect on vortex excited oscillation of a model stack with and without efflux stream. In: IUTAM - Symp. on Flow-Induced Structural Vibrations, Karlsruhe, W. Germany, Suppl. (not published in the Proceedings). pp. 101–103.

Saito, T., Matsumoto, M., Kitazawa, M., Oct 1994. Rain-wind excitation of cables on cable-stayed Higashi-Kobe bridge and cable vibration control. In: Proceedings of the International Conference on Cable-Stayed and Suspension Bridges, Deauville, France. Vol. 2. pp. 507–514.

Sallet, D. W., Berezow, J., 1972. Suppression of flow-induced vibrations by means of body surface modifications. The Shock and Vibration Bull., Nav. Res. Lab., Washington, DC 42 (4), 215–228.

Sallett, D. W., 1980. Suppression of flow-induced motions of a submerged moored cylinder. In: Proc. of the IUTAM/IHAR Symp. on Practical Experiences with Flow-Induced Vibrations, Karlsruhe. Springer, N.Y (1979), pp. 587–594.

Sarkar, P. P., Gardner, T. B., 2000. Model tests to study rain/wind-induced vibration of stay cables. In: Elgaaly, M. (Ed.), Proceedings of Structures Congress - Advanced Technology in Structural Engineering. Vol. 103. ASCE, pp. 45–45.

Sarkar, P. P., Phelan, S., Mehta, K. C., Gardner, T. B., Zhao, Z., May 2002. Cable stay aerodynamic damper band and method of use. United States Patent 6,908,063 B2.

Scruton, C., Walshe, D. E., Feb 1963. Stabilisation of wind-excited structures.

Scruton, C., Walshe, D. E. J., Oct 1957. A means for avoiding wind-excited oscillations of structures with circular or nearly circular cross section. Natl. Phys. Lab.(UK), Areo Report 335.

Shih, W., Wang, C., Coles, D., Roshko, A., 1993. Experiments on flow past rough circular cylinders at large reynolds numbers. Journal of Wind Engineering and Industrial Aerodynamics 49 (1-3), 351 – 368.

Simiu, E., Scanlan, R. H., 1978. Wind effects on structures: an introduction to wind engineering. New York: Wiley-Interscience.

Sirisup, S., Karniadakis, G. E., Saelim, N., Rockwell, D., 2004. DNS and experiments of flow past a wired cylinder at low reynolds number. European Journal of Mechanics - B/Fluids 23 (1), 181 – 188, bluff Body Wakes and Vortex-Induced Vibrations.

Solari, G., Lungu, D., Bartoli, G., Righi, M., Vacareanu, R., Villa, A., Aug 2002. Brancusi endless column, romania: Dynamic response and reliability under wind loading. In: Proceedings of the 2nd International Symposium on Advances in Wind & Structures, Pusan, Korea. pp. 79–86.

Stubler, J., Ladret, P., Domage, J., Jun 1999. Vibration control of stay cables. In: Proceedings of the IABSE Conference, Cable-Stayed Bridges - Past, Present and Future, Malmo, Sweden.

Szalay, Z., 1989. Drags on several polygon cylinders. Journal of Wind Engineering and Industrial Aerodynamics 32 (1-2), 135 – 143.

Szechenyi, E., 1975. Supercritical reynolds number simulation for two-dimensional flow over circular cylinders. Journal of Fluid Mechanics 70 (03), 529–542.

Taggart, S., Tognarelli, M. A., Jun 2008. Offshore drilling riser viv suppression devices - what's available to operators? In: Proceedings of the 27th International Conference on OFFSHORE MECHANICS AND ARTIC Engineering, Estoril, Portugal.

Tanner, M., 1972. A method for reducing the base drag of wings with blunt trailing edge. Aeronautical Quarterly 23, 15–23.

Taylor, H. D., jun 1947. The elimination of diffuser separation by vortex generators. Tech. Rep. R-4012-3, United Aircraft Corporation.

Trim, A., Braaten, H., Lie, H., Herfjord, K., King, R., Makrygiannis, C., Meling, T., Jul 2004. Experimental investigation of vortex-induced vibration of long marine risers. In: proceedings of the 8th International Conference on Flow-Induced Vibration (FIV2004), Paris, France.

Trim, A., Braaten, H., Lie, H., Tognarelli, M., 2005. Experimental investigation of vortex-induced vibration of long marine risers. Journal of Fluids and Structures 21 (3), 335 – 361, ¡ce:title¿Marine and Aeronautical Fluid-Structure Interactions¡/ce:title¿ ¡ce:subtitle¿Marine Acoustics¡/ce:subtitle¿ ¡xocs:full-name¿8th International Conference on Flow-Induced Vibrations¡/xocs:full-name¿.

Tsutsui, T., Jul 2011. Fluid flow around a cylindrical structure mounted on a plane turbulent boundary layer. In: Proc. of the 13th International Conference on Wind Engineering, Amsterdam.

Ünal, U. O., Atlar, M., 2010. An experimental investigation into the effect of vortex generators on the near-wake flow of a circular cylinder. Experiments in Fluids 48 (6), 1059–1079.

Vickery, B. J., Watkins, R. D., 1962. Flow-induced vibrations of cylindrical structures. In: Proceedings of the First Australian Conference on Hydraulics and Fluid Mechanics. pp. 213–241.

Virlogeux, M., May 1998. Cable vibrations in cable-stayed bridges. In: Proceedings of the International Symposium on Advances in Bridge Aerodynamics, Copenhagen, Denmark. pp. 213–233.

Virlogeux, M., 1999. Recent evolution of cable-stayed bridges. Engineering Structures 21 (8), 737 – 755.

Walsh, M. J., 1983. Riblets as a viscous drag reduction technique. AIAA Journal 21 (4), 485–486.

Walshe, D. E., Wootton, L. R., Feb 1970. Preventing wind-induced oscillations of structures of circular section. Institution of Civil Engineers 47 (1), 1–24.

Wang, F. H., Jiang, G. D., Lam, K., 2004. A study of velocity fields in the near wake of a wavy (varicose) cylinder by lda. Flow Measurement and Instrumentation 15 (2), 105 – 110.

Wang, F. H., Jiang, G. D., Lam, K., 2005. Flow patterns of cross-flow around a varicose cylinder. Journal of Visualization 8 (1), 49–56.

Weaver, Jr., W., Feb 1961. Wind-induced vibrations in antenna members. Journal of the Engineering Mechanics Division of the American Society of Civil Engineers 87 (EM1), 141–165.

Wenbo, L., Zhixing, L., 2005. A study on aerodynamic control countermeasures to rain-wind induced vibration. China Civ. Eng. J. 38 (5), 48–53, (In Chinese).

Wilkinson, S., Anders, J., Lazos, B., Bushnell, D., 1988. Turbulent drag reduction research at nasa langley: progress and plans. International Journal of Heat and Fluid Flow 9 (3), 266 – 277.

Williamson, C., Govardhan, R., 2008. A brief review of recent results in vortex-induced vibrations. Journal of Wind Engineering and Industrial Aerodynamics 96 (6-7), 713 – 735, 5th International Colloquium on Bluff Body Aerodynamics and Applications.

Wilson, J. F., Tinsley, J. C., 1989. Vortex load reduction: Experiments in optimal helical strake geometry for rigid cylinders. Journal of Energy Resources Technology 111 (2), 72–76.

Wong, H. Y., Sep 1977. An aerodynamic means of suppressing vortex excited oscillation. Proceedings of Institution of Civil Engineers 63 (3 Part 2), 693 – 699.

Wong, H. Y., Cox, R. N., 1980. The suppression of vortex induced oscillations on circular cylinders by aerodynamic devices. In: Proceedings of the 4th Colloquium on Industrial AerodynamicsFluid Mechanics Laboratory, Department of Aeronautics, Fachhochschule, Aachen, Germany. pp. 185–204.

Wong, H. Y., Kokkalis, A., 1982. A comparative study of three aerodynamic devices for suppressing vortex-induced oscillation. Journal of Wind Engineering and Industrial Aerodynamics 10 (1), 21 – 29.

Woodgate, L., Maybrey, J., Jun 1959. Further experiments on the use of helical strakes for avoiding wind excited oscillations of structures of circular or nearly circular section. Natl. Phys. Lab.(UK), Aero Rep 381.

Yagi, T., Narita, S., Okamoto, K., Shinjo, K., Shirato, H., Oct 2011a. Investigation of dry-state galloping of stay-cables with various kinds of surface configuration. In: 9th International Symposium on Cable Dynamics, Shanghai, China. pp. 215–222.

Yagi, T., Okamoto, K., Sakaki, I., Koroyasu, H., Liang, Z., Narita, S., Shirato, H., Jul 2011b. Modification of surface configurations of stay cables for drag force reduction and aerodynamic stabilization. In: Proc. of the 13th International Conference on Wind Engineering, Amsterdam.

Yagi, T., Okamoto, K., Sskski, I., Koroyasu, H., Liang, Z., Narita, S., Shirato, H., Dec 2010. Drag force reduction and aeerodynamic stabilization of stay cables by modfying surface configlations. In: The 21th Symposium on Wind Engineering, Tokyo, Japan. In Japanese.

Yamada, Y., Shiraishi, N., Toki, K., Matsumoto, M., Matsuhashi, K., Kitazawa, M., Ishizai, H., Dec 1991. Earthquake-resistant and wind resistant design of the higashi-kobe bridge. In: proceedings of the seminar on Cable-stayed bridges: recent developments and their future, Yokohama. pp. 397–416.

Yamagishi, Y., Oki, M., 2004. Effect of groove shape on flow characteristics around a circular cylinder with grooves. Journal of Visualization 7 (3), 209–216.

Yamagishi, Y., Oki, M., 2005. Effect of the number of grooves on flow characteristics around a circular cylinder with triangular grooves. Journal of Visualization 8 (1), 57–64.

Yamaguchi, H., Fujino, Y., 1998. Stayed cable dynamics and its vibration control. Bridge aerodynamics, 235–253.

Yamaguchi, K., Manabe, Y., Sasaki, N., Morishita, K., Jun 1999. Field observation and vibration test of the tatara bridge. In: Proceedings of the IABSE Conference, Cable-Stayed Bridges - Past, Present and Future, Malmo, Sweden. pp. 707–714.

Yamauchi, K., Uejima, H., Kuroda, S., Oct 2011. An investigation of the aerodynamic characteristics of cable with surface ribs. In: 9th International Symposium on Cable Dynamics, Shanghai, China. pp. 397–402.

Yeo, D., Jones, N. P., May 2010. Aerodynamic effects of strake patterns on flow around a yawed circular cylinder. In: The Fifth International Symposium on Computational Wind Engineering, North Carolina, USA.

Yeo, D., Jones, N. P., 2011. Computational study on aerodynamic mitigation of wind-induced, large-amplitude vibrations of stay cables with strakes. Journal of Wind Engineering and Industrial Aerodynamics In Press, Corrected Proof, –.

Yoon, J., 2005. Control of flow over a circular cylinder using wake disrupter. Master's thesis, School of Mechanical and Aerospace Engineering, Seoul National University., (in Korean).

Zdravkovich, M. M., 1981. Review and classification of various aerodynamic and hydrodynamic means for suppressing vortex shedding. Journal of Wind Engineering and Industrial Aerodynamics 7 (2), 145 – 189.

Zdravkovich, M. M., 1984. Reduction of effectiveness of means for suppressing wind-induced oscillation. Engineering Structures 6 (4), 344 – 349.

Zhan, S., Xu, Y., Zhou, H., Shum, K., 2008. Experimental study of wind-rain-induced cable vibration using a new model setup scheme. Journal of Wind Engineering and Industrial Aerodynamics 96 (12), 2438 – 2451.

Zhang, W., Daichin, Lee, S. J., 2005. Piv measurements of the near-wake behind a sinusoidal cylinder. Experiments in Fluids 38 (6), 824–832.

Zhou, T., Razali, S. M., Hao, Z., Cheng, L., 2011. On the study of vortex-induced vibration of a cylinder with helical strakes. Journal of Fluids and Structures 27 (7), 903–917.

Chapter 4

Static comparison study

This chapter contains the first part of the detailed direct comparison study of the two prevailing aerodynamic means. This part covers the experiments with statically fixed cable models.

Paper III

"Comparison of the aerodynamics of bridge cables with helical fillets and a pattern-indented surface"

K. Kleissl & C.T. Georgakis

Comparison of the aerodynamics of bridge cables with helical fillets and a pattern-indented surface

K. Kleissl*, C.T. Georgakis

Department of Civil Engineering, Technical University of Denmark, Building 118, Brovej, 2800 Kgs. Lyngby, Denmark

ARTICLE INFO

ABSTRACT

In this paper, the aerodynamics of bridge cables with helical fillets and a pattern-indented surface are examined. To this end, an extensive wind-tunnel test campaign was undertaken to measure the static force coefficients about the critical Reynolds number region, with varying relative cable-wind angles. The tests confirmed that the pattern-indented tubing exhibits the lowest drag coefficient, reaching its supercritical flow state for Reynolds numbers lower than the other cables tested. For this cable, vortex-shedding was found to be present throughout the supercritical range. The asymmetry of the surface pattern introduce a wind-angle of attack dependency that leads to a prediction of Den Hartog galloping instability. For yawed positions, flow transition was found to be independent of the relative cable-wind angle and therefore only governed by the along-wind flow velocity. The helically filleted cable was found to have a much slower flow transition for near normal flow and relatively large lift force components for the yawed positions. Flow visualizations confirmed the existence of specific flow structures which are often associated with the presence of lower drag or large lift forces. The visualization tests confirmed the presence of an axial flow that was greatly hindered by the presence of the helical fillets.

© 2012 Elsevier Ltd. All rights reserved.

1. Introduction

Over the last two decades, several bridge cable manufacturers have introduced surface modifications on the high-density polyethylene (HDPE) sheathing that is installed for the protection of inner strands or wires. The main purpose of these is rain rivulet impedance, leading to the suppression of rain–wind induced vibrations (RWIVs). The modifications are based on research undertaken predominantly in Europe and Japan, with two different prevailing systems: HDPE tubing fitted with helical fillets and HDPE tubing with pattern-indented surfaces. In the US and Europe, helical fillets dominate, whilst pattern indented surfaces are more common in Asia.

Research into the effectiveness of helical fillets and pattern-indented surfaces has shown that, besides their purported ability to suppress rain–wind induced vibrations, they also modestly reduce drag forces at design wind velocities. This is of particular interest to bridge designers, as wind on stay planes of long span bridges can now produce more than 50% of the overall horizontal load on a bridge (Gimsing and Georgakis, 2011). Nevertheless, there is no definitive aerodynamic performance comparison between the two systems. One of the problems of comparing them lies in the fact that different researchers, in different facilities, with varying wind-tunnel flow characteristics and performance, have developed each separately.

In this paper, the aerodynamics of bridge cables with helical fillets and a pattern-indented surface are examined through the determination of static aerodynamic force coefficients, analyses of lift force fluctuations, and through flow visualizations. For this purpose, an extensive wind-tunnel test campaign was undertaken to measure the force coefficients of several full-scale cable models, about the critical Reynolds number region, with varying relative cable-wind angles. Furthermore, flow visualization tests were performed on the same models for flow normal to the cables and for a relative cable-wind angle of 45°, to obtain insight into the structures of the flow around the modified profiles.

1.1. Historical overview

Helically wrapped wires were initially proposed in the fifties to combat vortex-induced vibrations (VIV). It was found that the presence of the helical protrusion significantly reduced the shedding correlation length. It was not until 1992, though, that tests on the use of such a system on a bridge stay cable were undertaken at CSTB (Nantes) in connection with the design of the

* Corresponding author. Tel.: +45 4525 5048; fax: +45 4588 3282.
E-mail address: kenk@byg.dtu.dk (K. Kleissl).
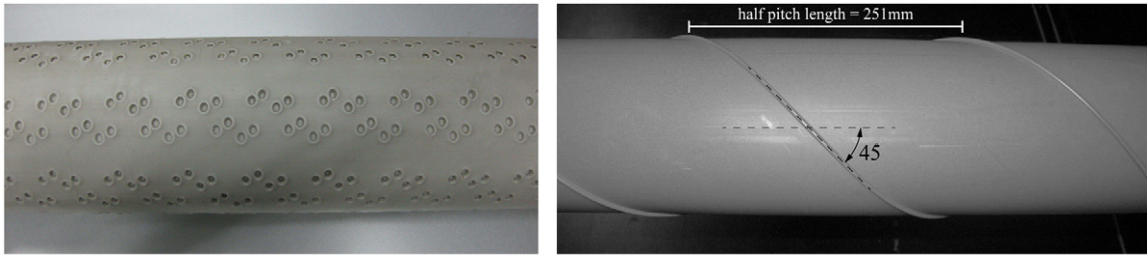URL: http://www.cesdyn.byg.dtu.dk (C.T. Georgakis).

Fig. 1. Cable with pattern-indented surface (left) and the surface with helical fillets (right).

Normandy Bridge (Flamand, 1995) and later at the Danish Maritime Institute by Larose and Smitt (1999), in relation with the design of the Øresund Bridge. Their tests showed a strong reduction of RWIVs through the disruption of the formation of a coherent upper rivulet in the presence of light rain. As a consequence, a variety of fillet designs have emerged in the last decade, often with varying pitch lengths and fillet sizes. It should be noted though that recent full-scale monitoring of the Øresund Bridge by Acampora and Georgakis (2011) has revealed that they may not be as effective as originally thought. A helically filleted cable is shown in Fig. 1 (right).

The pattern-indented surface, i.e. the application of a discrete roughness pattern, was initially proposed by Miyata et al. (1994b). Due to the thermal production procedure, the modifications consist of an indentation surrounded by a protruding periphery of displaced material (Katsuchi et al., 2010). The pattern-indented surface has been found to promote the stabilization of the separated flows over the surface of the cable and to inhibit the formation of rivulets (Miyata et al., 1999). Measured pressure distributions indicate that such a cable enters the supercritical flow state at the lower wind velocities, where RWIVs tend to occur. Furthermore, the flow separation point remains stable at 110° from stagnation in the supercritical region, resulting in a near constant drag coefficient (Hojo et al., 2000). It has also been found that these properties hold true, regardless of whether the discrete roughness has been generated by concavities or convexities (Miyata et al., 1994a). The pattern-indented surface was first applied to the cables of the Tatara Bridge in 1999 and later also to the Sutong and Stonecutters Bridges. For the Tatara Bridge, Miyata et al. (1998) reported a minimum drag coefficient of 0.61 and a design drag coefficient of 0.7. Similar values have been reported for the Sutong Bridge. Nevertheless, vibrations of pattern-indented cables have recently been observed both in the field and in the laboratory tests (Chen, 2011; Katsuchi, 2011). The pattern-indented surface of the Sutong Bridge cables is shown in Fig. 1 (left).

2. Material and methods

2.1. Wind tunnel

The comparative wind tunnel tests were performed at the $2 \times 2 \, \text{m}^2$ cross-section closed-circuit DTU/Force Climatic Wind Tunnel, located at Force Technology, Lyngby, Denmark (Georgakis et al., 2009). The flow conditions were measured with a cobra probe and turbulence intensities of 0.41–0.64% were found for 33/66/100% of the tunnel maximum flow velocity at the quarter point positions, both vertically and horizontally. For the yawed cable configuration, the reported flow conditions are correct for the upwind end of the cable. During the tests, the wind velocity was increased by regular increments of approximately 1 m/s, up to the maximum wind-tunnel velocity of 32 m/s, allowing for supercritical Reynolds numbers to be reached for all test angles and models.

2.2. Models

Three models were tested for comparison: a plain HDPE tube for reference, a HDPE tube fitted with helical fillets and a HDPE tube with a pattern-indented surface. The sectional models are original full-scale samples, supplied by bridge cable manufacturers. The plain HDPE tube has 160 mm outer diameter and a measured average surface roughness of $R_a \approx 1.8 \, \mu\text{m}$. The HDPE tube with two helically wrapped fillets also has an outer diameter of 160 mm. The fillets are rounded with a height of approximately 3 mm and a width of approximately 4 mm. Furthermore, they have a 3.14 tube diameter pitch length (502 mm and 45°). The average material surface roughness is in the order of $R_a \approx 3.0 \, \mu\text{m}$. The pattern-indented tube has a diameter of 140 mm, as this is an actual sample of the most common diameter of cable used on the Sutong Bridge. The relative surface roughness is defined by the depth of the indentations, measured to be approximately 1% of cable diameter.

2.3. Normal flow

The models were placed horizontally, resulting in a near two-dimensional flow normal to the cable sections. End plates with a diameter of approximately five cable diameters were fitted close to the model ends to eliminate undesirable end effects, whilst the drag and lift forces were measured using 6-DOF force transducers at either end. The transducers were covered with dummy pieces of the same cable. With an effective model length of 1.53 m, the aspect ratios were 9.6:1 and 10.9:1 for the two different cable diameters. The blockage ratios for all section models were within 7–8% and the drag coefficients have been corrected using the Maskell III method, according to Cooper et al. (1999).

2.4. Yawed flow

A photo of the yawed inclined dimpled cable used for the static tests, together with a drawing of the test setup, its angle configuration and the considered force coefficients, is shown in Fig. 2. Tube lengths of 1.93 m and 2.54 m were used to obtain inclinations of $\Theta = 40°$ and 55°. By varying the cable yaw angle β, relative cable-wind angles Φ of between 40° and 75° in steps of 5° could be achieved. A relative cable-wind angle of $\Phi = 90°$ corresponds to wind normal to the cable axis. The force coefficients were again measured with 6-DOF force transducers at each end of the cable. The force transducers were installed between the cable model and supporting cardan joints fixed to the walls. End plates with oval holes and a diameter of approximately five cable diameters were fitted near the ends to eliminate undesirable flow structures originating from the cable ends and cardan joints. Dummy tube pieces were mounted around the force transducers, leaving approximately a 2 mm gap to the cable model and extending beyond the end plates. For the helical model, the dummy tubing consisted of plain tubing, whilst for the pattern-indented model the dummy tubing was of the same surface type.
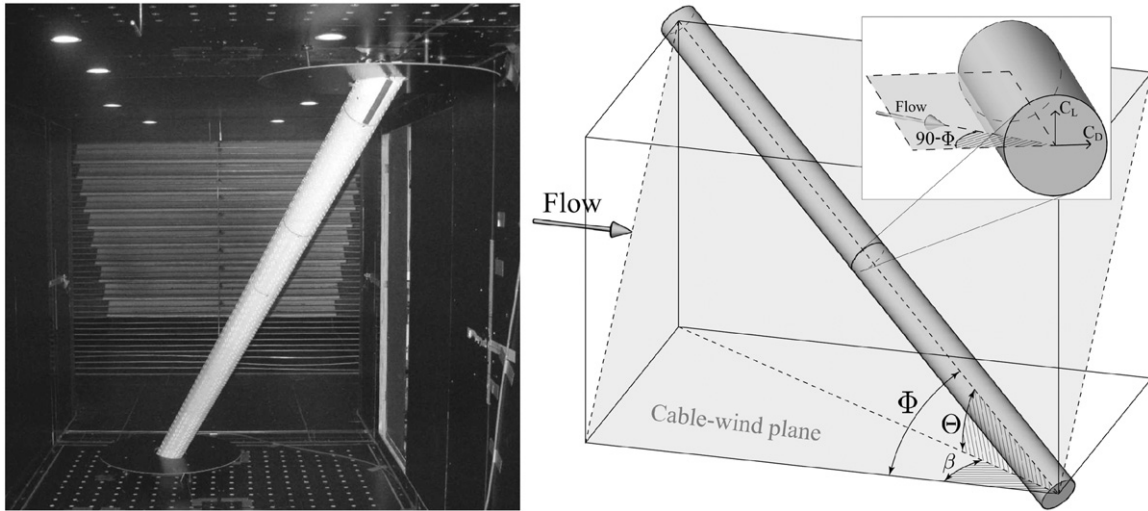
Fig. 2. Photo of the inclined pattern-indented cable (left) and a sketch showing the test set-up (right).

The aspect ratios of the inclined models (excluding dummy pieces) were between 12 and 18, depending on the cable diameter and inclination. Based on experimentally unverified CFD simulations of the development of the axial flow, Yeo and Jones (2011) recommend aspect ratios of 60 or higher for cable testing. Flow visualizations afterwards indicated though the existence of a strong axial flow and unchanging surface flow patterns along the cable length, leading to the assumption that the axial flow along the cable was fully developed. No blockage correction has been applied to the presented force coefficients, as the blockage ratio when considering a simplified section normal to the flow will for no angle be above 2%.

2.5. Flow visualization

For the flow visualization tests, two conditions were tested—flow normal to the cables and for a relative cable-wind angle of 45°. Smoke particles were added to a flow to trace the fluid motion. In order to visualize a slice of the fluid flow pattern, the particles were illuminated with a sheet of laser light. With smoke particle sizes in the order of 0.2 μm, it can be assumed that the particles faithfully follow the streamlines of the flow. For this, a high-output smoke generator was employed using a water-based quick dispersing smoke fluid. The high smoke output was necessary to keep the smoke visible when testing at higher flow velocities, whilst the quick dispersing smoke was needed to avoid recirculation of smoke. The laser sheet was generated with a green (532 nm) 3 W continuous-wave diode-pumped solid-state laser and a 45° Powell lens line generator ensuring a uniform intensity throughout the sheet. The laser sheet had a thickness of approximately 2 mm.

When the cable was installed normal to the oncoming flow, the smoke injection was applied approximately 0.5 m upwind of the cable model, with an injection tube supported by a wing-profile to avoid unnecessary flow disturbances. The laser sheet was arranged so as to visualize flow within a vertical plane normal to the cable. For the inclined cable, the laser sheet was arranged so as to illuminate the cable-wind plane from the downwind direction, as the smoke was injected along the leeward side at the upwind top end of the cable model. In this way, only smoke particles transported along the leeward channel of axial flow were visualized.

To supplement the near-wake smoke visualizations, surface flow visualizations were performed to reveal the flow streamlines

on the cable surface. By applying an oil mixture with colour pigments to the surface of the cable models, the oil responds to the surface shear stresses and forms patterns allowing for the visualization of the flow streamlines. In these tests again, visualization was performed for the cables installed normal to the flow and for the specific relative cable-wind angle of 45°.

3. Results and discussion

3.1. Force coefficients—normal flow

The average drag and lift coefficients obtained for each of the tested cable sections are shown in Fig. 3. The plain cable exhibits an entry into the critical Reynolds number region for $Re=2.3$–3.0×10^5. Within this region, the initiation of a large lift coefficient is observed. The aerodynamic force coefficients are in general agreement with the expectations for a smooth cylinder of this type. For this specific plain cable model, the dependency on the wind-angle of attack about the cable axis due to small surface distortion and imperfections has been further studied by Matteoni and Georgakis (2011a,b).

For the cable with the helical fillets, the transition to the critical flow state is very prolonged and the peak in lift coefficient much reduced. This is most likely due to the fillet's ability to generate variations in the flow and separation lines along the length of the cable. When only considering these mean force coefficients, such spatial variations in critical Reynolds number region will average into a prolonged transition. The drag coefficient of 0.72 reached at maximum velocity also matches well with the values previously reported in the literature, e.g. Flamand (1995) who measured a minimum drag coefficient of 0.65, despite a slight difference in fillet design.

The pattern-indented cable exhibits a very early transition into the supercritical region due to the high level of surface roughness, which here is also accompanied by the occurrence of non-zero lift force. The early flow transition agrees well with what has been observed for circular cylinders with uniform roughness. Unlike a rough cylinder though, the subsequent increase in drag through the supercritical region is limited, as the drag coefficient is always found to be below 0.64 throughout the tested range. This matches previous findings by Miyata et al. (1994b) of a near constant drag coefficient of 0.6 within supercritical Reynolds numbers.
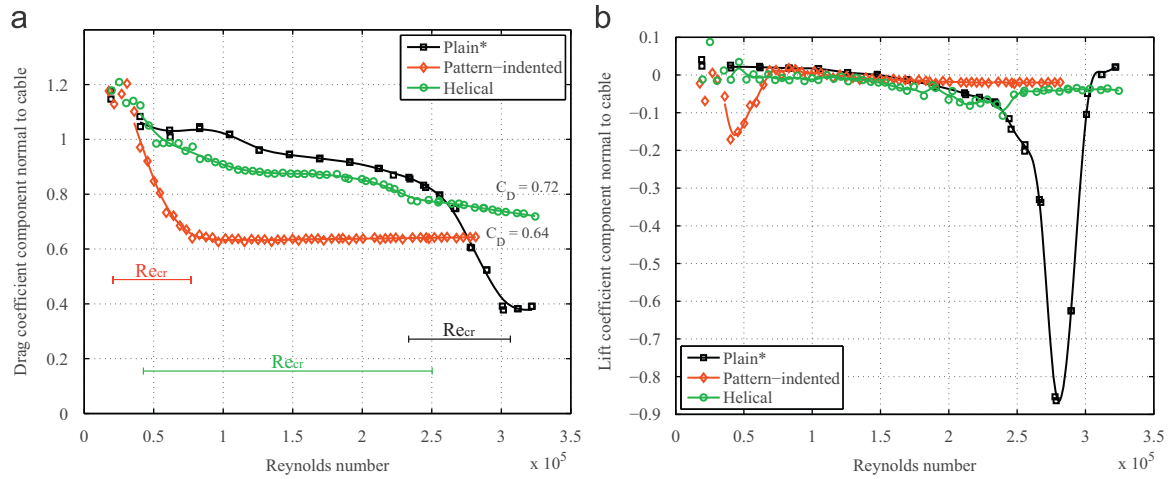
Fig. 3. Mean force coefficients as a function of Reynolds numbers for normal flow. Drag coefficients (left) and lift coefficients (right). *After Matteoni and Georgakis (2011a).
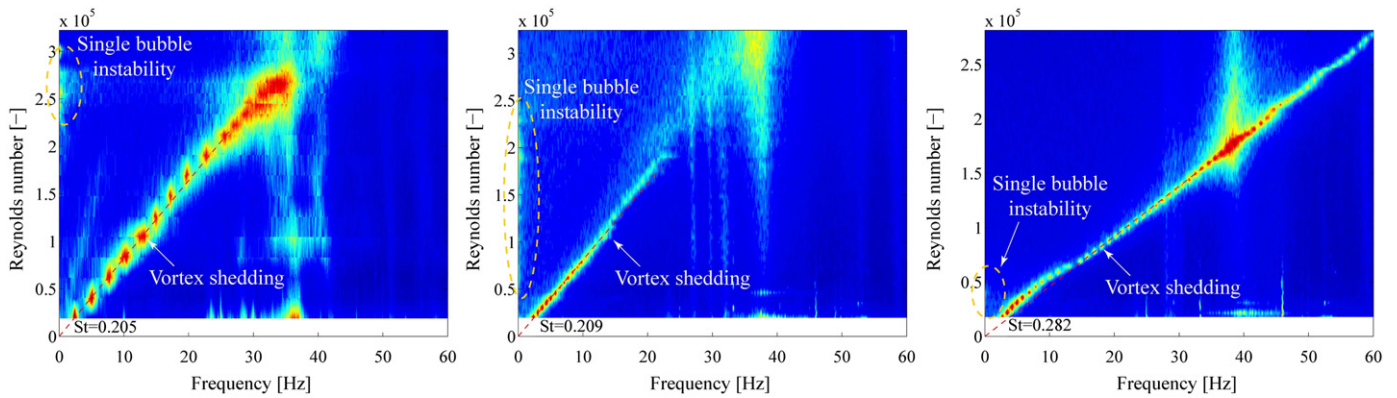

Fig. 4. Normal flow lift coefficient PSD: plain cable (left), helically filleted (middle), pattern-indented (right).

3.1.1. Fluctuating lift force

A frequency analysis of the unsteady cross-stream force (fluctuating lift) was undertaken. With the specific test setup employed, only the fluctuations of the total lift force on the model can be estimated. The frequency distributions of the lift force are determined using a fast Fourier transformation (FFT) to compute the power spectral density (PSD) of the lift coefficient. The PSD is computed for each of the flow velocities tested. This discrete number of flow velocity-specific spectra is then expanded into a two-dimensional contour plot, as seen in Fig. 4, for each of the three cable models. The linear trends identifying vortex shedding disappear around $Re \approx 2.6 \times 10^5$ and $Re \approx 1.8 \times 10^5$ for the plain and helical cables, respectively. This corresponds to the occurrence of flow transitions observed from the force coefficients in Fig. 3. In contrast, vortex shedding remains throughout the considered flow velocities for the patterned-indented surface, despite the early flow transition around $Re \approx 0.5 \times 10^5$. A determination of the Strouhal number reveals a significantly higher value of approximately $St = 0.28$ for the pattern-indented, relative to the other cables. The increased PSDs around 35–39 Hz can be understood as incidences of model resonance, which for the pattern-indented model is strongly excited due to the strong presence of vortex shedding. In the critical Reynolds number region, increased activity is observed for all three models at very low frequencies, which is believed to coincide with the presence of a single unstable separation bubble reappearing or shifting sides at a low rate.

3.1.2. Den Hartog galloping—pattern-indented cable

Due to the angular periodicity of the pattern on the pattern-indented cable, the force coefficient dependency with wind-angle of attack has been tested. Kleissl and Georgakis (2011b) presented the drag and lift coefficients obtained for several supercritical Reynolds numbers in detail. The results can be summarized as follows. From these tests it was found that the drag coefficient is nearly unaffected by the wind-angle of attack, whereas the lift coefficient experiences a significant dependency throughout the supercritical flow range. The trend for all the lift coefficients has a period length of approximately 25–27° and a peak-to-peak amplitude of 0.1. When evaluating the Den Hartog (1947) galloping criterion and neglecting structural damping, galloping instability is predicted, for all of the supercritical Reynolds numbers, as the Den Hartog value approaches -0.11 for the critical angle of approximately $\alpha = 20°$.

3.2. Force coefficients—yawed flow

The force coefficients presented henceforth are based on the measured drag and lift components normal to the cable axis. The components are normalized by the along wind flow velocity. The Reynolds numbers are defined as the along wind flow velocity in relation to the cable diameter.

The mean force coefficients for the cable with helical fillets are presented in Fig. 5. From this, several observations can be made. Firstly, the normal component of the drag coefficient system-atically drops for decreasing relative cable-wind angles, as would
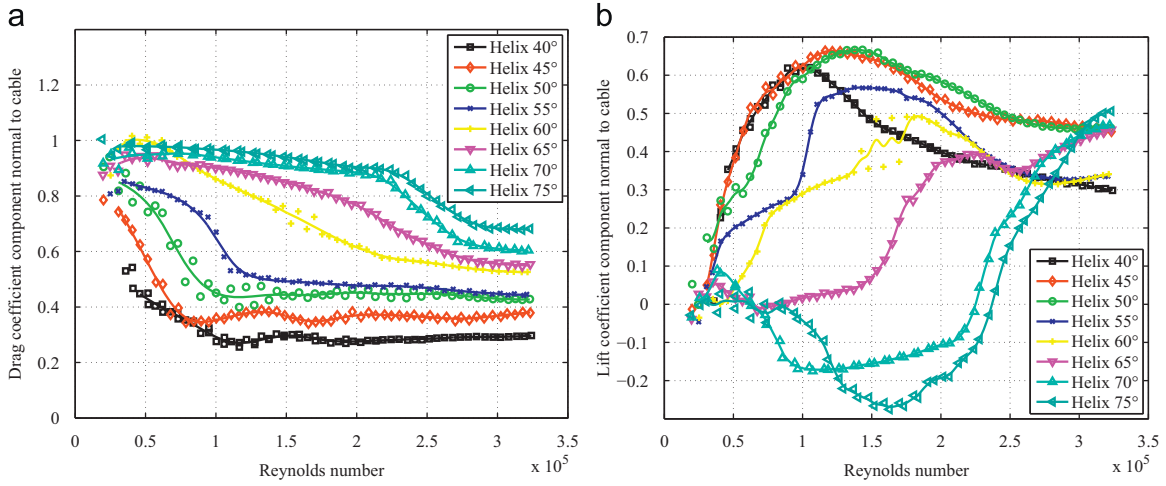
Fig. 5. Force coefficients for the helically filleted cable at varying relative cable-wind angles. Drag coefficient component normal to the cable (left) and lift coefficient component normal to the cable (right).
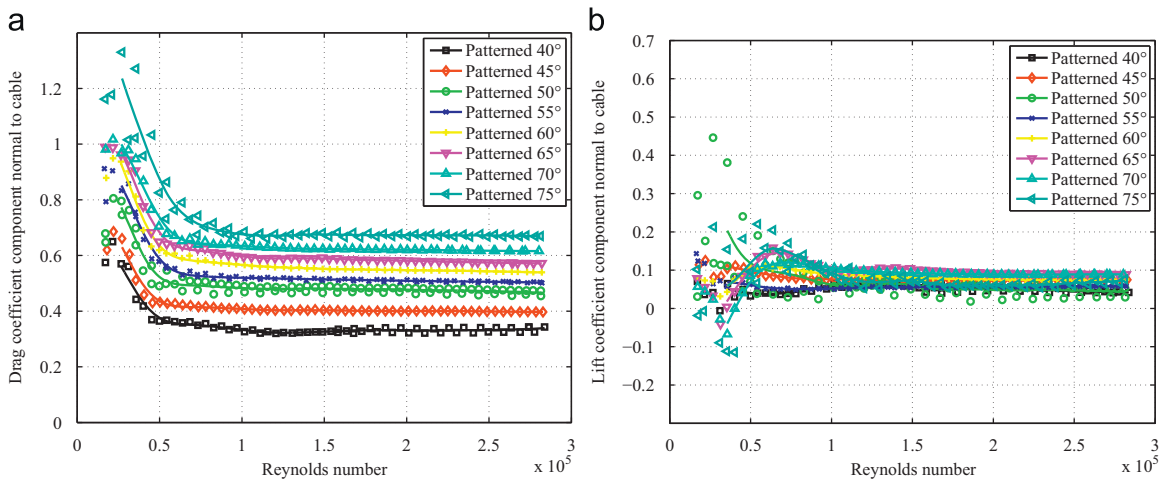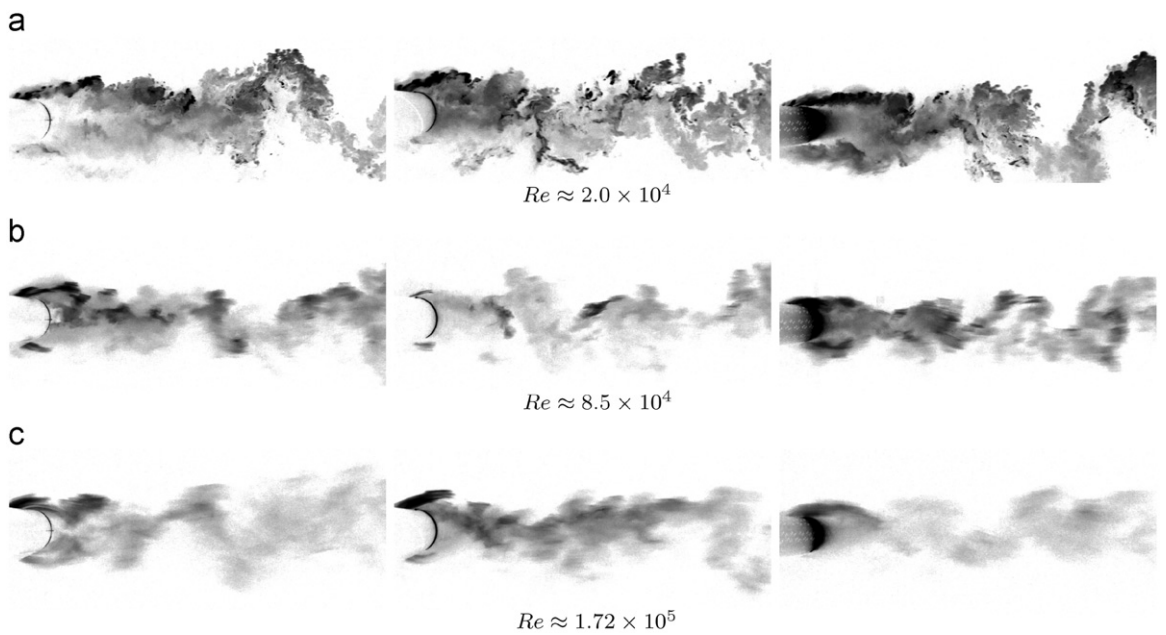

Fig. 6. Force coefficients for the pattern-indented cable at varying relative cable-wind angles. Drag coefficient component normal to the cable (left) and lift coefficient component normal to the cable (right).

Fig. 7. Near-wake smoke visualization: plain cable (left), helically filleted cable (middle), and pattern-indented cable (right). (a) $Re \approx 2.0 \times 10^4$. (b) $Re \approx 8.5 \times 10^4$. (c) $Re \approx 1.72 \times 10^5$.

intuitively be expected based on the definition of the force coefficients. Secondly and counter-intuitively, the flow velocities at which the flow transitions occur are found to decrease for decreasing relative cable-wind angles, even though there is a reduced flow component normal to the cable. A possible explanation for this could be that the fillets' trip the flow along the cable into an early flow transition. The closer the relative cable-wind angle gets to the fillet angle of 45°, the earlier the flow transition occurs. A further explanation might be found in the possible disturbance of the axial flow along the leeward side of the cable, though it is unknown how this may affect the flow transition. Thirdly, for decreasing relative cable-wind angles, an almost constant supercritical drag coefficient component is observed. This is a feature that is normally attributable to the pattern-indented cable (Kleissl and Georgakis, 2011a).

The corresponding lift coefficient components are all of a relatively significant magnitude and, for the relative cable-wind angles of 40°, 45° and 50°, the lift actually exceeds the drag component. It can also be observed that when the flow transition occurs, the lift component increases significantly. The largest lift component is found for the relative cable-wind angle of 45°, which coincides with the pitch angle of the helical fillet.

The force coefficients obtained for the pattern-indented cable are presented in Fig. 6. Here, the development of the drag coefficient component appears to be independent of relative cable-wind angle. As for flow normal to the cable (see Fig. 3(a)), the yawed cable exhibits a very early transition to the super-critical regime due to the high level of surface roughness, which is here accompanied by the occurrence of a non-zero lift coefficient component normal to the cable. While an early transition agrees well with what has been observed for circular cylinders with uniform roughness, the subsequent drag in the supercritical region is nearly constant for all relative cable-wind angles tested. Finally, it can be observed that the critical Reynolds number is determined by the along wind flow velocity alone, i.e. it is independent of the relative cable-wind angle. The small offsets among the supercritical lift coefficient components are most likely a result of minor deviations in the wind-angle of attack introduced when positioning the cable at a specific yaw angle.

Corresponding force coefficient measurements for the inclined plain cable have been reported by Matteoni and Georgakis (2011a). The authors found that the supercritical flow regime is reached at around 3.0×10^5 for all the relative cable-wind angles tested, whilst the slope of the drop in the drag coefficient reduced gradually with decreasing relative cable-wind angle. This is not the case here, thus implying that the surface modifications significantly affect the aerodynamic forces of the cables tested.

3.2.1. Effect of surface imperfections

Recent work by Matteoni and Georgakis (2011b) indicates that small imperfections or distortions on a bridge cable surface may lead to significantly varying force coefficients with wind-angle of attack. To check for any such potential effects on the surface modified cables, the cables were rotated by steps of 90° about their longitudinal axes for the relative cable-wind angle of 45°. Kleissl and Georgakis (2011b) present the results of these tests in detail. The results can be summarized as follows.

For the cable with a helical fillet, the resulting force coefficients are unaffected by wind-angle of attack, except for one case were an earlier flow transition seems to occur. This is believed to be due to the presence of increased roughness at a specific angular position, generated by stamped manufacturer's labelling. For the specific case, the roughness was positioned between the upwind stagnation line and the separation line, on the side of the cable where the fillets are near parallel to the oncoming flow.

This is potentially the most roughness-sensitive location on the surface. For the results presented herewith, the manufacturer's labelling was kept away from this critical area.
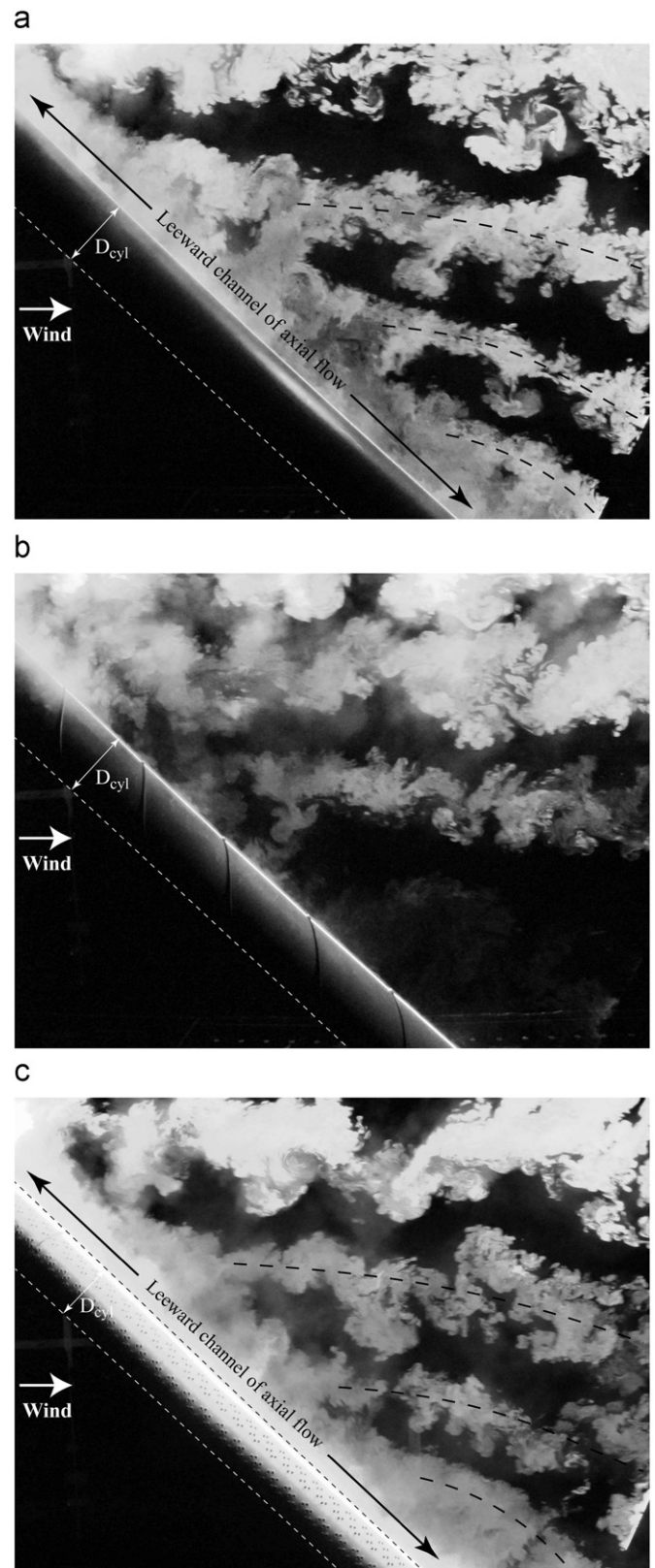
Fig. 8. Near-wake smoke visualization for the cable models at a 45° relative cable-wind angle. $Re \approx 2.0 \times 10^4$. (a) Plain cable. (b) Helically filleted cable. (c) Pattern-indented cable.

The same tests were performed for the pattern-indented cable. For this cable, no significant deviations in the force coefficients with wind-angle of attack could be discerned.

3.3. Near-wake smoke visualization

3.3.1. Flow normal to cable

The smoke visualizations of the near-wake flow structures for all three cables positioned normal to the flow are shown within Fig. 7.

At $Re \approx 2.0 \times 10^4$, all three cables experience the formation of Kármán vortex-shedding, although this is quite disturbed for the helically filleted cable, due to the generation of additional three-dimensional flow structures introduced by the fillets. At $Re \approx 8.5 \times 10^4$, all three cables exhibit a reduced width of their wakes, indicating a drop in drag. When comparing them, the pattern-indented cable has the narrowest wake, agreeing well with the measured low supercritical drag at the corresponding wind velocity (see Fig. 3(a)). Nevertheless, in the supercritical state the pattern-indented cable still experiences vortex shedding, as verified from the fluctuating lift forces in Fig. 4. For the highest visualization velocity of $Re \approx 1.72 \times 10^5$, the vortex shedding of the helical cable is nearly suppressed in the immediate wake, moving significantly further downstream. It is conjectured that the cable is entering the supercritical flow state, which from the analysis of lift force fluctuations happens at around $Re \approx 1.8 \times 10^5$. The other two cables remain in their previous flow state with the continued presence of vortex shedding.

3.3.2. Yawed flow

In Fig. 8, the smoke visualizations of the near-wake flow structures of the cables for a 45° relative cable-wind angle are presented. This angle was chosen because of its 0° yaw, thus producing a vertical cable-wind and laser sheet plane. The camera was mounted at a fixed position, capturing the same cable segment for all three cable models.

In all three photos 60% of the leeward cable surface is visible, while 12% lies downwind and 28% upwind of the view.

For the plain cable, two main observations can be made. First and as can be seen in the figure, a strong channel of axial flow is observed along the leeward side of the cable. Second, the axial flow is observed to have a discontinuous leakage into the wake, generating some characteristic flow structures highlighted in the figure by arched dashed lines. A similar wake structure observation was made by Thomson (1971).

The same inclined visualization is shown in Fig. 8(b) for the helical cable. Significantly, the axial flow is found to be almost completely suppressed by the fillets, with the near-wake flow structures also giving evidence to this.

Fig. 8(c) shows the inclined visualization for the pattern-indented cable. Like the plain cable, this cable exhibits the presence of a strong channel of axial flow along its leeward side, with its near-wake flow structures nearly identical to those of the plain cable. The axial flow appears relatively unaffected by the surface modifications and added surface roughness. Katsuchi (2011a) also measured this strong axial flow similar to that of a plain cable. When changing the laser sheet direction, so it is generating a tangential plane on the cable surface from the leeward side of the cable, it could be observed that the axial flow had a near constant width of approximately one cable diameter. When the same laser sheet was applied to the helical cable, it was observed that the fillets forced part of the axial flow to switch direction, thus continuously reducing its intensity.

3.4. Surface oil visualization

3.4.1. Flow normal to cable

Oil visualization tests were performed to further understand the effect of the surface modifications on the surface flow. Photos obtained during the oil visualization at varying Reynolds numbers are presented in Fig. 9. Flow separation lines on each side of the helical fillet are readily identifiable. The typical point of separation is generally only present in a region between two fillets, whilst near the
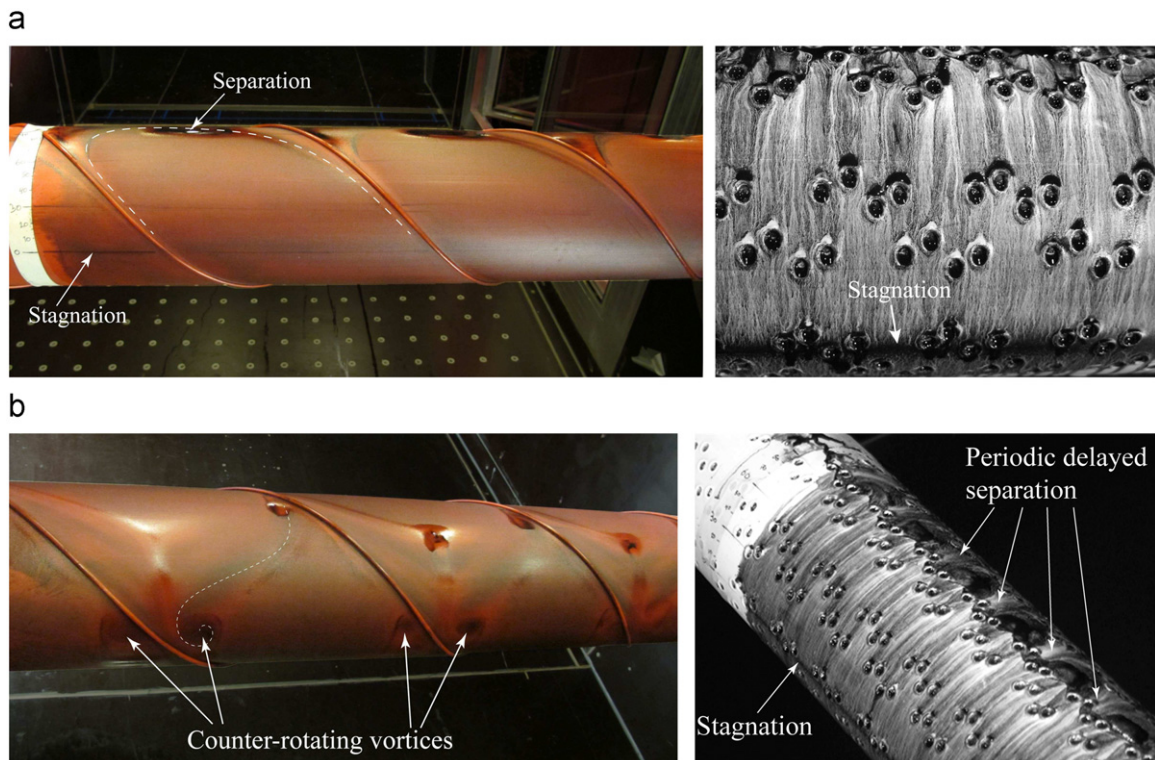

Fig. 9. Oil visualization: helical surface (left) and pattern-indented surface (right). (a) $Re \approx 1.7 \times 10^5$. (b) $Re \approx 3 \times 10^5$.

fillets, the fillets themselves govern the separation. On the pattern-indented surface, the protruding peripheries of the dimples seem to guide the flow around the dimples.

On the leeward side of the helical model (see Fig. 9(b)) a pair of counter-rotating vortices is observed at each of the helical fillets. On the pattern-indented surface a periodic waviness of the separation line is identified, which is often related to a higher base pressure and thus reduced drag (Lam et al., 2004). The wave period is identical to that of the surface pattern.

3.4.2. Yawed flow

Corresponding oil visualization tests were performed on the two surface-modified cables for a relative cable-wind angle of 45°, obtained through a 40° inclination (declining in the downwind direction) and 22.6° yawing. Photos obtained during the yawed oil visualization are shown in Fig. 10. The tests were performed for a flow velocity of 20.3 m/s, considered to be within the supercritical flow regime for both cables.

For the helically filleted cable, flow separation lines on each side of the cable were identified, although significantly different flow structures were observed, due to the difference in the fillet angle in relation to the oncoming flow. This agrees well with the measured non-zero lift force. The separation line on the right side of the cable is shown in Fig. 10(a). For this side, the fillet is near perpendicular to the oncoming flow, resulting in a strong interaction between the fillet and the separation line. In Fig. 10(b), the opposite separation line is shown, where the fillet is near parallel to the oncoming flow. On this side, most of the separation line is unaffected by the fillet. Exceptions can be found near the fillet, where either early (after fillet) or delayed (before fillet) separation occurs. Furthermore, on the leeward side of the helically filleted cable, a flow pattern was observed that can potentially be attributable to an axial flow or the disturbance of this by the fillets. This pattern is shown in Fig. 11 and

was found along the full length of the cable, except along the first two half-pitches near the top windward end of the cable.

For the pattern-indented surface, the protruding peripheries of the dimples seem to guide the flow around them. The flow visualization of the right separation line is shown in Fig. 12(a), while the stagnation and the left separation lines are shown in Fig. 12(b). The periodic waviness of the separation line observed in normal flow (see Fig. 9(b)) is significantly reduced and only some minor spanwise variations can be seen in Fig. 12(a). Even less periodicity is observed in Fig. 12(b), due to the separation occurring between two groups of dimples. The different locations of the separation may also explain the small variations in the measured lift coefficient components.
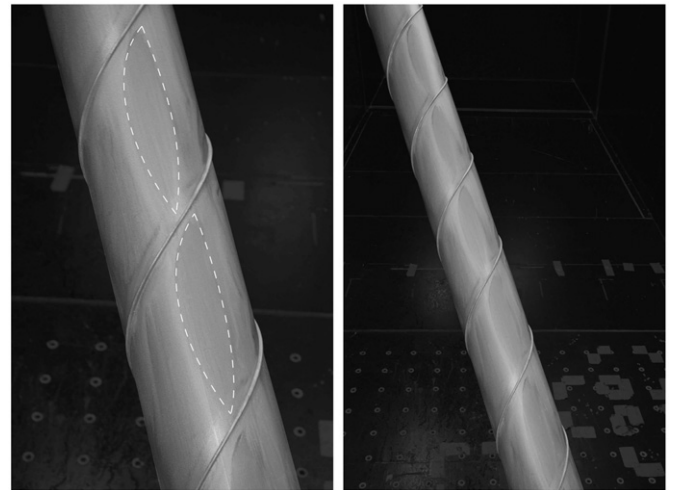

Fig. 11. Oil visualization of the leeward side of the helically filleted cable.
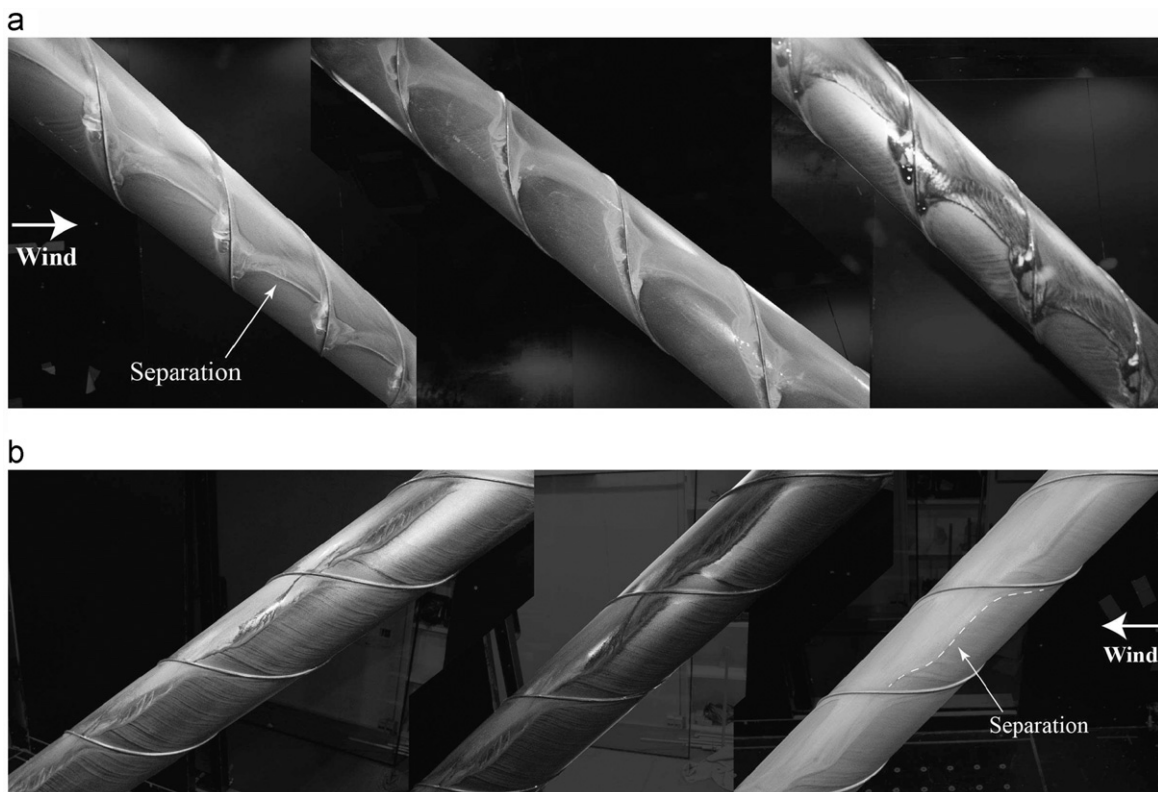

Fig. 10. Oil visualization of each side of the yawed helically filleted cable. (a) View of the separation line along the right side (seen from upwind). (b) View of the separation line along the left side (seen from upwind).
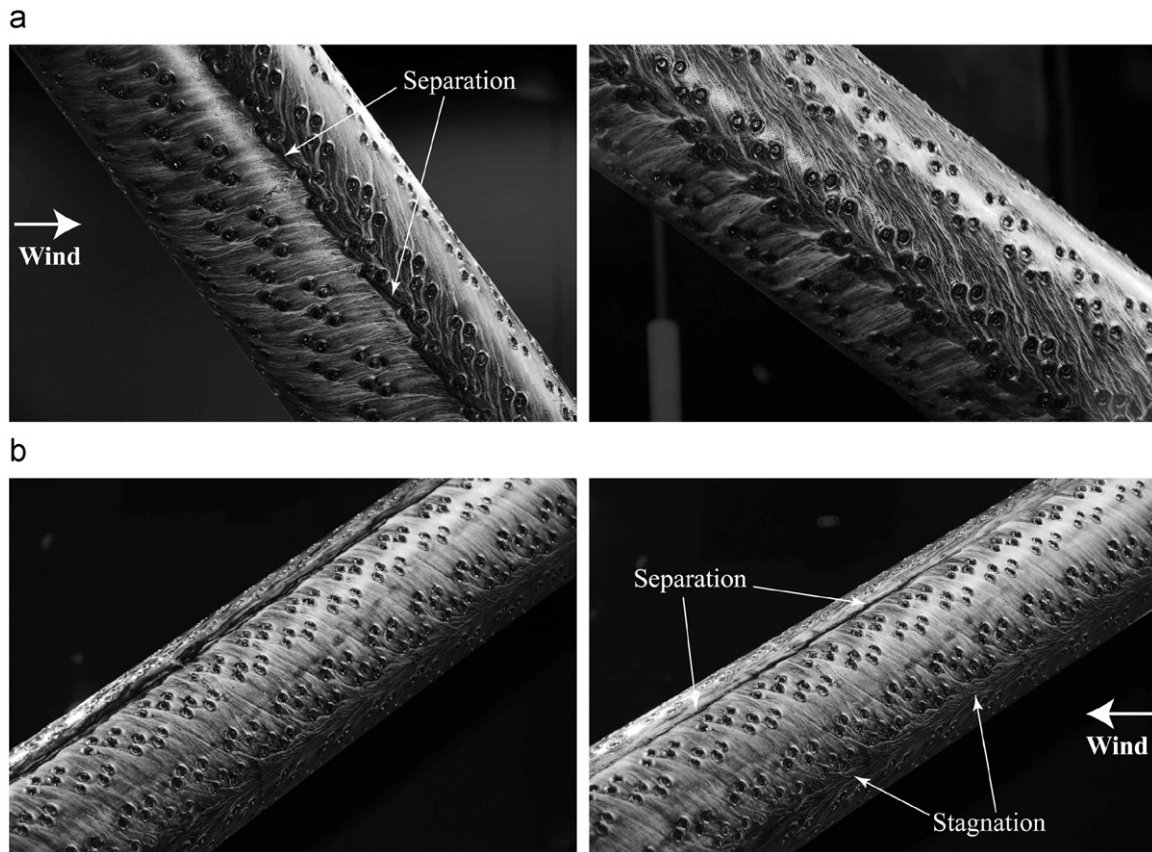
Fig. 12. Oil visualization of each side of the yawed pattern-indented cable. (a) View of the separation line along the right side (seen from upwind). (b) View of the separation line along the left side (seen from upwind).

4. Conclusions

The pattern-indented cable is found to exhibit the lowest drag coefficient, which remains relatively constant over the supercritical Reynolds number range tested. At wind velocities above 30 m/s, it appears that the tubing with the helical fillet exhibits a drag coefficient approaching that of the pattern-indented surface. The pattern-indented surface is observed to experience vortex shedding throughout the tested range of flow velocities, despite its early flow transition. The wind-angle of attack dependency for the pattern-indented cable leads to a prediction of Den Hartog galloping at 20° wind-angle of attack. Flow visualization confirmed the existence of flow structures associated with lower drag forces, such as periodic variations in flow separation along the axis of the cable and narrower wakes.

Static wind tunnel tests undertaken at varying yaw angles, showed that the helically filleted cable has a near constant drag in the supercritical regime and the flow transition occurs earlier for decreasing relative cable-wind angles, despite the reduced flow velocity component normal to the cable. Large lift force components were found for the helically filleted cable. This agrees with the findings of the surface visualizations, which showed significant differences in the flow patterns on either side of the cable. Flow visualizations also indicate that the fillets significantly disrupt the axial flow or similar flow structures on the leeward side of the cable. For the pattern-indented cable, the force coefficients varied with yaw angle and according to the reduction in flow velocity component, whilst the critical Reynolds number did not change for any of the tested relative cable-wind angles. Minor deviations in the supercritical lift component were identified. Through the flow visualizations, these could be understood as a result from a minor asymmetry in the surface pattern, and leading to a slightly different flow separation on either side of the cable model. Flow visualizations also showed that the pattern-indented cable experiences the same intensity of axial flow and near-wake flow structures as that of the plain cable.

Acknowledgements

References

Acampora, A., Georgakis, C.T., 2011. Recent monitoring of the Oresund bridge: rain–wind induced cable vibrations. In: Proceedings of the 13th International Wind Engineering Conference, Amsterdam.

Chen, Z.Q., 2011. Cable vibration incidence of the Jintang Bridge, Hunan University, private communication, July.

Cooper, K., Mercke, E., Wiedemann, J., 1999. Improved blockage corrections for bluff-bodies in closed and open wind tunnels. In: 10th International Conference Wind Engineering, Copenhagen, June, pp. 1627–1634.

Den Hartog, J., 1947. Mechanical Vibrations. McGraw-Hill, New York.

Flamand, O., 1995. Rain-wind induced vibration of cables. Journal of Wind Engineering and Industrial Aerodynamics 57 (2–3), 353–362.

Georgakis, C.T., Koss, H.H., Ricciardelli, F., 2009. Design specifications for a novel climatic wind tunnel for the testing of structural cables. In: 8th International Symposium on Cable Dynamics, Paris, France, September, pp. 333–340.

Gimsing, N.J., Georgakis, C.T., 2011. Cable Supported Bridges: Concept and Design, 3rd ed. John Wiley & Sons Ltd.

Hojo, T., Yamazaki, S., Okada, H., 2000. Development of Lowdrag Aerodynamically Stable Cable with Indented Processing. Nippon Steel Corporation, July (Special Issue on Steel Structure 82). URL ⟨http://www.nsc.co.jp/en/tech/report/pdf/8203.pdf⟩.

Katsuchi, H., 2011. Cable vibration incidence with pattern-indented surface, Yokohama National University, private communication, July.

Katsuchi, H., Yamada, H., 2011a. Dry galloping characteristics of indented stay cables in turbulent flow. In: 9th International Symposium on Cable Dynamics, Shanghai, China, pp. 359–364.

Katsuchi, H., Yamada, H., Sasaki, E., Inamori, K., Kaga, S., 2010. Study on dry-galloping of inclined cable with real indented surface. In: Proceedings of the 21st National Symposium on Wind Engineering, Japan, pp. 387–392 (in Japanese).

Kleissl, K., Georgakis, C., 2011a. Comparison of the aerodynamics of bridge cables with helical fillets and a pattern-indented surface in normal flow. In: Proceedings of the 13th International Conference on Wind Engineering, Amsterdam.

Kleissl, K., Georgakis, C., 2011b. Comparison of the aerodynamics of yawed bridge cables with helical fillets and a pattern-indented surface. In: Proceedings of the 9th International Symposium on Cable Dynamics, Shanghai, China.

Lam, K., Wang, F.H., Li, J.Y., So, R.M.C., 2004. Experimental investigation of the mean and fluctuating forces of wavy (varicose) cylinders in a cross-flow. Journal of Fluids and Structures 19 (3), 321–334.

Larose, G., Smitt, L.W., 1999. Rain/wind induced vibrations of parallel stay cables. In: Proceedings of the IABSE Conference, Cable-Stayed Bridges—Past, Present and Future, Malmo, Sweden, June.

Matteoni, G., Georgakis, C., 2011a. Aerodynamic coefficients of dry inclined cables in smooth flow. In: 9th International Symposium on Cable Dynamics, Shanghai, China.

Matteoni, G., Georgakis, C., 2011b. Investigation of the effects of bridge cable surface roughness and cross-sectional distortion on aerodynamic force coefficients. In: Proceedings of the 13th International Wind Engineering Conference, Amsterdam.

Miyata, T., Katsuchi, H., Tamura, Y., 1999. Comprehensive discussion on structural control for wind-induced responses of bridges and buildings. In: Wind Engineering into the 21st Century, Proceedings of the 10th International Conference on Wind Engineering, vol. 1, pp. 487–494.

Miyata, T., Yamada, H., Fujiwara, T., Hojo, T., 1998. Wind-resistant design of cables for the Tatara bridge. In: IABSE Symposium on Long-span and High-rise Structures, Kobe, Japan, September, vol. 79, pp. 51–56.

Miyata, T., Yamada, H., Hojo, T., 1994a. Aerodynamic response of PE stay cables with pattern-indented surface. In: Proceedings of the International Conference on Cable-Stayed and Suspension Bridges, Deauville, France, October, vol. 2, pp. 515–522.

Miyata, Y., Yamada, H., Hojo, T., 1994b. Experimental study on aerodynamic characteristics of cables with patterned surface. Journal of Structural Engineering 40A (March), 1065–1076.

Thomson, K.D., Morrison, D.F., 1971. The spacing, position and strength of vortices in the wake of slender cylindrical bodies at large incidence. Journal of Fluid Mechanics 50 (4), 751–783.

Yeo, D., Jones, N.P., 2011. Characterization of flow oblique to a circular cylinder with low aspect ratio using 3-d detached eddy simulation. Journal of Wind Engineering & Industrial Aerodynamics 99 (11), 1117–1125.

Chapter 5

Dynamic comparison study

This chapter present the second part of the detailed direct comparison study which covers the experiments with dynamic cable models.

Paper IV

"Comparison of the aerodynamic stability of bridge cables with a smooth surface, helical fillets and a pattern-indentation"

K. Kleissl & C.T. Georgakis

Comparison of the aerodynamic stability of bridge cables with a smooth surface, helical fillets and a pattern-indentation

K. Kleissl*, C.T. Georgakis

Department of Civil Engineering, Technical University of Denmark, Building 118, Brovej, 2800 Kgs. Lyngby, Denmark

Abstract

In this paper, the aerodynamic stability of bridge cables with a smooth surface, helical fillets and a pattern-indentation are examined in both dry and wet conditions. To this end, an extensive wind-tunnel test campaign was undertaken employing a passive dynamic rig. The tests confirmed that the cable with a smooth surface exhibits severe RWIV, whilst, despite the formation of both upper and lower rivulets, neither the helically-filleted nor the pattern-indented cable experienced any significant RWIV for the considered relative cable-wind angle. For the smooth cable surface, the oscillation of the water rivulets, together with lowered energy of the HDPE surface, was found to promote RWIV. In dry conditions, the plain cable was found to suffer from dry inclined galloping at the critical Reynolds number, whilst the helically-filleted cables suffered from a previously unreported dry limited amplitude vibration. This was confirmed through a variation of model frequency and laser-smoke visualization. Finally, although the aerodynamics of the pattern-indented surface showed a minor wind angle-of-attack dependency, significant vibration incidences were not recorded.

Keywords: bridge cable vibration, rain-wind induced vibration, helical fillet, pattern indentation, dimples, passive aerodynamic control, aerodynamic stability, yawed flow

1. Introduction

Eyewitness reports and video evidence of rain-wind induced vibrations (RWIV) of bridge stay cables in the late 80's and early 90's, led researchers and engineers to the hypothesis that these vibrations were the result of a change in the cross-sectional profile of the cable, due to the presence of one or more longitudinally running water rivulets on the surface (Païdoussis et al., 2011). This hypothesis drove to the development of several surface modifications for the cable's outer protective sheathing, with the main effect of these being rain rivulet suppression.

Two distinct surface modifications have prevailed: protective tubing fitted with helical fillets and the high-density polyethylene (HDPE) tubing with a heat-stamped pattern-indention. The first is used predominantly in Europe and the US, whilst the second is commonly used in East Asia. Although developed to inhibit the formation of the rain rivulet, the pattern-indented surface has also been found to provide a modest reduction in drag-induced forces at design wind velocities. This is of particular interest to bridge designers, as more than 50% of the overall horizontal wind load on long span bridges is generated through the stay planes (Gimsing and Georgakis, 2012).

For longer bridges, mechanical dampers are also often applied to the cables to increase their damping. Nevertheless, the combination of cable dampers and surface modifications are often not enough to completely suppress cable oscillations. Therefore, the dynamic characteristics of the different surface-modified cables are of general interest. Research to date into the two distinct

---

*Corresponding author. Tel.: +45 4525 5048; fax: +45 4588 3282.

Email address: kenk@byg.dtu.dk (K. Kleissl)

URL: http://www.cesdyn.byg.dtu.dk (C.T. Georgakis)

aforementioned modifications has been predominantly undertaken either in Europe or in Japan, respectively, and therefore there are no definitive comparisons of their dynamic performance under similar conditions.

The objective of the present study is the direct comparison of the aerodynamic stability of the currently applied bridge cable surfaces under varying meteorological conditions, i.e. dry and rainy. The surfaces are compared through the evaluation of vibration amplitudes and aerodynamic damping. No known similar direct comparison has previously been published. In addition to this, and in conjunction with a previous study where the static performance of the same surfaces has been compared for both normal and yawed flow in dry conditions (Kleissl and Georgakis, 2012b), the authors intend to highlight some of their aerodynamic benefits and drawbacks. This should act to enhance the understanding of their aerodynamic performance, whilst allowing for the further development of existing and innovative cable surfaces.

1.1. Historical overview

Helically wrapped wires (or fillets) on cylinders were initially proposed in the fifties to combat vortex-induced vibrations (VIV). It was found that the presence of the helical protrusions significantly reduced the shedding correlation length. It was not until 1992, though, that tests on the use of these fillets on a bridge stay cable were undertaken at the Centre Scientifique et Technique du Bâtiment (CSTB) in Nantes in connection with the design of the Normandy Bridge (Flamand, 1995). Similar exploratory tests were later undertaken at the Danish Maritime Institute by Larose and Smitt (1999), in relation to the design of the Øresund Bridge. A helically-filleted cable similar to those tested is shown in Figure 1 (left). The aforementioned tests showed a reduction of RWIVs through the disruption of the formation of a coherent upper rivulet in the presence of light rain. As a consequence, a variety of fillet designs have emerged in the last decade, often with varying fillet sizes, shapes and pitch lengths. Generally, the fillets have a near-circular cross-section with a more or less smooth transition to the plane surface of the cable tubing, depending on the manufacturers production and welding procedures (see Figure 1 (right)). The fillets typically have a height between $2-4$ mm and a pitch angle of $45°$. Furthermore the pitch angle and fillet size is often retained regardless of cable diameter, which further increases the variety of designs currently in use. Whilst a relatively low aerodynamic drag can be obtained using smaller fillets on tubes with larger diameters, the disturbance of rain rivulets is often compromised, thus increasing the risk for RWIV. Although relatively unreported, bridge cables with helical fillets are still susceptible to RWIVs. Recent full-scale monitoring of the Øresund Bridge by Acampora and Georgakis (2011) revealed that they might not necessarily be as effective as originally believed. Therefore, bridge operators still often require that helically-filleted cables are supplied with mechanical dampers to reduce the risk of vibrations. Nonetheless, in connection with RWIV, helically-filleted cables should still be considered aerodynamically superior to cables with plain surfaces.
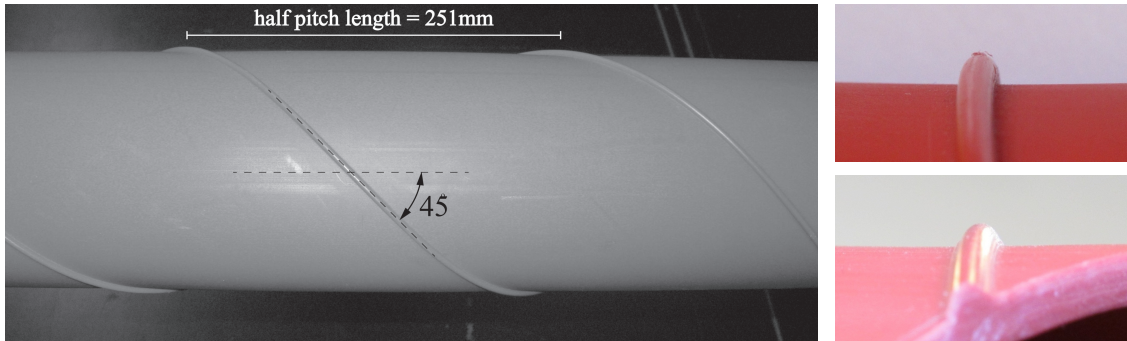

Figure 1: HDPE bridge cable tubing with helical fillets. Helix A (left), close-up of fillets for Helix A (top right) and Helix B (bottom right).

The pattern-indented bridge cable surface with a discrete surface pattern (also referred to as dimples) was originally proposed by Miyata et al. (1994b). Due to the thermal production

procedure, the specific modifications consist of an oval indentation surrounded by a protruding periphery of displaced melted material (Katsuchi et al., 2010). The pattern-indented surface has been found to promote the stabilization of the separated flows over the surface of the cable, purportedly leading to the mitigation of rain-rivulet formation (Miyata et al., 1999). Measured pressure distributions indicate that a dimpled cable enters the supercritical flow state at lower wind velocities, where RWIVs tend to occur. Furthermore, the flow separation point remains stable at 110° from stagnation in the supercritical region, resulting in a near constant drag coefficient (Hojo et al., 2000). It has also been found that these properties hold true, regardless of whether the discrete roughness has been generated by concavities or convexities (Miyata et al., 1994a). Kleissl and Georgakis (2012b) confirmed the occurrence of the early flow transition. The pattern-indented surface was first applied to the cables of the Tatara Bridge in 1999 and later on the Sutong and Stonecutters Bridges, amongst others. Figure 2 shows the unique pattern and the details around the indentations for actual cable samples from the Sutong Bridge. For the Tatara Bridge, Miyata et al. (1998) reported a minimum drag coefficient of 0.61 and a design drag coefficient of 0.7. Similar values have been reported for the Sutong Bridge. Nevertheless, vibrations of pattern-indented cables have recently been observed on bridges (Chen, 2011; Katsuchi, 2011) and in wind tunnel tests (Katsuchi and Yamada, 2011). On one bridge, helical wires were retrofitted around the pattern-indented cables in an attempt to stop what was believed to be RWIV. Finally, the authors have evidenced high frequency cable vibrations on a bridge with a pattern-indented surface in East Asia.
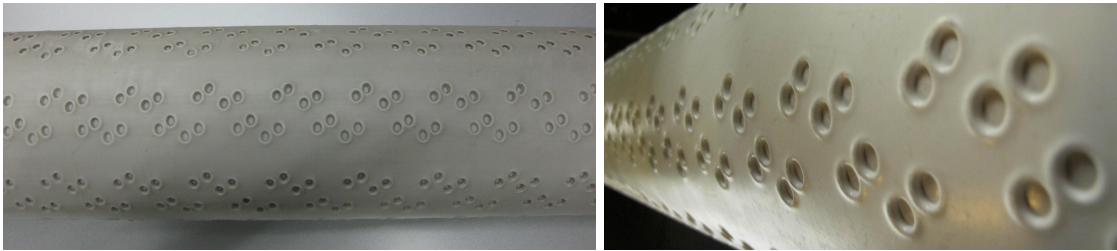
Figure 2: Original cable samples with pattern-indented surface from the Sutong Bridge. The pattern on a 140 mm diameter cable (left) and a close-up of the "dimples" on a 180 mm cable.

2. Materials and methods

2.1. Wind tunnel & flow conditions

The comparative wind tunnel tests were performed at the $2 \times 2 \, \mathrm{m}^2$ cross-section closed-circuit DTU/FORCE Climatic Wind Tunnel, located at FORCE Technology, Lyngby, Denmark (Georgakis et al., 2009). The flow conditions were measured with a cobra probe at wind velocities of 9, 12 and 15 m/s along the model axis. The flow was found to be uniform and a with turbulence intensity of $1.0 - 1.3 \%$, excluding a region 10 cm wide from the wall openings in which the flow was slightly more turbulent. The cable section model continued out of the test section on either side through rectangular wall openings (30 cm wide $\times$ 73 cm high) with rounded corners (see Figure 3).The size of the openings was kept at a minimum to reduce any undesirable flow effects at the cable ends. All tests were performed for 11 fixed wind velocities, with a distribution focusing on the range of $7 - 13$ m/s, where RWIVs are expected. The water spray system consisted of five evenly spaced light spray/mist nozzles mounted upwind of the cable along a projected line of the cable. Each nozzle was attached to the end of a 4 mm tube supported by two piano wires to minimize flow disturbance. The water used for the spray system passed through a filtration system to avoid the presence of surface tension altering minerals. A constant water pressure of 4 bar corresponding to 1.6 L/min was used for all the reported tests.

2.2. Dynamic test rig

A cable model within the test section and an illustrative sketch defining the various angles are shown in Figure 3. The cable models were kept at a yaw angle of $\beta = 60°$ and a cable inclination of $\Theta = 25°$. This corresponds to a relative cable-wind angle of $\Phi = 63°$, where $\Phi = 90°$ corresponds to wind normal to the cable axis. The chosen combination of angles have previously been shown to be within the range where RWIVs might be expected (Cosentino et al., 2003; Flamand, 1995).
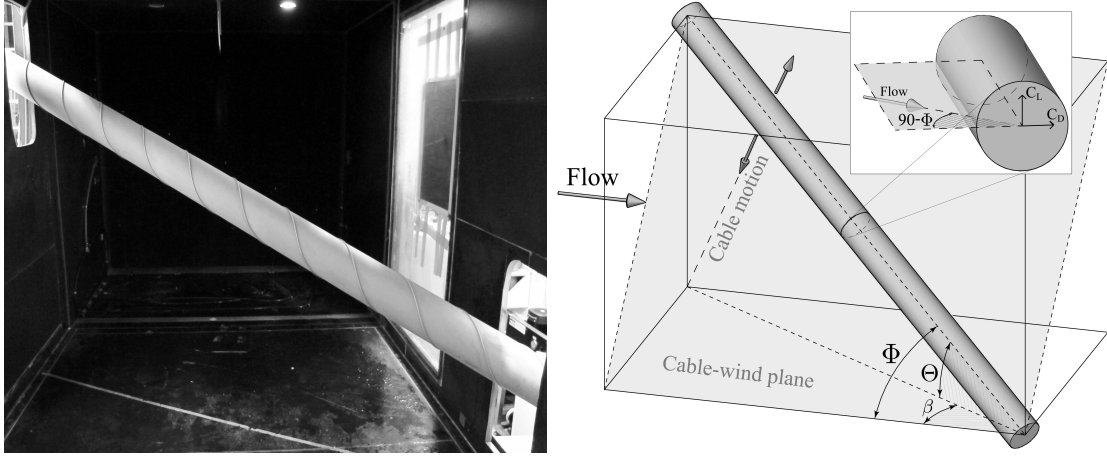
Figure 3: A cable section with helical fillets installed in the wind tunnel (left) and an illustration proving a definition of angles and the direction of cable motion (right).

With the selected angles, the effective cable model length was 2.55 m. For the most commonly tested cable diameter of 160 mm, this length leads to an aspect ratio of 16. Kleissl and Georgakis (2012b) confirmed the existence of a fully developed axial flow for similar aspect ratios. Thus, this aspect ratio was assumed sufficient for the build-up of a uniform axial flow along the leeward side of the cable within its wake. The test rig used for the dynamic tests, allows for both in- and out-of-plane cable motions, where both are orthogonal translational motions normal to the cable axis. During a preliminary study, the plain cable model was installed allowing movement in both degrees of freedom, but it was observed that, as long as the springs were perfectly orthogonally aligned, RWIVs resulted in near vertical motion. Similar purely vertical behavior was reported by Zhan et al. (2008). In the case of improper alignment of the springs, ovalised cable motions appeared. Therefore, it was decided to carry out the full test program using a 1-DOF setup, which only allowed vertical motions. To differentiate between divergent motion and limited amplitude motion, the test rig was designed to allow for larger amplitude displacements. To achieve this, whilst minimizing nonlinearities, the longest possible spring and stabilising wire lengths were chosen, limited only by space constraints. For the maximum peak-to-peak amplitude of 2.75 D ($D = 160$ mm), the cable was expected to experience accelerations larger than one 1 g. It was therefore necessary to implement both upper and lower vertical springs at each end of the cable. The springs were found to behave linearly, even for the largest amplitudes. The cable displacements were measure through the use of four laser displacement transducers, one within the cable's vertical plane and one normal to this, at each end of the cable. To counter the effect of gravity on the cable model, an axial spring was mounted at the top of the model, resulting in slightly lower amplitudes at the top end of the cable, in relation to the bottom.

2.3. Cable models

The tests were performed utilising four different cable models. The models included a plain HDPE tube for reference, two HDPE tubes with double helical fillets (designated here forth as Helix A and B) and a HDPE tube with a pattern-indented surface. The sectional models were all original full-scale samples, supplied by bridge cable manufacturers. The plain HDPE tube and Helix A both had a 160 mm outer diameter. The fillets on Helix A were rounded with a height

of approximately 4 mm (as shown in the top right of Figure 1). Furthermore, they had a 3.14 D pitch length corresponding to a pitch angle of 45°. Helix B had an outer diameter of 200 mm, with 3.5 mm high fillets, again at a 45° pitch angle. The pattern-indented tube had an outer diameter of 180 mm, matching that of the longest stays on the Sutong Bridge.

Scratches and other imperfections on the HDPE tubes where found to affect the uniformity of water beading and the continuity of rain rivulets, particularly in the case of the upper rivulet. To minimise these surface imperfections, the models were sanded. All models were finished with a fine P400-grade along-axis sanding.

The test section model characteristics, including mass, frequency, and damping, are summarized in Table 1. The effective linear mass was found as the total model mass including effective parts of spring masses divided by the effective model length (2.55 m) inside the flow, whilst the damping is shown as a percentage of critical. The corresponding Scruton number is defined as:

$$S_c = \frac{m\,\zeta}{\rho\,D^2} \tag{1}$$

where m is mass of cable per unit length, ζ is the damping ratio, ρ is the density of air, and D is the cable diameter. All damping estimates were determined by fitting an exponential function to the amplitude decay/buildup, within an amplitude range of $40 - 120$ mm, corresponding to $0.25 - 0.75\,D$ for $D = 160$ mm.

Cable model:	Plain tubing	Pattern-indented	Helix A	Helix B
Diameter	160 mm	180 mm	160 mm	200 mm
Linear mass	18.2 kg/m	18.3 kg/m	18.2 kg/m	21.4 kg/m
Frequency	1.09 Hz	1.09 Hz	1.10 Hz	1.09 Hz
Damping ratio, ζ	0.10 %	0.11 %	0.10 %	0.18 %
Scruton no. [-]:	0.58	0.51	0.58	0.79

Table 1: Overview of the dynamic test model characteristics.

The masses of the cables were approximately 1/3 of the lower-end mass of a full-scale cable. Therefore, the results presented herewith should be scaled to match equivalent full-scale mass and damping values.

2.4. Cable surface wettability and treatments

The conditions for the reproduction of RWIV are well described in literature (Gimsing and Georgakis, 2012; Cosentino, 2002). The critical conditions for the generation of RWIVs include wind velocities of $5-18$m/s, cable frequencies between $0.5-3.3$Hz, a cable diameter of $80-250$mm, yaw angles of $0 - 60°$, light to moderate rain fall, stays generally declining along-wind and low levels of turbulence intensity. Preliminary tests with stock HDPE pipes were undertaken with combinations of the aforementioned critical conditions, but RWIVs could not readily be initiated. In an attempt to create a repeatable initiation process, the surface tension of the stock pipes was modified. Lowering of the surface energy of the HDPE tube led to a repeatable and predictable initiation of RWIVs.

In principle, water beads, rolling off of a new untreated HDPE surface exhibiting a high bead contact angle, moves quickly compared with the lateral movement of a rain rivulet sliding over a wettable surface. Such beads or rivulets often form more random-like running patterns, as they are more sensitive to turbulence gusts, due to their high form drag and low surface friction. They are also very strongly attracted by other beads or rivulets which can easy disturb or relocate a rivulet path and redirect it for periods before it finds its way back to its original path. This mostly results in a higher, narrower, and wavier upper rivulet, often forming unpredictable routes.

On a wettable cable surface, the friction forces of the larger contact area slows down and stabilizes the rain rivulet, leading to a more consistent motion of the rivulet and eventually leading

to RWIV. When the HDPE surface has been treated to increase the wettability, the rivulet height lowers and its width increases due to the low contact angle. This reduces its form drag resulting in a lower and more stable upper rivulet position. The high surface tension, which before could force a rivulet or a bead to change direction, is now strongly reduced and the rivulet no longer avoids areas where the surface is initially dry. The path of the rivulet generally leaves a wide wetted track. This also made the rivulets more willing to oscillate laterally, as a result of the cable motion. Furthermore, the higher the HDPE surface energy, the lower is the position of the upper rivulet. If the surface energy become sufficiently high, the upper rivulet will during large vibration amplitudes, approach the stagnation point and at times it will drop to the lower part of the cable, thus joining the lower rivulet. The effect of this is a more limited amplitude RWIV. Specifically in this case, when the cable amplitude reduces the upper rivulet has the chance to slowly form again.

On the bridges, cables are generally subject to sun exposure, dust accumulation, saline deposits, and atmospheric pollution. Therefore, the HDPE surface over time tends to oxidise, erode and become more uneven, leading to a more wettable surface with a higher surface energy (Larose and Smitt, 1999; Flamand, 1995). Therefore, when testing for the evaluation of RWIVs, stock cable samples that are relatively new need to be treated to simulate this aging of the HDPE surface.

The wettability of the HDPE cable surface was found to increase in two ways. Treating it with an applied substance can increase the surface energy of the HDPE or the surface tension of the water can be reduced using a solvent.

Two distinct methods for increasing the wettability of an HDPE cable were found in literature (Larose and Smitt, 1999; Flamand, 1993). A comparison of these two methods was made, together with several new methods. Whilst most of the HDPE surface treatments tried were found to be highly effective in increasing the wettability of the surface, the duration of the effect varied. An overview of the treatments and the visual evaluations are given in Table 2.

Treatment	Duration	Wettability
Gohsenol KP-08R (partly resolved in alcohol)	$10 - 30$ minutes	high
Gohsenol KP-08R (fully resolved in water)	$20 - 60$ minutes	high
MDR KLEAN 210	< 10 minutes	high
Flame treatment*	> 1 day	medium
Soot treatment**	$10 - 30$ minutes	high

Table 2: Overview of the different surface treatments tested and the corresponding observed effectiveness and duration of effect. (*) Can be used as a pre-treatment to enhance a subsequent treatment. (**) Harmful substance.

During the preliminary test campaign, it was found that only when the HDPE surface was properly cleaned before treatment could the findings from the tests be reproduced. Even a small amount of grease, for example from the touch of human fingers, reduced the acceptance of the HDPE surface to the treatment, readily leading to varying levels of wettability along the cable model. Cleaning of the models with white spirit therefore became a standard component of all the treatment procedures.

The first treatment considered was a 5% Gohsenol (polyvinyl alcohol) concentration in alcohol, as originally proposed by Larose and Smitt (1999). As Gohsenol is only partly soluble in alcohol, the eventual concentration was somewhat lower, with unavoidable lumping in the mixture. Lumps were often transferred to the cable surface, sometimes leading to small protruding imperfections. The solvent, being alcohol, was found to dry quickly.

The second treatment explored is a further development of the first one. For this, a 5% Gohsenol concentration was dissolved in water. While Gohsenel is only partly soluble in water and alcohol at 20° C, it is fully soluble in water at $70 - 75°$ C. So, by slowly heating the mixture to $70 - 75°$ C and then cooling it again during stirring, any level of Gohsenol concentration could be achieved without lumping. This modification allowed for a longer lasting effect compared with

partly soluble approaches.

The third treatment involved the use of the MDR KLEAN 210 surfactant. It was selected, as it is highly soluble in water at room temperature and has a very low level of lathering. Unfortunately, its effect was found to last much less than the first two treatments. It worked well at the start of every test, but its effect rapidly diminished, as the surfactant quickly eroded due to its high solubility.

The fourth treatment involved the application of a flame to the surface, in a manner often employed in industrial applications. This involved the passing of a clean combustion oxygen/propane torch over the HDPE surface in gentle sweeping strokes. The HDPE surface was only exposed to the tip of the secondary flame (faint yellow portion) and only for approximately half of a second per stroke. This gentle flame exposure did not soot, deform, or melt the surface in any way, but the wettability was clearly increased compared to untreated areas. While this seemed to have the longest lasting effect among the treatments evaluated, it was found to be time-consuming and somewhat difficult to obtain a uniform effect. It was also found difficult to reapply when the model had already been positioned for testing.

The fifth and final surface treatment tested involved the use of soot as a surface pollutant, as proposed by Flamand (1993). To achieve this, a propane flame with a highly incomplete combustion was used. By licking the surface with the tip of this flame, the HDPE surface was quickly blackened by soot. Afterwards, excessive soot was washed off with a light misty spray, leaving a lightly greyed surface of increased wettability. During the tests, the soot slowly eroded, with larger droplets being particularly effective at loosening the soot. It should be noted that the use of soot lead to more hazardous working conditions that were enhanced by the recirculating nature of the wind tunnel. This necessitated the use of protective gear at all times.

The possibility of adding surfactant directly in the sprayed water was also explored in an attempt to keep a constant level of effect over time. Whilst reducing the time-dependency, the decreased surface tension also reduced the size of the free droplets, which prevented a proper distribution of the spray. Nevertheless, it is believed that a spray system with more nozzles, together with the MDR KLEAN 210 surfactant (due to its low foam production) might have made for an excellent solution. It should also be noted that the sizing of the rain droplets did not seem to affect the RWIV mechanism, except for in selected instances where disturbances where introduced by the impact of larger droplets.

Based on the evaluation of the five treatments, the treatment where Gohsenol was fully dissolved in water was found best suited for this study and was applied through a standard procedure for all of the tests reported herewith.

3. Results and Discussion

3.1. Rain-wind induced vibrations

3.1.1. Plain cable surface (reference model)

The results of the dynamic tests of the plain smooth-surfaced cable section model subjected to rain are shown in Figure 4. RWIVs were successfully reproduced within the velocity range of $8-15$m/s. Between 9 and 13m/s, the section model reached the maximum peak-to-peak amplitude of 2.75 D, as restricted by the allowable travel of the dynamic rig. Within this range, the largest negative aerodynamic damping was estimated to be -0.9% of critical, reached at a wind velocity of 11 m/s, corresponding to $Re = 1.14 \times 10^5$. The horizontal lines on Figure 4 (right) represent the zero level of the total cable damping (mechanical + aerodynamic) and the aerodynamic damping, as a percentage of critical. The difference between these levels was determined as the damping of the dry cable model for zero wind velocity. As can been seen from the figure, there is some noticeable scatter in the damping estimates that is most likely attributable to the surface treatment slowly loosing its effectiveness over time, in spite of the standardized procedure. Figure 5 shows the wide upper rivulet that was present during severe RWIVs.

Larose and Smitt (1999) observed that the RWIVs would often only appear immediately after their water spray system had been stopped. This was not the case here and any instability was
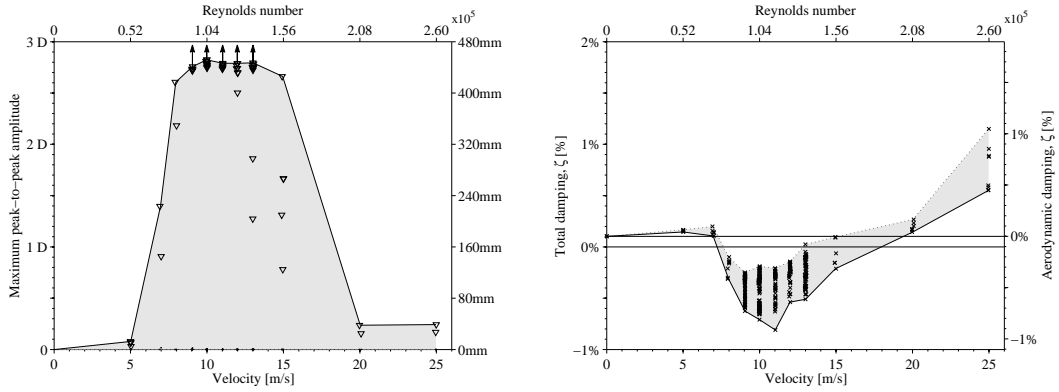
7

Figure 4: Maximum in-plane peak-to-peak amplitudes for the plain cable (left) and the corresponding estimates of the aerodynamic damping (right) during rain simulation.
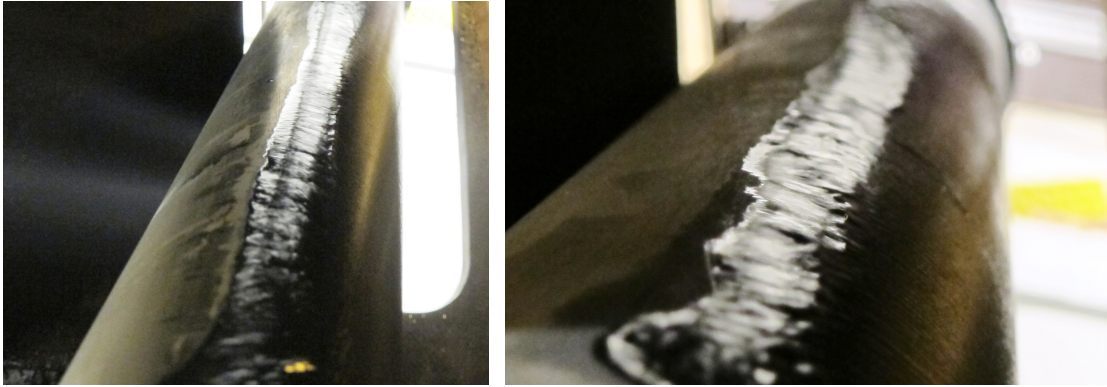

Figure 5: Wide upper rivulet present during large amplitude RWIVs.

found to disappear shortly after the spray system had been stopped. Generally, it was found that none of the tested models perform any worse during the drying phase.

3.1.2. Helically filleted surface

The cable models with helical fillets did not experience any RWIVs throughout the tests. Whilst no vibrations occurred, both the upper and the lower rivulets did fully form. The fillets disturb the flow of the rain rivulets locally, although the rivulets have the ability to quickly regroup again before reaching the next fillet. Therefore, the ability of the fillet to supress RWIV should most likely not be attributed to its capacity to mitigate rain rivulet suppression, but should instead be attributed to its ability to retard rivulet oscillation. Thus the fillets only allow for isolated parts of the rivulets between fillets to oscillate. Inter-fillet rivulet oscillation was observed, but no synchronisation of the isolated segments occurred. It is believed that this helped the cable in avoiding rain-induced oscillation. The vibration amplitudes and the measured damping for Helix A and Helix B are shown in Figure 6 and 7, respectively.

The formation of both upper and lower rivulets has previously been observed for the Helix A model during a static wind tunnel study with section models at 40° inclination and 22.5° yaw (Kleissl and Georgakis, 2012a). With the rivulets present, it must not be ruled out that RWIVs could appear at a different relative cable-wind angle.

The absence of RWIV in the presence of rain rivulets, led to a more detailed examination of the effects of surface wettability. Several of the other previously mentioned surface treatments were therefore applied to achieve varying levels of wettability. Whilst the change in wettability strongly affected the shape and size of the rivulets, no evidence of RWIV could be found.

8
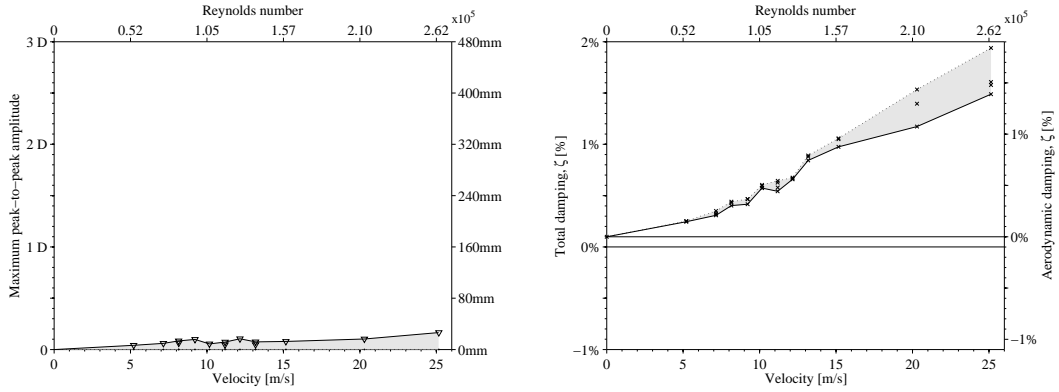
Figure 6: Helix A (Ø160). Maximum in-plane peak-to-peak amplitudes for the helically-filleted cable (left) and the corresponding estimates of the aerodynamic damping (right) during rain simulation.
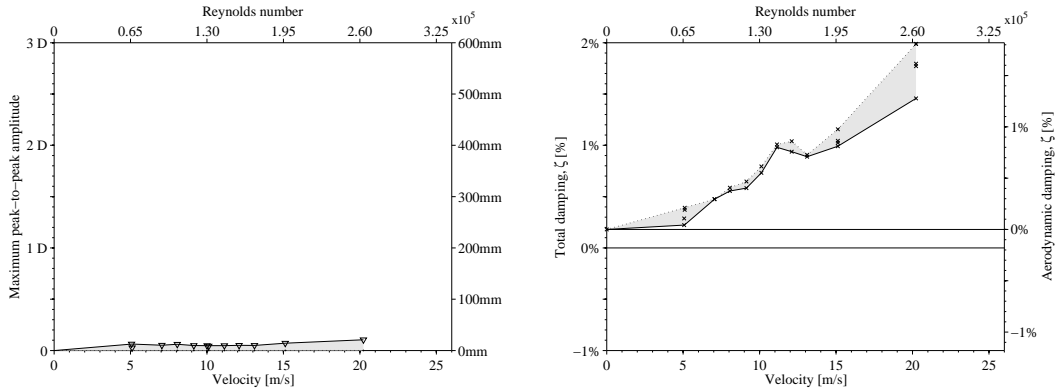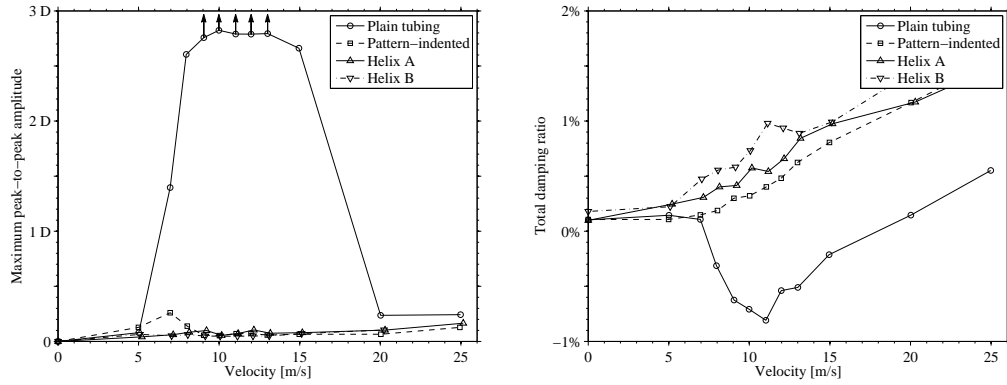

Figure 7: Helix B (Ø200). Maximum in-plane peak-to-peak amplitudes for the helically-filleted cable (left) and the corresponding estimates of the aerodynamic damping (right) during rain simulation.

3.1.3. Pattern-indented surface

On the pattern-indented cable, very straight upper and lower rivulets quickly formed in the presence of rain and were clearly enhanced by the longitudinal alignment of the surface roughness pattern. Nevertheless, despite the appearance of rivulets capable of oscillating, the cable model did not experience significant RWIVs. The measured vibration amplitudes and damping from the dynamic tests are shown in Figure 8.

For certain wind angles-of-attack and at the relatively low wind velocity of around 7 m/s, RWIV's weakly appeared. At this velocity, only the lower rivulet was present, as the wind pressure was not sufficient for a stable upper rivulet to form. For the most sensitive wind angle-of-attack, the rivulet formed in the transition between a strip of aligned roughness and a strip without, thus allowing the rivulet to oscillate into a smooth region. Whilst not completely preventing the phenomenon from occurring, the pattern-indented surface seemed to strongly limit the velocity range at which it does. At higher velocities, the upper rivulet formed, but without leading to any vibrations though. This is in disagreement with a hypothesis by Miyata et al. (1998), in which they outlined that the upper rivulet is prevented by the supercritical pressure distribution due to the early flow transition. It should be noted that Yagi et al. (2011) also observed the formation of an upper rivulet on a pattern-indented cable.

3.1.4. Comparison of wet performance

Figure 9 shows the comparison of the maximum amplitude and the corresponding aerodynamic damping of the different models, subjected to rain.

9
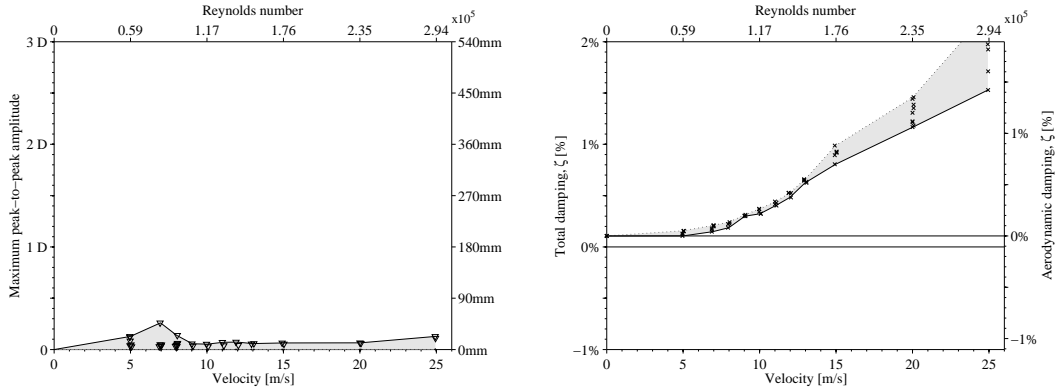
Figure 8: Maximum in-plane peak-to-peak amplitudes for the pattern-indented cable (left) and the corresponding estimates of the aerodynamic damping (right) during rain simulation.

Figure 9: Comparison of the maximum in-plane peak-to-peak amplitudes (left) and the corresponding estimates of the aerodynamic damping (right) during rain simulation.

3.1.5. Driving mechanism of RWIV

During both the preliminary testing and the testing of the plain cable in rain, some general observations regarding the behaviour of the rivulets were made. This is not intended as a complete explanation of the phenomena, but merely a description of what was observed during its occurrence. It is hoped that a qualitative description might be useful towards an improved understanding of the mechanism.

It was observed that the presence of straight lower and uppers rivulets alone do not seem to be enough to immediately lead to RWIV. It was apparent that some form of lateral rivulet oscillation is a necessary prerequisite for the initiation of oscillations. For a relatively new HDPE tube, this can be archived by increasing the wettability employing any of the previously described treatments. How and when the wettability of actual bridge cables increase is still unclear and further work needs to be done to understand this further.

Whilst the upper rivulet is often considered critical for the mechanism, the lower rivulet alone can drive vibration. The amplitudes of these vibrations are generally smaller than when the upper rivulet is present though. In any case, the lower rivulet clearly contributes to RWIV.

During RWIV, both the rivulets were observed to oscillate at the frequency of the vertical cable motion. In Figure 10 an attempt to map this cable-rivulet interaction is shown for the indicated wind direction. When the cable moves down, both rivulets moves in a counter-clockwise direction, while when the cable moves up the rivulets move clockwise. This appears to agree well with the instantaneous relative wind direction. Gravity has the effect of accelerating the rivulets faster downwards than upwards, which results in the rivulets spending more time at their lowest position than at their highest. This means that when the cable moves down, the upper rivulet

often reaches its lowest position slightly before the cable reaches its own. Until the cable begins moving up again, the rivulet briefly stays at the lowest position. When the cable moves upwards, it takes slightly longer for the rivulet to reach its highest position. The observed time difference decreases with increasing cable amplitude.
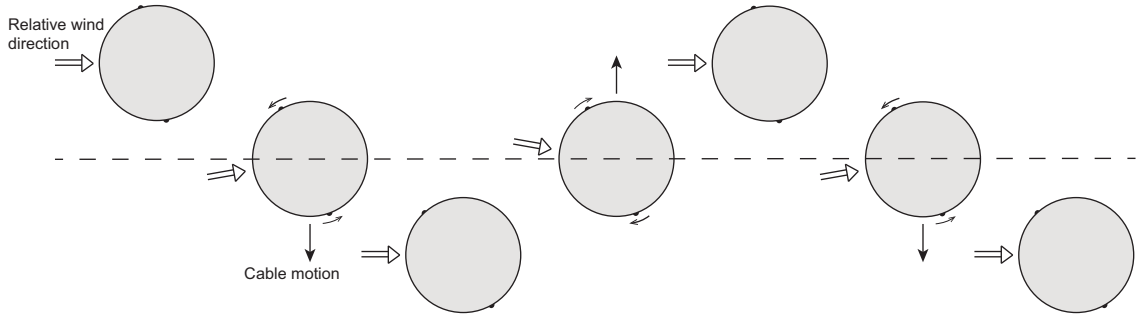
Figure 10: Qualitative mapping of the oscillatory cable-rivulet interaction during RWIV.

It is generally assumed that the rain rivulet "slides" on the surface of the cable. The actual rivulet behaviour might be somewhat more complex though. A more precise way of considering it would be as a periodic deformation of the rivulet, where the bulk mass of the water oscillates. An illustration of this is shown at Figure 11. Whilst the motion of a sliding rivulet may be sufficient to catch the mechanism of the phenomena, the understanding of bulk mass movement helps to clarify why only treated surfaces with wider rivulets result in regular rivulet oscillations.
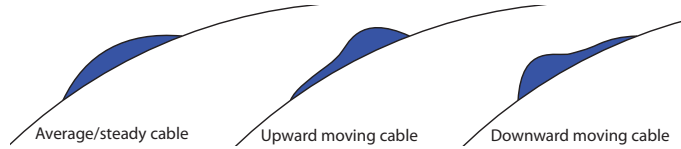
Figure 11: Shape of moving rain rivulet.

3.2. Dry vibrations

Following the testing with rain, a series of tests were undertaken to evaluate the aerodynamic stability and damping of the section models in dry conditions. A one-to-one correspondence between dry and wet tests was pursued, to ensure matching conditions such as spring alignment, wind flow, model position and model rotation. For the sake of correspondence, the water spray system upwind of the models was left in place.

Vibrations were observed and in several situations found to be limited in amplitude. The range of these steady-state amplitudes are indicated by the shaded range within the figures showing maximum cable amplitudes.

3.2.1. Plain cable surface

The results of the dynamic tests of the reference cable model with the plain surface in dry conditions are shown in Figure 12. For wind velocities broadly within the subcritical regime, no vibrations were observed and the aerodynamic damping was found to increase gradually, as might be expected following quasi-steady predictions. At higher wind velocities, where flow transitions were expected, the plain cable experienced an increase in the observed maximum vibration amplitudes. At 25 m/s, a strong divergent type instability was observed. This is generally believed to be a form of dry inclined galloping (Matsumoto et al., 2010). The decrease in aerodynamic damping measured at 15 m/s is believed to be due to a sudden decrease in the drag coefficient that is expected during a flow transition of this type. Therefore, it is conjectured that the observed dry inclined galloping observed is strongly related to the flow transition from the sub- to
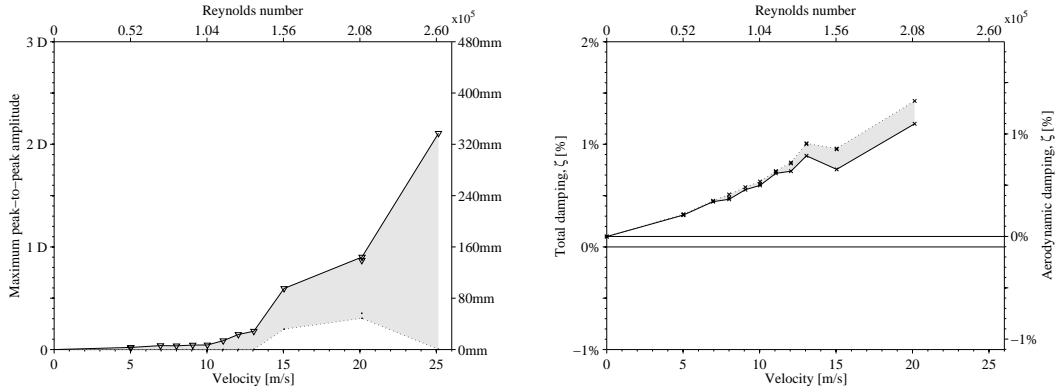
Figure 12: Cable with plain surface in dry conditions. Maximum in-plane peak-to-peak vibration amplitudes (left) and the corresponding estimates of the aerodynamic damping (right).

the supercritical flow regime. At the two highest velocities tested, the motion often appeared as a combination of symmetric and anti-symmetric vibration modes. Whilst only mean displacements are presented in Figure 12, the upward pointing arrows indicate that the combined vibration reached the maximum motion allowed by the wall openings.

Estimates for the aerodynamic damping varied for the large amplitudes, whilst no estimates could be obtained at 25 m/s, due to the extreme and fairly random nature of the vibrations. At $15 - 20$ m/s and before the appearance of divergent vibrations, the cable experienced stable limited-amplitude vibrations for periods. After oscillating within a certain range for a few minutes, the cable then dropped back to a somewhat lower random response. It is unclear how or if this contributes to the dry inclined galloping.

3.2.2. Helically-filleted surface

Both of the helically-filleted cable models suffered from limited amplitude vibrations, similar to those observed for the cable with a plain surface. The maximum peak-to-peak amplitudes for Helix A & B are shown in Figure 13. As can be seen, the helically-filleted models exhibited vibrations with larger amplitudes and within a smaller range than for the equivalent plain-surfaced cable, indicating a significantly stronger and more stable mechanism. The vibrations were observed to occur within a very specific range of velocities, peaking near 13 m/s - reminiscent of a high-velocity vortex-induced vibration (VIV). The Strouhal number was determined to be $St = 0.014$, based on the along-wind velocity. To the best of the authors' knowledge, this type of vibration has not previously been reported.
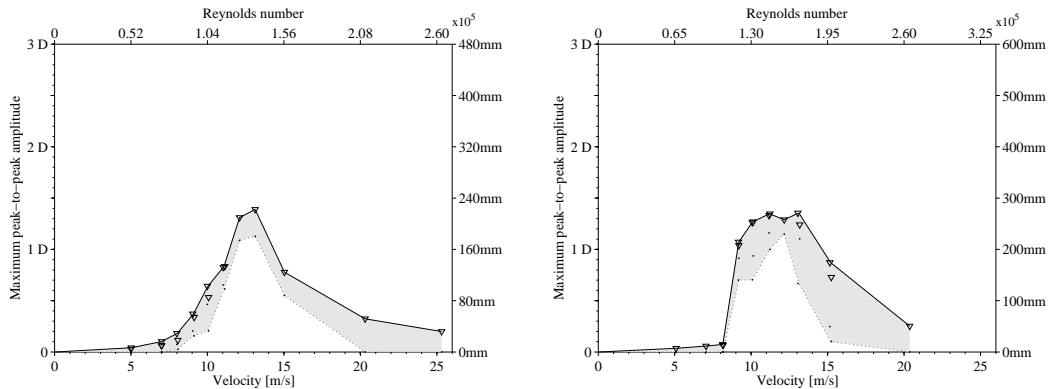
Figure 13: Maximum in-plane peak-to-peak vibrations amplitudes in dry conditions. Helix A, Ø160 (left) and Helix B, Ø200 (right).

Often, especially at the lower velocities, the limited amplitude vibration would not start on it's own. To trigger it, it therefore required a manually induced initial motion of the cable model. Somehow this motion helped the self-induced phenomena to initiate and synchronize, after which the amplitude quickly would go to the steady state limited amplitude vibration. At higher wind velocities, the random response was sometimes sufficient to initiate the vibration, though it could take up to 30 minutes before occurring.

It is believed that the mechanism is somehow related to the strong asymmetry the helically-filled cable experiences in yawed wind, which has also been highlighted in a previous study by the authors (Kleissl and Georgakis, 2012b).

To clarify whether the vibrations were some form of VIV, the tests with Helix A were repeated for three different model frequencies, ranging from $1.1 - 1,41$ Hz. The tests were performed sequentially, with the model mass adjusted through masses mounted outside the wind tunnel walls. The results are shown in Figure 14 and from this it can be observed that the critical VIV velocity remained unchanged for varying section model frequencies. High reduced-velocity vortex shedding, wake-induced vibrations from the upstream water spray system, and shear-layer instabilities at the wall openings should therefore all be ruled out as the driving mechanism. It is hypothesised that the vibrations are flow-transition induced and will here forth be referred to as flow-transition induced vibrations (FTIV).
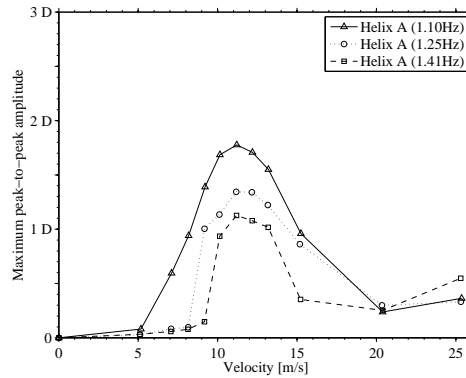
Figure 14: Maximum in-plane peak-to-peak vibration amplitudes for Helix A (Ø160) in dry conditions, for varying cable frequencies.

While a plain-surfaced cable only experiences a non-zero lift in the critical Reynolds number regime, the helically-filleted cable, at yawed angles, suffers from a constantly present non-zero lift which changes suddenly during the flow transition. This is predominantly because only one side of the helical cable is directly affected by the flow transition, as the other side is controlled by the fillets and their tripping wire effect. Whether it is the instantaneous relative wind velocity provoking periodic flow transition or the motion of the cable, which helps the formation of a periodically appearing single separation bubbles, is not known.

A laser-smoke visualization test was undertaken to better understand the flow during FTIV. Attention was directed to the side of the cable where the fillets are nearly parallel to the oncoming flow. Whilst it was generally difficult to photograph the flow at higher wind velocities and whilst the model was moving, photos obtained did point to the existence of a single separation bubble on the top of the helically-filleted cable. Both of the photos presented in Figure 15 where taken immediately before the cable reached the lowest point of oscillation. This is at the point where the model has a near-zero decreasing downward velocity and an increasing upward acceleration. The periodic separation bubble could be detected during amplitude build-up.

It is unclear if the plain cable might have experienced a form of asymmetric flow due to surface imperfections, leading to similar vibration.
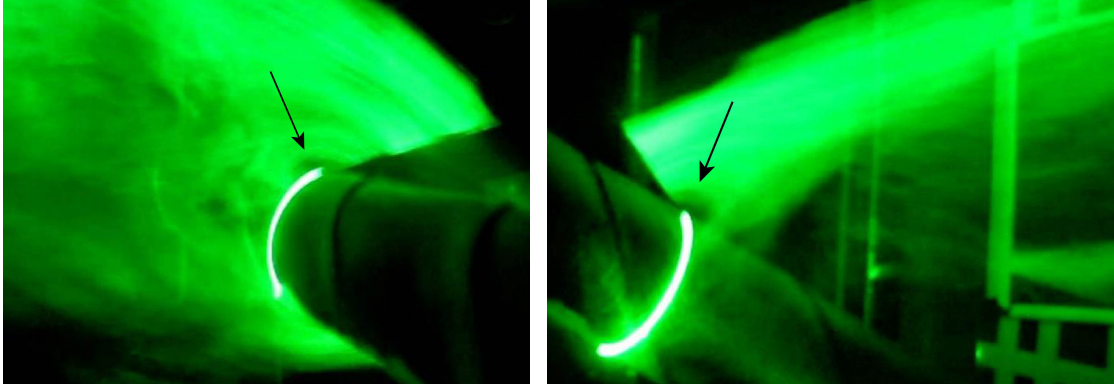
13

Figure 15: Laser-smoke visualization showing the appearance of a single separation bubble during FTIV.

3.2.3. Pattern-indented surface

No significant vibrations were found for the pattern-indented cable model in dry conditions (see Figure 16). Whilst the aerodynamic damping was never found to be below zero, it was found that changes in the wind angle-of-attack, through rotation of the cable model around its own axis, did affect the aerodynamic damping. The appearance of negative lift force gradients and thus the possibility of Den Hartog type galloping has previously been emphasised by the authors (Kleissl and Georgakis, 2011). For the present configuration, the negative aerodynamic damping introduced by the variation in lift did not overcome the level of positive aerodynamic damping introduced by the drag force. Nevertheless, the reduced aerodynamic damping will likely make cable fitted with these surfaces more prone to other forms of excitation.
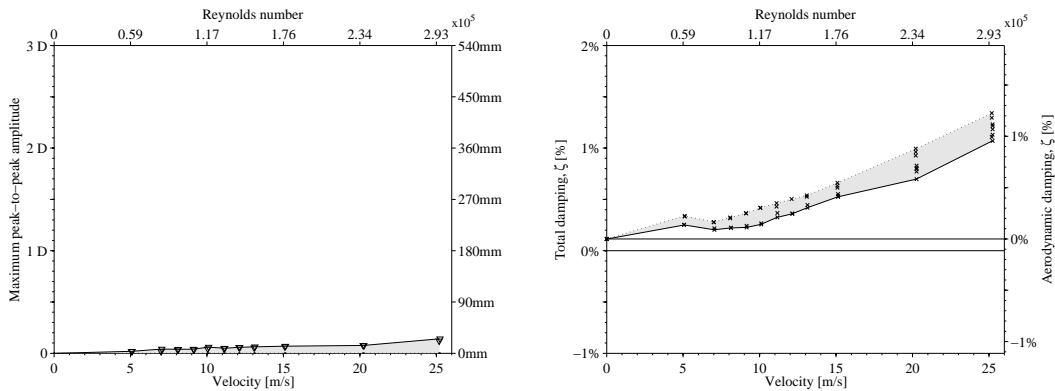
Figure 16: Cable with pattern-indented surface in dry conditions. Maximum in-plane peak-to-peak vibrations amplitudes (left) and the corresponding estimates of the aerodynamic damping (right).

3.2.4. Comparison of dry performance

Figure 17 shows the comparison of the maximum amplitude in dry conditions.

4. Concluding remarks

Severe RWIV for a section model of a cable with a plain smooth surface were successfully reproduced and in good agreement with previous works and reports from bridges.

The effectiveness of several HDPE surface treatments in generating RWIVs were compared. The effect of changing the HDPE surface energy were found to be most important. In addition, surface-rivulet interaction was mapped, whilst the oscillation of rain rivulets were found essential for the generation of RWIV.

14
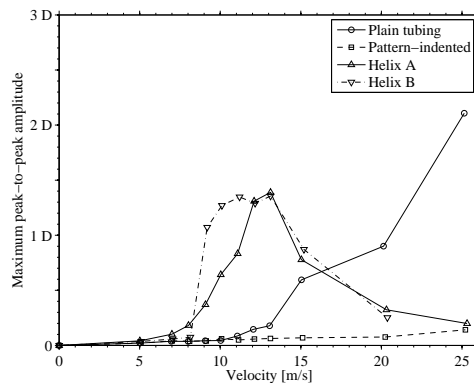
Figure 17: Comparison of the maximum in-plane peak-to-peak amplitudes in dry conditions.

Neither the pattern-indented nor the helically-filleted cables experienced any significant form of RWIV for the tested relative cable-wind angle. All of the modified surfaces did exhibit both upper and lower rivulets, which might lead them to exhibit RWIV for different cable-wind angles.

In dry conditions the plain-surfaced cable was found to suffer from dry inclined galloping, when approaching the critical Reynolds number region. The helically-filleted cables suffered from a dry limited amplitude flow-transition induced vibration (FTIV), which has not previously been reported. Laser-smoke visualization indicated the periodic appearance of a single separation bubble during FTIV.

The aerodynamic damping of the pattern-indented cable was found to be dependent on the wind angle-of-attack, in both wet and dry conditions. This did not result in significant vibrations for the specific relative cable-wind angle.

Acknowledgements

5. References

Acampora, A., Georgakis, C. T., 2011. Recent monitoring of the oresund bridge: Rain-wind induced cable vibrations. In: Proceedings of the 13th International Wind Engineering Conference, Amsterdam.

Chen, Z. Q., Hunan University, Jul 2011. Cable vibration incidence of the Jintang Bridge, private communication.

Cosentino, N., 2002. Rain-wind induced vibration of stay cables. Ph.D. thesis, DISTART Department of the University of Bologna.

Cosentino, N., Flamand, O., Ceccoli, C., 2003. Rain-wind induced vibration of inclined stay cables. part 1: Experimental investigation and physical explanation. Wind and Structures 6 (6), 471–484.

Flamand, O., Jun 1993. Rain-wind induced vibration of cables. In: et al., T. M. (Ed.), proceedings of the 2nd European Conference on Structural Dynamics, Trondhein, Norway. A.A. Balkema, Rotterdam, The Netherlands.

Flamand, O., 1995. Rain-wind induced vibration of cables. Journal of Wind Engineering and Industrial Aerodynamics 57 (2-3), 353 – 362.

Georgakis, C. T., Koss, H. H., Ricciardelli, F., Sep 2009. Design specifications for a novel climatic wind tunnel for the testing of structural cables. In: 8th International Symposium on Cable Dynamics, Paris, France. pp. 333–340.

Gimsing, N. J., Georgakis, C. T., 2012. Cable Supported Bridges: Concept and Design, 3rd Edition. John Wiley & Sons Ltd.

Hojo, T., Yamazaki, S., Okada, H., Jul 2000. Development of lowdrag aerodynamically stable cable with indented processing. Special Issue on Steel Structure 82, Nippon Steel Corporation.
URL http://www.nsc.co.jp/en/tech/report/pdf/8203.pdf

Katsuchi, H., Yokohama National University, Jul 2011. Cable vibration incidence with pattern-indented surface, private communication.

Katsuchi, H., Yamada, H., Oct 2011. Dry galloping characteristics of indented stay cables in turbulent flow. In: 9th International Symposium on Cable Dynamics, Shanghai, China. pp. 359–364.

Katsuchi, H., Yamada, H., Sasaki, E., Inamori, K., Kaga, S., 2010. Study on dry-galloping of inclined cable with real indented surface. In: Proceedings of the 21st National Symposium on Wind Engineering, Japan. pp. 387–392, in Japanese.

Kleissl, K., Georgakis, C., 2011. Comparison of the aerodynamics of bridge cables with helical fillets and a pattern-indented surface in normal flow. In: Proceedings of The 13th International Conference on Wind Engineering, Amsterdam, Netherlands.

Kleissl, K., Georgakis, C., 2012a. Comparison of several innovative bridge cable surface modifications. In: Proceedings of The 7th International Colloquium on Bluff Body Aerodynamics & Applications, Shanghai, China.

Kleissl, K., Georgakis, C., 2012b. Comparison of the aerodynamics of bridge cables with helical fillets and a pattern-indented surface. Journal of Wind Engineering and Industrial Aerodynamics 104 - 106 (0), 166 – 175.
URL http://www.sciencedirect.com/science/article/pii/S0167610512000554

Larose, G., Smitt, L. W., Jun 1999. Rain/wind induced vibrations of parallel stay cables. In: Proceedings of the IABSE Conference, Cable-Stayed Bridges - Past, Present and Future, Malmo, Sweden.

Matsumoto, M., Yagi, T., Hatsuda, H., Shima, T., Tanaka, M., Naito, H., Jun. 2010. Dry galloping characteristics and its mechanism of inclined/yawed cables. Journal of Wind Engineering and Industrial Aerodynamics 98 (6-7), 317–327.

Miyata, T., Katsuchi, H., Tamura, Y., 1999. Comprehensive discussion on structural control for wind-induced responses of bridges and buildings. In: Wind Engineering into the 21st Century, Proceedings of the 10th International Conference on Wind Engineering. Vol. 1. pp. 487–494.

Miyata, T., Yamada, H., Fujiwara, T., Hojo, T., Sep 1998. Wind-resistant design of cables for the tatara bridge. In: IABSE Symposium on Long-span and High-rise Structures, Kobe, Japan. Vol. 79. pp. 51–56.

Miyata, T., Yamada, H., Hojo, T., Oct 1994a. Aerodynamic response of PE stay cables with pattern-indented surface. In: Proceedings of the International Conference on Cable-Stayed and Suspension Bridges, Deauville, France. Vol. 2. pp. 515–522.

Miyata, Y., Yamada, H., Hojo, T., Mar 1994b. Experimental study on aerodynamic characteristics of cables with patterned surface. Journal of Structural Engineering 40A, 1065–1076.

Païdoussis, M., Price, S., de Langre, E., 2011. Fluid-Structure Interactions: Cross-Flow-Induced Instabilities, 1st Edition. Cambridge University Press, 32 Avenue of the Americas, New York, NY 10013-2473, USA.

Yagi, T., Okamoto, K., Sakaki, I., Koroyasu, H., Liang, Z., Narita, S., Shirato, H., Jul 2011. Modification of surface configurations of stay cables for drag force reduction and aerodynamic stabilization. In: Proc. of the 13th International Conference on Wind Engineering, Amsterdam.

Zhan, S., Xu, Y., Zhou, H., Shum, K., 2008. Experimental study of wind-rain-induced cable vibration using a new model setup scheme. Journal of Wind Engineering and Industrial Aerodynamics 96 (12), 2438 – 2451.

Chapter 6

Innovative surfaces

This chapter contains a study proposing some new innovative cable surface modifications based on the understanding and experience gained during the work before this.

Paper V

"Innovative bridge cable surface modifications for the avoidance of RWIV"

K. Kleissl & C.T. Georgakis

Innovative bridge cable surface modifications for the avoidance of RWIV

K. Kleissl*, C.T. Georgakis

Department of Civil Engineering, Technical University of Denmark, Building 118, Brovej, 2800 Kgs. Lyngby, Denmark

---

Abstract

In this paper, the aerodynamics of bridge cables with several new innovative surface modifications are examined in both dry and wet conditions. To this end, an extensive wind-tunnel test campaign was undertaken to measure drag coefficients, rivulet suppression ability, and both wet and dynamic performance. The static tests lead to selection of two surface modifications with superior upper and lower rain rivulet suppression, whereof one was found to exhibit a near constant super-critical drag coefficient of only 0.65. The dynamic tests found that none of the two innovations experienced any significant RWIV. Although in dry conditions one of these innovations was found to suffer from the same limited amplitude Flow-Transition Induced Vibration (FTIV) previously observed for helically filleted cable models.

Keywords: bridge cable vibration, Rain-wind induced vibration, surface modification, passive aerodynamic control, aerodynamic stability, yawed flow

---

1. Introduction

Over the last two decades, a plethora of eyewitness reports and video evidence of rain-wind induced vibrations (RWIV) of bridge stay cables has emerged. This has led bridge cable manufacturers to introduce surface modifications on the high-density polyethylene (HDPE) sheathing that is installed for the protection of the inner strands. The main purpose of these surface modifications is rivulet impendance, as it has been hypothesized that these vibrations are the result of the presence of one or more longitudinally running water rivulets on the cable surface. Today, two prevailing cable surfaces are used: the HDPE tubing fitted with helical fillets, as predominantly used in the US and Europe, and the HDPE tubing with a pattern-indented (dimpled) surface, which is more commonly used in Asia. The pattern-indented surface is known for also modestly reducing the drag forces at design wind velocities. Since more than 50% of the overall horizontal wind load on a long span bridge is induced through the stay planes (Gimsing and Georgakis,

---

2012), cable drag reduction is of great interest to bridge designers. An in-depth study of the aerodynamic performance of the currently applied surface modifications has been presented by Kleissl and Georgakis (2012b) and Kleissl and Georgakis (2013).

The introduction of helical fillets and dimples has not completely eliminated RWIVs often leading bridge operators to the installation of cable vibration dampers. It is hypothesized, though, that reasoned changes to the surface of the HDPE tube can lead to the elimination of RWIV, together with a substantial reduction in drag.

Therefore, the objective of the present study is to examine the performance of several innovative surface modifications, that combine and enhance the performance advantages of the existing modifications, in similar manner to that presented by Yagi et al. (2010, 2011).

Several new surface modifications are proposed herewith. Each of the proposed modifications were investigated through wind tunnel testing. The presented mean static force coefficients were obtained from wind tunnel tests, with the cables positioned normal to the wind. Using a static inclined rig, rivulet suppression was evaluated. Drag and rivulet suppression were subsequently used as "gateway" criteria for the following dynamic testing. Two innovative solutions were finally selected and tested in a dynamic rig to evaluate their performance in both dry and wet conditions. Their performance was then compared to that of existing surface modifications.

2. Material and methods

2.1. Static force coefficients

The wind tunnel tests were performed at the $2 \times 2 \, \mathrm{m}^2$ cross-section closed-circuit DTU/Force Climatic Wind Tunnel, located at Force Technology, Lyngby, Denmark (Georgakis et al., 2009). Without the rain spray system installed, flow conditions were measured with a cobra probe and turbulence intensities of $0.41 - 0.64\%$ were found for $33/66/100\%$ of the maximum tunnel flow velocity, at the cross-sectional quarter point positions both vertically and horizontally. The surface-modified sectional cable models were all based on original 160 mm diameter plain HDPE tubes, supplied by bridge cable manufacturers. For the determination of the force coefficients, the models were placed horizontally, resulting in a near 2-D flow normal to the models. The force coefficients were measured with 6-DOF force transducers at each end of the cable. The force transducers were installed between the cable model and supporting cardan joints fixed to the walls. End plates with a diameter of approximately five cylinder diameters were fitted close to the model ends to eliminate undesirable flow disturbances from the cable ends and cardan joints. Dummy tube pieces were mounted around the force transducers and extending beyond the end plates, leaving approximately a 2 mm gap to the cable model. A photo of the test set-up is presented in Figure 1.
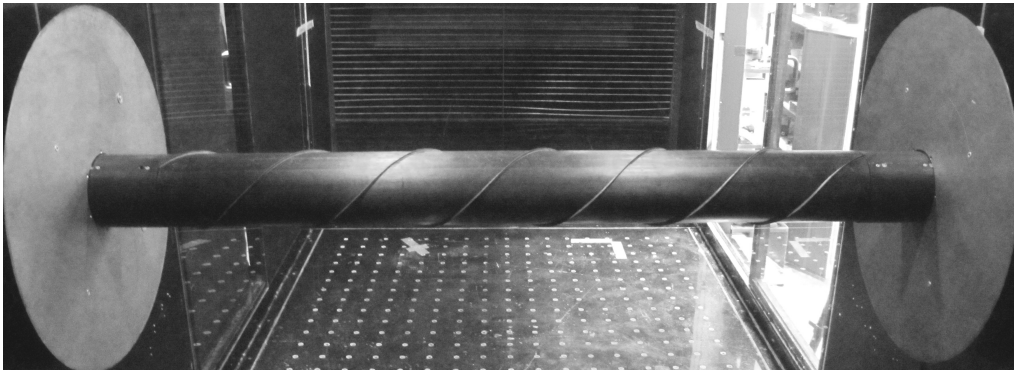
Figure 1: Test set-up used to determine the static force coefficients of the modified cable sections.

During the tests, the wind velocity was increased by regular increments of approximately 1m/s, up to the maximum wind tunnel velocity of 32 m/s, allowing for supercritical Reynolds numbers to be reached for all test models. With an effective model length of 1.53 m, the aspect ratio was $9.6 : 1$. The blockage ratio for all section models was 8% and the drag coefficients were corrected with the Maskell III method, according to Cooper et al. (1999). The force coefficients are found as $C_i = 2F_i/\rho U^2 DL$ where, $i = d$ or l and F_d and F_l are the drag and lift forces, respectively. ρ is the air density, D is model diameter, L the model length and U the upstream undisturbed wind velocity.

2.2. Rain rivulet suppression

When examining the modified cable surfaces for rain rivulet suppression in the yawed static set-up, the reported flow conditions were correct for the upwind end of the cable model. All of the rivulet suppression tests were performed with the cable declining along the wind direction at a cable inclination angle of $40°$ and with a yaw angle of $\pm 22.5°$ (see Figure 2). In both cases the relative cable-wind angle was $45°$. For this, the 1.53 m modified cable sections from the force measurements were reused to make up the central part of this inclined yawed set-up. The remaining parts consisted of plain HDPE dummy tubing continuing to the walls. Water was only added in the top end of the combined inclined cable so both the upper and the lower rivulets were fully establish before reaching the modified section. The approach was initially compared for a plain cable with rain covering the full length of the cable model. In the case of uniform rain the rivulets started out smaller. Further down the cable, the rivulets forming were visually confirmed to be the same. Kick-starting the rivulet was therefore seen as a more conservative approach in the evaluation of the rivulet suppression of the modified cable surfaces. Furthermore, only adding water at the top allowed for the easy evaluation of the distance the rivulets could travel along the modified cable section before significant suppression. All the tests were repeated for both 8m/s and 14m/s wind velocity, corresponding to representative values for the upper and

the lower velocity range for RWIV.

2.3. Dynamic tests

To examine the dynamic performance of the innovations, the selected surface modifications were installed in a dynamic rig, identical to that used by Kleissl and Georgakis (2013). In this way the plain tubing tests could be reused as a reference case and a comparison with other applications could readily be made. A surface modified cable installed in the test rig, together with an illustrative sketch of the cable model are shown in Figure 2.
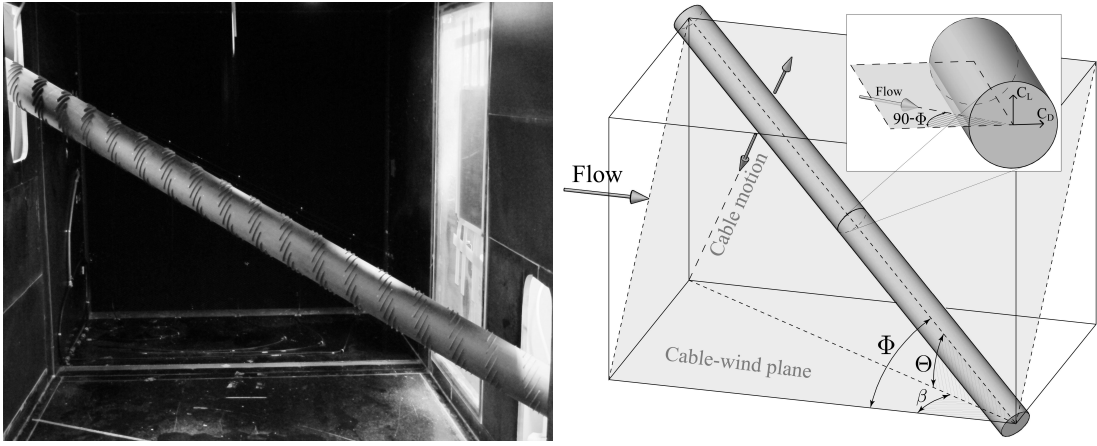

Figure 2: The cable section with staggered arranged strakes installed in the rig (left) and an illustration showing the arrangement of the cable models relative to oncoming wind, definition of angles and direction of cable motion (right).

The cable models were kept at a yaw angle $\beta = 60°$ and cable inclination $\Theta = 25°$. This corresponds to a relative cable-wind angle $\Phi = 63°$, where $\Phi = 90°$ corresponds to wind normal to the cable axis (see Figure 2).

The chosen angles match those where RWIVs were observed for the plain cable tubing. They also match the angles previously reported in literature (Cosentino et al., 2003; Flamand, 1995). With the selected angles, the effective cable model length was 2.55m. For the tested cable diameter of 160 mm, this gave an aspect ratio of 16. The test rig only allowed for in-plane cable motion (orthogonal motion within the cable-vertical plane) as indicated in Figure 2. The 1-DOF cable motion had previously been found sufficient for the reproduction of RWIV (Kleissl and Georgakis, 2013). The flow conditions were measured with a cobra probe at 9, 12 and 15 m/s wind velocity along the model axis. Exclusive of a 10 cm region from the wall openings, the flow was found uniform and with a turbulence intensity within $1.0 - 1.3$ %. The cable section model continued through rectangular wall openings (30×73cm) with rounded corners, which allowed for a maximum peak-to-peak displacement amplitude of 2.75 D. The size of the openings was kept at a minimum, so as to minimize undesirable end flow effects. The cable response normal to its axis was measure

using laser displacements transducers mounted outside of the flow. All tests were performed for 11 fixed velocities, with the distribution focussing on the expected range for RWIVs of $8 - 14\,\mathrm{m/s}$. The spray system consisted of five light spray/mist nozzles mounted upwind of the cable, along a projection line of the cable. Each nozzle was attached to the end of a 4 mm tube supported only by two piano wires, so as to minimize any turbulence introduced. The water used for the spray system was passed through a cleaning station to avoid the inclusion of surface tension influencing minerals. A constant water pressure of 4 bar, corresponding to 1.6 L/min, was used for all the reported tests. On bridges, it is generally believed that, due to sun exposure, dust accumulation, saline deposit, acid rain or atmospheric pollution, the HDPE surface will over time oxidise, erode and become more uneven, leading to a more wettable surface (Larose and Smitt, 1999; Flamand, 1995). To simulate this aging effect, the cable models were painted with Gohsenol, as proposed by Kleissl and Georgakis (2013), before the dynamic tests in wet conditions.

2.4. Models for dynamic testing

Two surface modifications were eventually selected for dynamic testing. The two selected modifications were reproduced on new HDPE tubes of the same type and long enough to pass outside the tunnel at both ends. The plain HDPE tubing used for these modifications was pre-sanded with a fine P400 grading to minimize the effect of localised surface imperfections which could affect the continuity or formation of rivulets.

The test model characteristics, such as mass, frequency and damping, are summarized in Table 1. The effective linear mass was found as the total model mass, including effective parts of spring masses, divided by the effective model length (2.55 m) inside the flow. The damping is given as damping ratio with the corresponding Scruton number defined according as:

$$S_c = \frac{m\,\zeta}{\rho\,D^2} \tag{1}$$

where m is mass of cable per unit length, ζ is the damping ratio, ρ air density, and D the cable diameter. All damping estimates were determined by fitting an exponential function to the amplitude decay/buildup, within an amplitude range of $40 - 120$mm, corresponding to $0.25 - 0.75 D$ for $D = 160$ mm.

The damping ratios matched the level of inherent structural damping in a real full-scale cable, typically in the order of $0.01 - 0.2\%$ (Gimsing and Georgakis, 2012).

3. Results and Discussion

3.1. Surface modifications

A selection of the surface modifications tested are shown in Figure 3. The code given to each modification is a combination of a letter assignment to a type of modification and a running index
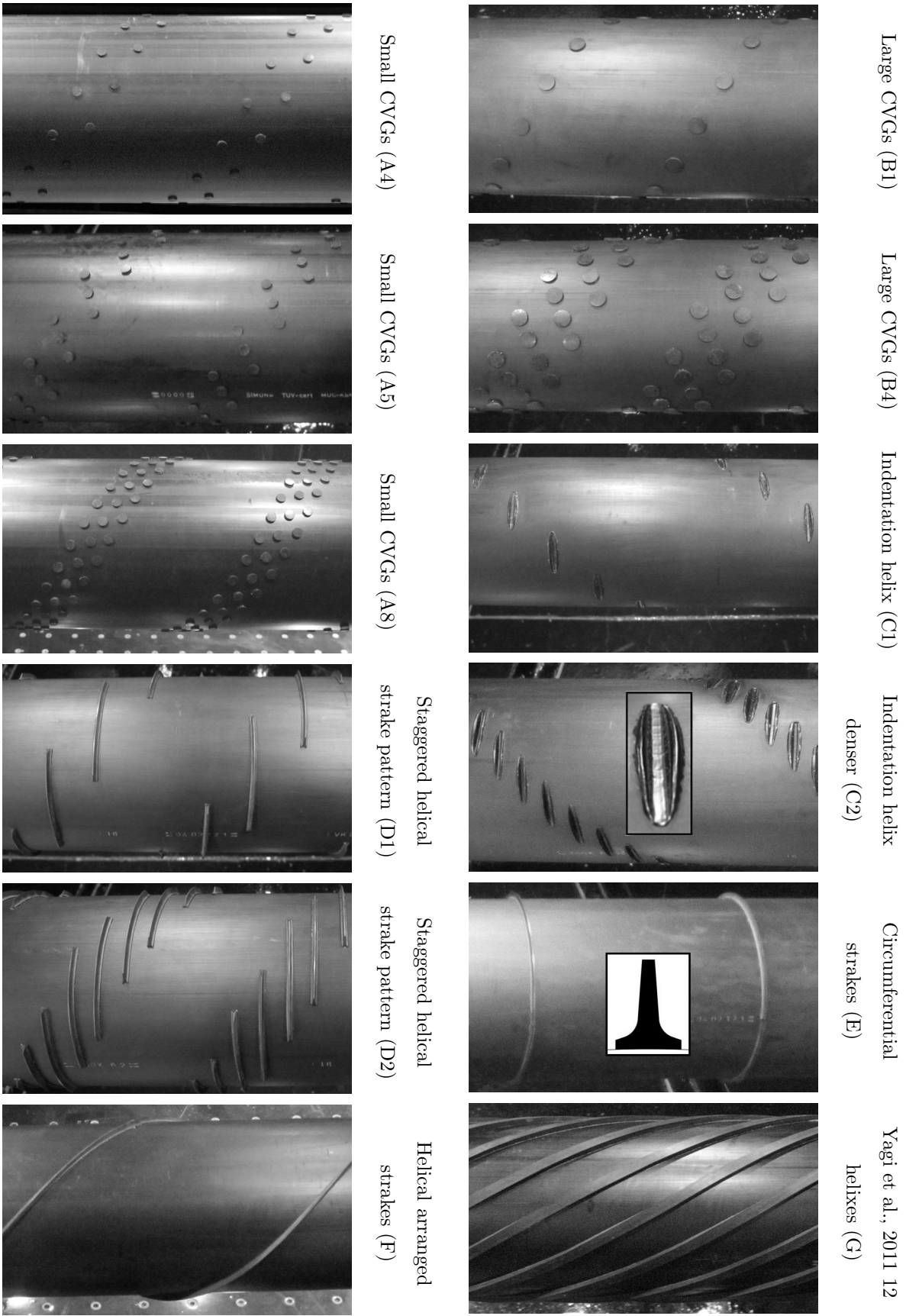
Figure 3: The various types of surface modifications tested.

Cable model:	Innovation 1	Innovation 2
Linear mass	18.3 kg/m	18.3 kg/m
Frequency	1.12 Hz	1.10 Hz
Damping ratio, ζ	0.10 %	0.11 %
Scruton no. [-]:	0.59	0.65

Table 1: This table summarizes the characteristics of the two dynamic cable test models.

number, specifying an increase in the number of add-ons and/or roughness. Therefore, letters A and B relate to the application of discrete sharp-edged cylindrical protrusions or Cylindrical Vortex Generators (CVGs) in various patterned distributions. The smaller CVGs (models A1-A8) had a height of 2 mm ($D/80$) and a diameter of 8 mm ($D/20$), whilst the larger ones (models B1-B4) had a diameter of 14 mm ($D/11$). The CVGs were selected so as to generate a localised increase in streamwise vorticity in the form of a pair of counter-rotating vortices. Through flow mixing, these enhance the near-wall streamwise momentum and thus delay the point of flow separation. A helical pattern with a 30° pitch was adopted, thus introducing waviness into the separation line along the cable axis and a wavy wake structure. This is known to disturb vortex shedding, whilst increasing base pressure. As the CVGs were not expected to sufficiently suppress rain rivulets, other modifications with the potential for drag reduction were developed, primarily with rivulet suppression in mind. The first of these modifications involved elongated channels (models C1-C2). Here, a thermal procedure was employed in the generation of the modification, which resulted in protruding lips on each side of the channels. Their streamlined shape cause a minimal form drag penalty. This was intentionally done, so as to increase the localised streamwise vorticity and introduce a wavy wake structure, whilst forming a barrier for rain rivulets running along the cable. The next three modifications (models D-F) all involve the application of protruding strakes. The strake cross-section has a triangular shape with concave sides and a height of 6 mm, corresponding to 3.75% of the cable diameter. The concave sides have two intended functions. Firstly, they work as a ramp for rain rivulets, forcing water to leave the surface of the cable. Secondly, the concave sides and the sharp tip lead to stronger directional guidance of the remaining water along the strake. In models D1-D2 the strakes were arranged laterally in a staggered helical pattern with a 30° pitch. This orientation leads to a minimum penalty to the form drag, whilst introducing a pair of counter-rotating streamwise vortices. On model E the strakes were positioned circumferentially around the cable at 1.25 D spacing along the cable. Model F replicates the typical fillet arrangement on current stay cables with helical fillets, leading to a double helix at a 45° pitch angle. Here though, there is a change of the cross-section of the filet, which is expected to enhance

the streamwise vorticity. Model G was originally proposed and tested by Yagi et al. (2010, 2011) and involves 12 rectangular protrusions (7.5 × 5 mm) that are placed in a helical pattern, so as to hinder the formation of water rivulets, whilst reducing the drag through the disruption of vortex shedding.

3.2. Static force coefficients

The mean drag and lift coefficients obtained for the models with CVGs are shown in Figure 4. For brevity, only the results for the modifications shown in Figure 3 are presented. Compared with the plain tubing, all of the models with CVGs experienced an earlier flow transition and a tendency for a near-constant drag coefficient in the supercritical region. With the appropriate number of CVGs, the flow transition occurred gradually and with a minimum of lift force appearing. At the same time, some of the tested modifications led to a rather low supercritical drag coefficient. The best performance was obtained with test model A5, shown in Figure 3. This model exhibited a near constant drag coefficient slope, resulting in a lift coefficient smaller than any of the currently applied surfaces. Throughout the tested supercritical Reynolds number range the drag coefficient remained below 0.59.
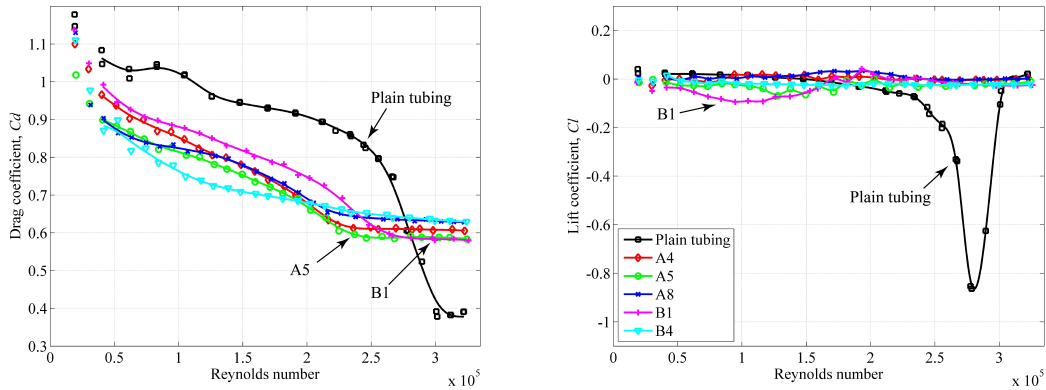
Figure 4: Mean static force coefficients for the tested surface modifications with CVG's. Drag coefficients (left) and lift coefficients (right).

The corresponding drag and lift coefficients for the remaining surface modified cable models, including the currently employed cables (Kleissl and Georgakis, 2012b), are shown in Figure 5. Amongst these, model D2 and F appear successful in generating a gradual flow transition and sustaining near-zero lift coefficients. The drag optimised staggered strake arrangement of model D2 reached a supercritical drag coefficient of 0.65, which was similar to that of the pattern-indented cable surface. While the drag performance of the helical strake arrangement of model F was similar to that of the currently applied cable with helical fillets, indicating that the increased streamwise vorticity from the sharp tip compensates for the form drag penalty due to the increased strake

8

height compared to the fillets. The reproduced cable surface with 12 rectangular helixes (G) resulted in a much larger drag coefficient than previously reported by Yagi et al. (2011) and was thus not further considered.
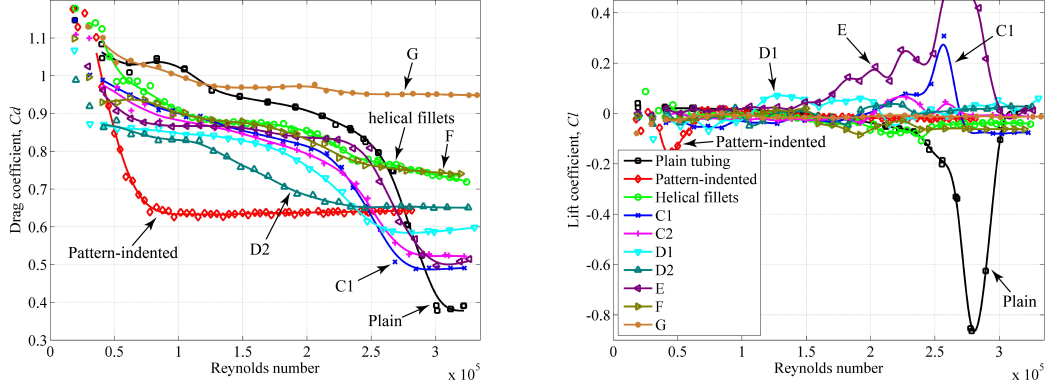
Figure 5: Mean static force coefficients for the tested surface modifications with indentations and strakes, compared with the currently applied cables having plain, pattern-indented, and helical fillets reproduced from Kleissl and Georgakis (2012b). Drag coefficients (left) and lift coefficients (right).

A comparison of the fluctuating lift force between the cable models was also made. With the test rig employed, the total RMS lift fluctuations could be evaluated. These are shown in Figure 6. Several of the tested models appear successful in generating small-scale vorticity, whilst avoiding any significant increase in lift force fluctuations. Among the models with CVGs, the smaller CVGs seem to perform well in this respect, with A5 having the optimal combination of low drag and fluctuating lift. Model F exhibited the lowest level of lift fluctuations, whilst model D2 and the traditional helical fillets also performed well. Amongst the largest fluctuations observed was the currently applied pattern-indented surface, with the lift experiencing a significant peak around $Re \approx 1.76 \times 10^5$.

3.3. Rivulet suppression

Preliminary static tests with the plain cable installed showed that a lower rain rivulet formed for all tested wind velocities, while an upper rivulet only formed within the range of approximately $7-15$ m/s. Outside this range, the upper rivulet did not form, as either gravity or the wind loading became dominant. As RWIVs typically occur within this velocity range, the presence of the upper rivulet is often considered critical for the generation of vibrations. Both the upper and lower rain rivulets on the plain cable can be seen in Figure 7.

Figure 8 (left) shows the cable model A8 with small CVGs and an upper rain rivulet, that still forms despite the small protrusions. While the rivulet has a strong presence, it also becomes slightly wavy as the CVGs tend to attract the water. Further optimization of the CVG positioning

9
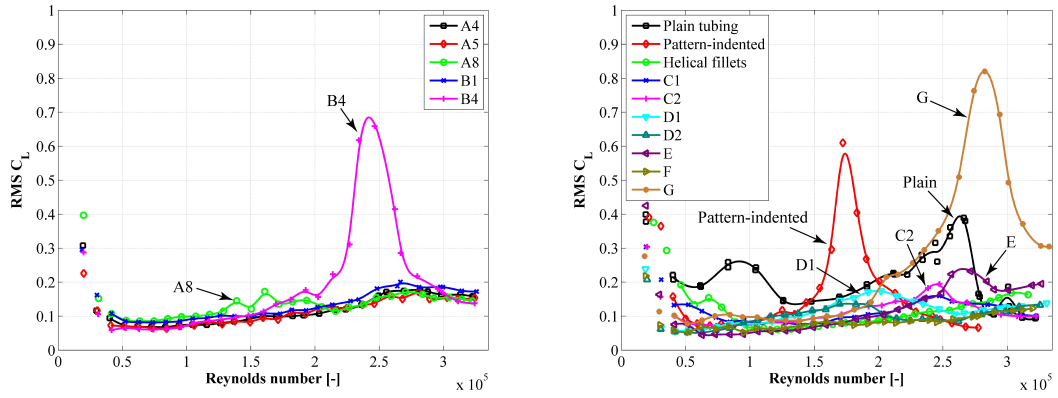
Figure 6: RMS values for the static lift force coefficients. Surface modified models with CVGs (left) and remaining surface modified models (right), including currently applied cables reproduced from Kleissl and Georgakis (2012a). Drag coefficients (left) and lift coefficients (right).
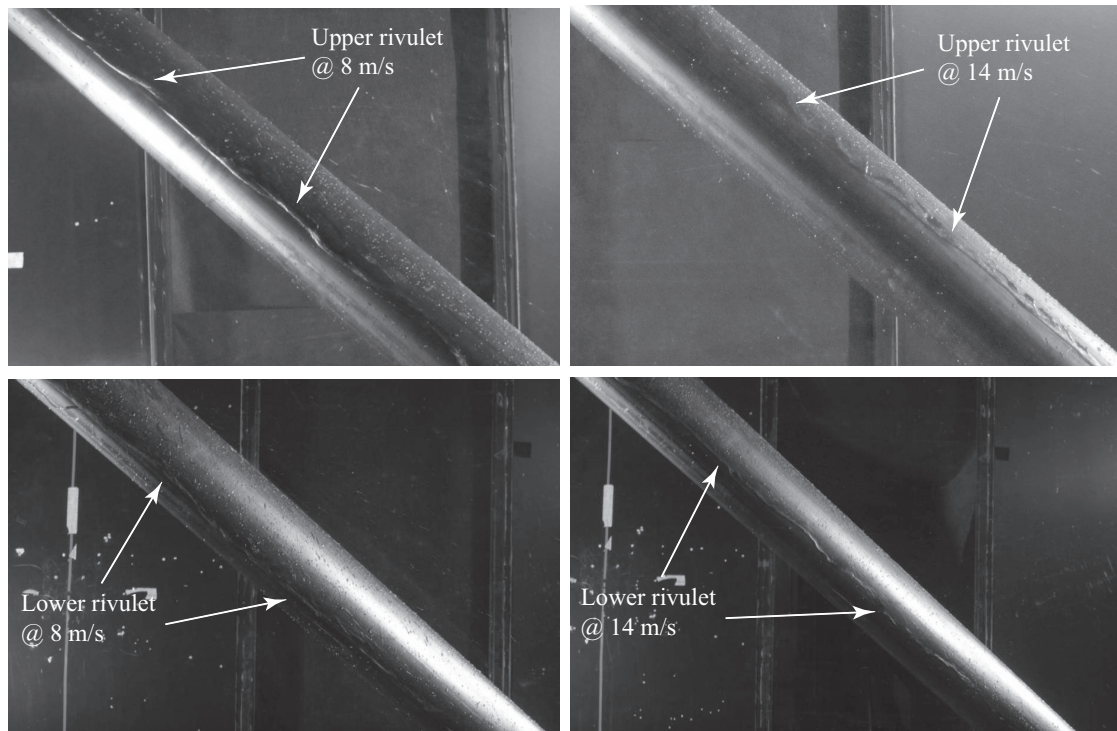
Figure 7: Plain tubing showing a strong presence of rain rivulets at different velocities. Upper rivulet at 8 m/s (top-left), upper rivulet at 14 m/s (top-right), lower rivulet at 8 m/s (bottom-left), lower rivulet at 14 m/s (bottom-right).
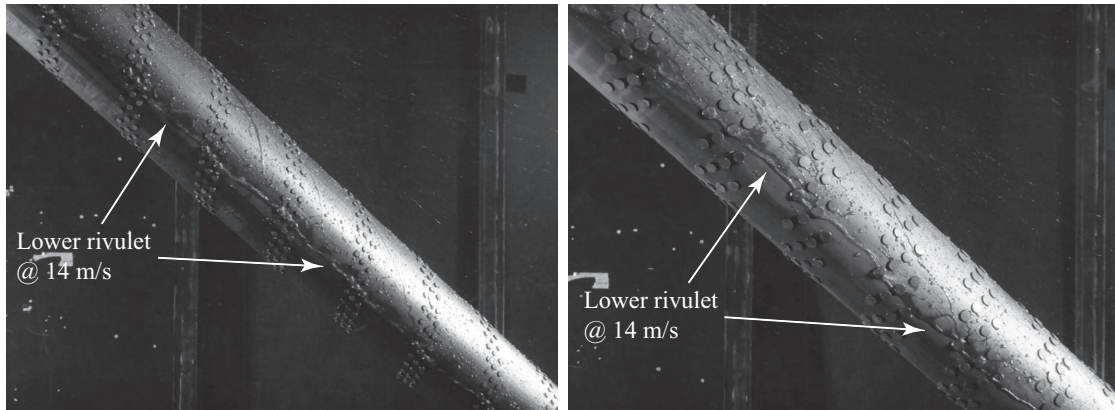
Figure 8: Model A8 with small CVGs (left) and model B4 with larger CVGs (right). Lower rivulet at 14 m/s.

could enhance this disturbance in the path of the rivulet and possibly make it even more wavy. A similar observation was made for the cable model B4 with the larger CVGs shown in Figure 8 (right). The CVGs attract the rivulet when it was near and thus reposition it until it leaves the helical area with modifications, whereafter it returns to its original position. Generally both sizes of CVGs introduces a disturbance in the rivulets, but none of them were capable of hindering their formation.

Photos of rivulets on the modified cable models C2 and model E are shown in Figure 9. The
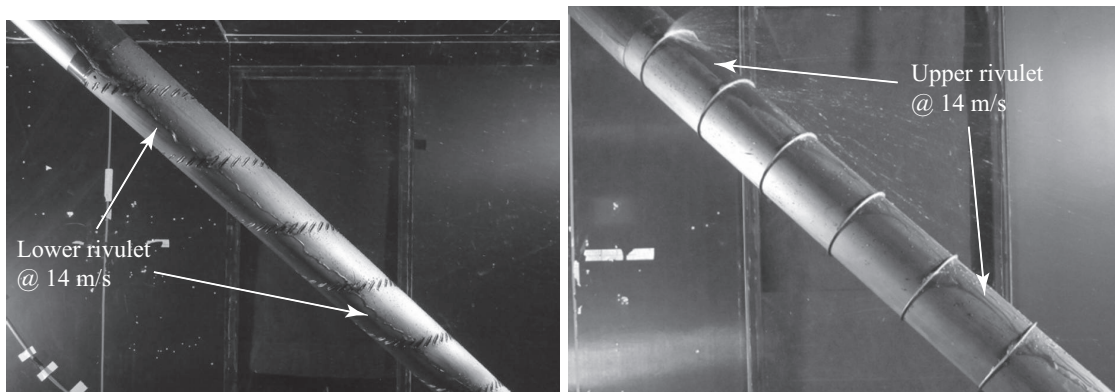
Figure 9: Lower rivulet forming on model C2 at 14 m/s (left) and model E with a weak upper rivulet at 14 m/s (right).

elongated indentations with protruding lips on the C2 model was not able to hinder the rivulet which crossed over them with ease. This type of surface modification was therefore found the least effective in suppressing rivulets, with the modifications having to be more significant if they are to have an effect. Cable model E, with circumferentially arranged strakes, did cause a weakening of the upper rivulet. Although some of the water was "knocked off" of the surface when a large rivulet tried to cross it, the strake arrangement failed to guide the remaining rivulet away from

the point of balance, were the upper rivulet is stable. The circumferential strakes were therefore only found effective in reducing the size of the rivulet, but incapable of removing it completely.

Figure 10 shows the upper and lower rivulets on cable model F with helical strakes. Both
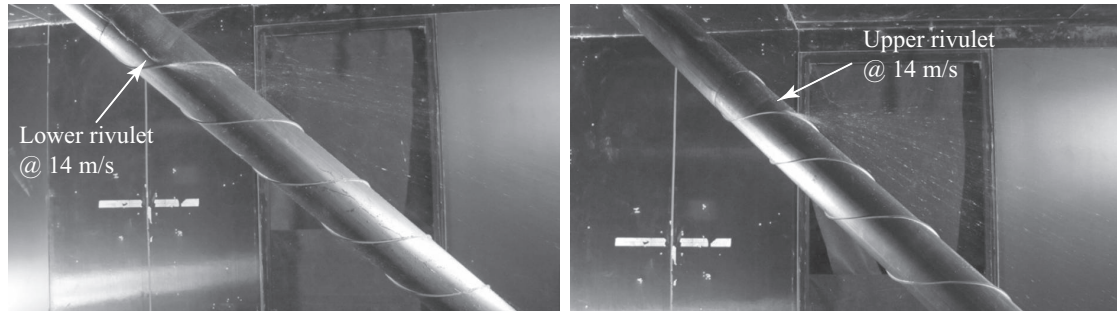
Figure 10: Model F with helical strakes completely suppressing the rivulets. Lower rivulet at 14 m/s (left) and upper rivulet at 14 m/s (right).

rivulets are completely suppressed by the strakes and no sign of the rivulets is visible at the lower part of the cable model. Similar observations were made at 8 m/s and when the sign of the yaw angle was changed, which effectively corresponds to a change in the pitch direction of the helixes. In all tested cases, the helical strakes were found successful in preventing rivulets from traveling along the cable model by "ramping" the rivulet off the cable surface.

The same ramping effect was also present on cable model D2 with the staggered arranged strakes shown in Figure 11. Neither the upper nor the lower rivulets could form during either
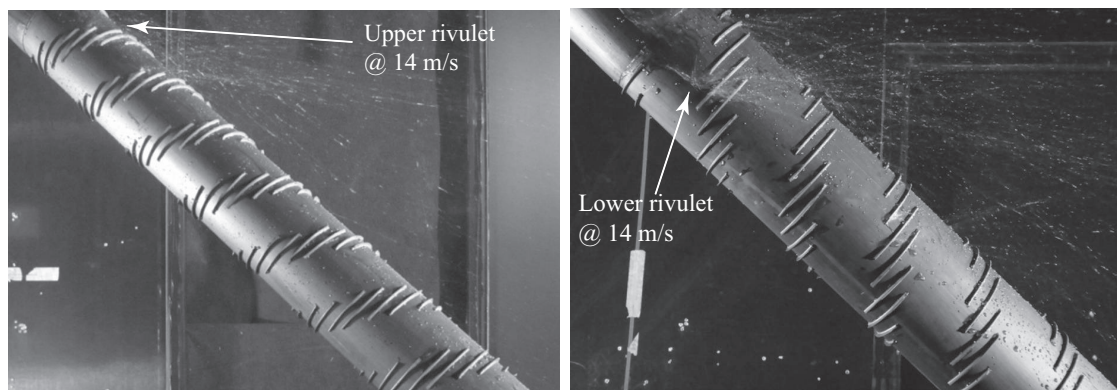
Figure 11: Model D2 completely suppressing the rivulets at all tested angles. Upper rivulet at 14 m/s (left) and lower rivulet at 14 m/s (right).

8 m/s or 14 m/s wind velocity. This surface modification, together with model F, were therefore found as the most effective surfaces in suppressing water rivulets.

For reference, an actual cable tubing sample of the currently applied helical fillets was tested under the same conditions. The cable sample also had an outer diameter of 160 mm and was equipped with a relatively large fillet height of 4 mm. To the authors' knowledge, this fillet is

amongst the largest currently applied on bridges. Figure 12 shows how both a lower and upper rivulet could form despite the fillets' presence. For the opposite sign yaw, the fillets were capable of
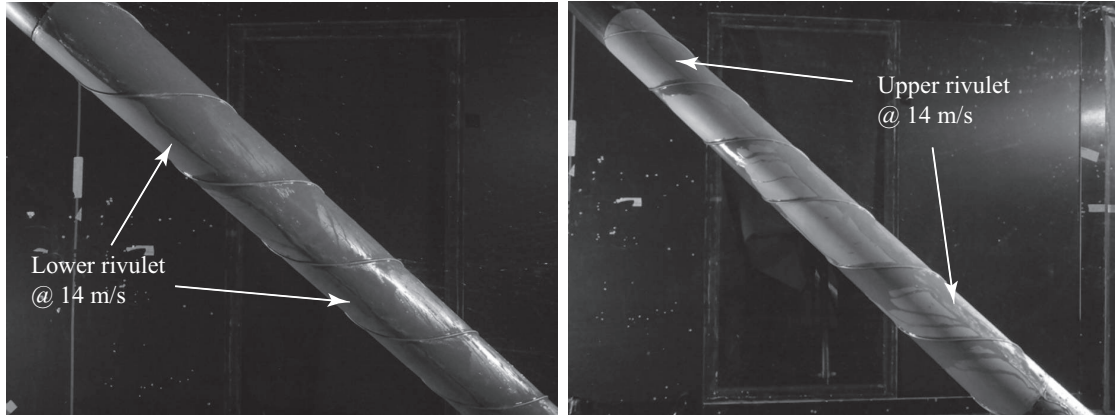
Figure 12: Currently applied cable surface with helical fillets. Strong presence of the lower rivulet at 14 m/s (left) and the upper rivulet at 14 m/s (right).

guiding the upper rivulet down so it joined the lower one, and in this way, prevented the presence of one of the rivulets. For the most part, though, the surface was only found capable of marginally disturbing the rivulets and was clearly outperformed in this respect by models D2 and F.

3.4. Aerodynamic stability

A series of dynamic tests were performed in both dry and wet conditions. Each of the dry tests were carried out together with the corresponding wet test to guarantee matching conditions, such as spring alignment, flow conditions, model position and model rotation. This also involved retaining the rain spray system in place, upwind of the cable models.

It is hypothesized that, whilst rivulet disturbance or repositioning can reduce the risk of RWIV, the complete removal of the rivulet will totally eliminate the mechanism leading to RWIV. Therefore, two surface modifications, one with helical concave strakes (model F) and one with the staggered arranged strakes (model D2), were selected for further testing in the dynamic test set-up. The two modifications will be referred to henceforth as Innovation 1 and Innovation 2, respectively.

3.4.1. Innovation 1 - Helical concave strakes

The results from the dynamic tests of Innovation 1 subjected to rain are shown in Figure 13. On the left, the maximum peak-to-peak cable model vibration amplitude is shown as a function of wind velocity. It was found that no vibration incidences occurred for the full velocity range where RWIV is usually observed, or beyond. On the right, the total and aerodynamic damping are shown. At no point did the aerodynamic damping approach zero or negative values. The
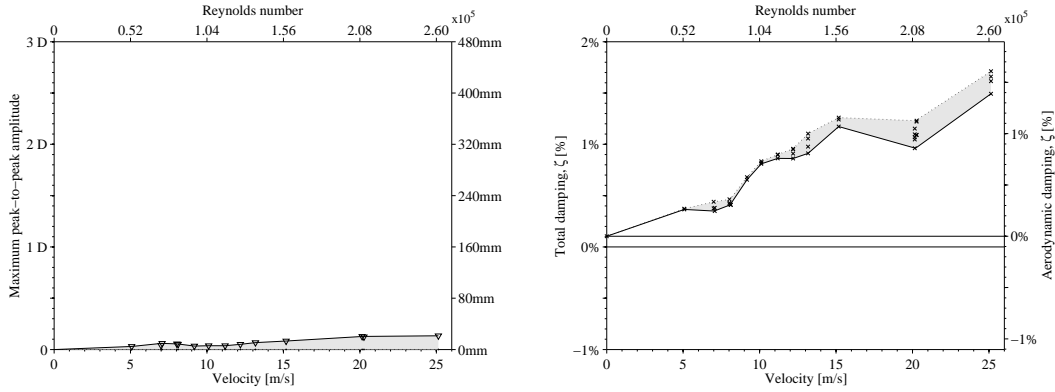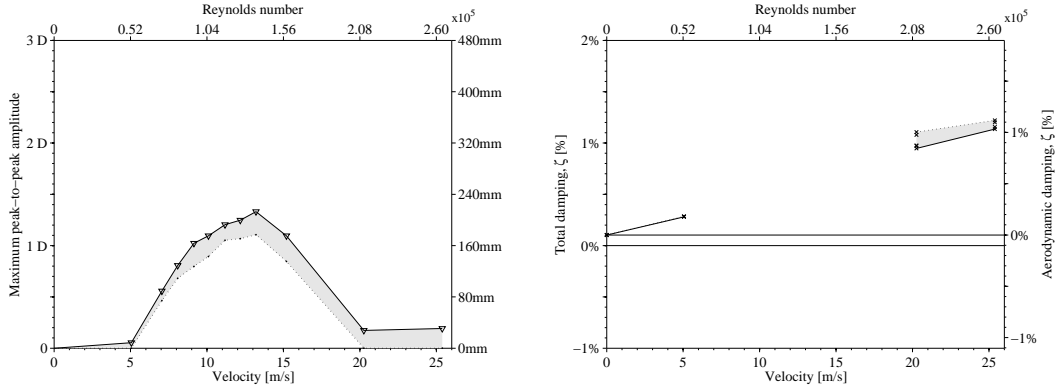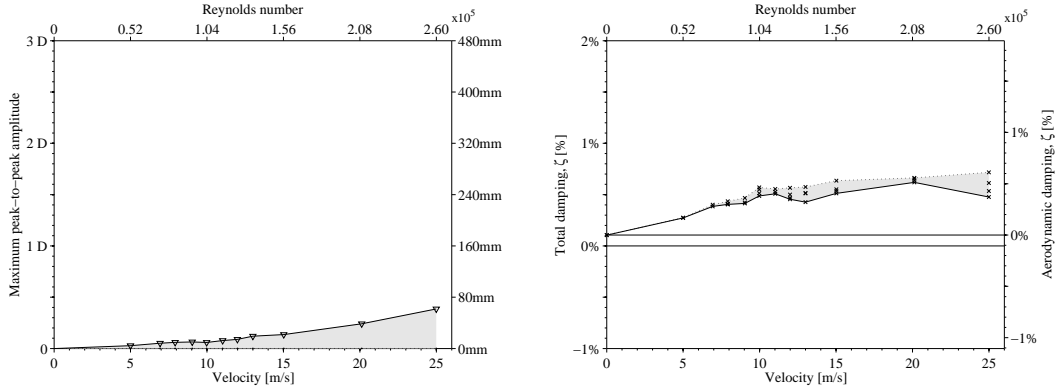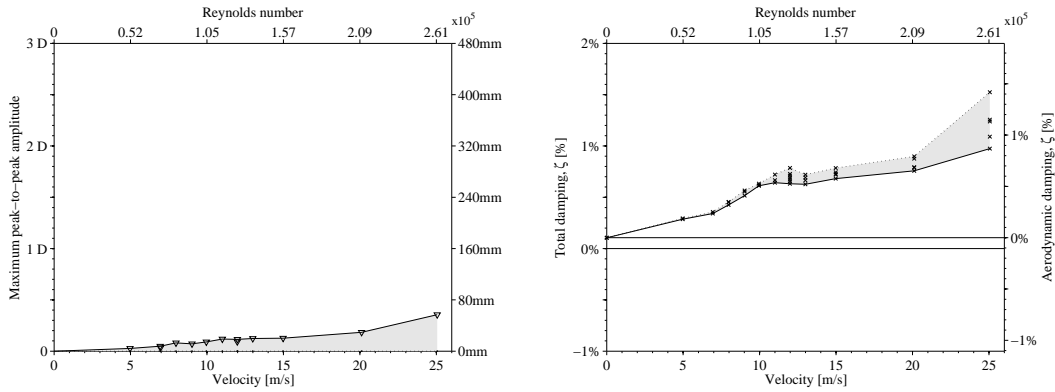
Figure 13: Cable model with helical concave strakes (Innovation 1) in wet conditions. Maximum in-plane peak-to-peak model amplitude (Left) and measured damping ratios (right).

aerodynamic damping was determined by measuring the total damping through free-decay tests for each of the considered velocities and then by subtracting the structural damping which was assumed to correspond to the damping at zero wind velocity.

For the same test during dry conditions, the results are shown in Figure 14. Here the cable

Figure 14: Cable model with helical concave strakes (Innovation 1) in dry conditions. Maximum in-plane peak-to-peak model amplitude (Left) and measured damping ratios (right).

surface with helical strakes was observed to experience a steady state vibration, where the amplitudes remained within a limited amplitude range for several minutes or longer, between the wind velocities of $7 - 15$ m/s. The amplitudes observed were well beyond the range of the expected buffeting response. The vibrations observed were more in-line with the flow transition induced vibration (FTIV) that has also previously been observed for cable models with helical fillets (Kleissl and Georgakis, 2013). The corresponding aerodynamic damping is shown on the right. During the presence of dry vibrations the damping could not be determined, as the process was not sufficiently stationary. Thus, this region has been excluded from the plot.

3.4.2. Innovation 2 - Staggered concave strakes

The maximum vibration amplitudes and damping during the dynamic testing, as determined for Innovation 2 when subjected to rain, are shown in Figure 15. No RWIV was observed and only

Figure 15: Cable model with staggered concave strakes (Innovation 2) in wet conditions. Maximum in-plane peak-to-peak model amplitude (Left) and measured damping ratios (right).

a slow increase in maximum amplitude was found with increasing wind velocity. The aerodynamic damping also remained above zero for all of the tested wind velocities.

Figure 16 Shows the corresponding dry test results. The maximum amplitude is similar to

Figure 16: Cable model with staggered concave strakes (Innovation 2) in dry conditions. Maximum in-plane peak-to-peak model amplitude (Left) and measured damping ratios (right).

what was observed during simulated rain, while the aerodynamic damping was found a bit higher.

3.5. Comparison

Kleissl and Georgakis (2013) presented similar findings for a selection of the currently applied cable surfaces. A comparison with the present findings is shown in Figure 17. From this comparison it is clear that only the plain cable tubing experienced significant RWIV. Neither the present innovative modifications nor the currently applied surfaces experience any significant RWIV. This,
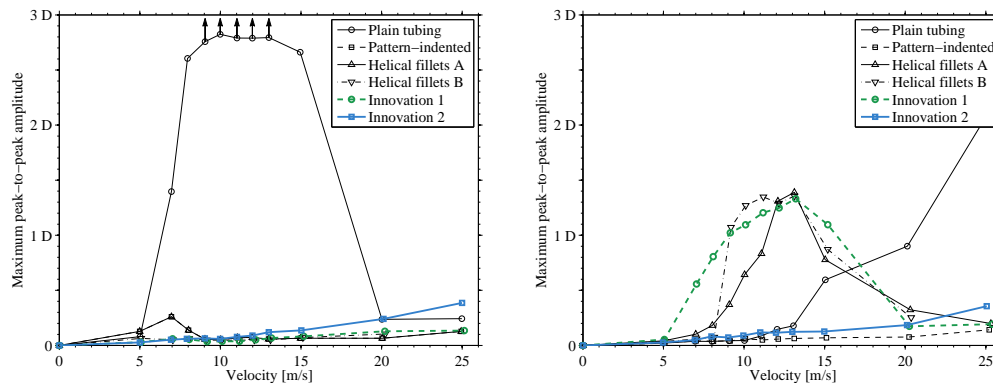
Figure 17: Comparison of the maximum in-plane peak-to-peak cable model vibration amplitudes measured in the present study with previous measurements for existing applications (Kleissl and Georgakis, 2013). In wet conditions (left) and in dry conditions (right).

though, may not be the case for other relative cable wind angles, as the presence of the rain rivulets on all of the models, excluding the new innovations, might lead to some level of vibration, in line with what has been visually observed on existing bridges.

In dry conditions, a general trend appears for all the cable surfaces with helical applications, which from the flow direction appear asymmetric. Innovation 2, with the staggered concave strakes is an exception here. While its overall helical pattern leads to an asymmetric appearance, all of the strakes have the same angle in relation to the flow on each side. This alone was found sufficient for the avoidance of dry limited amplitude FTIV. Finally it was seen that the buffeting response of the staggered strakes at 25 m/s wind velocity was, in both dry and wet conditions, near 0.4 D.

4. Concluding remarks

Several novel and one previously proposed cable surface modification were wind tunnel tested for the determination of aerodynamic force coefficients and rain rivulet suppression. Two of the proposed surface modifications were found to outperform or match the current cables with helical fillets, both in terms of drag reduction and rivulet suppression. Most of the other proposed modifications were unable to do both. While one of these newly proposed surfaces had a similar drag coefficient to that of an existing helically filleted cable, the other outperformed it, with a drag coefficient of only 0.65. This is similar to what is found for a cable with a pattern-indented surface. Neither of the two new innovative surfaces were found to suffer from RWIV when tested dynamically. In dry conditions one of the innovations with helically arranged strakes was observed to experience the same limited amplitude FTIV as observed for other cables with helical fillets. The innovative cable with staggered concave strakes was dynamically stable under all conditions.

Acknowledgements

5. References

Cooper, K., Mercke, E., Wiedemann, J., jun 1999. Improved blockage corrections for bluff-bodies in closed and open wind tunnels. In: 10th International Conference Wind Engineering, Copenhagen. pp. 1627–1634.

Cosentino, N., Flamand, O., Ceccoli, C., 2003. Rain-wind induced vibration of inclined stay cables. part 1: Experimental investigation and physical explanation. Wind and Structures 6 (6), 471–484.

Flamand, O., 1995. Rain-wind induced vibration of cables. Journal of Wind Engineering and Industrial Aerodynamics 57 (2-3), 353 – 362.

Georgakis, C. T., Koss, H. H., Ricciardelli, F., Sep 2009. Design specifications for a novel climatic wind tunnel for the testing of structural cables. In: 8th International Symposium on Cable Dynamics, Paris, France. pp. 333–340.

Gimsing, N. J., Georgakis, C. T., 2012. Cable Supported Bridges: Concept and Design, 3rd Edition. John Wiley & Sons Ltd.

Kleissl, K., Georgakis, C., 2012a. Comparison of several innovative bridge cable surface modifications. In: Proceedings of The 7th International Colloquium on Bluff Body Aerodynamics & Applications, Shanghai, China.

Kleissl, K., Georgakis, C., 2012b. Comparison of the aerodynamics of bridge cables with helical fillets and a pattern-indented surface. Journal of Wind Engineering and Industrial Aerodynamics 104 - 106 (0), 166 – 175.
URL http://www.sciencedirect.com/science/article/pii/S0167610512000554

Kleissl, K., Georgakis, C., 2013. Comparison of the aerodynamic stability of bridge cables with a smooth surface, helical fillets and a pattern-indentation. Submitted for Journal of Wind Engineering and Industrial Aerodynamics.

Larose, G., Smitt, L. W., Jun 1999. Rain/wind induced vibrations of parallel stay cables. In: Proceedings of the IABSE Conference, Cable-Stayed Bridges - Past, Present and Future, Malmo, Sweden.

Yagi, T., Okamoto, K., Sakaki, I., Koroyasu, H., Liang, Z., Narita, S., Shirato, H., Jul 2011. Modification of surface configurations of stay cables for drag force reduction and aerodynamic stabilization. In: Proc. of the 13th International Conference on Wind Engineering, Amsterdam.

Yagi, T., Okamoto, K., Sskski, I., Koroyasu, H., Liang, Z., Narita, S., Shirato, H., Dec 2010. Drag force reduction and aeerodynamic stabilization of stay cables by modfying surface configlations. In: The 21th Symposium on Wind Engineering, Tokyo, Japan. In Japanese.

Chapter 7

Conclusion

In the present thesis, passive aerodynamic means for stay cables have been extensively studied in relation to vibration mitigation and drag performance.

Firstly, the present knowledge and findings relevant for surface or shape modifications on stay cables has been summarized in the literature review, together with a successful categorization of the various modifications based on the control technic applied. The four classifications introduced are: (a) direct transition to turbulence by using a boundary-layer instability, (b) early separation and reattachment by the use of a shear-layer instability, (c) wake dephasing and 3-D disturbance by the generation of three-dimensional wake structures, and (d) outer-layer-devices affecting the entrainment layers. Moreover, the literature study identified two important and advantageous key mechanisms for maintaining a low drag force within the supercritical flow regime, based on delaying or disturbing supercritical vortex shedding. This involves the minimization and increase of the spanwise and streamwise boundary layer vorticity, respectively, whilst introducing three-dimensional wake structures by having spanwise variations.

Secondly, a detailed wind tunnel investigation and comparison of cables with helical fillets and pattern-indented surfaces was completed, where several verifications and new findings were made. The drag measurements for the pattern-indented cable model agreed with previous reports and confirmed the presence of an early flow transition and thus a drop in drag coefficient followed by a near constant supercritical drag coefficient. This beneficial feature of maintaining a low supercritical drag coefficient is explained as a result of the unique dimples with protruding periphery introducing a high intensity of streamwise vorticity. In contrast with the pattern-indented surface, the drag coefficient development of the cable with helical fillets was found to have a smooth and gradual drop in the critical Reynolds number regime, which is believed to be the result of the spanwise surface variations provoking

flow transition to occur at different wind velocity at different spanwise positions. Determination of the drag coefficient would therefore have to consider the average force over a certain spanwise distance of the cable to obtain a proper estimate. Furthermore, the drag performance of the cables with helical fillets was found very dependent on the fillet size to cable diameter ratio, which is currently not maintained for varying cable diameters. Individual drag measurements will therefore be needed for each of the different cable sizes. When the cable models were positioned in a yawed inclined configuration, the critical Reynolds numbers was found to behave counter-intuitively in relation to the cable-wind angle. The "cosine rule" or independence principle may therefore not be applied on cylinders with surface modifications for the determination of the critical Reynolds number in skew wind. The axial flow forming on the leeward side of skew cables was found through flow visualization to be unaffected by the pattern-indented surface while significantly reduced by the helical fillets. Though despite the presence of axial flow behind the pattern-indented cable, it did not trigger neither RWIV nor dry inclined galloping, which were both observed for the plain cable model. It is therefore unclear if the axial flow has any negative affect on stay cables in relation to this mechanism. The straight alignment of discrete areas of roughness on the pattern-indented surface was also found to introduce a wind-angle of attack dependency sufficient to trigger the Den Hartog galloping criteria. While this affected the level of aerodynamic damping, it was not severe enough to result in any vibrations. During simulation of RWIV on the plain cable model several different surface treatments of the HDPE were compared and the resulting level of surface energy was found essential, as the phenomenon would only occur when the surface allowed for lateral oscillations of the rivulets. Under similar conditions neither of the two currently prevailing systems were found to suffer from severe RWIV, despite the presence of both upper and lower water rivulets. But with the rivulets still present on the cable surfaces it is difficult to rule out the existence of another configuration where RWIV could occur. While avoiding RWIV, both types of helical filleted cable models experienced a previously unreported limited amplitude Flow-Transition Induced Vibration (FTIV) under dry conditions. The vibration is believed to be a result of the asymmetric appearance of the helical applications under skew wind, which during flow transition leads to a sudden significant change in the non-zero lift coefficient.

Finally, the understanding from the literature review and the experience with the currently applied solutions was used to propose a selection of enhanced applications, of which three were found with superior properties.

- A discrete helical pattern of CVGs (Cylindrical Vortex Generators) pro-

viding both high streamwise vorticity and spanwise variation resulting in an exceptional low supercritical drag coefficient of only 0.58. But this excellent dry performer was found incapable of completely preventing the water rivulets and can therefore not guarantee avoidance of RWIV.

- An optimized helical fillet where the fillet cross-section is replaced by a "mini-strake" having a triangular shape with concave sides. These successfully hindered the water rivulets as they form a ramp forcing the water rivulets to leave the surface of the cable, together with a stronger directional guidance of the remaining water along the helix. While the sharp tip enhance the streamwise vorticity, the height give rise to a drag penalty resulting in a supercritical drag coefficient near 0.7 comparable to the cable with helical fillets.

- An even further optimized version of the above, also using "mini-strakes" but in a new innovative staggered helical arrangement still preventing the water rivulets but also reducing the supercritical drag coefficient to 0.65 comparable to the pattern-indented surface.

With a complete removal of the water rivulets from the cable surface the continuously present risk of RWIV has been eliminated. As a result of these findings two patent applications have been filed (Georgakis and Kleissl, 2012); one covering the enhanced cross-sectional shape of the helix and one covering the new staggered helical arrangement.

7.1 Future work

A vast list of further investigations originates from the present study and surely more will appear in the future. But the most significant are elaborated on in this section.

Further testing and optimization of the proposed innovations

The present work has presented some promising candidates with some most attractive properties, though no optimization of these surface modifications were done and many geometric parameters were defined trough availability, intuition, and experience. Further development and optimization of the proposed innovations should therefore be done to fully utilize these findings. Due to the superior prevention of rivulet formation, one such optimization could be to lower the strake height to a minimum still providing sufficient

suppression of rivulets. This would reduce the device form drag penalty and may therefore provide even further reduction of the drag coefficient.

Further tests looking at the overall performance of these newly proposed innovative surface modifications including e.g. the performance during ice accretion should also be carried out.

Understanding the FTIV observed for dry inclined cables with helical windings

Two tube samples currently applied by cable manufactures were found to suffer from a previously unreported type of vibration. A possible explanation, related to the asymmetric performance of helical surface modifications in skew wind, has been given though further clarification is certainly needed to make sure this is not something also occurring on the bridges. Imperfect flow conditions near the wall openings and a possible shear layer instability interfering with the model were ruled out by varying the model frequency and mass. One thing could be the presence of minor localized increase in turbulence generated from the upwind spray system. This may trigger a position dependent flow state which combined with the asymmetric performance of the cable surface could lead to amplitude dependent lift force and thus a risk of vibrations occurring.

Energy state of the HDPE cable surface

During the present experimental work under wet conditions it became clear that changes to the surface energy of the HDPE surface of the cable model or the surface tension of the water had a tremendous effect on the appearance, maximum amplitude, and rate of growth for the RWIV phenomenon. It is therefore a most essential parameter which deserves further attention. Several questions could be raised, such as:

- Could there be a relation between the presence of RWIV and the nearby environment of a bridge?

- What levels of surface energy and rain water surface tension are realistic to have at the bridge location?

- Could the cable tubing or the material be treated and changed in such a way that critical conditions would never occur?

On site measurements and better documentation of this parameter during wind tunnel studies are needed to further understand its effect.

Bibliography

Christos T. Georgakis and Kenneth Kleissl. A cable or stay comprising one or more strakes, 2012. Patent application number 12174089.8 and 12174090.6.

Y. Hikami. Rain vibrations of cables of cable-stayed bridges. *Journal of Japan Association of Wind Engineering*, 27:17–28, 1986. In Japanese.

Kenneth Kleissl. Vibration control of bridge cables. Master's thesis, DTU Byg, DTU, Building 118, Brovej, 2800 Kgs. Lyngby, Denmark, Aug 2009.

Appendix A

Appended Conference Papers

This appendix contains conference papers prepared and presented during this work in chronological order for easy access.

Paper VI

"Bridge ice accretion and de- and anti-icing systems: A review"

K. Kleissl & C.T. Georgakis

Bridge ice accretion and de- and anti-icing systems: A review

K. Kleissl, C.T. Georgakis

Department of Civil Engineering, Technical University of Denmark
Building 118, Brovej, 2800 Kgs. Lyngby, Denmark

Abstract

Blocks of ice or snow falling from bridge members can cause accidents, damages on passing vehicles, and reduced security and human safety. The lack of a successful de- or anti-icing system results in traffic hindrance and bridge closure which causes severe financial losses. This paper presents a review of the different de- and anti-icing techniques, already developed and in development, which could be applied to bridge cables or pylons. Also the fundamentals of ice accretion and the basic principles of icing caused by freezing precipitation and in-cloud icing are presented together with the physical mechanisms expected to induce ice shedding.

1 Introduction

Atmospheric icing causes severe financial losses and reduced security and human safety. With the potential risk of falling chunks of ice frightening or hitting vehicles passing when temperature rises, traffic safety at the bridge is not secured until the removal of accreted ice is finished.

All traffic on the bridge has to be suspended until the snow removal operation is completed. The Great Belt Bridge have over a 3-year period (2004-2007) been closed for 12 hours per year because of falling ice, which compared to a total yearly average of 14.3 closed hours is quite significant (Vincentsen, 2006). Also the Øresund Bridge had to close 5 times during the last 9 years and a range of other Scandinavian bridges such as Uddevalla Bridge in Sweden and both the Severn Bridges had suffered from similar experiences (BBC News, 2009).

To secure traffic safety on the bridge and to reduce long bridge closures, it is important to develop novel measures against ice accretion to mitigate the risk of falling ice. Thus a literature study of existing de- and anti-icing techniques within the fields of bridges, wind turbines, airplanes and power lines have been carried out and those with potential use on bridges are then reviewed in this paper. The paper mainly focuses on the cable supported type of bridges and uses the large bridges of Denmark as a benchmark.

Also the fundamentals of ice accretion and the basic principles of icing caused by freezing precipitation and in-cloud icing are presented together with the physical mechanisms expected to induce ice shedding.

2 Generally on Ice Accretion

Having high humidity combined with frequent changes between passing cold and warm fronts results in a high risk of atmospheric icing. The Icing conditions are typically with very high humidity, temperatures slightly below freezing, mild to mediocre wind speeds, and with the icing mostly appearing on bridge members more than 150 m above water level. Also the

1

duration of the icing event can be quite an important parameter for the development of the ice accretion.

2.1 Fundamentals of icing

When natural ice forms on structures the source may either be cloud droplets (fog), raindrops, snow or water vapour. These results in three types of icing: In-cloud icing, precipitation icing, and hoar frost, where hoar frost is a direct phase transition of water vapour and is usually negligible (Makkonen, 2000).

In-cloud icing can form through both a dry and a wet growth process. The most common type is dry growth which is when there is no liquid layer and the resulting ice is called rime. Rime often forms on the windward side of the structure and entraps air which lowers its density. The wet growth is when the freezing takes places beneath a liquid layer on the surface of the accretion and the resulting ice is called glaze. Glaze is the type of ice having the highest density and normally causes a smooth evenly distributed ice accretion, though it may also result in formation of icicles.

Also freezing rain results in formation of glaze and is when warm air aloft melts snow crystals which afterwards falls through a freezing air layer near the ground (Fikke et al., 2007) or in the case of a rapid air temperature rise where the temperature of the structure is still below freezing. The other type of precipitation icing is wet snow, which is partly melted snow crystals (0-3°C) adhering to the surface of the structure and when followed by a temperature decrease the snow will freeze.
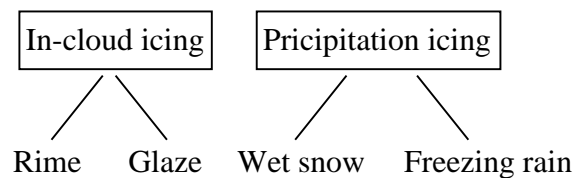
Figure 1: The different types of icing.

2.2 Ice shedding phenomena

Chunks of accreted ice falls from bridge members when their weight increases a critical limit or when the temperature rises.

There exist three physical mechanisms which induce ice shedding: ice melting, ice sublimation, and mechanical ice breaking (Druez et al., 1995).

- In the case of ice melting, the principal characteristic is the air temperature which has to be above 0°C. When melting occurs at the cable-ice interface, ice chunks start falling as a result of wind and gravity forces.

- The sublimation phenomenon occurs at the ice-air interface and is a rather low rate of ice mass reduction.

- Ice shedding by mechanical breaking is produced by a complex adhesive or cohesive failure.

3   Counter Measure Systems

Most ice prevention methods can generally be classified into two types of categories: Active and passive methods. Where the active protection systems requires an external energy supply while passive methods only needs the natural forces such as wind, gravity, incidental radiation, and temperature variations.

Another way to distinguish the counter measure systems are according to when and how they work. A de-icing system removes the ice from the surface after its formation while anti-icing prevents the initiation of icing.

There have over the years been developed various ideas and designs for different de- and anti-icing techniques, most of which are listed in reviews such as (Laforte et al., 1998; Farzaneh et al., 2008; Dalili et al., 2009). The counter measure techniques identified can be classified as:

- Mechanical methods based on the breaking down of the ice.

- Thermal methods based on the melting of the ice.

- Passive methods based on natural forces.

The preferable solution would be a passive anti-icing application, but as along such solutions are unsuccessful, de-icing methods have to be considered. Among these the mechanical methods were demonstrated by (Laforte et al., 1998) to require around 100 times less energy than thermal methods to force ice shedding.

3.1   Mechanical removal

So far as a de-icing counter measure, the ice is removed manually, requiring closing down the bridge traffic completely. The manual removal is done my physically breaking off the icing. For manual snow removal, workers have to be lifted in a crane gondola (main towers) or walk on the cables. However, the work conducted in these heights cannot be secured on days with snowfall or strong winds, which delays the commencement of snow removal.

Another method is by using forced vibrations of the cables to break the ice loose. The disadvantage is that thin layers of ice can adhere quite strongly to the surface and may not be brittle enough. Also an alternative removal approach, though only working for clearing the hangers, is to hit the hangers with a baseball bat as applied on the George Washington Bridge.

Electro-mechanical Expulsion De-icing Systems (EMEDS) use a mechanical force to knock the ice off the surface and depends on very rapid current discharges into electromagnetic coils, giving rise to magnetic fields of like polarity, that result in an electro-mechanical excitation (Al-Khalil, 2007). The electro-mechanical excitation could be either surface vibrations or strong pulses to effect de-icing. It is a potential safety concern that the system utilizes high voltage, but it still requires less power compared to electro-thermal systems.

The Electromagnetic-Impulsive De-Icing (EIDI) system operates by inducing strong and sudden magnetic forces from a high-current DC pulse through the coil resulting in a rapid acceleration and flexure of the icing surface, causing the debonding and expulsion of the ice. Such system has been found successful in the aviation industry but typically with the actuators installed underneath the icing-prone surface. When applied to bridge cables this is not possible without significantly increasing the diameter of the cables and is therefore instead installed as coils along the exterior surface of the cable. To verify the effectiveness of such an external EIDI system, tests on hangers described in (Vincentsen and Jacobsen, 2001) were performed. Though it was found effective at de-icing it also resulted in a quite violent explosion of the ice. With the explosion of ice, a short-time closing of the bridge is still necessary while the de-icing procedure is performed. The EIDI system was afterwards installed as a pilot project on the top $100\,\mathrm{m}$ of two hangers next to the pylon on the Great Belt East Bridge (Laursen, 2004). For three years the system successfully de-iced the hangers, but the a sudden icing of up to $50\,\mathrm{mm}$ thickness was found to have fatal consequence for the de-icing system which was found completely ineffective against the heavy icing (Laursen and Zwieg, 2007).
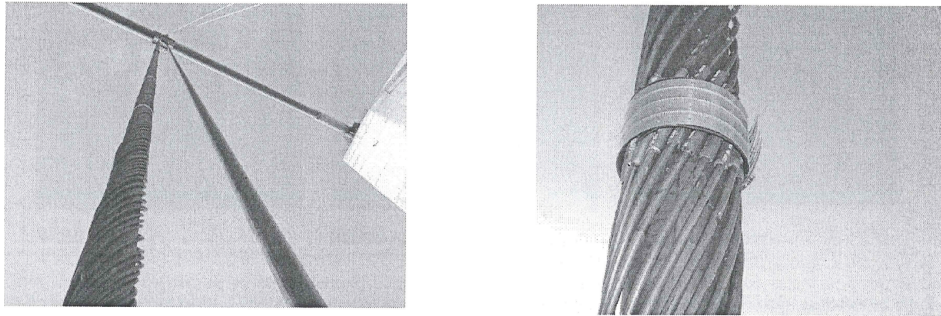
Figure 2: Photo of the EIDI system installed on the top part of hangers next to the pylon on the Great Belt East Bridge, reproduced from (Laursen, 2004).

One alternative electro-magnetic de-icing system is the Eddy Current De-icing Strip (EDS) which use induced eddy currents which act on the surface to effect de-icing (Shin and Bond, 1993; Zieve et al., 1991). With EDS, the impulse coils are built thin and flexible with printed circuit board technology (Ingram et al., 1998). This allows the application to be significantly less flow intrusive (Adams et al., 1992), but known to the author neither this, nor any of the following mechanical methods have ever been applied on bridges.

The last of the electro-mechanical systems is piezoelectric de-icing using a piezoelectric covering material. The piezoelectric material converts an available electrical alternating current into mechanical force by realignment of its crystalline structures. This realignment causes the material to expand and retract in continuous motion and, thereby, insures that ice formation will be prevented, or rapidly removed.

Another mechanical solution could be to have a mechanical device, like the ROV de-icer Fig. 3 developed for overhead lines (Farzaneh et al., 2008) or a mobile pulley system manually pulled (Laforte et al., 1998), going down the cable removing the ice accretion, though no designs have been proposed for bridge cables.

The two last mechanical techniques are the Pneumatic Impulse Ice Protection (PIIP) and the Small Tube Pneumatic (STP). Both utilize inflatable rubber bladders, such that when they expand, ice is sheared, cracked, and flaked off. These types of de-icing methods have
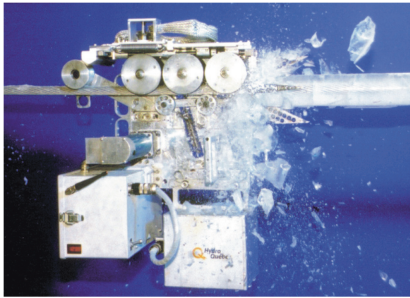
Figure 3: Prototype of the ROV de-icer, reproduced from (Leblond et al., 2002).

earlier been successfully used on aeroplanes though prone to damage from weather and foreign objects, thus the durability falls far short of those systems using metals.

3.2 Thermal systems

There exist a range of different thermal applications, as these systems are reliable and simply work by heating the ice prone surfaces to a temperature sufficient to prevent the formation of ice. Although they generally consume a great deal of energy in operation.

The electrical resistance heating systems use resistive elements embedded within thin sheets of material placed over and/or under the ice prone surfaces. When electricity are passed through these heating membranes or elements, they generates heat to melt the ice (Ingram et al., 1998).

Field tests on bridge pylons by (Numata and Kitada, 2008) examined the performance of three types of heaters: aluminium foil heater, sheet heater, and heating tubes. Although the aluminium foil heater was the simplest to apply and found to give the highest temperatures with the least amount of power, it still had a very large energy consumption.

Instead of electrical heating, an indirect heating method can be applied using warm air to heat the ice prone areas so as to melt the ice or prevent it from forming. Such method was applied on the Uddevalla Bridge where a high-pressure system pushed warm air through a small opening in the cable protecting pipe and therefore kept the whole cable strand at temperatures above freezing (Kuhn, 2006). The cable heating system was successful, but the total energy demand was exceptionally high.

Another de-icing method is to use far-infrared radiation. When transmitting energy by means of electromagnetic waves or rays, the energy travels in straight lines from the heat source and without significantly heating the air it passes through and could be a way of reaching out-of-range ice prone areas. Beside the high energy demand, tests conducted with a mobile infrared de-icing system (Ruggi and Pole, 1998) also found the method to be quite time consuming.

The most cost effective of the thermal solutions seems to be a new Pulse Electro-Thermal De-icing (PETD) method which uses short pulses of electricity applied directly to the ice-material interface. To apply heat directly at the interface the surface need to be covered with a thin electrically-conductive film. The film is then heated with a milliseconds-long pulse creating a thin melt-water layer on which the ice above drops off. Because only a micrometer-thin layer of ice is melted, PETD achieves a quite good energy efficiency compared the other thermal methods. The PETD system has been installed on part of the Uddevalla Bridge where both a cable stay and part of the pylon was covered in a PETD foil. To avoid having a negative

effect on the conductivity the foil needed to be mounted in one piece which was successfully installed using a robe access method (Kuhn, 2006). Known to the author this system is still effective in keeping the bridge clear of ice.

3.3 Passive Anti-Icing

None of the passive techniques hinders ice formation, but only help to limit its problematic effects. Some of these are:

- Thermal absorbent coating will only be effective when there is a sufficient level of incidental radiation (Laforte et al., 1998).

- Hydrophobic coatings with characteristic adhesion and surface tension provide only some effectiveness in wet snow conditions (Laforte et al., 1998).

- Solid icephobic coatings still got ice adhesion forces more than ten times too great for ice to detach itself under the action of gravity or wind.

- Viscous products and anti-icing greases have a limited protection duration because these product lose their efficiency under the effects of precipitation and could form a potential risk for the environment.

One of the newly developed materials is a black coloured coating called StaClean purported by the manufacturer to be non-wetting, slicker than Teflon, highly impact and abrasion resistant (Dalili et al., 2009). When applied to wind turbine blades it was found effective at reducing icing issues even though the black colour had no affect on surface temperatures.
Another type of anti-icing coating based on the sol-gel technology was applied on the main suspension cable at the Great Belt Bridge (Laursen and Zwieg, 2007). These tests was later found unsuccessful and further development of the coating is ongoing.
Rather than completely preventing the formation of ice, a more realistic goal is to focus on the production of durable, industrially viable coatings (Nadine and Volkmar, 2009).
A passive method other than these coatings is a covering of the cable bands Fig. 4 (Numata and Kitada, 2008). The prototype cover consisted of a simple square blanket with eyelets and was through field testing found to mitigate snow accretion.

Figure 4: Cable band cover, reproduced from (Numata and Kitada, 2008).

The last passive technique is a special developed lattice fence which have been verified effective in trapping accreted snow at the upper parts of the bridge members and preventing it from falling in chunks (Takemoto et al., 2006).

4   Conclusion

Overall only a limited amount of work has been carried out regarding the safety issues with ice accretion on bridges. To secure traffic safety on the bridge and to reduce long bridge closures, it is important to develop novel measures against ice accretion to mitigate the risk of falling ice.

It was found that the preferable passive anti-icing methods are still not good enough and only reduces the problem, and that there still are a long way to go before they are capable of completely eliminating the problem.

Among the mechanical techniques the Electromagnetic-Impulsive De-Icing (EIDI) systems appears the most promising. When installed on the Great Belt Bridge hangers it proved effective over a period of three years against diverse light cases of icing, though it still failed against a sudden heavy icing.

The many different thermal applications simply heating the ice prone surface are very reliable and actually seems to work, although they generally consume a great deal of energy in operation. The only thermal technique achieving good energy efficiency is a Pulse Electro-Thermal De-icing (PETD) method which uses short pulses of electricity applied directly to the ice-material interface and therefore only has to melt a micrometer-thin layer of ice. The system has been installed on the Uddevalla Bridge and seems very promising.

5   References

References

Adams, L., Weisend Jr, N., Wohlwender, T., Jul. 14 1992. Attachable electro-impulse de-icer. US Patent 5,129,598.

Al-Khalil, K., 2007. Thermo-Mechanical Expulsion Deicing System - TMEDS. AIAA-0692.

BBC News, February 2009. Severn bridge ice falls close m4. Online.
    URL http://news.bbc.co.uk/1/hi/wales/7873359.stm

Dalili, N., Edrisy, A., Carriveau, R., 2009. A review of surface engineering issues critical to wind turbine performance. Renewable and Sustainable Energy Reviews 13 (2), 428 – 438.

Druez, J., Louchez, S., McComber, P., 1995. Ice shedding from cables. Cold Regions Science and Technology 23 (4), 377 – 388.

Farzaneh, M., Volat, C., Leblond, A., 2008. Atmospheric Icing of Power Networks. Springer Science+Business Media B.V. 2008, Ch. Anti-icing and De-icing Techniques for Overhead Lines, pp. 229–268.

Fikke, S., Ronsten, G., Heimo, A., Kunz, S., Ostrozlik, M., Persson, P., Sabata, J., Wareing, B., Wichura, B., Chum, J., 2007. COST 727: atmospheric icing on structures: measurements and data collection on icing: state of the art. Meteo Schweiz.

Ingram, R., Codner, G., Gerardi, J., July 1998. Electro-magnetic expulsion de-icing system. US Patent 5,782,435.

Kuhn, E., May 2006. Maintenance with industrial rope access: Uddevalla bridge - a case study. In: IABSE Conference 'Operation, Maintenance and Rehabilitation of Large Infrastructure Projects, Bridges and Tunnels', Copenhagen, 2006.

Laforte, J. L., Allaire, M. A., Laflamme, J., 1998. State-of-the-art on power line de-icing. Atmospheric Research 46 (1-2), 143 – 158.

Laursen, E., 2004. The great belt bridge, denmark structural monitoring. In: The 4th International Cable Supported Bridge Operators' Conference. pp. 89–98.

Laursen, E., Zwieg, T., 2007. Kan anvendelse af nanoteknologi forhindre overisning på storebæltsbroen. In: Dansk Vejtidsskrift, feb 2007.

Leblond, A., Montambault, S., St-Louis, M., Beauchemin, R., Laforte, J., Allaire, M., 2002. Development of new ground wire de-icing methods. In: Proceedings of the 10th International Workshop on Atmospheric Icing of Structures, Brno, Czech Republic. Vol. 17. p. 20.

Makkonen, L., 2000. Models for the growth of rime, glaze, icicles and wet snow on structures. Philosophical Transactions: Mathematical, Physical and Engineering Sciences, 2913–2939.

Nadine, R., Volkmar, S., 2009. Anti-ice technologies - coating concepts and evaluation. In: IWAIS.

Numata, H., Kitada, K., 2008. Measures against snow accretion on suspension bridges in snowy regions: Hakucho bridge. In: The 6th International Cable Supported Bridge Operators' Conference (ICSBOC). pp. 121–125.

Ruggi, E., Pole, C., 1998. Deicing with a mobile infrared system. Tech. rep., Montreal, Quebec: APS Aviation Inc.

Shin, J., Bond, T., 1993. Surface roughness due to residual ice in the use of low power deicing systems. AIAA-0031, 31st Aerospace Sciences Meeting & Exhibit, Reno, NV.

Takemoto, H., Ueno, H., Takeuchi, M., Chiba, T., Asano, Y., 2006. Evaluation of measures against snow and ice accretion on bridge members and the development of an anti-accretion lattice fence. Journal of Snow Engineering of Japan 22 (5), 357–362.

Vincentsen, L., 2006. The large fixed links in denmark - experience and developments. In: IABSE. pp. 29–35.

Vincentsen, L., Jacobsen, H., 2001. Operation and maintenance of the great belt bridge. In: IABSE.

Zieve, P., Ng, J., Fiedberg, R., October 1991. Suppression of radiating harmonics Electro-Impulse Deicing (EIDI) systems. NASA STI/Recon Technical Report N 92, 19764.

Paper VII

"Shape modification of bridge cables for aerodynamic vibration control"

K. Kleissl & C.T. Georgakis

Shape modification of bridge cables for aerodynamic vibration control

K. Kleissl & C.T. Georgakis
Department of Civil Engineering, Technical University of Denmark, Kgs. Lyngby, Denmark

In this paper, the viability of modifying cable shape and surface for the purpose of controlling wind-induced vibrations is examined. To this end, an extensive wind-tunnel test campaign was carried out on various cable sections in the critical Reynolds number region under both smooth and turbulent flow conditions. Shape modifications of a plain cylinder included waviness, faceting and shrouding. The aerodynamic damping of each section is evaluated by applying 1- and 2-DOF quasi-steady aerodynamic models, which allow for the prediction of regions of aerodynamic instability. Whilst the plain, wavy and faceted cylinders are found to suffer from either dry inclined galloping, "drag crisis" or Den Hartog galloping, the shrouded cylinder is found to be completely stable for all wind angles of attack, albeit with a slight increase in drag at traditional design wind velocities. The wavy cylinder is found to eliminate the risk of dry inclined galloping, with a reduction in lift fluctuations. Nevertheless, the particular cylinder is at risk of "drag crisis" instability. Finally, turbulent flow is shown to introduce a significant amount of aerodynamic damping by proving a more stable lift force over tested wind velocities.

1 INTRODUCTION

Through improved bridge monitoring and a greater openness between bridge owners and engineers, it has become increasingly apparent that a large number of the world's long-span cable-supported bridges suffer some form of cable vibration (Kumarasena et al. 2007). These vibrations have the potential to lead to long-term fatigue damage and economic loss, through a reduction of consumer confidence. Examples of bridges with a history of cable vibrations include the First and Second Severn Crossings, Øresund Bridge, Great Belt East Bridge, Humber Bridge and the Fred Hartman Bridge.

Attempts to eliminate or dampen these vibrations have been met with varying degree of success. To date no ultimately successful cable vibration control system has been devised for all types of cable under all conditions. This is most probably due to the fact that the observed vibrations are a result of varying excitation mechanisms, several of which may need differing control strategies to combat. Tested control systems have included cable-ties, viscous/magnetoreological dampers, tuned mass dampers, spiral strands and dimples.

Nevertheless, recent work on aerodynamic control of cables through cross-sectional shape modification has shown great promise. Aerodynamic control refers to the means of eliminating undesirable vibrations of a structure through careful modification of the structural shape and surface, either passively or actively. Kleissl (2009) recently showed that circular cylinders that exhibit galloping instability, at specific wind angles of attack, can be modified passively so that these instabilities are eliminated altogether.

This paper is part of the preliminary investigations of an ongoing research project, with the objective of examining the viability of modifying cable shape and surface, for the elimination of not only cable galloping, but also vibrations due to vortex shedding - always under the prevalent meteorological conditions in Scandinavia.

2 EXPERIMENTAL INVESTIGATION

The experiments undertaken for varying flow conditions, angles of attack and cable inclination were performed at the closed circuit wind tunnel facility at FORCE Technology, Lyngby, Denmark. The test section has a height of $0.70\,\mathrm{m}$ and a width of $1.00\,\mathrm{m}$. The wind tunnel can produce a maximum wind velocity of $60\,\mathrm{m/s}$ in smooth flow ($< 1\%$ turbulence intensity) and $35\,\mathrm{m/s}$ in turbulent flow with an intensity of approximately 7%. Turbulence is generated through a turbulence grid installed upstream of the test section. An inclined test rig, as shown in Fig. 1, was designed so that cable models could be tested at varying cable-wind angle ϕ in the range $60° - 90°$, where this flow angle ϕ is defined so that $\phi = 90°$ correspond to flow perpendicular to the cable axis, as shown in Fig. 2. To minimize the error on the force coefficients due to end effects, the results are corrected based on measurements made with only the arms of the inclined setup installed. Finally, to ensure the end-effects did not af-

fect the results, tests undertaken on a perpendicular section were compared with and without the use of the inclined test rig. The comparison was favouable, although a slight increase in drag was observed when using the inclined test rig. Based on a literature re-
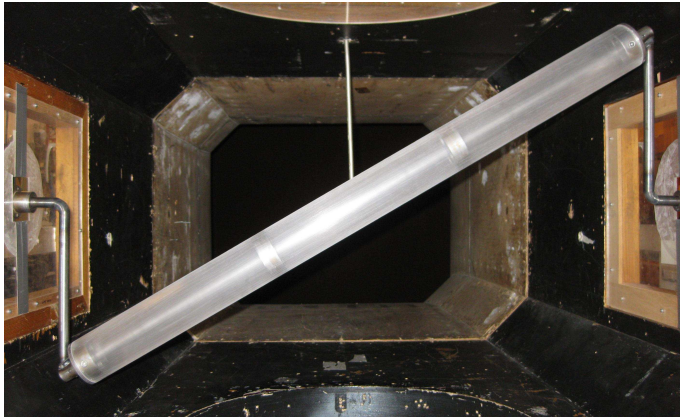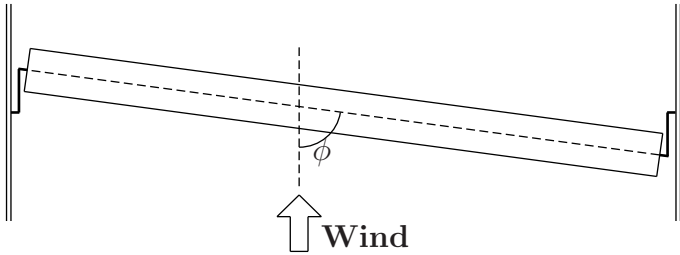

Figure 1: Illustration of the test rig.

Figure 2: Plan view of the cable-wind angle ϕ.

view of the different types of cable surface modifications (Kleissl 2009), three types of modified sections were chosen for further wind tunnel investigation. Furthermore, a plain circular cylinder was included in the test program as a reference case. The modified sections chosen for testing are shrouded, wavy and faceted hexagonal cylinders (Fig. 3).

Figure 3: Section models (from right to left), plain cylinder, wavy cylinder, faceted cylinder and shrouded cylinder.

3 TEST RESULTS

Only the force coefficients from the smooth flow tests with $\phi = 90°$ are presented herewith. As a basis for the performance evaluation of the modified sections, all force coefficients are determined using the internal circular diameter, which is the same for all sections. The results presented are corrected for a test section blockage of 10%.

The drag, lift and moment coefficients obtained for a slightly roughened cylinder in smooth flow are presented at Fig. 4. A slight roughening of the surface of the cylinder was introduced to emmulate surface pollutants that might be found on an actual bridge cable. The roughness had the added effect of ensuring that the cylinder´s critical Reynolds number region fell within the testable wind velocity range. Furthermore, the increased surface roughness produced an increased minimum drag coefficient of around 0.6 (instead of 0.3 for a perfectly smooth cylinder), as often specified for bridge design. From Fig. 4, it can be seen that the lift coefficient strongly indicates the existence of a single separation bubble precisely within the critical Reynolds number range for drag.
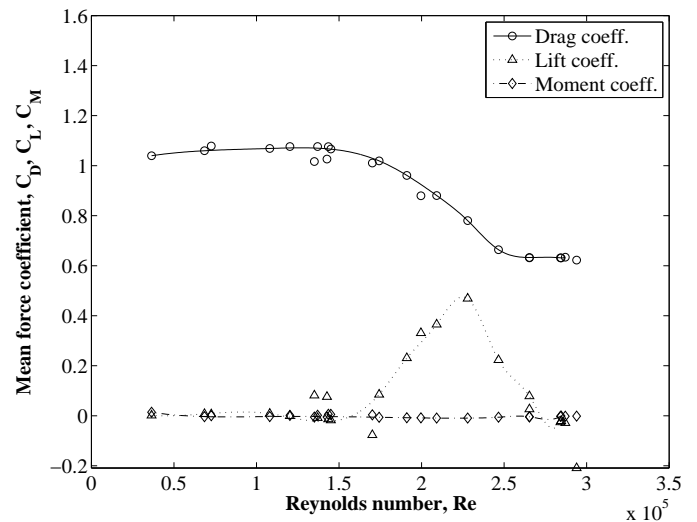
Figure 4: Force coefficients for the plain cylinder for flow $\phi = 90°$.

The results for the wavy cylinder in the smooth flow, shown in Fig. 5, look overall very much like a typical circular cylinder with a significant amount of surface roughness. The transition to the turbulent shear layer happens earlier and the dip in drag is even steeper than for the plain cylinder, although this could be the result of the surface of the RPT (Rapid Prototyping) material being slightly rougher. The drag coefficient lies around 1.2 in the subcritical region, but only drops to approx. 0.7 at the end of the critical region and slowly climbs up again through the supercritical region. A small single separation bubble can be observed from the lift coefficient, but with less than half the magnitude of the one observed for the plain

2

circular cylinder, indicating that the waviness does reduce the vortex correlation along the cylinder axis.
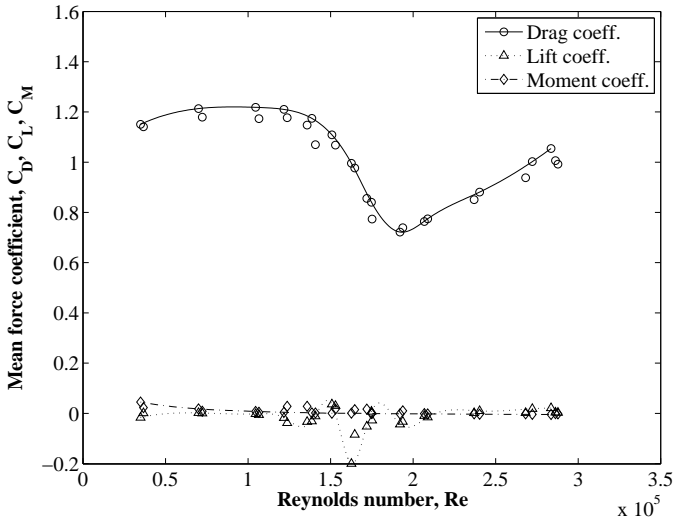
Figure 5: Force coefficients for wavy cylinder for flow $\phi = 90°$.

The faceted cylinder is not presented as the drag is found to be independent of Reynolds numbers and in the range of $1.5 - 2.0$, which is too high to be used on an actual bridge. The cylinder did also experience significant variation in drag over angle of attack, which led to the prediction of Den Hartog galloping.

In smooth flow the results for the shrouded cylinder (see Fig. 6) shows that the shroud eliminates the Reynolds number dependency. The almost constant drag coefficient slightly above 1.0 based on the inner cylinder diameter is not as low as expected. Tests described in the literature review (Kleissl 2009) indicates that a constant drag coefficient lower than 0.9 should be possible with the an efficient shroud design. With the lack in the understanding of the different shroud parameters and the "optimal" design covering a relative wide parameter region, an additional reduction of the drag coefficient should be possible by further development of the shroud by mainly focusing on drag reduction instead of reducing vortex-formations. The lift coefficient are found completely steady compared to the two other cylinders, indicating that the shrouding successfully disrupts the coherence of the vortex formation.

4 INSTABILITY ANALYSIS

The aerodynamic damping of the tested cylinders have been evaluated by applying both 1- and 2-DOF quasi-steady aerodynamic instability models (Macdonald and Larose 2006; Macdonald and Larose 2008a). Though in this paper only the plots from the 1-DOF instability model are presented as the 2-DOF model leads to similar observations. The reasons for applying both models is that when a system starts getting detuned, it asymptotically moves towards the 1-
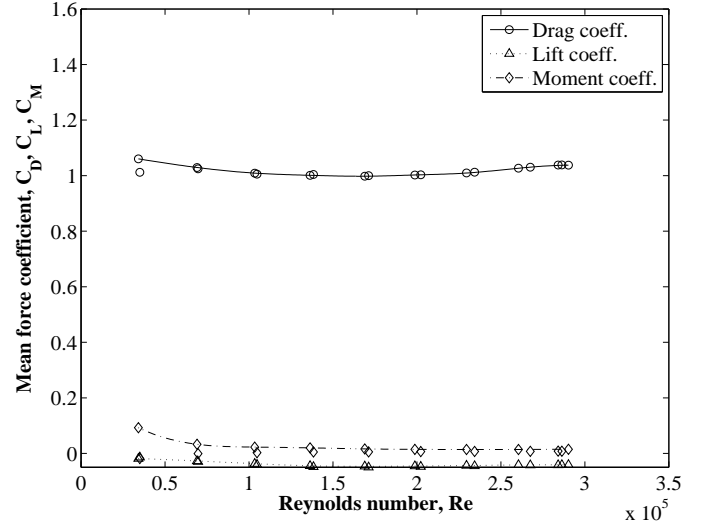
Figure 6: Force coefficients for shrouded cylinder for flow $\phi = 90°$.

DOF solution covering perfectly tuned systems (Macdonald and Larose 2008b). So by considering both models, both stay cables and hangers are covered.

The evaluation of instability is based purely on the aerodynamic damping in the nondimensional form, ignoring any form of structural damping. The nondimensional aerodynamic damping parameter Z_a is defined as

$$Z_a = \frac{\zeta_a m f_n}{\mu} \qquad (1)$$

where ζ_a is the aerodynamic damping, m is mass per unit length, μ is the dynamic fluid viscosity and $f_n = \omega_n / 2\pi$ where ω_n is the undamped natural frequency. By using this nondimensional aerodynamic damping parameter a function is obtained that is only dependent on the Reynolds number, the cable-wind angle ϕ and the angle of attack α. In both of the stability plots, the evaluation of the aerodynamic damping is computed based on splined field approximations of the force coefficients from the inclined tests. The continuous contour line represents the transition to negative aerodynamic damping and thus the risk of instability in the case of neglectable structural damping.

From the stability plot of the plain circular cylinder, shown in Fig. 7, instability regions clearly emerges in the critical Reynolds number region and are mainly the result of the sudden dip in the drag coefficient i.e. "drag crisis" instability. Both models also predict some instability at the edge of the tested yawing range which appear outside the critical region. The fact that the models predict large instability regions for the plain cylinder at skew winds is to be expected, as several preceding investigations already have pointed this problem out as dry inclined galloping. Matsumoto et al. observed galloping instability as a result of an artificial axial flow corresponding to yawed angles in the range of $45° - 60°$. This corresponds well with the observed instability region occurring at the edge of the
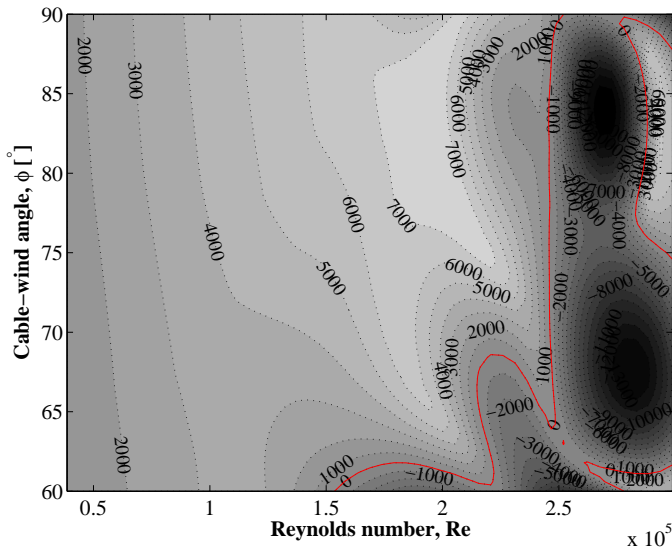
tested yawed angles of $60°$.

Figure 7: Nondimensional aerodynamic damping for plain circular cylinder in yawed smooth flow.

For the wavy cylinder the results for the aerodynamic damping are shown in Fig. 8. For this the instability region are seen to be very localized around the critical Reynolds number region. But because the waviness significantly reduces the secondary axial flow, the section appears more stable outside the critical Reynolds number region. This also indicates that the secondary axial flow plays an important role regarding dry inclined galloping. Never the less the wavy cylinder has some unattractive aerodynamic properties in the critical region, where "drag crisis" instability is predicted.
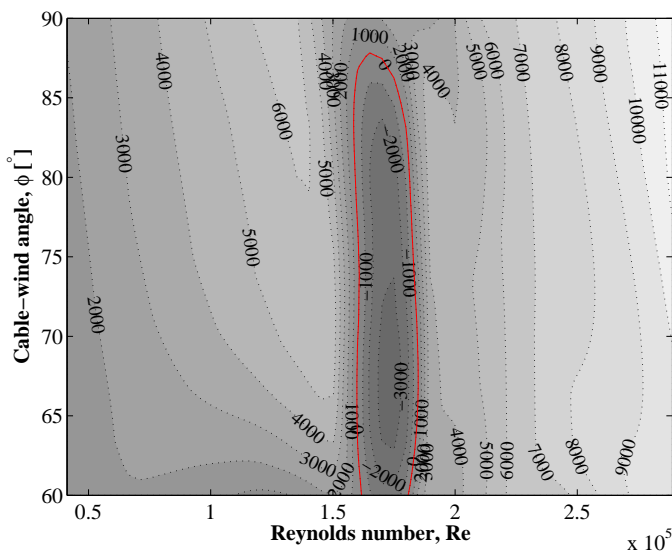
Figure 8: Nondimensional aerodynamic damping for wavy cylinder in yawed smooth flow.

The stability plot for the shrouded cylinder is not presented as the cylinder is predicted to be completely stable in the whole parameter range considered. So besides the slight increase in drag, the shroud appears very effective at aerodynamic vibration control of the cylinder.

5 CONCLUSIONS

The evaluation of aerodynamic instability shows that the plain cylinder could be prone to both "drag crisis" and dry inclined galloping at specific skew winds. The wavy cylinder have the properties similar to a typical rough circular cylinder where no significant drag increase is found, indicating some effectiveness of the waviness. The steep dip in drag results in the prediction of a "drag crisis" instability. Outside the critical Reynolds number region, it is more stable than the plain cylinder which could be a result of the reduced axial flow. The hexagonal faceted cylinder had too large a drag coefficient $(1.5 - 2.0)$ and depending on the angle of attack and the angular variation of the geometry, Den Hartog galloping is predicted. The shrouded cylinder is found to have a very low dependency on the Reynolds number and a drag coefficient slightly above 1.0 based on the inner diameter. The shroud is found to stabilize the cylinder against any type of dry state instability and it also significantly reduces the vortex-induced oscillating lateral forces. Finally, turbulent flow is shown to introduce a significant amount of aerodynamic damping by proving a more stable lift force over tested Reynolds numbers.

REFERENCES

Kleissl, K. (2009, Aug). Vibration control of bridge cables. Master's thesis, DTU Byg, DTU, Building 118, Brovej, 2800 Kgs. Lyngby, Denmark.

Kumarasena, S., N. P. Jones, P. Irwin, and P. Taylor (2007, Aug). Wind-induced vibration of stay cables. Report FHWA-HRT-05-083, US Federal Highway Administration.

Macdonald, J. H. G. and G. L. Larose (2006). A unified approach to aerodynamic damping and drag/lift instabilities, and its application to dry inclined cable galloping. *Journal of Fluids and Structures 22*(2), 229 – 252.

Macdonald, J. H. G. and G. L. Larose (2008a). Two-degree-of-freedom inclined cable galloping–part 1: General formulation and solution for perfectly tuned system. *Journal of Wind Engineering and Industrial Aerodynamics 96*(3), 291 – 307.

Macdonald, J. H. G. and G. L. Larose (2008b). Two-degree-of-freedom inclined cable galloping–part 2: Analysis and prevention for arbitrary frequency ratio. *Journal of Wind Engineering and Industrial Aerodynamics 96*(3), 308 – 326.

Paper VIII

"Comparison of the aerodynamics of bridge cables with helical fillets and a pattern-indented surface in normal flow"

K. Kleissl & C.T. Georgakis

In proceedings: *The 13th International Conference on Wind Engineering (ICWE), Amsterdam, the Netherlands, July 2011*

Comparison of the aerodynamics of bridge cables with helical fillets and a pattern-indented surface in normal flow

Kenneth Kleissl, Christos T. Georgakis

Department of Civil Engineering, Technical University of Denmark, Building 118, Brovej, Kgs. Lyngby, Denmark, kenk@byg.dtu.dk, cg@byg.dtu.dk

1 INTRODUCTION

Over the last two decades, several bridge cable manufacturers have introduced surface modifications on the high-density polyethylene (HDPE) sheathing that is often installed for the protection of inner strands. The main goal of this is rain rivulet impedance, leading to the suppression of rain-wind induced vibrations (RWIVs). The modifications are based on research undertaken predominantly in Europe and Japan, with two different systems prevailing; HDPE tubing fitted with helical surface fillets and HDPE tubing with pattern-indented surfaces. In the US and Europe, helical fillets dominate, whilst pattern indented surfaces are more common in Asia.

Research into the effectiveness of helical fillets and pattern-indented surfaces has shown that, besides their potential to suppress rain-wind induced vibrations, they are also modestly reducing drag forces at design wind velocities. This is of particular interest to bridge designers, as wind on stay planes of long bridges can now produce more than 50% of the overall horizontal load on a bridge. Nevertheless, there is no definitive aerodynamic performance comparison between the two systems. One of the problems of comparing them lies in the fact that different researchers, in different facilities, with varying wind-tunnel flow characteristics and performance, have developed each separately.

As part of a comprehensive review of the aerodynamics of existing cable surface modifications, the resulting static force coefficients obtained from wind-tunnel tests on cables normal to flow and employing both systems are presented herewith and compared to those from a plain reference cylinder. This is the first known direct comparison of this type. Evaluation of lift force fluctuations and flow visualisation tests are also undertaken to obtain insight into the structures of the flow around the modified profiles.

1.1 *Historical overview*

Helically wrapped wires were initially proposed in the fifties to combat vortex-induced vibrations (VIV). It was found that the presence of the helical protrusion significantly reduced the shedding correlation length. It was not until 1992, though, that tests on their use on a bridge stay cable were undertaken at CSTB (Nantes) in connection with the design of the Normandy Bridge (Flamand, 1995). The tests showed that suppression of RWIVs could be achieved by applying a 1.3 mm diameter wire at a 0.30 m step. To ease production, a symmetric double helix of 1.3 mm height, 2 mm width and a pitch length of 0.6m was applied. The minimum drag coefficient of this section was measured to be 0.62. In connection with the design of the Øresund Bridge, further wind tunnel tests on double helical fillets (2.1 mm high) were performed at the Danish Maritime Institute by Larose and Smitt (1999). Their tests showed a strong reduction of the RWIVs, by disrupting the formation of a coherent upper rivulet in the presence of light rain. Even though the fillets were found to significantly reduce the RWIV

amplitudes, recent full-scale monitoring of the Øresund Bridge has shown the continued presence of modest RWIVs (Acampora and Georgakis, 2011).

An alternative to the helical fillet, the pattern-indented surface was first proposed by Miyata et al. (1994b), as a further development of the application of uniformly distributed dimples. The pattern-indented surface is found to promote the stabilization of the separated flows over the surface of the cable and inhibits the formation of rivulets (Miyata et al., 1999). Measured pressure distributions indicate that such a cable enters the supercritical flow state at the lower wind velocities, where RWIVs tend to occur. Furthermore, the flow separation point remains stable at 110° in the supercritical region, resulting in a near constant drag coefficient (Hojo et al., 2000). It has also been found that these properties hold true, regardless of whether the discrete roughness has been generated by concavities or convexities (Miyata et al., 1994a).

The pattern-indented surface was first applied to the cables of the Tatara Bridge in 1999. For the specific bridge, Miyata et al. (1998) reported a minimum drag coefficient of 0.61 and a design drag coefficient of 0.7. Similar values have been reported for the Sutong Bridge, for which the system has also been applied. The pattern-indented surface of the Sutong Bridge cables is shown in Figure 1.
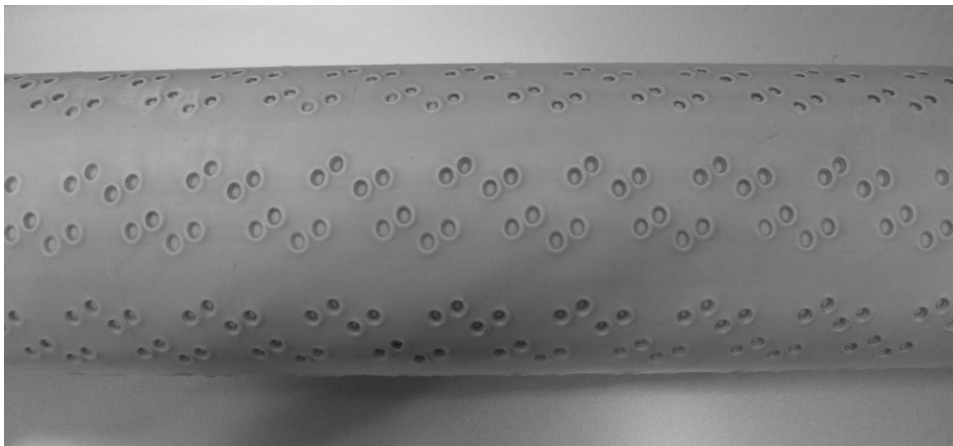
Figure 1. Photograph illustrating the pattern-indented surface applied to the cables of the Sutong Bridge.

2 WIND TUNNEL TESTS

The comparative wind tunnel tests were performed at the new DTU/FORCE Climatic Wind Tunnel, located in Lyngby, Denmark (Georgakis et al., 2009). The wind tunnel is of the closed-circuit type, with a test section of 2x2 m^2. The maximum flow velocity of 32 m/s is achieved with a turbulence intensity of approximately 1.1%.

Three models were tested for comparison: a plain HDPE cylinder, an HDPE cylinder fitted with helical fillets and an HDPE cylinder with a pattern-indented surface. The sectional models are all original full-scale samples, supplied by bridge cable manufacturers. The models were placed horizontally, resulting in a near 2-D flow normal to the models. End plates with a diameter of approximately five cylinder diameters were fitted close to the model ends to eliminate undesirable end effects, whilst the drag and lift forces were measured using 6-DOF force transducers at either end, covered with dummy pieces of the same cable. During the tests, the wind velocity was increased by regular increments of approximately 2 m/sec, up to the maximum wind-tunnel velocity. At maximum wind velocity, the corresponding Reynolds numbers were $Re = 3.3 \times 10^5$ and $Re = 2.8 \times 10^5$, for the model with the helical fillet and the model with the pattern-indented surface, respectively. With an effective model length of 1.53 m, the aspect ratios were 9.6:1 and 10.9:1 for the aforementioned cases. The blockage

ratios for all section models were within 7-8% and the drag coefficients have been corrected with the Maskell III method, according to Cooper et al. (1999).

The plain HDPE tube has a 160 mm outer diameter and a measured average surface roughness of $R_a \sim 1.8$ μm. The test setup with the plain tubing is shown in Figure 2a.

The HDPE tube with two helically wrapped fillets also has an outer diameter of 160 mm. The fillets are rounded with a height of approximately 3 mm and a width of approximately 4 mm. Furthermore, they have a 3.13 tube diameter pitch length (500 mm and 45°). The average surface roughness is in the order of $R_a \sim 3.0$ μm. The test setup with the helically wrapped cable is shown in Figure 2b.

The pattern-indented HDPE cylinder has a diameter of 140 mm, as this is an actual sample of the most common diameter of cable used on the Sutong Bridge. The relative surface roughness was based on the depth of the indentations measured to be approximately 1% of cable diameter. The corresponding test setup is shown in Figure 2c.
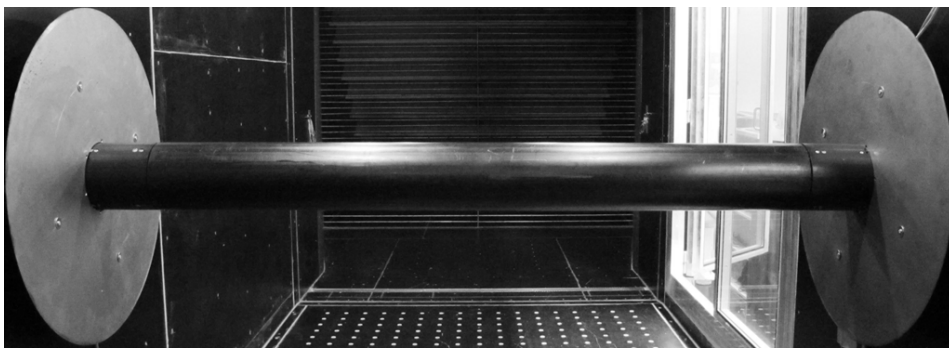
Figure 2a. Test setup for the plain HDPE tube.
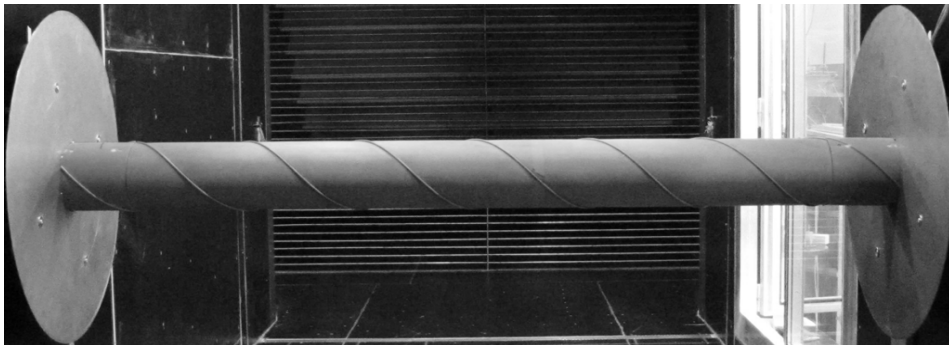
Figure 2b. Test setup for the helically filleted HDPE tube.
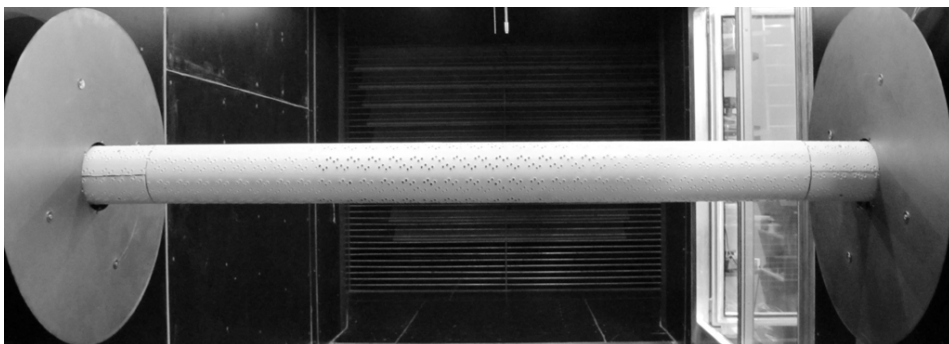
Figure 2c. Test setup for the patter-indented HDPE tube.

3 RESULTS AND DISCUSSION

3.1 *Force coefficients*

The average drag and lift coefficients obtained for each of the tested sections are shown in Figure 3. The plain cylinder exhibits an entry into the critical Reynolds number region between $Re = 2 - 2.5 \times 10^5$. Within this region, the initiation of a large lift coefficient is observed. The aerodynamic force coefficients are in general agreement with the expectations for a smooth cylinder of this type. Note that these tests were only performed for one wind angle of attack. Imperfections could result in variations in these force coefficients with varying wind angle of attack as reported by Matteoni and Georgakis (2011).

For the cylinder with the helical fillets, the transition to the critical flow state is very prolonged and the peak in lift coefficient much reduced. This is most likely due to the fillet's ability to generate a variable separation line along the length of the cylinder. The drag coefficient of 0.66 reached at maximum velocity also matches very well with what previously found in literature, e.g. Flamand (1995) who measured a minimum drag coefficient of 0.65.

The cylinder with the pattern-indented surface exhibits a very early transition to the supercritical region due to the high level of surface roughness, which also here is accompanied by the occurrence of nonzero lift force. This early transition agrees well with what has been observed for circular cylinders with uniform roughness. Unlike a rough cylinder, though, the subsequent increase in drag through the supercritical region is limited, as the drag coefficient is always found to be below 0.63 throughout. This matches previous findings of a near constant drag coefficient of 0.6 (Miyata et al., 1994b).
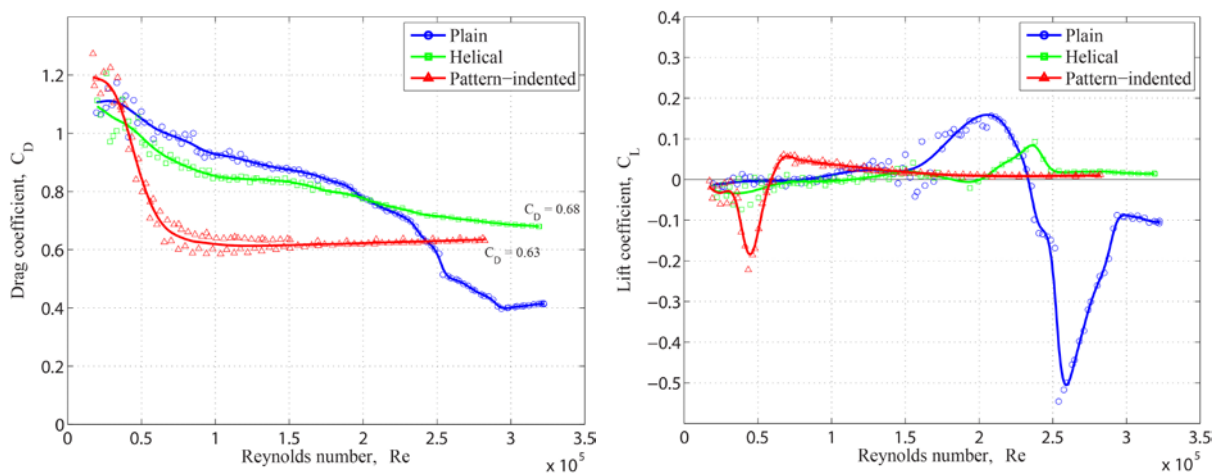
Figure 3. Mean force coefficients over Reynolds numbers (left) Drag coefficients, (right) Lift coefficients.

3.2 *Fluctuating lift force*

An analysis of the unsteady cross-stream force (fluctuating lift) is also made. With the test setup employed, only the total RMS lift fluctuations can be estimated. These are shown in Fig. 4. While the pattern-indented surface starts off with the lowest lift force fluctuations, an unexpected peak occurs around $Re \sim 1.76 \times 10^5$. In comparison, the helical cable has the lowest fluctuations in the midrange, whilst increasing significantly near the maximum velocity considered. For the plain cable, the flow transition can be identified by increased fluctuations within $Re \sim 2.5 - 2.8 \times 10^5$, corresponding to the single separation bubble flow regime translated as an increased lift coefficient in Fig. 3. A low constant RMS value can be observed after the transition into the supercritical flow state at $Re \sim 3.0 \times 10^5$.
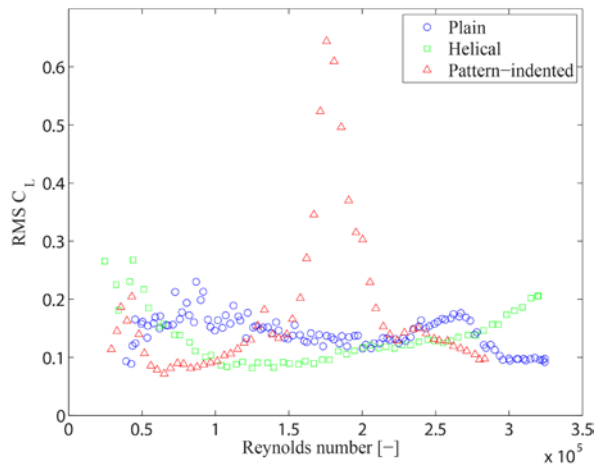
Figure 4. RMS for static lift force coefficients.

To fully understand the development of the RMS of the lift coefficients, an analysis of the lift fluctuations in the frequency domain is made. The frequency distributions of the lift force are determined using Fast Fourier Transformation (FFT) to compute the power spectral density (PSD) of the lift coefficient. The PSD is computed for each of the flow velocities tested, based on a discrete number of spectra, leading to two-dimensional contour plots, as seen in Fig. 5. The linear trends identified as vortex shedding disappears around $Re\sim2.0\times10^5$ and $Re\sim1.6\times10^5$ for the plain and helical cable, respectively. This matches the occurrences of flow transition. In contrast, vortex shedding remains throughout the considered flow velocities for the patterned-indented surface, in spite of the early transition. The peak in RMS forces for the pattern-indented surface is here identified as an incidence of model resonance, which the other two models avoid due to the suppression of vortex shedding. In the critical Reynolds number region, increased activity is observed for all three models at very low frequencies, which are believed to be the occurrence of unstable single separation bubbles reappearing or shifting sides at a low rate.
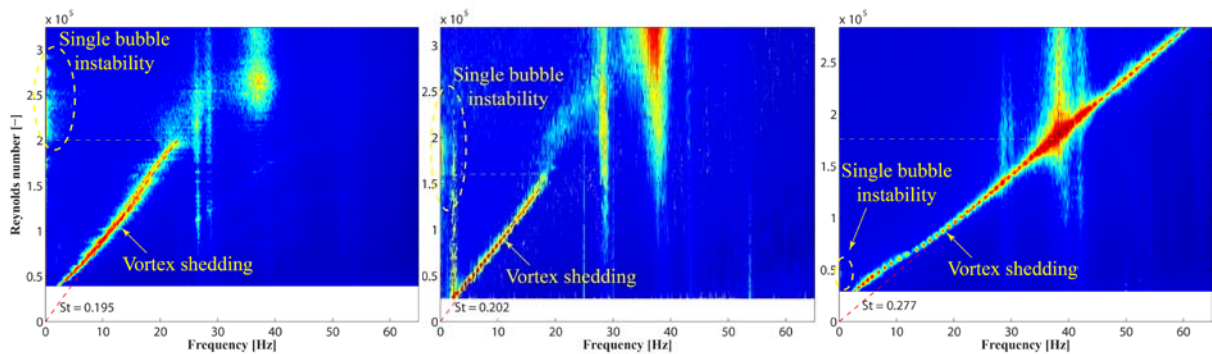
Figure 5. Lift force PSD - (left) Plain surface, (middle) Helical surface, (right) Pattern-indented surface.

3.3 *Angle of attack dependency*

Due to the angular periodicity of the pattern, the force coefficient dependency on wind angle of attack for the pattern-indented surface was tested (see Fig. 6). The drag coefficient is only slightly affected by the angle of attack, whereas the lift coefficient experiences a significant dependency throughout the supercritical flow range. The trend is not completely following the periodicity of the pattern that is repeated every 45 degrees, as might be expected. When evaluating the Den Hartog galloping criterion (Den Hartog, J., 1947) at the apparent critical

angle of approximately α = 20 degrees, all the curves result in the prediction of galloping instability, as the Den Hartog value approaches -0.11.
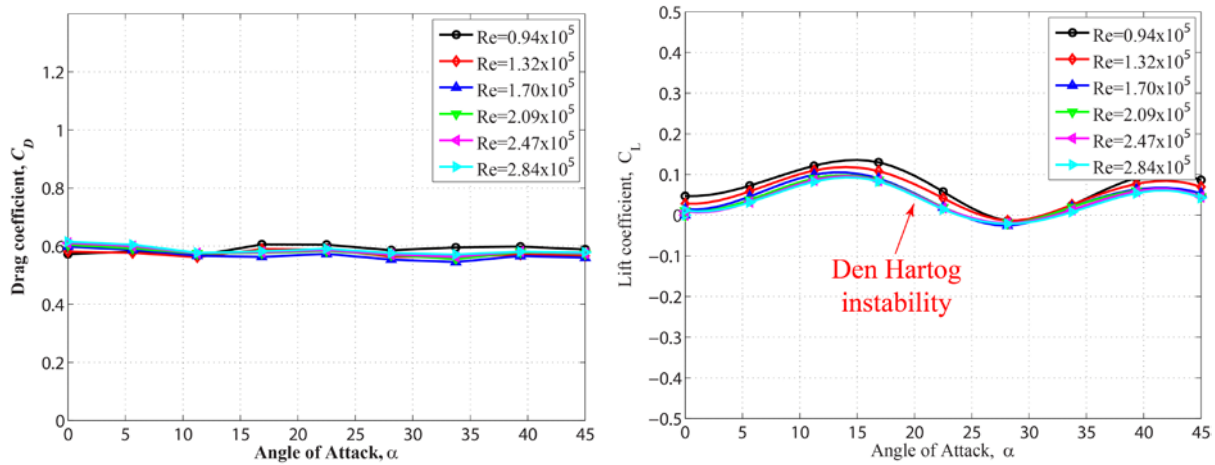
Figure 6. Drag force coefficient as a function of angle of attack (left) and corresponding lift coefficient (right) for the pattern-indented cable.

3.4 *Near-wake flow visualization*

The near-wake flows for all three cylinders were observed through smoke visualization. At Re~2.0×10^4, the helical fillets are seen to delay the Kármán vortex-shedding formation further downstream, which confirms the increased vortex formation lengths, as previously observed with helical protrusions (Nebres and Batill, 1992). Meanwhile, the plain and pattern-indented surfaces experience traditional Kármán vortex-shedding.
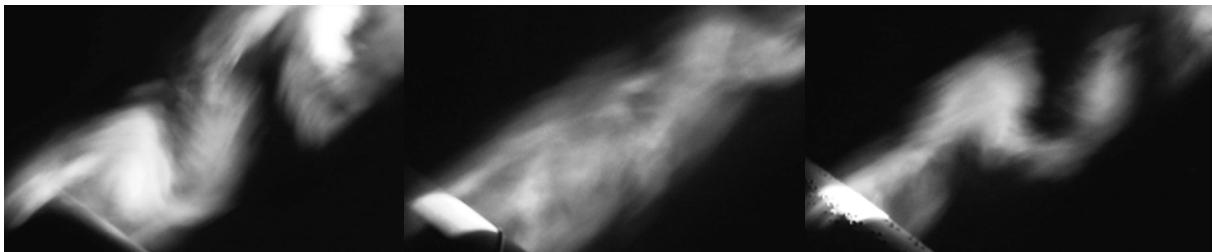
Figure 7. Near-wake smoke visualization at Re ~2.0×10^4: plain surface (left), helically filleted surface (middle), and pattern-indented surface (right).

At Re~8.5×10^4, the flow around the pattern-indented surface is observed to change to a supercritical flow state, with the absence of strong Kármán vortex-shedding. Meanwhile, for the plain and helically filleted cable the vortex formation state is unchanged, only moving slightly downstream.
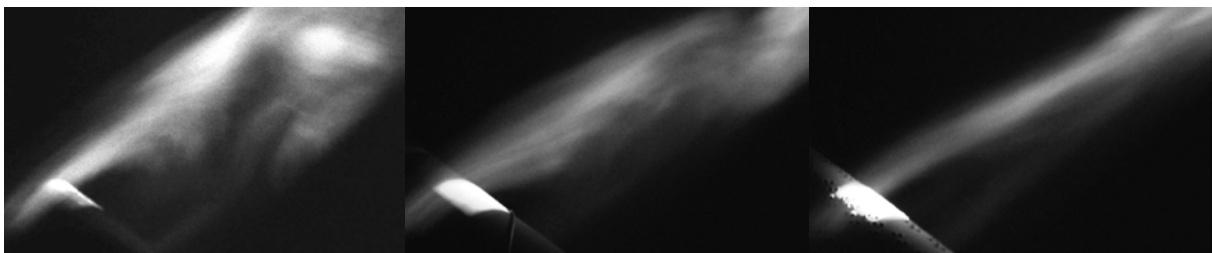
Figure 8. Near-wake smoke visualization at Re ~8.5×10^4: plain surface (left), helically filleted surface (middle), and pattern-indented surface (right).

At Re~1.72×10^5, the helically filleted model changes flow state, with only the plain model still experiencing vortex shedding. This matches the observations from the force coefficients, indicating flow transitions around Re~2.0×10^5 and Re~1.6×10^5 for the plain and helically filleted cable, respectively.

Figure 9. Near-wake smoke visualization at Re~1.72×10^5: plain surface (left), helically filleted surface (middle), and pattern-indented surface (right).

3.5 *Surface flow visualization*

Oil visualization tests were performed to better understand the effect of the surface modifications on the surface flow. Photos obtained during oil visualization at varying Reynolds numbers are shown in Figs. 10-11. Flow separation lines on each side of the helical fillet are identified. The typical separation line is only present in a region between two fillets. On the pattern-indented surface, the protruding peripheries of the dimples seem to guide the flow around the dimples.
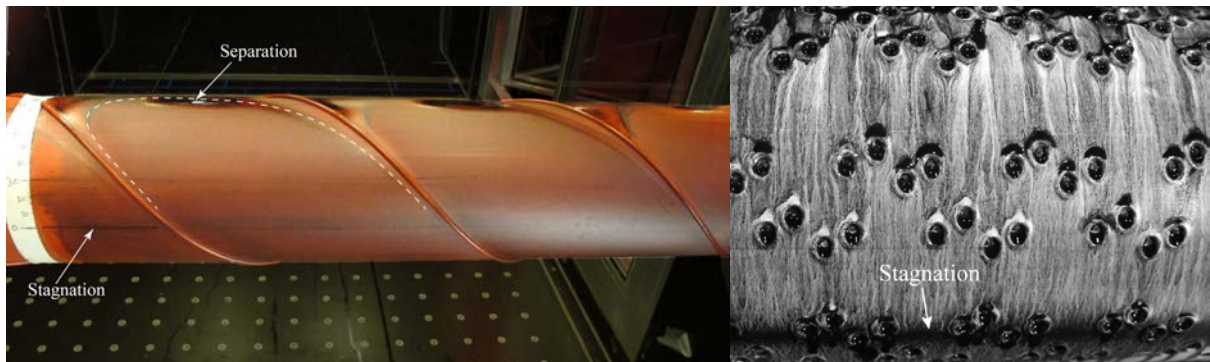
Figure 10. Oil visualization at Re~1.7×10^5: helical surface (left) and pattern-indented surface (right).
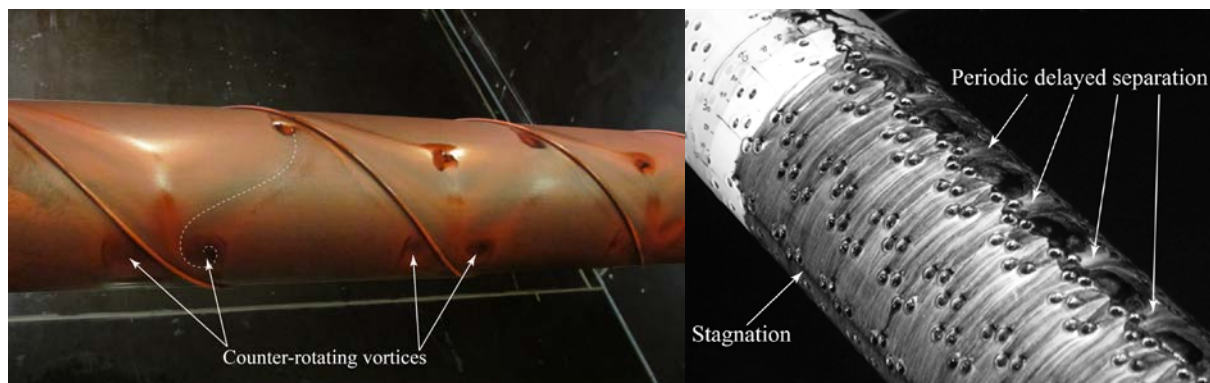
Figure 11. Oil visualization at Re~3×10^5: helical surface (left) and pattern-indented surface (right).

On the leeward side of the helical model (see Fig. 11) a pair of counter-rotating vortices is observed at each of the helical fillets. On the pattern-indented surface a periodic waviness of

the separation line is identified, which is often related to a higher base pressure and thus reduced drag (Lam et al., 2004). The wave period is identical to that of the surface pattern.

4 BRIEF CONCLUSION

The tubing with the pattern-indented surface was found to exhibit the lowest drag coefficient, which remained relatively constant over the supercritical Reynolds number range tested. At wind velocities above 30m/sec, it appears that the tubing with the helical fillet exhibits a drag coefficient approaching that of the pattern-indented surface. The pattern-indented surface was observed to experience vortex shedding throughout the considered range of flow velocities, despite its early flow transition. The angle of attack dependency for the pattern-indented cable leads to a prediction of Den Hartog galloping at 20 degrees wind angle of attack. Flow visualisation confirmed the existence of flow structures associated with lower drag forces, such as periodic variations in flow separation along the axis of the cylinder. Further dry and wet static wind tunnel tests are currently being undertaken for all of the cylinders at varying yaw angles.

5 ACKNOWLEDGEMENTS

6 REFERENCES

Acampora, A.; Georgakis, C.T., 2011. Recent monitoring of the Øresund Bridge: Rain-wind induced cable vibrations. Proceedings of the 13th International Wind Engineering Conference, Amsterdam, July 10-15, 2011

Cooper, K.; Mercke, E. & Wiedemann, J., 1999. Improved blockage corrections for bluff-bodies in closed and open wind tunnels. Proceedings of the 10th International Conference Wind Engineering, Copenhagen, 1627-1634.

Den Hartog, J., 1947. Mechanical Vibrations. McGraw-Hill, New York.

Flamand, O., 1995. Rain-wind induced vibration of cables. Journal of Wind Engineering and Industrial Aerodynamics, 57, 353 – 362.

Georgakis, C.T.; Koss, H.H., Ricciardelli, F., 2009. Design specifications for a novel climatic wind tunnel for testing of structural cables. Proceedings of the 8th International Symposium on Cable Dynamics, 333-340

Hojo, T.; Yamazaki, S. & Okada, H., 2000. Development of Lowdrag Aerodynamically Stable Cable with Indented Processing. Nippon Steel Technical Report 82.

Lam, K., Wang, F. H., Li, J. Y., So, R. M. C., 2004. Experimental investigation of the mean and fluctuating forces of wavy (varicose) cylinders in a cross-flow. Journal of Fluids and Structures 19 (3), 321 – 334

Larose, G. & Smitt, L. W., 1999. Rain/Wind Induced Vibrations of Parallel Stay Cables. Proceedings of the IABSE Conference, Cable-Stayed Bridges - Past, Present and Future, Malmo, Sweden

Matteoni, G.; Georgakis, C.T., 2011. Investigation of the effects of bridge cable surface roughness and cross-sectional distortion on aerodynamic force coefficients. Proceedings of the 13th International Wind Engineering Conference, Amsterdam, July 10-15, 2011

Miyata, T.; Yamada, H. & Hojo, T., 1994a. Aerodynamic response of PE stay cables with pattern-indented surface. Proc. of IABSE Conference, Cable-stayed and suspension bridges, Deauville, France, 2, 515-522.

Miyata, Y.; Yamada, H. & Hojo, T., 1994b. Experimental Study on Aerodynamic Characteristics of Cables with Patterned Surface. Journal of Structural Engineering, 40A, 1065-1076.

Miyata, T.; Yamada, H.; Fujiwara, T. & Hojo, T., 1998. Wind-resistant Design of Cables for the Tatara Bridge. IABSE Symposium on Long-span and High-rise Structures, Kobe, Japan, 79, 51-56.

Miyata, T.; Katsuchi, H. & Tamura, Y., 1999. Comprehensive Discussion on Structural Control for Wind-Induced Responses of Bridges and Buildings. Wind Engineering into the 21st Century, Proceedings of the 10th International Conference on Wind Engineering, 1, 487-494.

Nebres, J. V. & Batill, S. M., 1992. Flow about cylinders with helical surface protrusions. 30th AIAA Aerospace Sciences Meeting and Exhibit, Reno, Nevada, Vol. 92.

Paper IX

"Comparison of the aerodynamics of yawed bridge cables with helical fillets and a pattern-indented surface"

K. Kleissl & C.T. Georgakis

In proceedings: *The 9th International Symposium on Cable Dynamics (ISCD), Shanghai, China, October 2011*

COMPARISON OF THE AERODYNAMICS OF YAWED BRIDGE CABLES WITH HELICAL FILLETS AND A PATTERN-INDENTED SURFACE

Kenneth Kleissl, Christos T. Georgakis
Department of Civil Engineering, Technical University of Denmark
Building 118, Brovej, Kgs. Lyngby, Denmark
kenk@byg.dtu.dk, cg@byg.dtu.dk

Introduction

Over the last two decades, several bridge cable manufacturers have introduced surface modifications on the high-density polyethylene (HDPE) sheathing that is installed for the protection of inner strands. The main goal of this is rain rivulet impedance, leading to the suppression of rain-wind induced vibrations (RWIVs). The modifications are based on research undertaken predominantly in Europe and Japan, with two different prevailing systems: HDPE tubing fitted with helical fillets and HDPE tubing with pattern-indented surfaces. In the US and Europe, helical fillets dominate, whilst pattern indented surfaces are more common in Asia.

Research into the effectiveness of helical fillets and pattern-indented surfaces has shown that, besides their purported ability to suppress rain-wind induced vibrations, they also modestly reduce drag forces at design wind velocities. This is of particular interest to bridge designers, as wind on stay planes of long bridges can now produce more than 50% of the overall horizontal load on a bridge. Nevertheless, there is no definitive aerodynamic performance comparison between the two systems. One of the problems of comparing them lies in the fact that different researchers, in different facilities, with varying wind-tunnel flow characteristics and performance, have developed each separately.

As part of a comprehensive review of the aerodynamics of existing cable surface modifications [1], the resulting static force coefficients obtained from wind-tunnel tests on inclined and yawed cables employing both systems are presented herewith. Furthermore, flow visualisation tests are also undertaken to obtain insight into the structures of the flow around the modified profiles.

BACKGROUND

Helically wrapped wires were initially proposed in the fifties to combat vortex-induced vibrations (VIV). It was found that the presence of the helical protrusion significantly reduced the shedding correlation length. It was not until 1992, though, that tests on the use of such a system on a bridge stay cable were undertaken at CSTB (Nantes) in connection with the design of the Normandy Bridge [2] and at the Danish Maritime Institute by Larose and Smitt [3], in relation with the design of the Øresund Bridge. Their tests showed a strong reduction of the RWIV through the disruption of the formation of a coherent upper rivulet in the presence of light rain. As a consequence, a variety of fillet designs have emerged in last decade, often with varying pitch lengths and fillet sizes. It should be noted though that recent full-scale monitoring of the Øresund Bridge by Acampora and Georgakis [4] has revealed that they may not be as effective as originally thought.

The pattern-indented surface, i.e. the application of a discrete roughness pattern, was initially proposed by Miyata et al. [5]. Due to the thermal production procedure, the modifications consist of an indentation surrounded by a protruding periphery of displaced material [6]. The pattern-indented surface has been found to promote the stabilization of the separated flows over the surface of the cable and to inhibit the formation of rivulets [7]. Measured pressure distributions indicate that such a cable enters the supercritical flow state at the lower wind velocities, where RWIVs tend to occur. Furthermore, the flow separation point remains stable at 110° from stagnation in the supercritical region, resulting in a near constant drag coefficient [8]. The pattern-indented surface was first applied

to the cables of the Tatara Bridge in 1999 and later also the Sutong Bridge. Nevertheless, there have been recently observed cable vibrations in lab tests and on bridges that are fitted with these cables [9, 10].
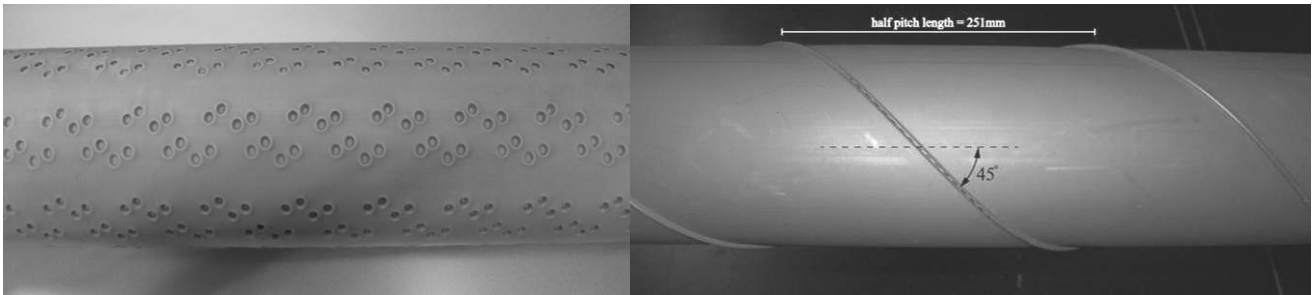

Figure 1. Photographs illustrating the pattern-indented surface (left) and the surface with helical fillets (right).

WIND TUNNEL TESTS

The comparative wind tunnel tests were performed at the $2x2m^2$ cross-section closed-circuit Climatic Wind Tunnel, located at FORCE Technology, Lyngby, Denmark. The flow conditions were measured with a cobra probe and turbulence intensities of 0.41-0.64% were found for 33/66/100% of the tunnel maximum flow velocity at the quarter point positions in both vertical and horizontal directions, all at the upwind end of the cable.

The yawed inclined test setups used for these static tests are shown in Fig. 2. The sectional models are original full-scale samples, supplied by bridge cable manufacturers. The HDPE tube with two helically wrapped fillets has an outer diameter of 160 mm. The fillets are rounded with a height of approximately 3 mm and a width of approximately 4 mm. Furthermore, they have a 3.14 tube diameter pitch length (502 mm and 45°). The average material surface roughness is in the order of R_a ≈ 3.0 μm. The pattern-indented HDPE cylinder has a diameter of 140 mm, as this is an actual sample of the most common diameter of cable used on the Sutong Bridge. The relative surface roughness was determined as the depth of the indentations, measured to be approximately 1% of cable diameter.

Tube lengths of 1.93 and 2.54 metre were used to obtain inclinations of 40 and 55 degrees. Varying the yaw then allowed for relative cable-wind angles in the range of 40-75 degrees in steps of 5 degrees, where 90 degrees relative wind angle corresponds to wind normal to the cable axis. The corresponding aspect ratios (excluding dummy pieces) are within 12-18, depending on cable model and inclination. The force coefficients were measured with 6-DOF force transducers at each end of the cable. The force transducers were installed in between the cable model and the supporting cardan joints fixed to the walls. End plates with a diameter of approximately five cylinder diameters were fitted close to the model ends to eliminate undesirable flow disturbances from the cable ends and cardan joints. Dummy tube pieces were mounted around the force transducers, leaving approximately a 2 mm gap to the cable model and extending beyond the end plates. For the helical model, the dummy tubing consisted of plain tubing, while for the pattern-indented model the dummy tubing was of the same surface type.

No blockage correction has been applied to the presented force coefficients, as the blockage ratio, if considering a simplified section normal to the flow, will for no angle be above 2%.

During the tests, the wind velocity was increased by regular increments of approximately 1 m/s, up to the maximum wind-tunnel velocity of 32 m/s, allowing for supercritical Reynolds numbers to be reached for all test angles and models.

Figure 2. Yawed inclined static test setups: helically-filleted cable (left), pattern-indented cable (right).

RESULTS AND DISCUSSION

Force coefficients

All of the force coefficients presented herewith are based on the measured force components normal to the cable axis, normalised by the along wind flow velocity. All Reynolds numbers are defined as the along wind flow velocity in relation to the cable diameter.

Figure 3 shows the determined average force coefficients for the cable with helical fillets. From this, several observations can be made. Firstly, the normal component of the drag coefficient is observed to systematically drop for increased degrees of yawing, as should be expected based on the definition of the force coefficients. Secondly and counter-intuitively, the flow velocities at which critical Re flow transitions occur is found to decrease for increasing degrees of yawing, i.e. the flow transitions occur earlier when decreasing the flow component normal to the cable. A possible explanation for this could be the turbulence generated by the fillets. The closer the wind angle gets to the fillet angle of 45 degree, the earlier the flow transition occurs. A further explanation might be found in the possible disturbance of the axial flow along the leeward side of the cable. Thirdly, an almost constant supercritical drag coefficient component is obtained, a feature that is normally attributable to flow normal to a pattern-indented cable [1].

The corresponding lift coefficient components are all of a significant magnitude and, for the relative wind angles of 40, 45 and 50 degrees, the lift actually exceed the drag component. It is also observed that when the flow transition occurs, the lift component increases significantly. The largest lift component is found for the relative wind angle of 45 degrees, which coincides with the pitch angle of the helical fillet.
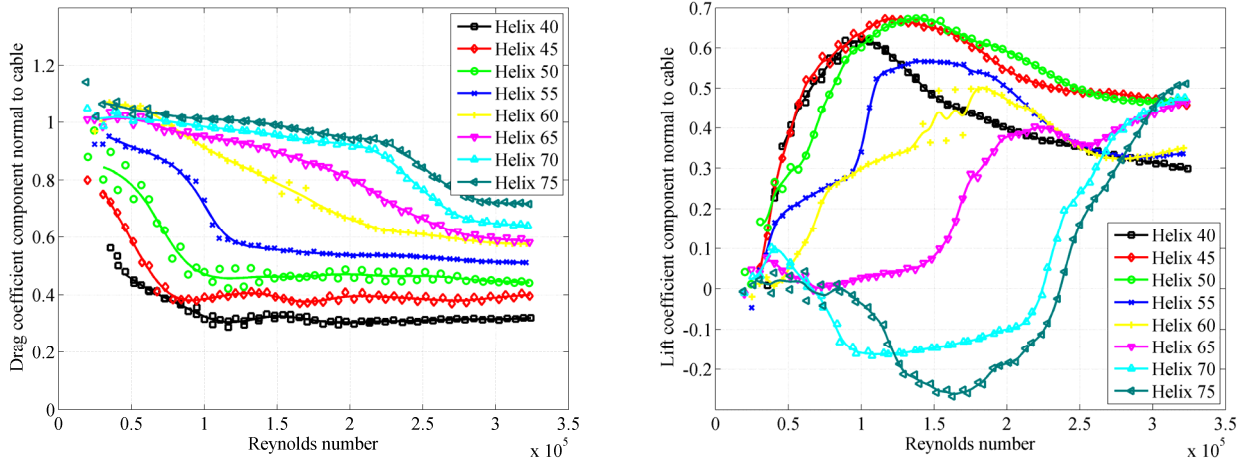
Figure 3. Force coefficients for the helically-filleted cable at varying cable-wind angle: drag coefficient component normal to cable (left), lift coefficient component normal to cable (right).

Figure 4 shows the force coefficients obtained for the pattern-indented cable. For this cable, the development of the drag coefficient component appears to be independent of flow angle. As for flow normal to the cable [1], the yawed cable exhibits a very early transition to the supercritical region due to the high level of surface roughness, which also here is accompanied by the occurrence of nonzero lift coefficient component normal to the cable. While an early transition agrees well with what has been observed for circular cylinders with uniform roughness, the subsequent drag in the supercritical region is nearly constant.

Finally, it can be observed that the critical Reynolds number is determined by the along wind flow velocity alone, i.e. it is independent of the wind angle.
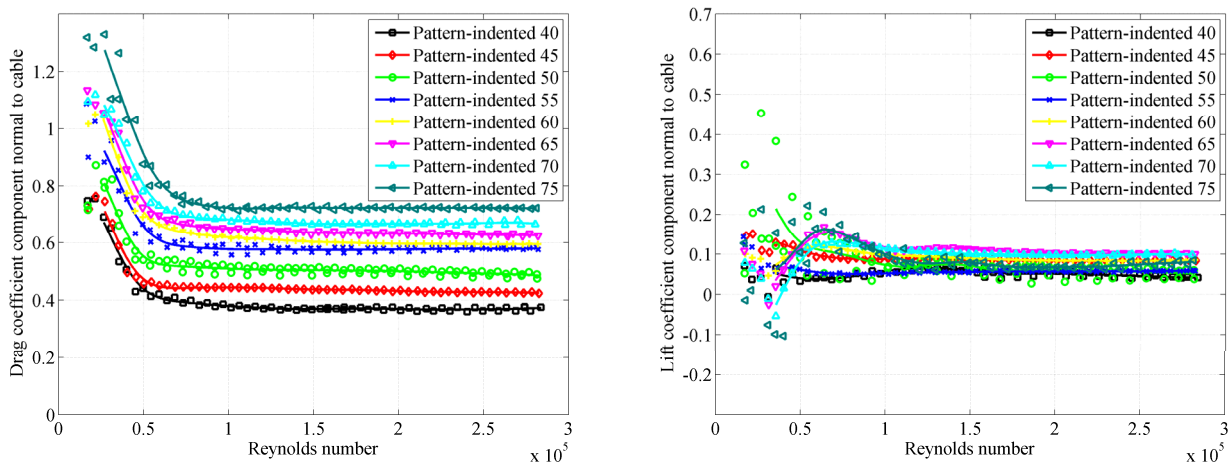
Figure 4. Force coefficients for the pattern-indented cable at varying cable-wind angles: drag coefficient component normal to cable (left), lift coefficient component normal to cable (right).

Angle of attack dependency

Matteoni and Georgakis [11] recently published work indicating that small imperfections on the cylinder surface may affect measured force coefficients with wind angle-of-attack. To investigate this affect, the cables were rotated by steps of 90 degrees about their longitudinal axes. The resulting force coefficients for the specific case of 45-degree relative cable-wind angle for the cable with a helical fillet are presented first.

Figure 5 shows the force coefficients obtained for the helically-filleted cable. While most of the tested positions seem to produce similar coefficients, 270 degrees deviates through the appearance of an earlier flow transition. This is believed to be due to the presence of increased roughness at a specific angular position, generated by a stamped manufacturer's logo. Here, the roughness was positioned

between the upwind stagnation line and the separation line, on the side of the cable where the fillets are near parallel to the oncoming flow. This is potentially the most roughness-sensitive location on the surface.
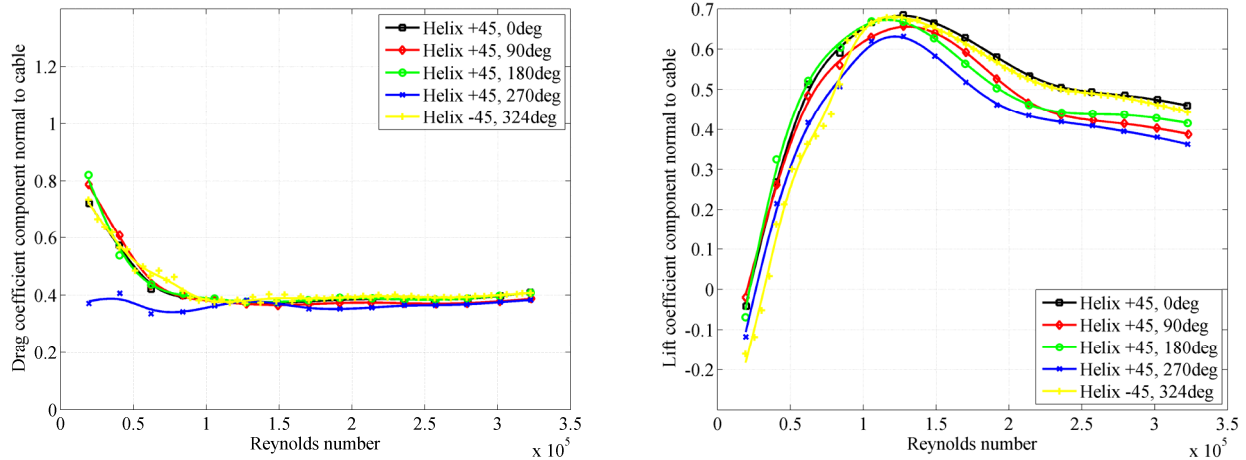
Figure 5. Force coefficients for the helically-filleted cable at 45 degrees relative wind angle for varying angles of attack: drag coefficient component normal to cable (left), lift coefficient component normal to cable (right).

The same tests were performed for the pattern-indented cable (see Fig. 6). For this cable, no significant deviations in the force coefficients with wind-angle of attack could be discerned. It should be noted, though, that steps in angle of attack of 90 degrees might be too coarse. In an earlier study, with flow normal to the pattern-indented cable, the angle of attack was varied with much smaller increments between 0 and 45 degrees [1]. This showed steady drag coefficients, but a periodicity in the lift coefficients, nearly matching the distribution of the surface pattern.
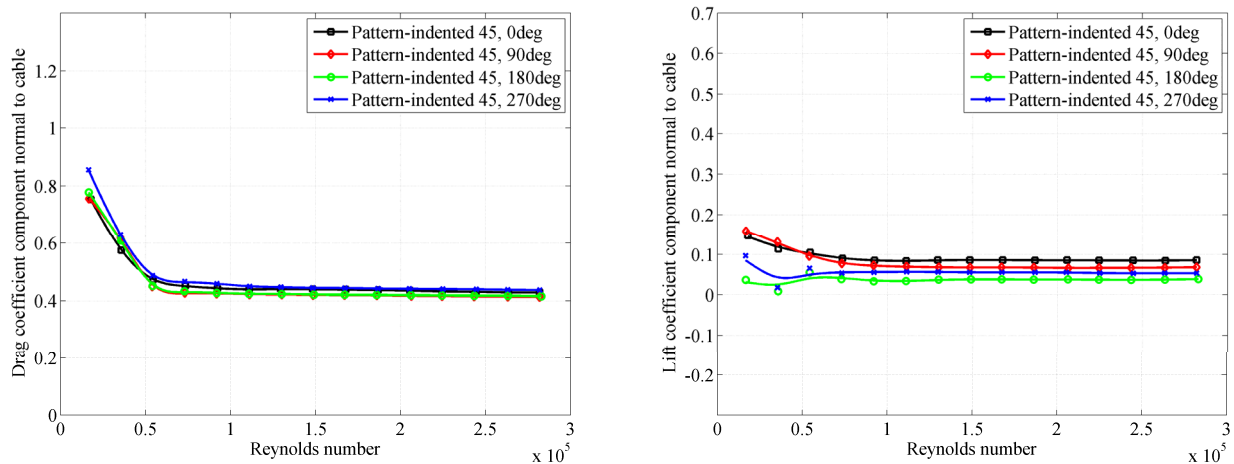
Figure 6. Force coefficients for the pattern-indented cable at 45 degrees relative wind angle for varying angle of attack: drag coefficient component normal to cable (left), lift coefficient component normal to cable (right).

Surface flow visualization

Oil visualization tests were performed to better understand the effect of the surface modifications on the surface flow. Photos obtained during the oil visualization are shown in Figs. 7-11. The tests were performed at 20.3 m/s, well within the supercritical flow regime for both cables, and only at the relative wind angle of 45 degrees, which was obtained through a 40 degree inclination (declining in the downwind direction) and a 22.6 degree yawing.

For the helically-filleted cable, flow separation lines on each side of the cable were identified, although significantly different flow structures are observed due to the difference in the fillet angle in relation to the oncoming flow. This agrees well with the measured nonzero lift force. The separation

line on the right side of the cable is shown in Fig. 7. For this side the fillet is near perpendicular to the oncoming flow resulting in a strong interaction between the fillet and the separation line.
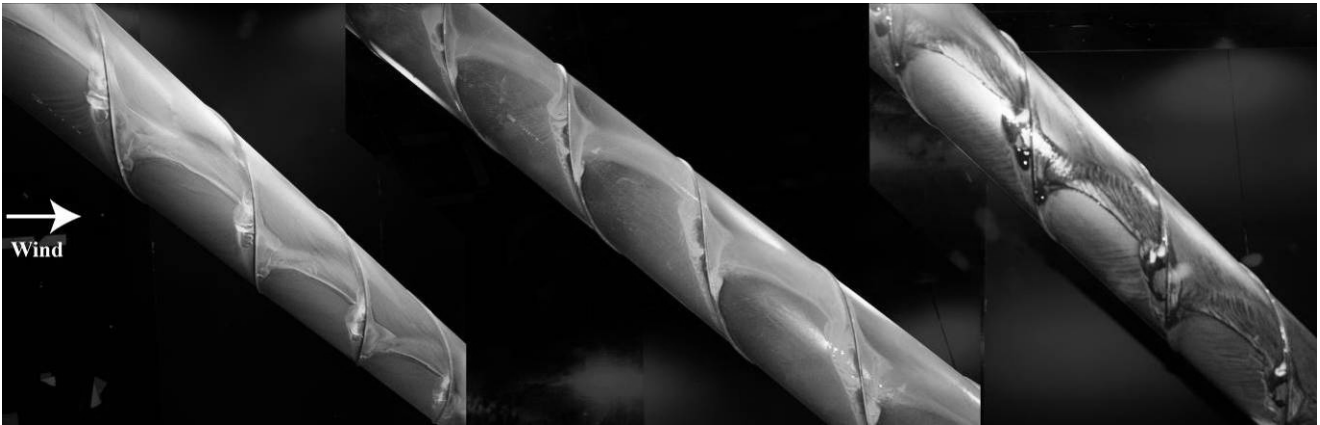
Figure 7. Oil visualization of the separation line along the right side (seen from upwind) of the helically filleted cable.

In Fig. 8, the opposite separation line is shown, where the fillet is near parallel to the oncoming flow. On this side, most of the separation line is unaffected by the fillet. Exceptions are near the fillet where either early (after fillet) or delayed (before fillet) separation occurs.

Figure 8. Oil visualization of the separation line along the left side (seen from upwind) of the helically filleted cable.
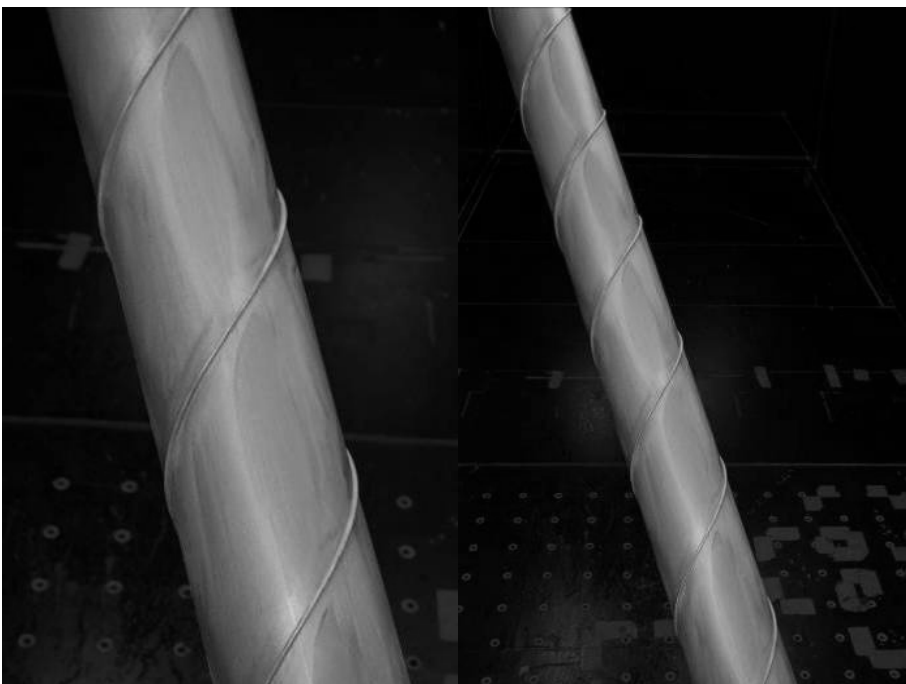
Figure 9. Oil visualization of the leeward side of the helically filleted cable.

On the leeward side of the helically-filleted cable, a flow pattern potentially attributable to an axial flow was observed. This pattern is shown in Figure 9 and was found along the full length of the cable except along the first two half-pitches.
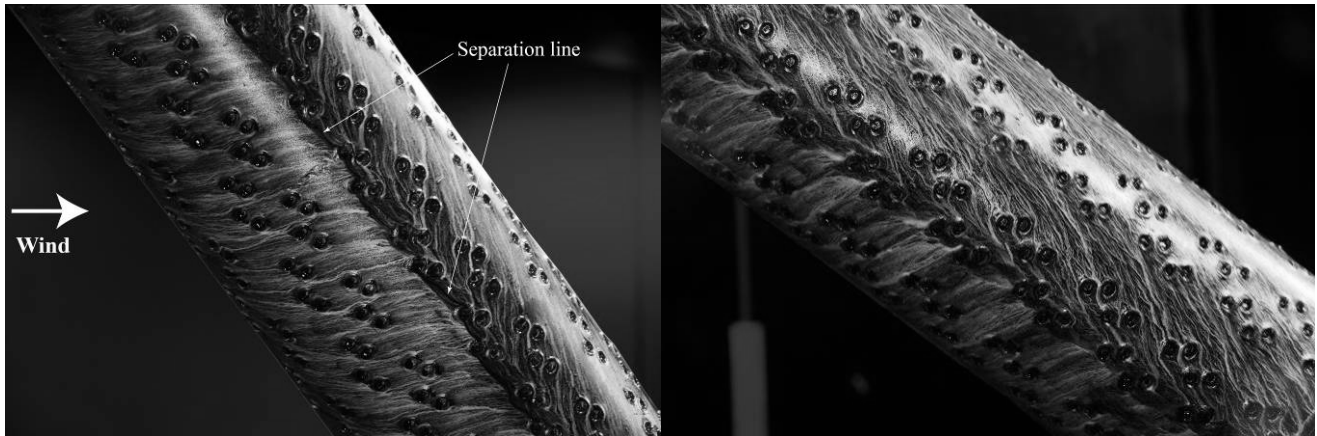
Figure 10. Oil visualization of the separation line along the right side (seen from upwind) of the pattern-indented cable.

On the pattern-indented surface, the protruding peripheries of the dimples seem to guide the flow around the dimples. The flow visualization of the right separation line is shown in Fig. 10, while the stagnation and the left separation lines are shown in Fig. 11. The periodic waviness of the separation line observed in normal flow [1] is significantly reduced and only some minor span wise variations are seen in Fig. 10. Less periodicity is observed in Fig. 11 due to the separation occurring between two groups of dimples. The different locations of the separation also explain the small variations in the lift coefficient components found.
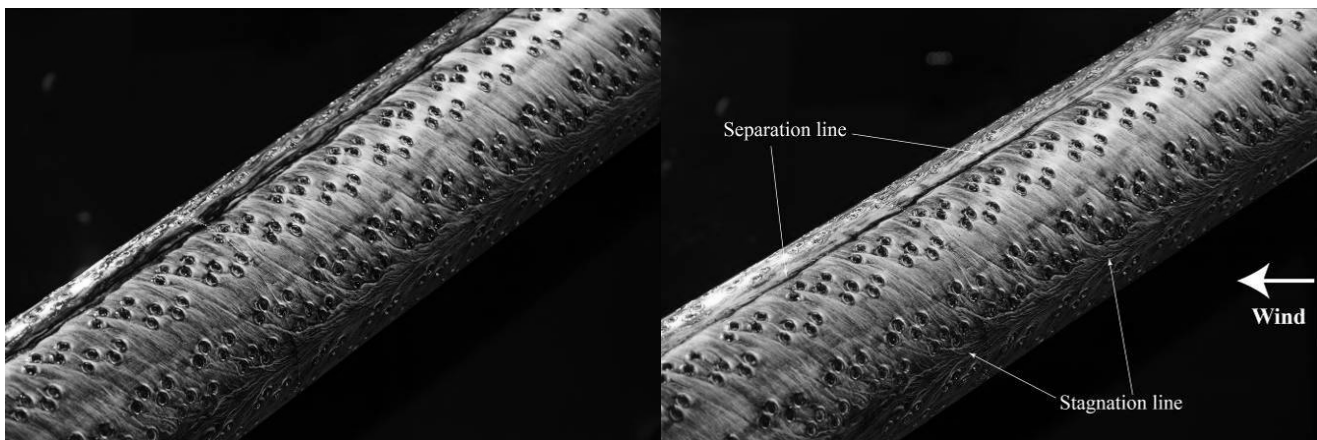
Figure 11. Oil visualization of the upwind stagnation and left separation line on the pattern-indented cable.

BRIEF CONCLUSION

The helically-filleted cable has a near constant drag in the supercritical regime and the flow transition occurs earlier for increased degree of yawing, despite of the reduced flow velocity component normal to the cable. Large lift forces were found for the helically-filleted cable. This agrees with the findings of the surface visualizations, which showed significant differences in the flow patterns on either side of the cable. Flow visualisations also confirmed the existence of a possible axial flow or similar flow structure on the leeward side of the cable.

For the pattern-indented cable, the force coefficients varied with yaw angle, according to the reduction in flow velocity component, whilst the critical Reynolds number did not change for any of the tests.

REFERENCES

[1] K. Kleissl & C.T. Georgakis, 2011, "Comparison of the aerodynamics of bridge cables with helical fillets and a pattern-indented surface in normal flow", *Proceedings of the 13th International Conference on Wind Engineering*, Amsterdam.

[2] O. Flamand, 1995, "Rain-wind induced vibration of cables", *Journal of Wind Engineering and Industrial Aerodynamics*, 57, 353 – 362.

[3] G. Larose, L.W. Smitt, 1999, "Rain/Wind Induced Vibrations of Parallel Stay Cables", *Proceedings of the IABSE Conference, Cable-Stayed Bridges - Past, Present and Future*, Malmo, Sweden.

[4] A. Acampora, C.T. Georgakis, 2011, "Recent monitoring of the Øresund Bridge: Rain-wind induced cable vibrations", *Proceedings of the 13th International Wind Engineering Conference*, Amsterdam.

[5] Y. Miyata, H. Yamada, T. Hojo, 1994, "Experimental Study on Aerodynamic Characteristics of Cables with Patterned Surface", *Journal of Structural Engineering*, 40A, 1065-1076.

[6] H. Katsuchi, H. Yamada, E. Sasaki, K. Inamori, S. Kaga, 2010, "Study on dry-galloping of inclined cable with real indented surface", *Proceedings of the21st National Symposium on Wind Engineering*, p. 387-392, Japan (in Japanese).

[7] T. Miyata, H. Katsuchi, Y. Tamura, 1999, "Comprehensive Discussion on Structural Control for Wind-Induced Responses of Bridges and Buildings", *Proceedings of the 10th International Conference on Wind Engineering, Wind Engineering into the 21st Century*, 1, 487-494.

[8] T. Hojo, S. Yamazaki, H. Okada, 2000, "Development of Lowdrag Aerodynamically Stable Cable with Indented Processing", Nippon Steel Technical Report 82.

[9] *Private communication,* July 2011, Professor Zheng Qing Chen, Hunan University, China

[10] *Private communication,* July 2001, Professor Hiroshi Katsuchi, Yokahama University, Japan

[11] G. Matteoni, C.T. Georgakis, 2011, "Effects of bridge cable surface roughness and cross-sectional distortion on aerodynamic force coefficients", *Proceedings of the 13th International Wind Engineering Conference*, Amsterdam.

Paper X

"Comparison of several innovative bridge cable surface modifications"

K. Kleissl & C.T. Georgakis

Comparison of several innovative bridge cable surface modifications

Kenneth Kleissl, Christos T. Georgakis

Department of Civil Engineering, Technical University of Denmark, Kgs. Lyngby, Denmark,
kenk@byg.dtu.dk, cg@byg.dtu.dk

INTRODUCTION

Over the last two decades, several bridge cable manufacturers have introduced surface modifications on the high-density polyethylene (HDPE) sheathing that is installed for the protection of inner cable strands or wires. The modifications are based on research undertaken predominantly in Europe and Japan, with two different prevailing systems: HDPE tubing fitted with helical fillets and tubing with pattern-indented surfaces. In the US and Europe, helical fillets dominate, whilst pattern indented surfaces are more common in Asia, particularly for long-span cable-stayed bridges.

Research into the effectiveness of helical fillets and pattern-indented surfaces has shown that, besides their purported ability to suppress rain-wind induced vibrations, they also modestly reduce drag forces at design wind velocities. This is of particular interest to bridge designers, as wind on stay planes of long-span bridges can now produce more than 50% of the overall horizontal load on the bridge (Gimsing and Georgakis, 2012). Recently, the authors presented a comprehensive comparative study of the aerodynamic performance of these existing cable surface modifications (Kleissl and Georgakis, 2011, 2012). The comparison helped to eliminate uncertainties in previous studies, due to the fact that several researchers, in different facilities, with varying wind-tunnel flow characteristics and performance, have developed each separately. During the study, the authors were able to document the performance advantages of each of the modifications, but often not to the levels that have been commonly reported.

Therefore, similarly to Yagi et al. (2011), several new surface modifications are proposed herewith, in an attempt to combine and enhance the performance advantages of each of the existing modifications. Each of the proposed modifications was investigated through wind tunnel testing. The resulting mean static force coefficients were obtained from wind tunnel tests, with the cables positioned normal to the wind, and were used as "gateway" criteria for the subsequent investigation of rain rivulet suppression.

SURFACE MODIFICATIONS

Several variations of the surface modifications tested are shown in Table 1. The code given to each modification is a combination of a letter assignment to a type of modification and a running index number, specifying an increase in the number of add-ons and/or roughness. Therefore, letters A and B relate to the application of discrete sharp-edged cylindrical protrusions or Cylindrical Vortex Generators (CVGs) in various patterned distributions. The smaller CVGs (models A1-A8) have a height of 2 mm (D/80) and a diameter of 8 mm (D/20), whilst the larger ones (models B1-B4) have a diameter of 14 mm (D/11). The CVGs were selected so as to generate a localised increase in streamwise vorticity in the form of a pair of counter-rotating vortices. Trough flow mixing, these enhance the near-wall streamwise momentum and thus delay the point of flow separation. The helical pattern with a 30-

degree pitch was adopted, thus introducing waviness into the separation line along the cable axis and a wavy wake structure, which is known to disturb vortex shedding, whilst increasing base pressure.

As the CVGs were not expected to sufficiently suppress rain rivulets, other modifications with the potential for drag-reduction were developed, primarily with rivulet suppression in mind. This first of these modifications involves elongated channels (models C1-C2). Here, a thermal procedure was employed in the generation of the modification, which resulted in protruding lips on each side of the channels. This was intentionally done, so as to increase the localised streamwise vorticity and introduce a wavy wake structure, whilst forming a barrier for rain rivulets running along the cable.

The next three modifications (models D-F) all involve the application of protruding strakes. The strake cross-section has a triangular shape with concave sides and a height of 6 mm, corresponding to 3.75% of the cable diameter. The concave sides have two intended functions. Firstly, they work as a ramp for rain rivulets, forcing water to leave the surface of the cable. Secondly, the concave sides and the sharp tip lead to stronger directional guidance of the remaining water along the strake. In models D1-D2 the strakes were arranged laterally in a staggered helical pattern with a 30-degree pitch. On model E the strakes were positioned circumferentially all around the cable at 1.25 D spacing along the cable. Model F replicates the typical fillet arrangement on current stay cables with helical fillets, leading to a double helix at a 45-degree pitch angle.

Model G was originally proposed and tested by Yagi et al. (2011) and involves 12 rectangular protrusions (7.5 x 5 mm) that are placed in a helical pattern, so as to hinder the formation of water rivulets, whilst reducing the drag through the disruption of vortex shedding.

Finally and for comparison, the most prevalent cable surfaces were also tested. These include plain, pattern-indented and twin helically filleted.

WIND TUNNEL TESTS

The comparative wind tunnel tests were performed at the $2 \times 2 m^2$ cross-section closed-circuit DTU/Force Climatic Wind Tunnel, located at Force Technology, Lyngby, Denmark. The flow conditions were measured with a cobra probe and turbulence intensities of 0.41-0.64% were found for 33/66/100% of the tunnel maximum flow velocity at the quarter point positions, both vertically and horizontally. When examining the yawed cable for rain rivulet suppression, the reported flow conditions are correct for the upwind end of the cable. The surface modified sectional cable models were all based on 160mm diameter original plain full-scale HDPE samples, supplied by bridge cable manufacturers. For the determination of the force coefficients, the models were placed horizontally, resulting in a near 2-D flow normal to the models. The force coefficients were measured with 6-DOF force transducers at each end of the cable. The force transducers were installed in between the cable model and supporting cardan joints fixed to the walls. End plates with a diameter of approximately five cylinder diameters were fitted close to the model ends to eliminate undesirable flow disturbances from the cable ends and cardan joints. Dummy tube pieces were mounted around the force transducers, leaving approximately a 2 mm gap to the cable model and extending beyond the end plates. During the tests, the wind velocity was increased by regular increments of approximately 1 m/s, up to the maximum wind-tunnel velocity of 32 m/s, allowing for supercritical Reynolds numbers to be reached for all test models. With an effective model length of 1.53 m, the aspect ratio was 9.6:1. The blockage ratios for all section models are 8% and the drag coefficients have been corrected with the Maskell III method, according to Cooper et al. (1999). The force coefficients are found according to $C_i = 2F_i/\rho U^2 D L$ where, F_d and F_l are the drag and lift forces, respectively. ρ is the air density, D is model diameter, L the model length and U the upstream undisturbed wind velocity.
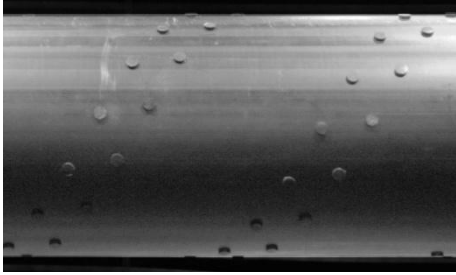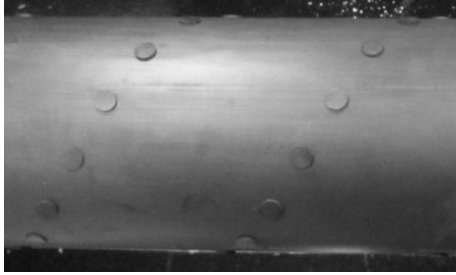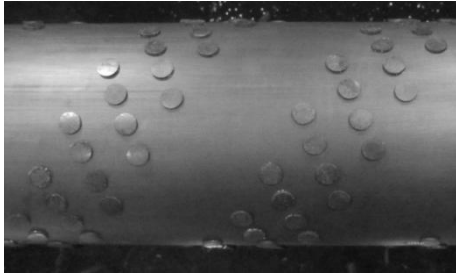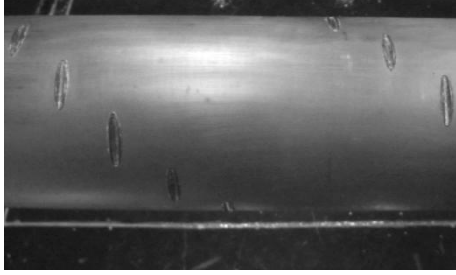
Small CVGs (A4)

Small CVGs (A5)

Small CVGs (A8)

Staggered helical strake pattern (D1)

Staggered helical strake pattern (D2)

Helical arranged strakes (F)
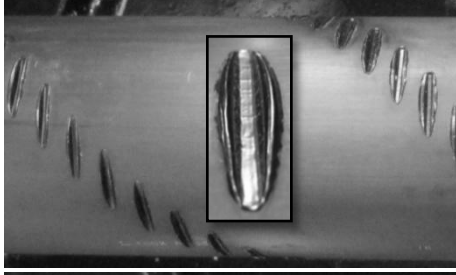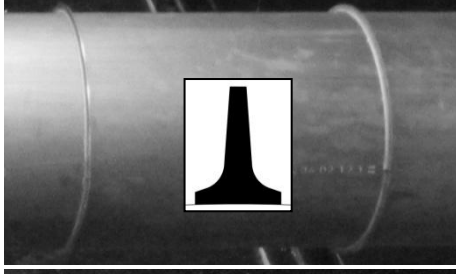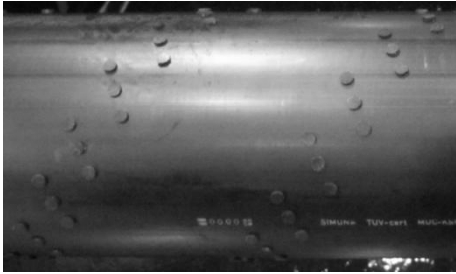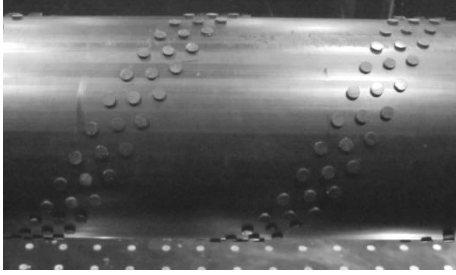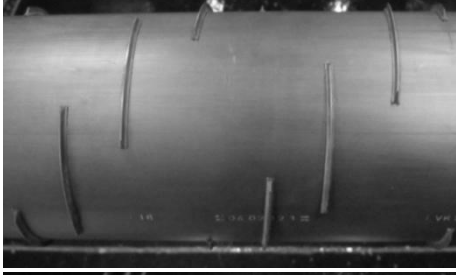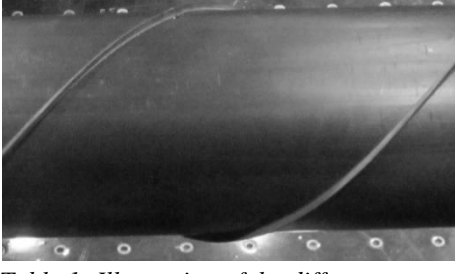
Large CVGs (B1)

Large CVGs (B4)

Indentation helix (C1)

Indentation helix denser (C2)

Circumferential strakes (E)

Yagi et al., 2011 12 helixes (G)

Table 1: Illustration of the different types of surface modifications tested.

RESULTS AND DISCUSSION

FORCE COEFFICIENTS

The average drag and lift coefficients obtained for all the tested models with CVGs applied are shown in Figure 1. For brevity only the results for the modifications shown in Table 1 are presented. Compared with the plain tubing, all of the models with CVGs experienced an earlier flow transition and a tendency for a near-constant drag coefficient in the supercritical region. With the appropriate number of CVGs, the flow transition occurs very gradually and with a minimum of lift force appearing. At the same time some of the tested modifications lead to a rather low supercritical drag coefficient. The best performance is obtained with test model A5, shown in Table 1. This model exhibits a near constant drag coefficient slope, resulting in a lift coefficient smaller than any of the currently applied surfaces. Throughout the tested supercritical Reynolds number range the drag coefficient remained below 0.59.
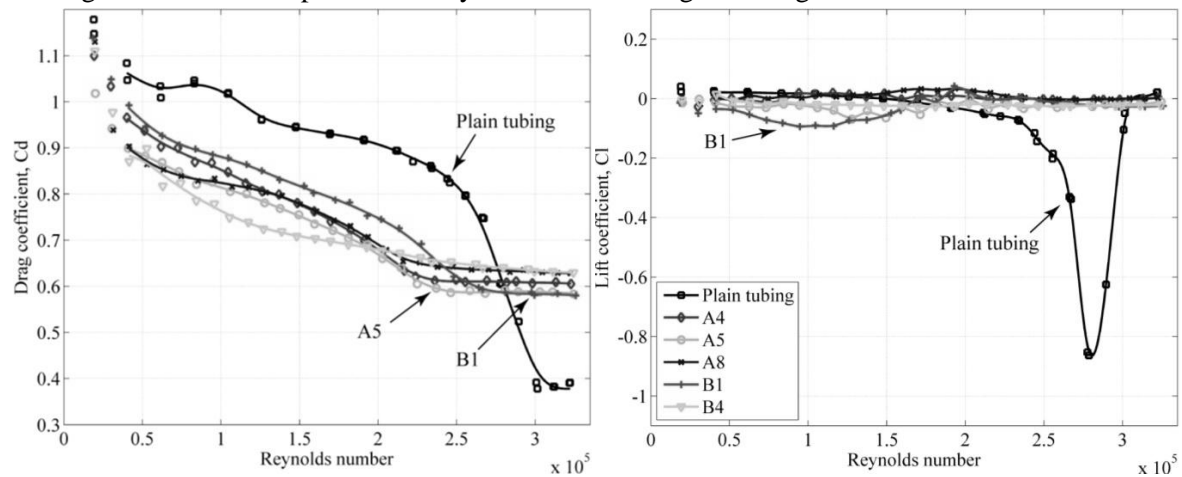
Figure 1. Drag (left) and lift (right) coefficients for the test models with CVG's.

The corresponding drag and lift coefficients for the remaining surface modified cable models, including the currently applied cables, are shown in Figure 2. Among these, model D2 and F appear successful in generating a gradual flow transition and sustaining near-zero lift coefficients. The drag optimised staggered strake arrangement of model D2 reaches a supercritical drag coefficient of 0.65, which is very similar to that of the pattern-indented cable surface. While the drag performance of the helical strake arrangement of model F is very similar to that of the currently applied cable with helical fillets. The reproduced cable surface with 12 rectangular helixes (G) proposed by in Yagi et al. (2011) resulted in a much larger drag coefficient than previously reported and was thus not further considered.
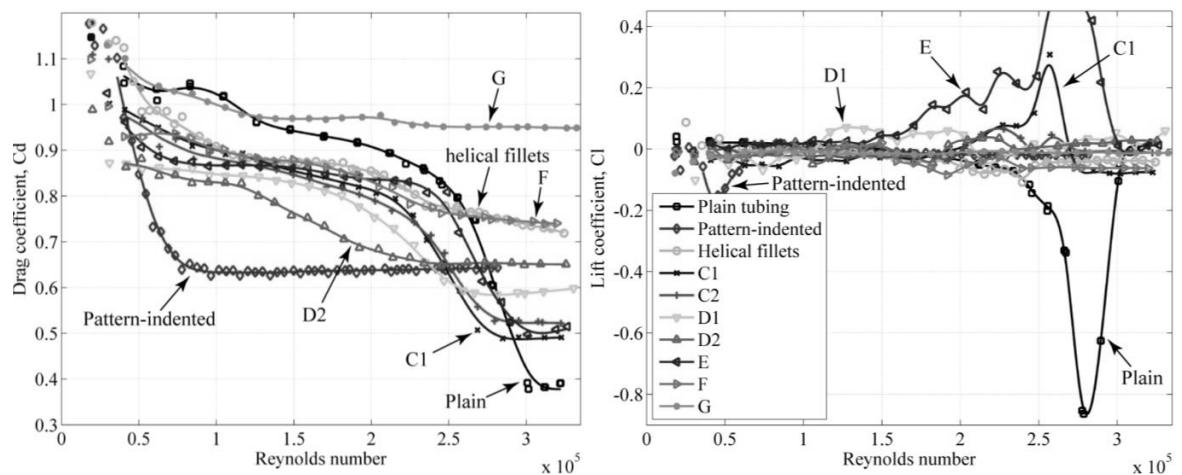

Figure 2. Drag (left) and lift (right) coefficients for the test models with indentations and strakes, compared with the currently applied cables having plain, pattern-indented, and helical fillets.

LIFT FORCE FLUCTUATIONS

A comparison of the fluctuating lift force between models was also made. With the test rig employed, only the total RMS lift fluctuations could be estimated. These are shown in Figure 3. Several of the tested models appear successful in generating small-scale vorticity, whilst avoiding any significant increase in lift force fluctuations. Among the models with CVGs, the smaller CVGs seem to perform best in this respect, with A5 having the best combination of low drag and lift. Model F exhibited the lowest level of lift fluctuations, whilst model D2 and the traditional helical fillets also performed well. The largest fluctuations were observed with the pattern-indented surface, with the lift experiencing a significant peak around Re~1.76×10^5.
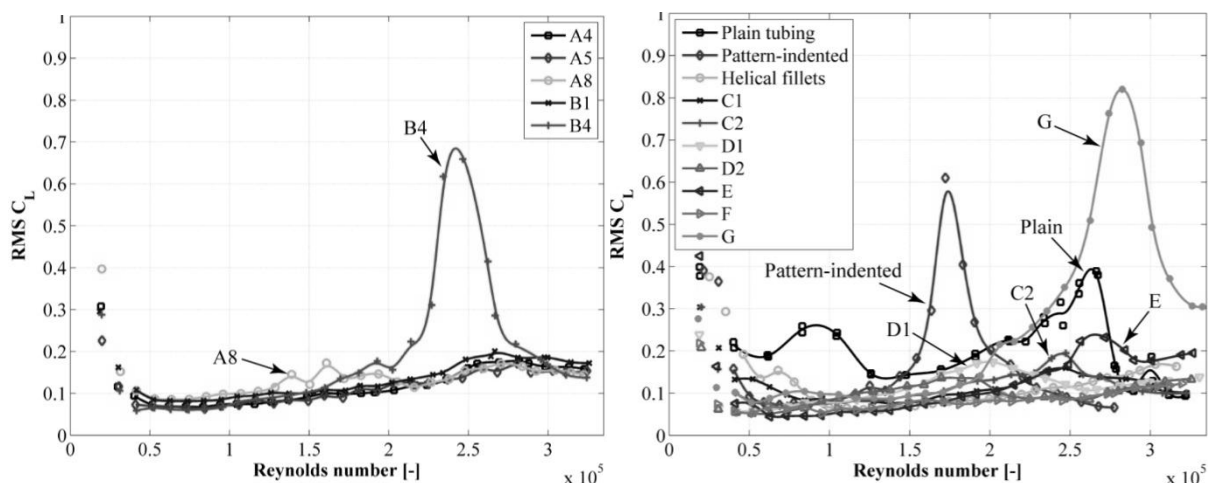
Figure 3. RMS values for the static lift force coefficients. Surface modified models with CVGs (left) and remaining surface modified models including currently applied cables (right).

RIVULET SUPPRESSION

Preliminary static tests on a plain cable showed that a lower rain rivulet formed for all tested wind velocities, while an upper rivulet only formed within the range of approximately 7-15m/s. Outside this range, the upper rivulet did not form as either gravity or the wind loading became dominant. As RWIVs typically occur within this velocity range, the presence of the upper rivulet is often considered critical for the generation of vibrations. The upper rain rivulet on a plain cable can be seen in Figure 4, whilst the lower rivulet is shown in Figure 5. All of the rivulet suppression tests were performed with the cable declining along the wind direction at a cable inclination angle of 40 degrees and with a yaw angle of +/- 22.5 degrees (relative to the along wind direction). In both situations the relative cable-wind angle is 45 degrees. See Kleissl and Georgakis (2012) for definition of angles.

The appearance and position of the rivulets were initially identified during simulation of uniform rain. Afterwards it was confirmed that by adding water only at the upper end of the cable, the same rivulets still formed along the full length of the cable. Based on this, it was decided that the inclined cable should consist of plain tubing at the upper part, where water was added, and then changed into the modified surface, in the central part of the section model, where the rivulets had been fully established. This allowed for a more conservative evaluation of the rivulet suppression ability of the modified cable surfaces.
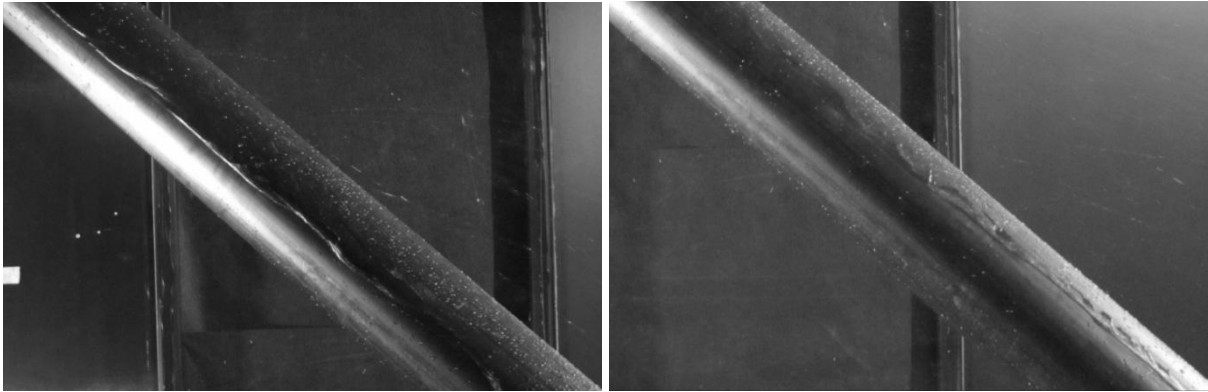
Figure 4. Plain tubing – strong presence of the upper rivulet. 8 m/s (left) and 14 m/s (right).
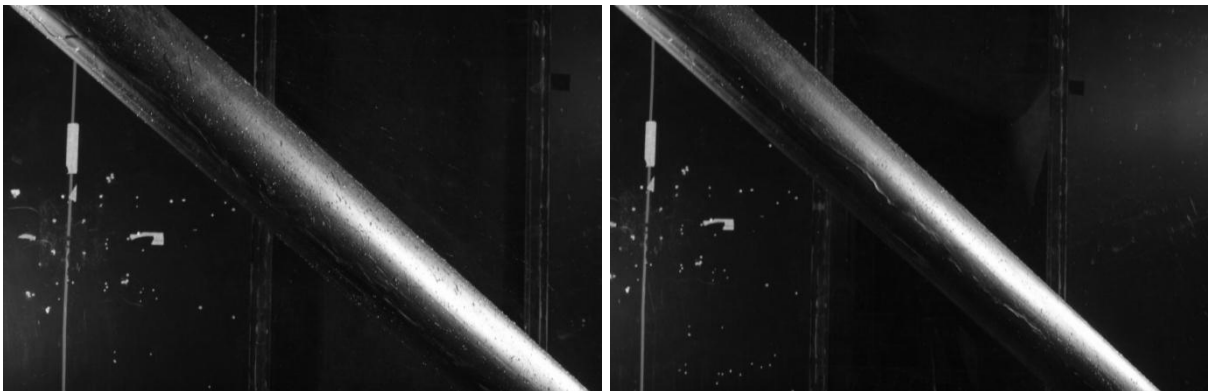

Figure 5. Plain tubing – strong presence of the lower rivulet. 8 m/s (left) and 14 m/s (right).

Figure 6 shows the upper rivulets forming on cable models A8 and B4. Neither of the two CVG sizes was capable of hindering the rivulets. Only minor rivulet disturbances were observed.
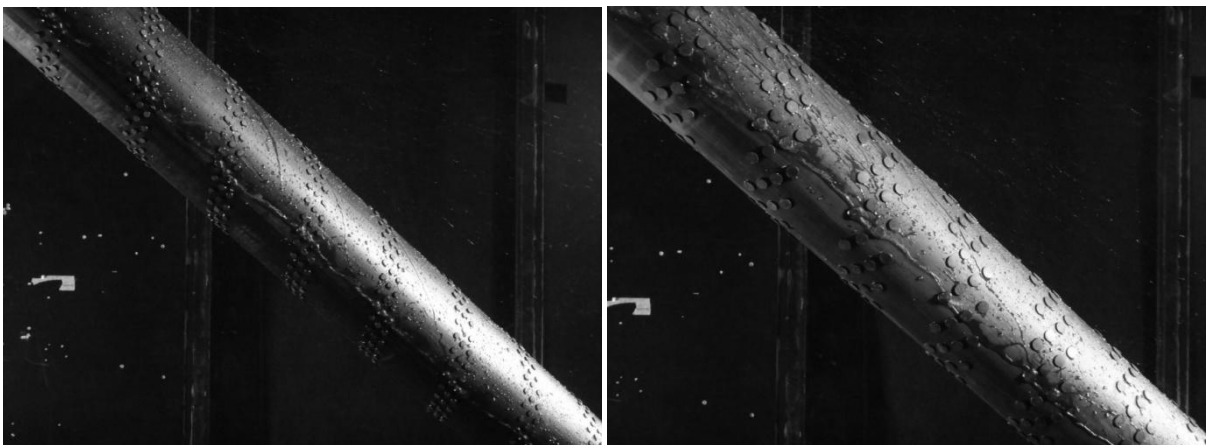

Figure 6. Strong presence of the lower rivulet at 14 m/s. Model A8 with small CVGs (left) and model B4 with larger CVGs (right).

Modified cable models C2 and model E are shown in Figure 7. Whilst neither of them completely suppressed the rivulets, the model with circumferentially arranged strakes (E) only experienced a weak upper rivulet. Although some of the water was knocked off of the surface, the strake arrangement failed to guide the remaining drops away from the point of balance, were the upper rivulet is stable.
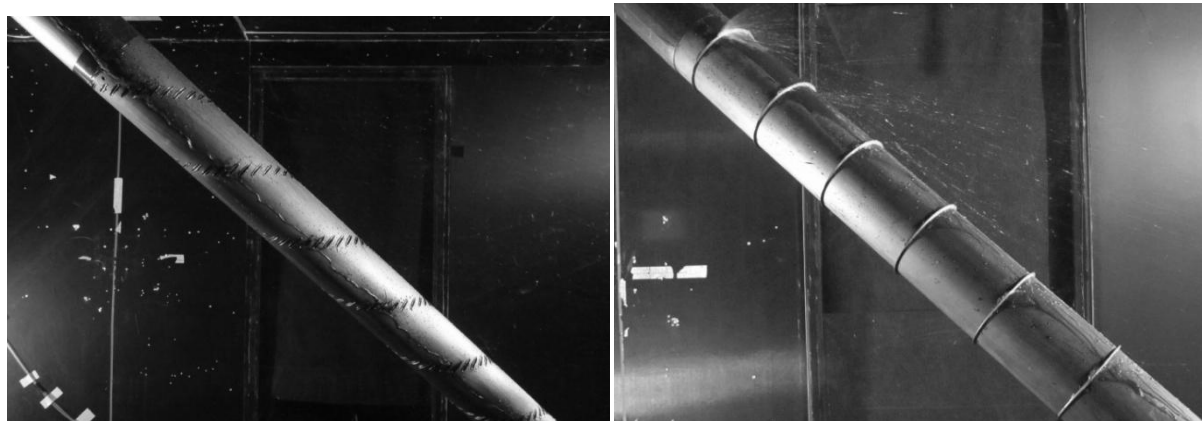
Figure 7. Lower rivulet forming on model C2 at 14 m/s (left) and model E with a weak upper rivulet at 14 m/s (right).

Figures 8-9 show how model D2, with the staggered arrangement of strakes, and model F, with helical strakes, both completely suppress the rivulets. In both cases the strakes work as ramps, which knock off the water rivulet from the surface of the cable.
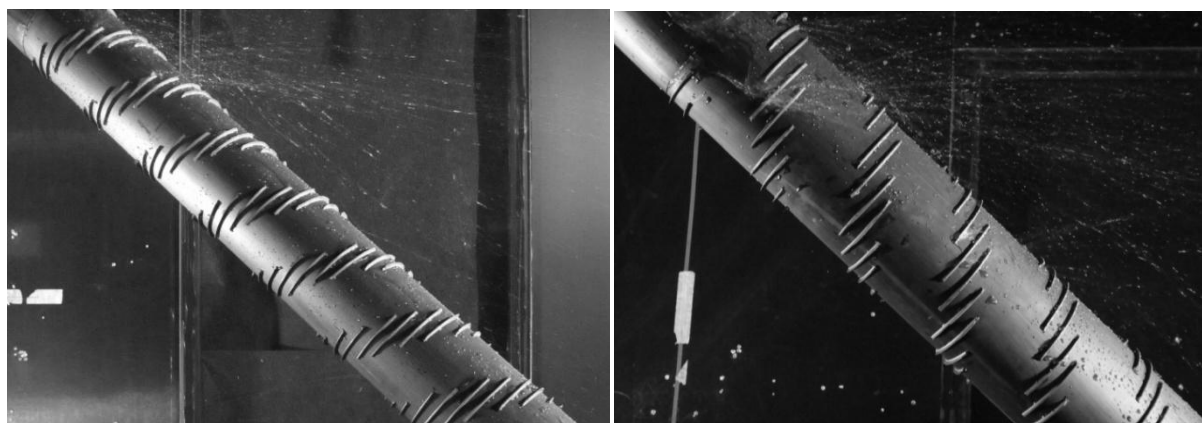

Figure 8. Model D2 completely suppressing the rivulets at all tested angles. Upper rivulet at 14 m/s (left) and lower rivulet at 14 m/s (right).
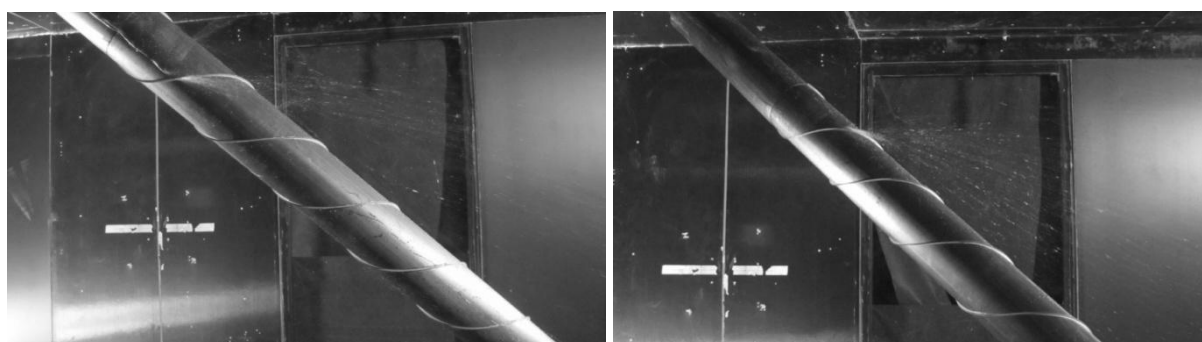

Figure 9. Model F with helical strakes completely suppressing the rivulets. Lower rivulet at 14 m/s (left) and upper rivulet at 14 m/s (right).

The cable with the currently applied helical fillets was found to be partly effective. Figure 10 shows how both a lower and upper rivulet could form despite the fillets' presence.
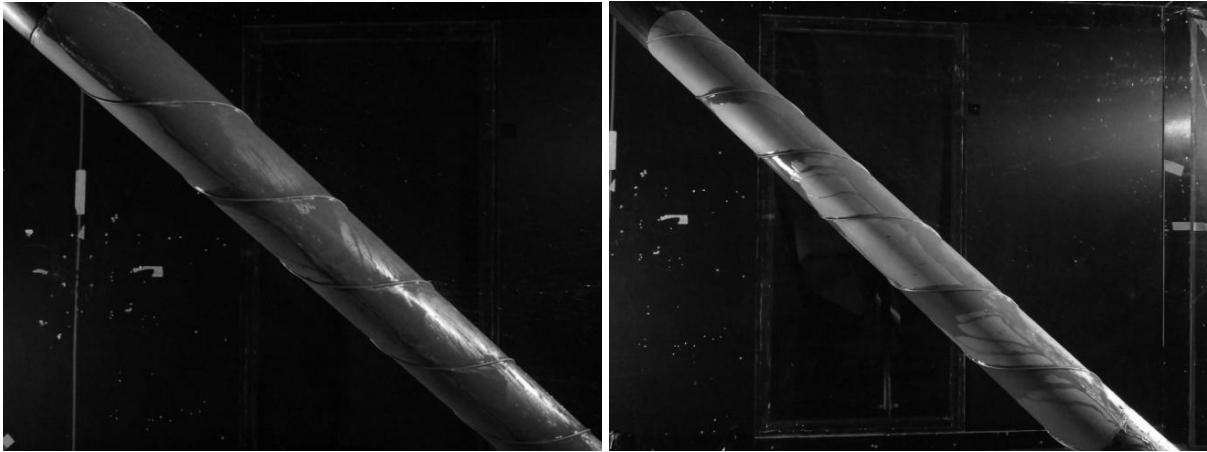
Figure 10. Currently applied cable surface with helical fillets. Strong presence of the lower rivulet at 14 m/s (left) and the upper rivulet at 14 m/s (right).

BRIEF CONCLUSION

Several novel and one previously proposed cable surface modification have been wind tunnel tested for the determination of aerodynamic force coefficients and rain rivulet suppression. Two of the proposed surface modifications outperform or match the current cables with helical fillets, both in drag reduction and rivulet suppression, whilst most of the other proposed modifications were unable to do both. While one of these newly proposed surfaces have similar drag coefficient to that of the current helically filleted cables, the other outperforms it and reaches a drag coefficient of only 0.65; at a level similar to that of the pattern-indented surface.

ACKNOWLEDGEMENTS

REFERENCES

Cooper, K., Mercke, E., Wiedemann, J., 1999. Improved blockage corrections for bluff-bodies in closed and open wind tunnels. Proc. of the 10th International Conference Wind Engineering, Copenhagen.

Gimsing, N.J., Georgakis, C.T., 2012. *Cable Supported Bridges, Concept and Design,* 3rd Edition, John Wiley & Sons

Kleissl, K., Georgakis, C., 2011. Comparison of the aerodynamics of bridge cables with helical fillets and a pattern-indented surface in normal flow. Proc. of the 13th International Conference on Wind Engineering, Amsterdam.

Kleissl, K. & Georgakis, C., 2012. Comparison of the aerodynamics of bridge cables with helical fillets and a pattern-indented surface. Journal of Wind Engineering and Industrial Aerodynamics, 104 - 106, 166 - 175.

Yagi, T., Okamoto, K., Sakaki, I., Koroyasu, H., Liang, Z., Narita, S. & Shirato, H., 2011. Modification of surface configurations of stay cables for drag force reduction and aerodynamic stabilization. Proc. of the 13th International Conference on Wind Engineering, Amsterdam, The Netherlands.